University of Strathclyde
Department of Mechanical & Aerospace Engineering

Quantifying AAAs and developing FEA models for stent grafts

Faidon Kyriakou

A thesis presented in fulfilment of the requirements
for the degree of Doctor of Philosophy

2018

Declaration of author's rights

This thesis is the result of the author's original research. It has been composed by the author and has not been previously submitted for examination which has led to the award of a degree.

Faidon Kyriakou

December 2018

To the AAA victims.

Abstract

Abdominal Aortic Aneurysm (AAA) is an irreversible dilation of the lower section of the aorta that poses lethal threat to the patient. Medical intervention has been conducted for decades via open surgery, yet more recently, the minimally invasive technique of endovascular aneurysm repair (EVAR) is preferred, via the introduction of a stent graft into the aneurysmal region. In this thesis, finite element analysis (FEA) techniques have been developed to model the Anaconda^{TM} stent graft. The aim is to produce the necessary numerical tools to allow for personalized EVAR simulations for mechanical and clinical evaluation.

The basic unit of an Anaconda^{TM} is modelled with a novel FEA approach acquiring computationally efficient solutions without sacrificing precision. By taking into account the manufacturing process, the developed strains and forces can be predicted, allowing for fatigue life and anchoring evaluation. The mean strain of the unit is found to be strongly affected by the oversize of the device, yet its radial force is mainly influenced by the friction of the vessel/stent interface. The effects of non-circular aortic cross sections are also examined and mean aortic diameter approximations are shown to be superior. For all analyses, a phenomenological model of the abdominal aorta is created, able to accurately mimic the pressure-radius response of the artery.

Furthermore, a separate model of lower fidelity and higher computational efficiency is developed, allowing the simulation of the full Anaconda^{TM} stent graft. The model has the ability to predict the deployed position of the device and demonstrates that inclusion of fabric folds can allow for more insightful hemodynamic studies that capture blood recirculation.

Finally, an extensive statistical analysis of 258 patient geometries is conducted and a set of 10 angles is proposed as a way to quantify the AAA shape. No anterior/posterior or lateral symmetries are identified. The measurements of angular and dimensional variables correspond to the most thorough study of the AAA shape available in the literature and allow the identification of average and worst case topologies for future EVAR simulations.

Acknowledgments

This body of work would not have been conducted if it wasn't for a few very dear people.

First of all, I would like to thank Dr William Dempster and Professor David Nash for allowing me the opportunity to participate in this fascinating project and experience a most supportive supervision. Their help and guidance have been much appreciated throughout the course of this work.

My grateful acknowledgement needs also to be directed towards Medical Research Scotland and Terumo Aortic for my scholarship funding (project PhD-723-2013). Not a page of this thesis would have been written without their help.

I would also like to personally thank the Terumo Aortic team (David Bow, Robbie Brodie and Craig Maclean) for the valuable discussions we had and their insightful ideas, directions and input throughout the project; all their efforts allowed me to improve the quality of this work.

The medical data used in the thesis were kindly provided by m2s, Inc. West Lebanon, NH, USA. I owe them my gratitude.

I would also like to thank my academic colleagues and friends, Nick Ioannou, Sofia Alves, Thomas Burel, Ferdin Don Bosco (and all the rest which will remain anonymous yet equally important) who shared my academic and non-academic troubles. A special thanks also needs to go to Dimitra Touliatou for her important CAD input and Lampros Giourntas, without whom my initial settlement period in Glasgow would have been significantly harder.

Lastly, I want to express my warmest appreciation and gratitude towards my parents, who wholeheartedly supported me throughout this endeavour; as they had done so in the past and, as I know, they will keep doing in the future – no matter what. I couldn't wish for anyone better than you. Thank you.

Contents

Selective Nomenclature

AAA	Abdominal Aortic Aneurysm
CAD	Computer Aided Design
CFD	Computational Fluid Dynamics
COF	Chronic Outward Force
CT	Computed Tomography
CTA	Computed Tomography Angiography
ER	Elliptical Ratio
EVAR	Endovascular Aneurysm Repair
FE	Finite Element
FEA	Finite Element Analysis
F_R	Radial force
FSI	Fluid Structure Interaction
FVS	Fast Virtual Stenting
HGO	Holzapfel, Gasser and Ogden model
ILT	Intraluminal Thrombus
$L_{unstheath}$	Assigned displacement to elongate the device
P_m	Time-weighted arterial blood pressure
P-R	Pressure-Radius
RRF	Radial Resistive Force
TAWSS	Time Averaged Wall Shear Stress
U	Strain energy density function
WR	the ratio $Wire\ diameter/Ring\ diameter$

$\Delta\varepsilon$	Delta strain (between diastolic and systolic pressure)
ε	Strain
μ	Friction coefficient
$M\varepsilon$	Mean strain (of diastolic and systolic pressure)

Chapter 1

Introduction

An Abdominal Aortic Aneurysm (AAA) is an irreversible dilation of the lower section of the aortic vessel. In this pathology, the aortic wall weakens and it becomes susceptible to expansion and eventually to rupture, a highly dangerous incident which if not treated immediately, leads almost certainly to death. Prevention or emergent intervention of rupture has been conducted for decades via open surgery but more recently and as technology progresses, an endovascular approach is preferred.

The minimally invasive technique of endovascular aneurysm repair (EVAR), i.e. the insertion of a medical device in the aneurysmal region, consists of the compaction of a stent graft into a catheter, the delivery of it in the pathological region and the subsequent deployment it undergoes inside the aorta so as to create a controlled boundary wall for the blood stream. Even in cases of excellent surgical execution though, the mechanical aspects of the stent graft device itself often affect the outcome of the intervention. And despite all recent developments in the medical sector, no device can be fully optimised if the environment under which it will operate is unknown at the time of manufacture. That is to say, since every AAA patient has a unique aneurysm, tailor-made stent grafts are the best way to provide treatment.

In this thesis, finite element analysis (FEA) techniques have been developed to simulate stent grafts for the treatment of patient specific AAAs. The goal is to create models that can predict key mechanical variables under all vascular geometries.

Towards this end, the commercially available software Abaqus (version 6.13-2, Dassault Systemes Simulia Corp., RI, USA) has been used for the modelling of the Anaconda^{TM} stent graft (Terumo Aortic) and host arterial topologies. These simulations can be used to mechanically evaluate existing devices, to virtually assess the use of them in patient specific geometries and to develop new designs, optimized or tailor made. With such tools, it is hoped that in the future, suitability of the EVAR procedure will be increased whilst the complications that sometimes follow will be successfully minimized.

Further to the FEA analyses, a large study on the morphology of the AAA has been undertaken in order to define the geometrical configuration stent grafts encounter. With the development of a geometry-assessing framework, accurate AAA reporting has been enhanced and a variety of virtual cases that correspond to representative and worst case geometries can be constructed. This study bares clinical usefulness as it improves the current understanding of AAA morphology and provides data that can advance FEA EVAR studies.

The next section offers a brief overview of the chapters that follow.

Chapter 2 introduces the pathology and epidemiology of AAAs. The origin, the benefits and the limitations of EVAR are discussed highlighting the need of using numerical methods to improve the outcomes of the technique. In that context, the FEA method is explained and various examples from the literature are presented to illustrate the current understanding on the mechanics of EVAR. Material modelling challenges and limitations of the simulations are also examined. The section concludes by setting the goals of the thesis.

Chapter 3 presents an extensive statistical study of AAA geometries. A set of 10 angles is proposed as a way to quantify the AAA shape and measurements are conducted in 258 patients. Along with a set of dimensional variables, these values are used to identify average and worst case geometries for the deployment of stent grafts. Furthermore, the common assumption of aortic circularity is challenged by

examining the cross section of the neck of AAAs, revealing the existence of necks with significant ovality. The identification of correlations between a series of variables is also conducted.

The chapter continues with a critical review of the existing material models of the aortic wall available in the literature and identifies challenges and problems with current FEA implementations. Thereafter, a methodology to create a phenomenological material model that can be implemented in a variety of FEA codes is presented. Finally, validation of the developed arterial model is reported along with a technique to recover the unloaded shape of a vascular section when scanned under pressure during computed tomography (CT) scanning.

Chapter 4 examines a novel way to model the basic unit of an Anaconda^{TM} using FEA; the aim is to develop computationally efficient techniques without sacrificing precision. Towards the goal of creating a robust stent graft model for tailor-made simulations, a combined beam and surface element approach proves able to predict the strains and the radial forces exerted by the device by taking into account manufacturing strain effects, an often neglected modelling aspect of utmost importance. Validation with experimental data and comparison with models of higher fidelity establishes confidence towards the technique.

With the proposed beam and surface element model in place, the effects of stent oversizing and friction coefficient alterations at the vessel/stent interface are examined. It is noticed that if friction values are below 0.3, the oversize is not a crucial factor for the success of EVAR, as far as total radial force is concerned. The same is not true, though, in the case of high friction coefficients, where increase of oversize leads to increase of the total radial force.

Finally, in this chapter, the cross section results of Chapter 3 are utilised by deploying stent rings into vessels of various ovalities. Results show that the commonly used circular approximations of the aortic cross section may introduce significant inaccuracies in the estimation of the mechanical state of the stent device.

Chapter 5 describes the development of a full Anaconda^{TM} model, which although shares similarities with the model of Chapter 4, it employs more simplifications. A graft design is developed and tied to the stent rings while a series of features are introduced to allow the model to simulate an efficient delivery and device deployment into any arterial geometry. The techniques and strategies used to overcome the computational complexities of this task are thoroughly discussed.

Experimental testing of the fabric for multiple device sizes is also conducted. In addition, it is demonstrated how these results can allow the definition of the fabric design for both the models of Chapter 4 and 5.

Furthermore, an idealized mock artery was 3D printed and an endograft was introduced and deployed inside it. The experiment is recreated numerically and the results from both deployments are compared showing the satisfactory accuracy of the simulation. Most importantly, the computational efficiency of the model is displayed to outperform the runtimes mentioned in the literature for similar FEA analyses, establishing its cost effectiveness.

Finally, the capability of the model to be used for hemodynamic analyses is demonstrated. The result of the structural investigation are used as input to a computational fluid dynamics (CFD) solver and a fluid flow analysis is performed. It is shown that contrary to the common approximation of a smooth graft boundary, the inclusion of fabric wrinkles can allow the exploration of local flow disturbances, enabling a better clinical assessment.

Chapter 6 concludes the thesis by discussing and summarizing the key finding of the current body of work. The main outcomes and contributions are highlighted, the limitations are reviewed and future work is proposed.

Chapter 2
Background and Literature Review

Abdominal Aortic Aneurysm (AAA) is a life threatening yet frequently asymptomatic condition of the cardiovascular system. Although its initiating mechanism is unclear, significant progress has been made in the treatment of AAAs when they reach a critical size, beyond which catastrophic rupture is considered highly likely. In this Chapter, the minimally invasive technique of endovascular repair (EVAR) is explained along with its merits and its complications. Stent grafts, the essential element of EVAR, are also discussed. The material characteristics, the geometrical effects and the modelling challenges of the devices are presented through the framework of the finite element analysis (FEA) technique. The literature review presented herein will allow an in-depth understanding of the reasoning behind the Chapters that follow.

2.1 Abdominal aortic aneurysm: pathology, epidemiology and treatments

The aorta is the largest artery of the human body. It begins at the left ventricle of the heart and delivers oxygenated blood to the rest of the arteries. It is commonly divided into three sections, the ascending aorta, the aortic arch and the descending aorta which in turn is divided into the thoracic and the abdominal part with the diaphragm separating the two (Fig. 2.1 a). Finally, the (abdominal) aorta terminates in the aortic bifurcation where it splits into the left and right common iliac arteries.

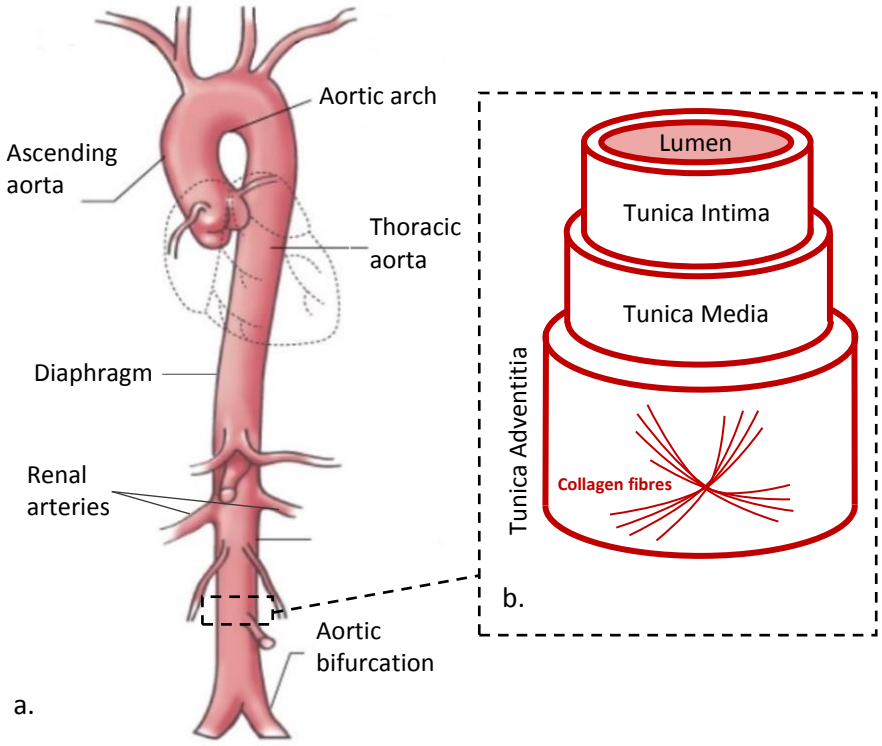

Fig. 2.1 The human aorta [206] (a.) and its structure (b.).

Looking closer into the histology of the structure, it can be seen that, like all arteries, the aortic wall has three layers (Fig. 2.1 b). The innermost layer, which comes into direct contact with the blood lumen, is the tunica intima and consists mainly of endothelial cells. The tunica media lies on top of it and is made up of smooth muscle cells and sheets of elastin while the outermost layer is tunica adventitia and consists primarily of collagen fibres. The overlay of these three layers results in a significantly thick wall (typically around 2 mm) with its own network of small blood vessels that supply the outer parts of the wall with blood and oxygen to keep it healthy. Nevertheless, a healthy state is not always achieved and sometimes, for reasons that surpass our current understanding, aneurysms occur.

Despite all the research that has been conducted, the causes of abdominal aortic aneurysms (AAAs), i.e. the permanent enlargement of the lower aorta, remain poorly understood. There are many factors statistically linked to an increased risk of developing AAA including sex (male), age (>65), smoking, hypertension, atherosclerosis, Marfan syndrome and genetic predispositions [1,2]. The precise underlying mechanisms of AAA initiation and progression though, are yet to be discovered.

2.1.1 Pathology

AAA is a permanent and irreversible dilation of the abdominal aorta (Fig. 2.2), but the definition of the necessary amount of expansion is not unique. Among the criteria that have been used to evaluate an aneurysm are:

- infrarenal aortic diameter larger than 3 cm [3]
- infrarenal aortic diameter larger than 4 cm or large enough to exceed the suprarenal aortic diameter by at least 5 mm [3]
- infrarenal aortic diameter 50% larger than the suprarenal aortic diameter [3]
- infrarenal aortic diameter 50% larger than its normal value [4]

The latter definition can account for differences between sex, age and other factors that affect the normal aortic size and is considered to be the standard one [5]. However, with this definition, it is mandatory to know the physiological diameter of the abdominal aorta, since this is taken as the baseline.

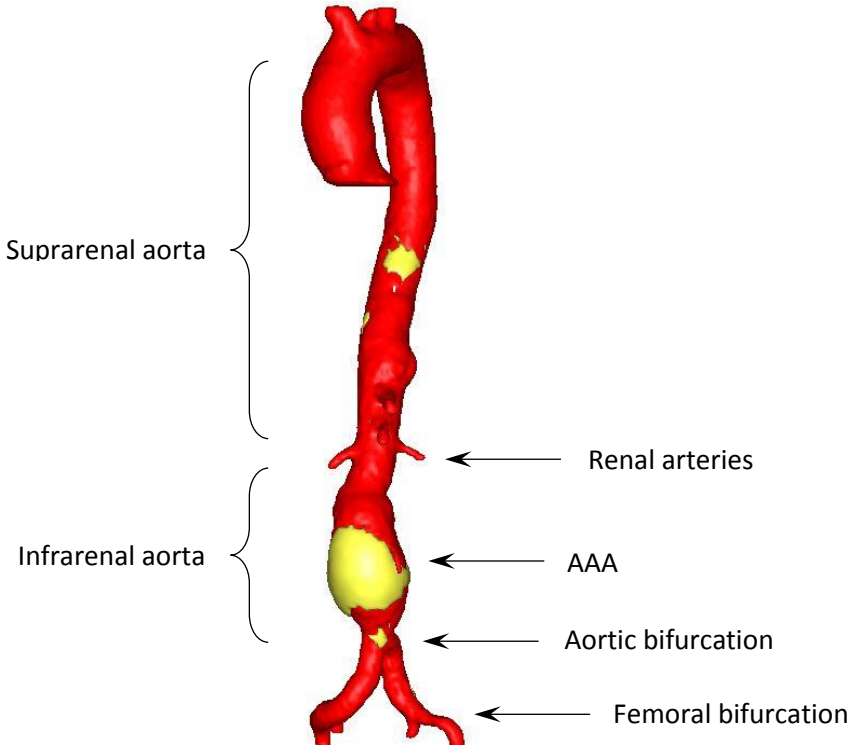

Fig. 2.2 An AAA, as reconstructed from Computed Tomography Angiography (CTA) data. The blood lumen (red) is partly covered in thrombus (yellow).

The first to measure the abdominal aorta *in vivo* were Steinberg et al. in 1965 using aortography [6] and since then, multiple researchers have explored the aortic dimensions [7–9]. For non-aneurysmal individuals, a study [8] that included 1926 participants found that their mean aortic diameter was 18.8 mm at 5 cm proximal to the aortic bifurcation and increased to 19.0 mm just above it. Also, the aortic diameter was significantly larger in men than in women, independent of age, body surface area, height and ethnicity. The size difference of the aortic diameter between men and women has been reported in other studies as well [10] and is accepted as common knowledge.

Moreover, the aortic diameter of people of Chinese, African and Hispanic origin is considered to be smaller than the diameter of Caucasians even after adjusting for differences such as body size [8]. In a large study of 1229 Koreans, the maximal diameter of the aorta was measured with ultrasound and the values reported were considered lower than the respective ones of western people [11]. What is interesting is that while Caucasians have been repeatedly documented to have larger physiological-size arteries, evidence also suggests that AAAs affect them more than peoples of other ethnic groups [8].

As already mentioned, the continual enlargement of the AAA poses the life-threatening possibility of rupture. Hence, by weighting the risk of rupture versus the dangers of surgery, the appropriate time of intervention can be decided. In clinical practice, AAA's maximum diameter is the parameter most widely used to access the probability of rupture [2]. However, it is known that size criterion is not enough in itself. Aneurysms with a diameter less than 5 cm are considered small, yet 10% of occurrences are likely to rupture at that level [12]. Incorporating different risk criteria, the American Association for Vascular Surgery and Society for Vascular Surgery's guidelines suggest intervention on an AAA if the maximum diameter of the aneurysm is greater than 5.5 cm, if it enlarges at 1 cm per year, or when it becomes symptomatic [13]. Recent results, though, suggest that neither the size nor the growth rate may be sufficient to assess the risk of rupture.

While clinicians closely monitor the largest diameter of the AAA, Davies et al. [14], in an extensive analysis of 1326 patients suffering from thoracic aortic aneurysm, found that an index which takes into account both the aortic diameter and the body surface area of the patient can better predict post-operative rupture, dissection or death, than the largest diameter alone can. It is possible that a similar conclusion exists for AAAs.

An alternative approach has suggested that the total volume of the aneurysmal sac affects rupture regardless of the maximum diameter present in the AAA [15,16]. The reason being that size changes of the aneurysm cannot be observed as changes of the maximal diameter in over one-third of the cases [15]. Adding to the difficulty of finding a single rupture metric, the shape of the AAA has also been reported as a possible rupture indicator, fuelling the respective research.

The importance of curvature and its changes has been highlighted by many researchers, some emphasising that it may be the only significant predictor of wall stress [5], a variable that is inherently linked to the risk of rupture. Shape is considered to be of great importance for the stress field developed in the aortic wall [17] and more specifically, it has been found that aortic wall's curvature significantly affects hoop stress [18]. According to Pappu et al., tortuosity of an aneurysm (i.e. how much the vessel turns and twists) changes significantly prior to rupture [19]. Although the number of their experiments was low, they noticed that their tortuosity index increased by 29.3% before the rupture of AAAs, whereas the mean diameter increased just by 3.3%. In another study though, Fillinger et al. observed the opposite trend stating that ruptured AAAs had a less tortuous anatomy than non-ruptured ones [10]. More studies have to be undertaken towards this end, however, the indications suggests that tortuosity can give an insight on the risk factors of rupture. Besides that, no relation between the shape and the size of the aneurysm seems to exist [20] making the need for shape exploration even more urgent.

In addition to the indicators discussed above, there are also pre-rupture radiological signs clinicians search for. These signs include the "crescent sign" which is a

haematoma within either the thrombus or the aneurysmal wall that appears crescentic on CT or MRI, the “draped aorta sign” which happens when the aorta drapes on the posterior vertebra and finally and most rarely, a discontinuity in the circumferential calcification [2].

The morphology of the AAA is also important for risk assessment. Aneurysms are described to be either fusiform or saccular. Saccular aneurysms are balloon like expansions that bulge out of the vessel only on a specific side. On the contrary, fusiform aneurysms bulge out on all sides of the vessel creating a “uniform” expansion. The latter type is the most common one and is considered more dangerous than the former at a given size [21].

Finally, inside most AAAs, there is usually intraluminal thrombus (ILT), a large, stagnant blood clot consisting of blood cells, proteins and cellular debris [22]. The existence of ILT causes hypoxia to the vessel by reducing the oxygen flow to the underlying aortic wall by as much as two-thirds [2]. This effect, in conjunction to biochemical reactions initiated by the presence of ILT, compromises the tensile strength of the aortic wall by up to 36% [23]. Nevertheless, the presence of thrombus has been reported to have contradictory effects. Researchers do not agree whether it increases or decreases the stress of the aneurysmal wall and both positive and negative effects on the rupture risk have been hypothesised [24]. Furthermore, the mechanical properties of it are not well understood and it is indicative that the elastic modulus of it reported in the literature range from 1.3 to 57 N/cm^2 [25]. Because of all these uncertainties, ILT has not been taken into account in the current study.

2.1.2 Epidemiology

The rupture of the AAA sac results in a very high mortality rate varying from 76% [26] to 90% [27], ranking AAA rupture as the 13^{th} leading cause of death in developed countries [28]. In the United States alone, 200,000 people are diagnosed with AAA annually [29] (6.5% of the population) and Silverberg & Lubera [30] reported that ruptured AAAs are the 10^{th} cause of death for men over 55 and women

over 75. In the UK, the National Records of Scotland reported that in 2016 out of all deaths related to diseases of the circulatory system, 2.8% occurred due to AAAs and dissections and resulted in 427 deaths [31].

Regarding the demographics, AAA incidents are four to six times more frequent in men than in women, however, when considering small aneurysms, the rupture ratio is three times higher in women than in men [32]. The greater risk of small aneurysms in female patients might be related to their smaller initial aortic diameter. Furthermore, it has been shown that females exhibit faster growth rate and larger proportional dilatation than males [33] and may actually benefit more than males from EVAR procedures [34].

Currently, in the UK, the guidelines of NHS suggest that AAA surveillance imaging should be conducted every year for small AAAs (3.0 – 4.4 cm) and every 3-months for AAAs with diameter of 4.5 – 5.4 cm. For larger AAAs, the instruction is to refer to a surgeon to consider elective repair of the aneurysm so as to prevent rupture [35].

2.1.3 Open aortic surgery vs EVAR

Because of the extreme severity of ruptured AAAs, elective surgery becomes a necessity once the aneurysm reaches a critical level. The traditional approach for decades has been open aortic surgery, where the aneurysm is cut open, a graft is sewn into the proximal and distal part of the vessel and ultimately the aneurysmal sac is sutured together again, enclosing the graft. Recent advancements in technology though, have allowed a second approach to emerge. Endovascular repair is a minimally invasive technique during which a stent graft device (also known as an endograft) is introduced into the femoral or iliac artery of the patient and with the aid of a delivery system is placed inside the aneurysmal region. Upon positioning and deployment of the stent, an artificial lumen is created for the blood flow leading to the decrease of pressure at the aneurysmal wall. More commonly, the stent graft consists of 3 parts (or modules), namely the main body and two iliac legs (Fig. 2.3).

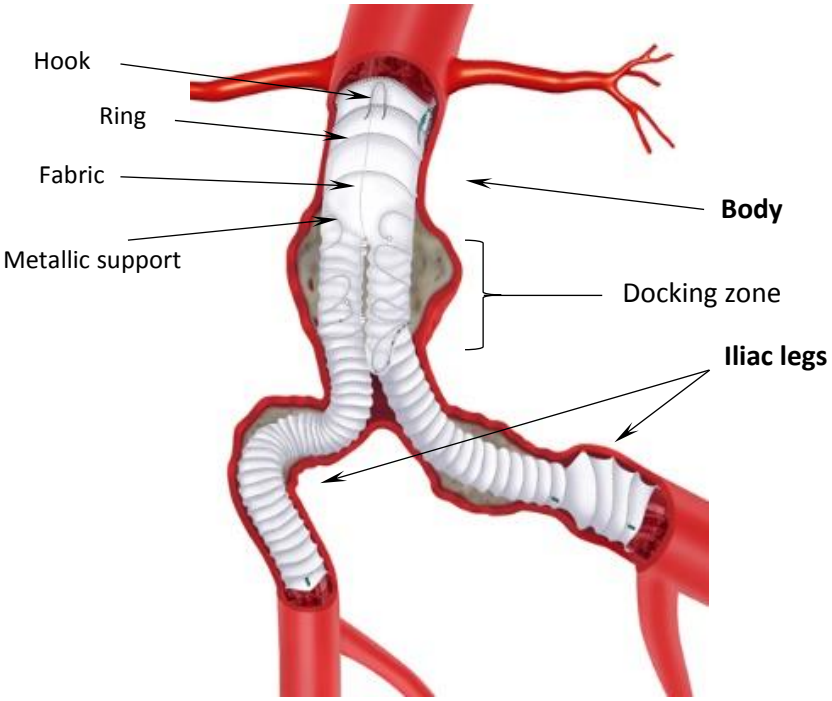

Fig. 2.3 The Anaconda^{TM} stent graft (Terumo Aortic), deployed into an AAA [207]. All the major building blocks of the device have been highlighted.

Stents for the treatment of stenosis date back to the work of Dotter [36] who inserted plastic tubes into the femoral and popliteal artery of dogs in 1969. These medical devices, though, were not implanted into humans until a decade later, after limitations of balloon angioplasty were identified [37]. The first coronary stent procedure was performed by Jacques Puel in Toulouse, France, in 1986 [38], however, a further five years were required until the use of stent grafts in AAAs. Following the work of the earlier pioneers, Juan Parodi [39] was the first to perform an EVAR procedure in Buenos Aires, Argentina, in 1991. Since then the technique has been significantly developed and has become mainstream.

A US study reported that the percentage of patients who underwent elective EVAR was over 30% in 2001 and increased to over 40% in the following two years [40], showing an increasing trend in preference. A recent study showed that EVAR is nowadays the most common technique for repairing AAAs although part of the reason might be hospital competition to offer new procedures and better patient experience rather than clinical indications alone [41].

When compared to open repair, EVAR has shown to have lower short-term rates of death and complications [42]. This initial survival benefit, though, is lost a few years after the operation [42,43]. Moreover, EVAR is more expensive [43]. Over an 8-year follow-up period, Propper & Abularrage [44] calculated that because of aneurysm-related readmissions, the total cost of EVAR is more than £3000 higher than open surgery per patient.

These assessments show that EVAR, although minimally invasive and hence significantly more convenient for the patient (shorter operating time, less blood loss and shorter hospitalization), has yet to prove its long term superiority. Stent grafts need to improve to become safer and gain a stronghold when it comes to criticism regarding medical economics.

2.1.4 EVAR suitability

Various percentages of patient suitability for EVAR have been reported in the literature. Different researchers have presented values of 30% [45], 50% – 61.6% [46] or even 66% [47] of patients being suitable for endovascular repair. However, when taking into account large AAAs with a diameter greater than 5.0 cm, less than 33% of them are reported to be morphologically suitable for the procedure [48]. Despite the actual percentage, it is true that EVAR is considered to be intrinsically more suitable for small aneurysms; hence, it has been argued that it might be preferable to decrease the threshold of AAA intervention when it comes to endovascular operations [2]. Adding to that, it has been reported that a large aneurysm diameter is associated with a shorter aneurysmal neck length [46] i.e. shorter available landing zone for the stent graft, a fact that impedes EVAR. The same study suggested that endovascular surgery is more promising for aneurysms less than 6 cm.

In contrast, intervening too early will have its own adverse effects. From a population of more than 30,000 patients it has been estimated that early EVAR will result in 482 fewer deaths related to AAA rupture while at the same time will lead to 140 extra deaths due to EVAR complications [49]. Early intervention for the same

population will also result in 21.9% more EVAR procedures and $300 million increase in health costs (expenses were calculated for the USA). Note that for this study an intervention at a 5.0 cm AAA was considered early and was chosen after arguing that, in clinical reality, it is rare to wait until the aneurysm reaches the 5.5 cm threshold. Choosing even smaller diameter thresholds would only worsen the results.

Patient suitability for EVAR is also related to sex and age. Because of anatomical differences, men are almost twice more likely than women to meet the criteria for EVAR [47], although women have been shown to have better results when examining the early outcomes of the endovascular repair [34]. Similarly, older patients are higher risk candidates for open aortic surgery, hence EVAR should be preferred. At the same time, though, older candidates are more likely to be disqualified from the process due to the anatomy of their aortic neck or iliac arteries [50]. As a result, it seems like those who have the greater difficulty to undertake EVAR are the ones who would benefit the most from the procedure.

EVAR suitability is most often connected to the arterial topology of the patient. As will be discussed in Chapter 3, short aneurysmal neck and tortuous arteries are the most common criteria for EVAR exclusion. Because of the latter, it has been argued that if stent grafts could be delivered via thinner catheters the number of patients suitable for EVAR would increase from less than 50% to 60% [51].

Since suitability challenges are intrinsically linked to the geometrical parameters of the host vessel and the endograft, better stent designs could address most of them. This, in part, drives the research in the field. Stent grafts should become more tolerable to demanding geometries and ideally be an available treatment option for every AAA patient.

2.1.5 EVAR complications

The EVAR procedure can have a variety of complications with endoleaks being the most common [52]. An endoleak occurs when the aneurysm is not completely

excluded from the circulation, hence the pressurization of the aneurysmal sac progresses despite stenting. There are five types of endoleak (Table 2.1).

Table 2.1 The five types of endoleak

type I	inadequate seal – leakage occurs at any of the stent graft ends
type II	flow from a branch vessel (e.g. lumbar or inferior mesenteric artery)
type III	leakage through a defect on the fabric or separation of the modular components
type IV	leakage from porous fabric
type V	continual expansion of aneurysm without evidence of leakage

The frequency of endoleak occurrence ranges in the literature from 10% to 45% [53]. It is interesting to note, though, that unlike the other types, type II endoleak may have a positive impact on EVAR thanks to a mild reduction of pressure difference between the stent-graft and the aneurysmal sac, thus helping the stent graft to stay in place [25].

Despite the fact that sometimes endoleaks may resolve spontaneously, permanent surveillance is necessary since untreated endoleaks that persist can lead to late aneurysm rupture. To that end, wireless pressure sensors (that can be implanted during EVAR) are being developed, aiming for constant surveillance of the aneurysmal pressure [54].

Apart from endoleak complications, EVAR can also be compromised during the surgical procedure (by arterial thrombosis, dissection, contrast-induced nephropathy), after surgery (by ischemic complications due to clot embolization or coverage of an important vessel) and even months after the operation (due to limb thrombosis caused by stent graft kinking) [52]. Stent-graft infection is another complication that can be lethal if untreated, but this occurs in less than 1% of EVAR procedures. [55]

A later complication of EVAR that can result in a series of the aforementioned issues is stent graft migration. During migration, the device alters position and at least

a section of it axially relocates in the vascular tree. This can directly lead to type I endoleak, graft tear which will result in type III endoleak and stenosis of stent-graft limbs or limb occlusion; incidents like these have been reported even 5 years after EVAR [56,57].

Migration can be attributed to short aneurysmal neck, device deployment close to the proximal end of the aneurysm, insufficient stent anchoring and inadequate columnar strength [58,59]. Zarins et al. [59] reported the endograft migration rate to be just below 19%, underlying the necessity for careful EVAR planning and patient inclusion criteria.

To tackle migration, stent grafts have a variety of design features ranging from barbs and pins to hooks and anchors. Such metallic parts, though, are susceptible to fatigue fracture. Although cases of fractured anchoring mechanisms rarely occur, Najibi et al. [60] reported hook fracture in two EVAR patients 3 years after the procedure. In a more extended analysis, Jacobs et al. [61] studied 7 stent designs over a 10 year period (1992-2002) and found that fatigue failure occurred in different frequencies among them with the percentages ranging anywhere from 0% to 72%. In this analysis, suture disruption, metal fracture or fabric wear, were all considered as fatigue failure.

Sometimes, unsuccessful EVAR will lead to surgical re-intervention. Migration after the first post-op year is the main reason for such a development, frequently because of late dilation of the proximal neck [25]. Within 4 years post EVAR, it is estimated that 40% of patients will experience some form of a device-related complication and half of them will undergo a second operation [53]. Note that despite the fact that different stent graft devices have the ability to treat different subsets of patients depending on the challenges of their anatomy, most of the EVAR complications are not specific to any device [62].

All these facts point out the intrinsic challenges of EVAR. The need for a landing zone, the low tolerance of the delivery system for tortuous paths and the necessity to monitor EVAR patients post-op for the detections of endoleaks are elements that are inextricably linked with the procedure. As a result, the need to develop tools

and methods to allow improvements upon the endograft designs and the EVAR process itself becomes self-evident. Stent grafts that can operate in tortuous geometries, that can provide patent flow lumens, be resilient to fatigue and have enough anchoring to prevent migration are some of the most important design needs. Similarly, endografts should be able to compact into narrower delivery systems while the delivery systems should become more flexible. Further to that, tools that can allow for virtual stent deployments prior to surgery can provide vital help to EVAR planning through the examination of different endograft design options, different methods/locations of device placement and long-term assessment of the stent graft and blood flow states.

The realization of new technologies and the advancement of the existing ones can mitigate those challenges and allow new possibilities leading to more successful surgeries and higher survival rates.

2.2 FEA and stent grafts

Because of the intricacies associated with the stent devices described below, as well as the inherent complexities of the vascular environment which will be illustrated in Chapter 3, analytical solutions for the mechanical assessment of EVAR are generally not possible. As a consequence, numerical techniques are being used to model and analyse the introduction, deployment and operation of stent grafts inside aortic sections. Herein, the widely used numerical method of FEA is being applied.

The finite element technique is a discretization method which meshes a structure into a number of simple-shaped elements. Then the quantities of interest (e.g. displacements) are assumed to vary over each one of these elements in a way that can be approximated with polynomial functions. The attempt to solve a complex structure is thus turned into the effort to solve an assembly of numerous simple geometrical elements. To acquire solutions with a discretization technique, time needs to be discretised as well. By either requiring in each time step to use variable values

from the new or the old/current time step, implicit and explicit approaches are defined respectively. Implicit approaches are stable for any time interval and are preferred for static analyses whereas explicit approaches require very small time steps, hence, are deemed suitable for either dynamic analyses or highly non-linear problems. As will be seen later on, an implicit approach was used in Chapter 4 while an explicit one was employed in Chapter 5.

In the following section, the key FEA developments on stent grafts are discussed. The section starts by introducing the physical structure of stent grafts and continues by presenting an overview of Nitinol, currently the most popular material for endograft devices. The section proceeds with the modelling challenges of the material and concludes with both the advancements and difficulties in EVAR simulations.

2.2.1 General features

An EVAR stent graft is a metallic structure covered with fabric. Since its purpose is to create and preserve an artificial lumen for the blood flow, the device has to be structurally stable to stay in place and its fabric has to have low porosity to prevent blood transfer into the aneurysm. The metallic section serves as scaffolding

(a) (b) (c)

Fig. 2.4 Most EVAR stents have Z-type configurations, either in a series of Z-shaped loops (a – Endurant®, Medtronic) or in Z-shaped spirals (b – Zenith Spiral-Z®, Cook Medical). Exception is the helical shape of Aorfix® (Lombard Medical) (c) and the bundle rings of Anaconda® (Terumo Aortic) (Fig. 2.3).

that supports the fabric and ensures the device's fixation so as to ensure sealing. The shape of the metallic section for most devices has a Z-type configuration; exception to that is Aorfix™ (Lombard Medical Technologies PLC, Didcot, UK) which has a helical wire and Anaconda™ (Terumo Aortic, Glasgow, UK) which has a series of circular rings (Fig. 2.4).

Regarding the materials, Nitinol alloy is currently the most widely used metal for the scaffolding of endografts with stainless steel and Elgiloy alloy following. For the fabric of the device, either woven PET or ePTFE are usually chosen (both belonging to the polymer family) [63]. A list of commercially available stent grafts can be found in [64].

The choice of the appropriate material is crucial for any device. Apart from the need to be biocompatible, materials need to be able to deform significantly to fit the delivery system without permanent deformations and have good fatigue properties to withstand a minimum of 10 years of usage. Additionally, devices need to have the least amount of material necessary (thin Nitinol wires and thin fabric graft) so as to be able to be tightly compacted into the catheter while still be durable. Similarly, devices need to be stiff enough to stay in place and keep the lumen open while at the same time be flexible to handle the delivery process and any excess tortuosity of the arteries. All these demanding and conflicting aspects have to be taken into account and be optimized for every stent graft design.

The current study focuses on the Anaconda™ stent graft. This device consists of a series of Nitinol rings and woven PET fabric and while both these materials have been used in many FEA simulations over the last years, there are very few studies at this particular system. Most analyses have simulated Z-type stents as these all share common geometrical features meaning that outcomes from such investigations can be applied to the majority of available devices. An overview of key research outcomes useful for the current study are presented below.

2.2.2 Nitinol material

Nitinol is a metal alloy that contains nickel and titanium at approximately equal atomic percentages. It was discovered at the Naval Ordnance Laboratory (Maryland, USA) in 1959 and over the last decades has become a very popular material in the medical world due to a series of properties which make it ideal for implant use.

Nitinol has two distinct crystal phases (austenitic and martensitic) and has the ability to transform from one to the other under temperature changes or strain application. The austenitic phase is usually stable at high temperatures and low stresses while the martensitic phase is stable at the opposite conditions [65]. The transformation between the two gives rise to the following special characteristics:

- Shape memory effect: the material can be cooled down, be plastically deformed and then heated to the original temperature where it recovers its original shape.
- Superelasticity: the material undergoes severe deformations with practically no permanent strains.

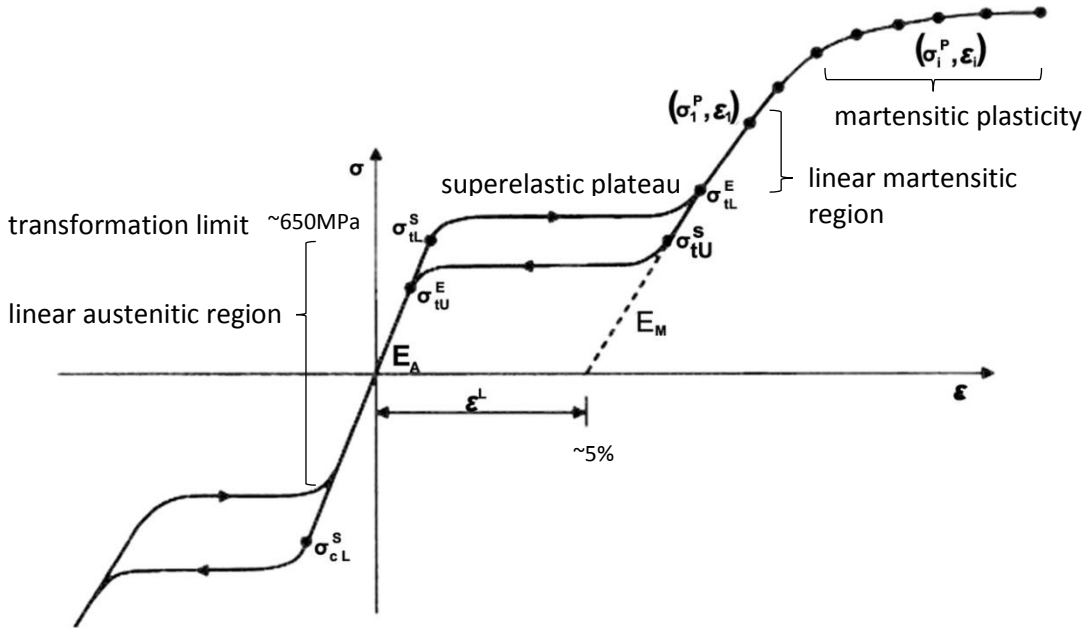

Fig. 2.5 Stress-strain curve of Nitinol under uniaxial loading. The variables correspond to the Abaqus material implementation [208].

Regarding EVAR applications, the superelastic behaviour of Nitinol is vital for the operation of stent grafts.

When Nitinol is stressed, it deforms elastically up to its transformation limit (Fig. 2.5). Then, Nitinol changes its crystal structure from austenite to martensite which allows the material to undergo a superelastic plateau (usually between 1-8% strain). If not excessively deformed (i.e. beyond the martensitic linear region), Nitinol will unload from a lower stress plateau and restore its austenite phase with practically no plastic deformations; only strains over 9-10% will usually induce residual strains. The response of the material in tension and compression is asymmetric, with the transformation limit in compression being greater (in absolute value) than the tensile one and the superelastic plateau generally shorter. The superelastic behaviour makes Nitinol an ideal candidate for stent grafts since for EVAR to be performed, endografts have to undergo significant deformations when compacted into the delivery system.

At the same time, Nitinol is one of the very few alloys that apart from being superelastic it is also biocompatible [66]. As a merit of passivation, Nitinol can resist corrosion by creating a thin protective film of titanium based oxide. It should be noted though that upon the application of the cardiac loading, which induces pulsatile motion to the endograft, this shield layer may break, undermining the biostability of the stent [64]; hence attention must be taken regarding surface treatment. Nevertheless, the material has been successfully used in stents for decades with the first medical Nitinol devices dating back to the mid-1970s [67].

Another characteristic that makes Nitinol popular for stent grafts is its very good fatigue properties. Currently, European standards require that all stents must be tested to withstand 10 years of equivalent *in vivo* pulsatile loading and that translates into 400 million cycles of fatigue testing [68].

Contrary to linear elastic materials, Nitinol increases its fatigue life when ε_{mean} increases over 1.5%, due to the formation of stress induced martensite [69]. This is very encouraging since *in vivo* $\varepsilon_{mean} \neq 0$. In fact, *in vivo*, the critical areas have $\varepsilon_{mean} > 0$. This is because when a stent is deployed, the rings (or struts for most designs) are

under bending, thus one side of the wire is under tension and the other under compression. Nevertheless, because Nitinol has a higher compressive than tensile transformation stress, the side under tension will enter the superelastic plateau earlier, leading to a larger tensile (i.e. positive) strain; hence it is this region that will dominate the fatigue fracture.

In general, though, $\varepsilon_{amplitude}$ has a greater effect on fatigue life than ε_{mean} has [70] and it has been found that fracture tends to occur for $\varepsilon_{amplitude} > 0.4\%$ in high-cycle ($\geq 10^5$ cycles) [69], which is used as a threshold for endograft manufacturers.

Furthermore, Nitinol exhibits better fatigue behaviour in strain rather than stress controlled environments [71]. Once again, this proves to be very convenient since in stent applications, materials are loaded under a strain controlled way, in a sense that loading due to blood motion moves the vessel and the motion of the vessel dictates the endograft's deformation. Blood vessels pulsate between systolic and diastolic pressure creating the boundary conditions of the EVAR environment. Blood pressure, the age of the patient, local aortic geometry and any possible disease, all affect the compliance of the vessel. The more compliant the vessel is, the greater the $\varepsilon_{amplitude}$. From a fatigue perspective, the worst case vessel is the most compliant, which normally is a young and healthy one; Duerig et al. [71] documented a 5% diameteral change during a $\Delta P = 100$ mmHg for a vessel like that. This value though can drop to 2% when the artery is stented, and it is this constrained environment that stent manufacturers have to ultimately consider.

The characteristics of Nitinol have also been shown to be very sensitive to temperature changes [72]. With the increase of temperature both the loading and unloading stress plateaus shift upwards while the opposite is true for a temperature decrease [73]. If an unloaded Nitinol wire is heated, then A_f can be defined as the temperature at which all martensite crystals are transformed into austenite. For stent grafts to operate successfully, A_f has to be lower than body temperature but quite often manufacturers seek to be marginally below this limit [71]. The reason being that the higher A_f is, the more compliant the stent becomes [66].

Lastly, apart from temperature sensitivity, Nitinol has been demonstrated to be sensitive to the rate at which it is strained as well [74], posing extra difficulties on its characterization and as a result on its optimum implementation on EVAR.

The fact that Nitinol is a non-linear, temperature-dependent material that exhibits memory and hysteresis effects, makes its mathematical and physical characterization very challenging and that inevitably translates into challenges during the modelling and simulation procedures.

2.2.3 Nitinol modelling

The highly non-linear, temperature and path dependent behaviour of Nitinol has been modelled by various researchers with a number of constitutive models. The two most notable stem from the works of Auricchio et al. [65] and Qidwai & Lagoudas [75] with the former being the one adopted herein. This choice follows most Nitinol stents modelled in the literature and it is also in agreement with the works of Bow [76] and Boukis [77] whose results have been important to the current thesis.

Auricchio's model is based on the generalized plasticity theory. By assuming isotropy and splitting strain into a linear elastic part and a transformation part that follows plasticity rules and is further split into a dilatational and a distortional component, all major behaviours of Nitinol are modelled.

Auricchio's model has also been implemented into the commercially available Abaqus software, the numerical environment used in the present body of work. For this purpose, a user defined subroutine (UMAT) has been used, with 15 input variables that help construct a detailed stress-strain graph (Fig. 2.5). Through these key variables, different elastic properties for the austenite and martensite phases can be implemented, as well as different transformation stresses in tension and compression. The model can also take plasticity into account, yet this feature has not been used in the present work since no relevant data were available during the conduction of the study.

2.2.4 FEA stent graft modelling

AAA rupture occurs when the wall stress of the aneurysm surpasses its wall strength; and unfortunately, AAA dilation results in both an increase in wall stress and a decrease in wall strength [78].

Although the stress distribution of an AAA is highly dependent on the shape of the aneurysm [18], researchers have attempted to identify the peak stress values for the aortic wall. Through the use of FEA, Giannoglou et al. [5] studied 39 patients and reported that the peak wall stress among them varied from 10.2 to 65.8 N/cm^2. However, similar values have been measured for the yield stress of the AAA wall. Raghavan et al. [79] measured ex-vivo the yield stress of AAA and found it to be 71 N/cm^2 for the circumferential and 65 N/cm^2 for the longitudinal direction (in comparison to 121 N/cm^2 for the surrounding healthy tissue). Very similar values have been reported by other researchers as well (68, 65 and 121 respectively in [80]).

Knowledge of the distribution and the magnitude of the wall stresses, though, is not sufficient for AAA rupture prediction. AAA wall strength is also location dependent, meaning that regions with lower stresses may be at greater risk of failure than regions with higher stresses just because they may correspond to areas with low wall strength [78].

In any case, FEA studies have reported that stresses in the aneurysmal wall can decrease by a factor of 10 [81] or even 20 [82] after the application of a stent graft since the device acts as a cushion of pressure for the aneurysmal region. As a result, a successful EVAR can effectively shield the aneurysmal sac from excessive stresses. Similarly, the sac pressure is reduced by a factor of 10 when sealing is secured [82]. The remaining pressure seems to be the result of the luminal blood pressurizing the stent graft against the stagnant blood of the aneurysmal sac.

FE analyses have also allowed significant insights in the stent graft structure itself. The stress/strain state of a stent from manufacturing to deployment changes multiple times and since Nitinol is a load history dependent material, all of these changes have to be followed in order to correctly identify the final state of the material *in vivo*; a process that can be simulated sequentially with FEA. As Fig. 2.6 a shows

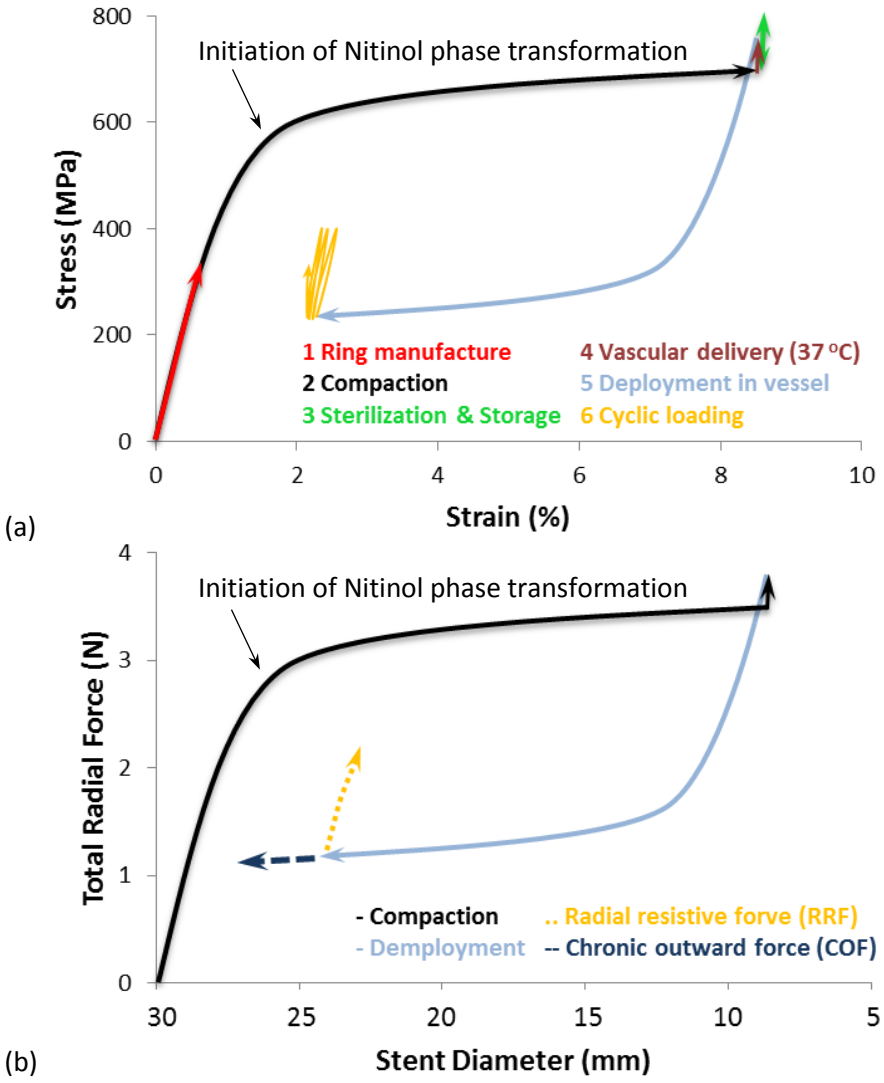

Figure 2.6 Stress-strain curve of Nitinol during Anaconda's life cycle (a). Total radial force-stent diameter curve of Anaconda™ during EVAR (b).

for the Anaconda™, during the manufacturing process of the device, Nitinol wires are stressed (details on the manufacturing process are discussed in Section 4.1) and then compacted into the delivery system with part of the Nitinol rings entering the superelastic plateau. Sterilization and transfer into the human body are heat treatments which increas the stresses without strain alteration. After that, deployment allows the material to unload from a lower stress plateau exhibiting hysteresis before the final *in vivo* cycling stage which converges into a repeatable non-hysteresis curve which is followed for the rest of the stent's operation. It is worth noting that each

point of the stent will be at a different stress/strain state having been affected differently by the compaction/deployment process; and with FEA the most critical regions can be identified.

If we define the total radial force exerted from a stent as the sum of the radial components of the forces developed at the device/vascular wall interface, then a behaviour similar to the one described above can be observed on a force-diameter graph (Fig. 2.6 b). The total radial force will increase during compaction and at deployment will reduce to a lower plateau. What is interesting is that at the deployed state, any force of the vessel against the stent will generate a strong opposing force from the device, named the radial resistive force (RRF). At the same time, the stent graft exerts a stable, gentle force against the vessel, named the chronic outward force (COF). This double-standard response is a consequence of hysteresis and has proven to be very useful in stents, especially when treating stenosis. While for those stents, though, it is clear that devices should exhibit as high RRF and as low COF as possible [66], for stent grafts treating AAA the design objective is less clear. Low COF means that the stent will not damage the endothelial cells, but too low a COF will compromise sealing. At the same time, RRF should be high enough to keep vessels from collapsing (especially tortuous iliac arteries) but not too high to prevent the endograft from adapting the vascular shape. Too high a RRF can also create a strong compliance discontinuity between the vessel and the stent's ends leading to hinge points at the vascular wall which will increase local stresses [83]. Ideally, stent grafts need to ensure anchoring and sealing while providing the necessary compliance. Nevertheless, it is exactly this compliance that increases the pulsatile motion of the stent and can eventually challenge the fatigue limits of Nitinol.

Although, as mentioned above, safety guidelines suggests a 400 million cycle fatigue test under the *in vivo* conditions for assessing stent graft's durability, a study tried to map the fatigue failure of Nitinol by testing it under a range of possible ε_{mean} and $\varepsilon_{amplitude}$ combinations, both physiological and not [69]. The authors concluded that *in vivo* pulsatile motion is not sufficient to cause fracture on its own and hypoth-

esised that non-pulsatile cyclic motions such as off-axis vascular deflection and musculoskeletal deformations could induce significant fatigue damage. Although their study focused on peripheral arteries, the aortic environment might bear similarities.

Fatigue performance of endografts obviously depends on their design and by setting appropriate objectives, FEA can help optimize various geometrical aspects of them. Such a study was conducted by Azaouzi et al. [84] for a Z-stent and improved its fatigue life by minimizing the strut volume without decreasing its radial stiffness below a set threshold. Similarly, on an analysis that considered different kinds of fabric, researchers studied the effect of various grafts on the fatigue life of the scaffolding itself and found that PET, when combined with Nitinol stents, can result in a device with greatly improved fatigue life due to its stiffer response and as a result, its reduced pulsatile motion [70]. Studies like these can generate valuable outcomes, which only numerical analyses can deliver.

Despite all the complications a stent fracture will bring though, and despite the fact that fatigue fracture is a variable well taken into account during design and manufacturing through the use of conservative safety factors, it should be noted that it cannot be a sole criterion of EVAR failure. A stent may very well be intact and yet fail to perform its intended function by either failing to anchor and/or seal appropriately or by creating blood occlusions. As a result, the stent's radial strength and flexibility are two key mechanical aspects that also need special attention.

A decrease in radial forces can jeopardize anchoring and induce a type I endoleak. It has been shown that radial strength (measured in N/mm) is the clinically relevant variable most sensitive to stent design; during a Z-stent analysis it was shown that a 30% increase of the width of the struts resulted in a 61% increase of its radial strength [85].

For a more direct evaluation of sealing, Von Sachsen et al. [86] created a numerical tool for assessing the sealing potential of endografts by dividing the ring-vessel area that is in contact at deployment over the total ring-vessel interface that needs to be in contact. Furthermore, in their work, FEA results were integrated into

a surgical planning software, recognizing the need for user friendlier software environments when the end users are practitioners. Such efforts are useful because they direct research into clinical implementation, allowing practitioners to make more informed decisions when most needed.

By adjusting and optimizing the design of endografts, radial strength and sealing performance of stents can be improved. Through alterations in the geometrical dimensions of a braided stent, Kim et al. [37] demonstrated the ability of fabricating stents with tailored mechanical stiffness. The choice between a stiffer versus a more flexible endograft, though, is a difficult one to make and is always central in the design and manufacturing decision process. A stiffer device can reduce the pressure wave transmitted to the aneurysmal wall protecting it from high stresses, although it cannot match irregular geometries as successfully as a softer one. It has been mentioned that when tortuous aorto-iliac aneurysms are stented, flexible stent-grafts could prove beneficial as they may decrease complications [87]. Moreover, their metallic scaffolding could be spiral or circular, since it has been shown that these designs provide greater flexibility as well as lower stress values compared to Z-stents [88].

Stent grafts, especially when stiff, tend to straighten the host vessel, an effect that is possible to result in arterial kinking or strain concentrations in the arterial wall. The ability of a stent to adopt the path of a vessel is called “conformability” and it has been shown that it depends primarily on the stent’s design and secondly on the material of construction [66].

Simulations of either the insertion of a guide wire alone [89] or a guide wire with a stent [90] have replicated the straightening of the host vessel. Similarly, using a 3D reconstruction technique, Liao et al. [91] compared the pre and post-op images of coronary stented arteries and documented a 21.5% reduction of mean arterial curvature. Furthermore, De Bock et al. [92] showed that the straightening of vessels is not only device specific but it cannot be predicted even when the pre-op tortuosity index of the vessel is known. In other words, straightening happens and can only be estimated in a case by case manner.

The efforts to improve the mechanical behaviour of stent grafts in order to reduce EVAR complications is accompanied by the research on endograft design optimization so as to increase their suitability. Towards that end, a major objective among manufacturers is to decrease the profile of stent grafts so as to increase the range and number of patients treated with EVAR. Reducing the thickness of the delivery system will prove very beneficial in patients who typically have narrower and more challenging femoral and iliac arteries such as Asian patients and women in general [93]. It has been argued that decreasing the diameter of the delivery system can raise patient suitability by up to 10%, leaving only inadequate aneurysmal neck morphology to remain an exclusion criteria of endovascular repair [51].

The numerical tools to drive such design improvements are under constant development, yet for most studies, only Z-stents are taken into account. The Anaconda™ stent (along with similarly designed devices like the Thoraflex™ Hybrid (Terumo Aortic)), which is the focal point of this study, is a distinct and rarely considered geometry. Unfortunately, as it will be discussed in Chapter 4, there is no model currently available in the literature that can accurately capture the mechanical state of the entire Anaconda™ Nitinol scaffolding.

The existing models usually adopt the 'equivalent beam' simplification [88,94,95] which tries to capture the bending stiffness of the rings; nevertheless, with this approach, the exaggeration of strain magnitudes is unavoidable. Additionally, these models disregard the manufacturing process of the device which is proven herein to be critical for the correct mechanical assessment of the endograft.

In the works of McCummiskey [96] and Van Zyl [97], manufacturing strains have been taken into account on a single turn ring, a basic version of the structural unit of the Anaconda™. These works were important because they captured the mechanical state of the ring more reliably and they allowed for accurate multi-turn analyses to be realised later on by Bow [76]. Nevertheless, all these studies utilized the double symmetry of the ring, making the models inadequate for multi-ring (let alone for full device) simulations. Furthermore, the use of continuum elements made these

approaches computationally demanding, sometimes requiring a full day for a simulation to run; a challenging time-frame for research and development use.

All these limitations are addressed herein, in Chapter 4.

2.2.5 Stent graft modelling beyond FEA

Finite element analysis is a powerful tool for EVAR and what is more, the technique itself is constantly improving. Along with faster computers and more elaborate FEA software, researchers try to produce more sophisticated finite elements for stent modelling [98] and new material models are often implemented into commercial codes. In the meantime, non-commercial software attempt to optimize the technique even further. Strbac et al. [99] developed a custom FE code based on graphics processing unit (GPU) technology that could calculate the stress state of an AAA from 10 to 17 times faster than a standard finite element code. These advances are promising and strengthen FEA technology to keep delivering useful insights; yet not all computational analyses are about FEA. Below, a few different numerical techniques are discussed briefly for completeness.

Computational fluid dynamics (CFD)

Computational fluid dynamics (CFD) is a numerical technique that allows the study of the behaviour of complicated flows and has been used extensively for the investigation of AAAs. Some studies concentrate on idealized AAAs, others on patient specific geometries and others on stented arteries. The field is wide and promising with various interesting observations having been made already.

CFD is very useful when examining occlusions and flow disturbances. *In vitro* flow visualisation has shown that flow separation and low velocity can be associated with thrombosis [100]. As a result, such phenomena could be eventually predicted in a patient-by-patient case numerically, with the use of advanced models.

In 2014, the first patient-specific analysis of the fenestrated Anaconda^{TM} was conducted in order to examine the drag forces acting on the device [101]. Although the endograft was idealized, the study showed that the blood pressure is the principle contributor of the overall force, hence the waveform of the two variables closely matched.

It is important to bear in mind that the correct geometrical representation of vessels is crucial for all hemodynamic analysis since idealized topologies bring significant limitations. Morris et al. [102] studied the blood flow patterns between an idealized, in-plane and a realistic, out-of-plane stent graft and concluded that geometry has greater influence on the outlet flow rates, flow patterns and drag forces than boundary conditions have. Moreover, drag forces were 26% higher in the realistic than in the idealized model.

Similarly, correct geometrical representation is critical for the stent graft as well. In the vast majority of CFD studies, the EVAR devices are simulated with an unwrinkled fabric surface that serves as a smooth boundary wall for the blood flow (for some recent examples the reader is referred to [103–106]). Yet the wrinkles on the surface of the graft can induce micro recirculation and reverse flow that has been connected to the formation of thrombus [105]. Similarly, thrombus is formed in low shear stress areas that result in increased blood viscosity [107] and these regions will be affected by the flow boundary. Furthermore, the presence of kinks and occlusions can increase the drag forces and can possibly lead to the migration of the endograft [25]. Hence, accurately capturing the graft shape is for many reasons favourable for a high fidelity hemodynamic analysis.

Recognizing the usefulness of CFD, Section 5.4 demonstrates the ability of the developed model to be used in detailed hemodynamic analysis that captures the effects of fabric wrinkling.

Fluid structure interaction (FSI)

Fluid structure interaction (FSI) is an approach to study the synergy of a deformable structure and a flow that are coupled together. It is usually addressed by combining FEA with CFD, and despite the complexities involved, it is a very suitable technique for the investigation of AAAs. The reason being that the dynamic blood flow induces a radial deformation to the vessel (and endograft) which serves as boundary condition for the hemodynamics of the system.

FSI models which have been proposed until now are compelled to make numerous simplifications, nevertheless, they provide initial insights into the topic. Li et al. [82] created a homogeneous stent (no separation between metallic wires and graft) and deployed it in different AAA environments to measure the peak migration force versus 12 biomechanical parameters. Note that the migration force acting on the endograft is produced by the blood pressure and the friction on the graft, and can be split into a downward and a transverse component. The former affects the fixation of the proximal neck while the latter, which is significantly smaller, the fixation of the legs [58].

Li et al. [82] also showed that the migration force increases primarily with the increase of the stent graft diameter, body-to-leg diameter ratio, neck angle, iliac bifurcation angle and hypertension. The reported migration forces were between 1.4 and 7 N, although no validation was provided. In the meantime, fixation forces have been measured to range from 4.5 to 25 N depending on stent design, with the devices that have hooks and barbs performing better [108]. Needless to say that if fixation forces are higher than migration forces, the stent will stay in place. Note, however, that apart from the attaching mechanisms, oversizing, the stent columnar strength and contact at the bifurcation region, all enhance fixation as well.

In contrast to the above, some FSI analyses have considered the unstented AAA. Papaharilaou et al. [109] demonstrated that although FEA can produce reliable results regarding wall stress distribution, it underestimates the magnitude of the peak wall stress by up to 12.5% when compared to a dynamic, FSI analysis.

The advantages of FSI analyses are apparent since they can provide a holistic view of EVAR. Nevertheless, such analyses usually require many assumptions and tens of runtime hours making the technique very computationally demanding. Despite the many merits, further advancements need to be made for FSI to be more extensively used.

Fast virtual stenting (FVS)

Because of the long runtime needed to obtain results from an FE (and even more from an FSI) analysis, computationally faster approaches have been proposed. Fast virtual stenting (FVS) describes models that forecast the final configuration of a stent in a matter of seconds or few minutes. Such models cannot predict the mechanical state at which the involved structures will be after surgery, but may give valuable estimations of the positioning of the deployed stent in times acceptable to clinical practice.

A FVS approach described by Larrabide et al. [110] used a deformable simplex model (a technique that uses a partial differential equation to move a mesh under the effect of forces) to virtually deploy a coronary stent and acquired results that resembled the experimental deployment on a phantom model.

A different study utilized a spring analogy [111], in which the FVS method assumes the mesh edges to be springs. In this study, different spring types were considered and the lineal one, although the simplest, was found to be adequate enough to capture most responses the more sophisticated models predicted. This model was further developed and validated against FEA for a Z-stent deployed in various anatomies [112]. Results showed that the mean discrepancy of the nodal positioning of the stent between FEA and FVS was anywhere from 4% to 10%. Calibration of the stiffness of the springs according to FEA followed and although nodal positions were not significantly improved, residual forces were drastically reduced (<0.2 N), showing great potential for the technique.

Further development of the FVS approach might prove very useful in the future. Advancements in the mathematical implementation and the modelling of contact could make it a very popular choice for analysts and clinicians alike. Although FVS cannot inherently predict strains, stresses and possibly radial forces, the satisfactory estimation of stent's final position in combination with the extremely quick solution times suggest that, one day, this technique could be used alongside FEA for the treatment of patient specific AAAs.

2.3 Summary

EVAR is established as a standard surgical approach for AAA treatment. Despite the short-term benefits this minimally invasive approach exhibits though, long-term studies show no statistically significant difference between the outcomes of endovascular repair and open aortic surgery. The disadvantages of EVAR lay mainly in the engineering of the endografts and include endoleaks and device migration, complications that raise the need for long-term post-op surveillance adding to patients' inconvenience and cost.

In the recent years, a great amount of effort has been put into simulating EVAR. Computational techniques try to model endografts and virtually deliver and deploy them inside AAAs. These advancements have allowed for a significant understanding into the mechanical environment under which a stent graft operates and the consequences of such environment into the device itself. Nevertheless, endografts still struggle to prove their post-op superiority.

Clinicians look for manufacturing improvements while manufacturers seek for research findings to address those needs. Yet the tools to allow such advancements are still unavailable. As was illustrated in this chapter, EVAR suitability is linked to the design of the stent graft, meaning that it is vital to have the tools to examine a great variety of case studies that can take into account different geometries so as to explore different endograft design possibilities. In addition, it was recognized that those who would benefit the most from EVAR (e.g. elder and women in general) are those

who currently exhibit the greatest difficulties in undertaking it because of challenging arterial geometries; this unfortunate reality could be improved by models that examine the results of further compacting the endografts to tackle narrower arterial paths. Furthermore, surgical planning assistance in order to avoid migration and endoleak complications needs to be realized. If clinicians have access to a tool with which they can evaluate different EVAR possibilities pre-op, then necessary re-interventions could be reduced and the EVAR success rate be improved.

In order for these needs to be addressed, the appropriate computational tools have to be created and currently the development of reliable, efficient and robust FEA methods to allow the progress of EVAR is far from sufficient, especially when considering non Z-type stent grafts. Recognizing that migration and sealing assessment, fatigue analysis and blood flow evaluation are the most critical outcomes a numerical analysis can offer, the objectives that were set in the current thesis were to deliver an FEA tool that can predict:

- $\varepsilon_{amplitude}$ and ε_{mean} of the stent structure to address fatigue related questions (further-on mentioned as $\Delta\varepsilon$ and $M\varepsilon$ respectively)
- Radial forces (in the form of COF) to help assess the threat of migration and consequently type I endoleak
- the deployed position of the endograft for overall EVAR assessment and utilization of it as a starting point for detailed CFD analysis

and all that for any target geometry, which is to say, for any patient specific host vessel.

As a result of this effort, Chapters 4 and 5 will demonstrate the development of two models that address those key desiderata for the AnacondaTM stent graft using the commercial FEA software Abaqus. Before that, however, Chapter 3 will illustrate the variety of geometrical configurations in which AAAs manifest themselves and will create a geometrical framework that can help endograft development in all

future studies. After all, it is exactly this geometrical variability that make patient specific endografts a highly desirable evolution in the EVAR world. The hope is to bring those numerical tool advancements a little closer to reality; a little closer to patients that need them.

Chapter 3

Patient Specific Aorta

Abdominal aortic aneurysms are extremely diverse in their morphology and the need for patient specific EVAR simulations derives from the challenging fact that no two AAAs are the same. In this chapter, a new framework for the description of the AAA geometry is proposed and used to identify representative and worst-case aortic geometries for the deployment of endografts. The statistical distribution of various crucial angles and dimensions is examined along with the investigation of a popular assumption regarding the cross section of the aorta. These data can enhance the in-depth understanding of the boundary conditions stent grafts experience. The outcomes of the analysis can help address more efficiently the variety of AAA patients as well as allow virtual models to be built in order to test various stent designs under extreme, yet realistic anatomies.

Furthermore, a material model that simulates the overall response of the abdominal aorta is produced. After critically examining the literature, a phenomenological model is developed by using available experimental data. Pressure-Radius curves of the artery are recreated and utilized to fit a new mathematical model that can be implemented into Abaqus, the development platform used in the thesis. The resulting material model imitates the inflation of the abdominal aorta with great accuracy, as validation demonstrates. Finally, a methodology to identify the unloaded vessel size from (*in vivo*) CT images is presented and discussed.

3.1 An extensive geometry study

When it comes to the clinical reporting of AAAs, a series of different measurements are taken into account in addition to the maximum aneurysmal diameter. An early reporting model on aortic aneurysm was published in 1997 regarding infrarenal AAAs [113]. This document covered both anatomical and clinical aspects of the aneurysm with the purpose of establishing a uniform standard for analysing and presenting patient's data. In 2002, the Ad Hoc Committee for Standardized Reporting Practices in Vascular Surgery of The Society for Vascular Surgery/American Association for Vascular Surgery published an updated procedure of reporting AAAs by classifying the aneurysms according to their anatomy, etiology and clinical presentation (e.g. symptomatic or asymptomatic) [114].

Regarding the anatomy, until now, several methods for defining, grading and evaluating the aneurysmal site have been proposed [47,113,115–117], but with small variations, all of them take into account the same characteristics. A summation of all anatomical variables recorded in clinical practise results in the following list:

1. Proximal aortic neck
    - morphology (straight, taper, reverse taper or bulging)
    - length
    - diameter
    - angle between the flow axis of the neck and the body of the aneurysm
    - amount of thrombus and calcification
2. Aneurysm
    - maximum AAA diameter
    - tortuosity
    - aortic angle, defined as the most acute angle of the centreline between the lowest renal artery and the aortic bifurcation
    - amount of thrombus and calcification
3. Distal aortic neck

- length
- diameter

4. Iliac arteries (common, internal, external)
    - diameter
    - evaluation of the presence of stenosis/occlusion
    - sealing zone length, defined as the length of the vascular region available for stent deployment
    - angulation as defined for the aneurysm
    - tortuosity
    - amount of thrombus and calcification

Despite the technical difficulties that arise from measuring medical images and the different estimations that emerge due to the subjectiveness of the clinicians, most of the above metrics are straightforward to acquire. The same is not true, though, for tortuosity (Fig. 3.1). In a detailed analysis, Wolf et al. [117] evaluated the aortoiliac tortuosity of 75 patients using 4 different approaches:

1. Observers: 2 surgeons graded the severity of the tortuosity qualitatively, in a scale of 1 to 5.
2. Tortuosity index: curvature (named as point tortuosity) was measured at 1-mm intervals along the centreline and when greater than 0.3 cm^{-1}, was accumulated. The 0.3 cm^{-1} limit was considered as a threshold of significance.
3. MLC–straight line ratio: the ratio of the centreline's length over the straight line that connects the renal arteries to the femoral bifurcation (points A and B respectively in Fig 3.1).
4. Cumulative angulation: the sum of all angles that diverge from a straight path at the points of angulation. This, though, was done manually from 2D images, so the metric was criticised as ill-structured.

Researchers concluded that all of the metrics correlated significantly with each other but the MLC ratio was found to be the closest to the grading of the observers. The former is the metric most commonly used in the literature and is the one adopted herein as well.

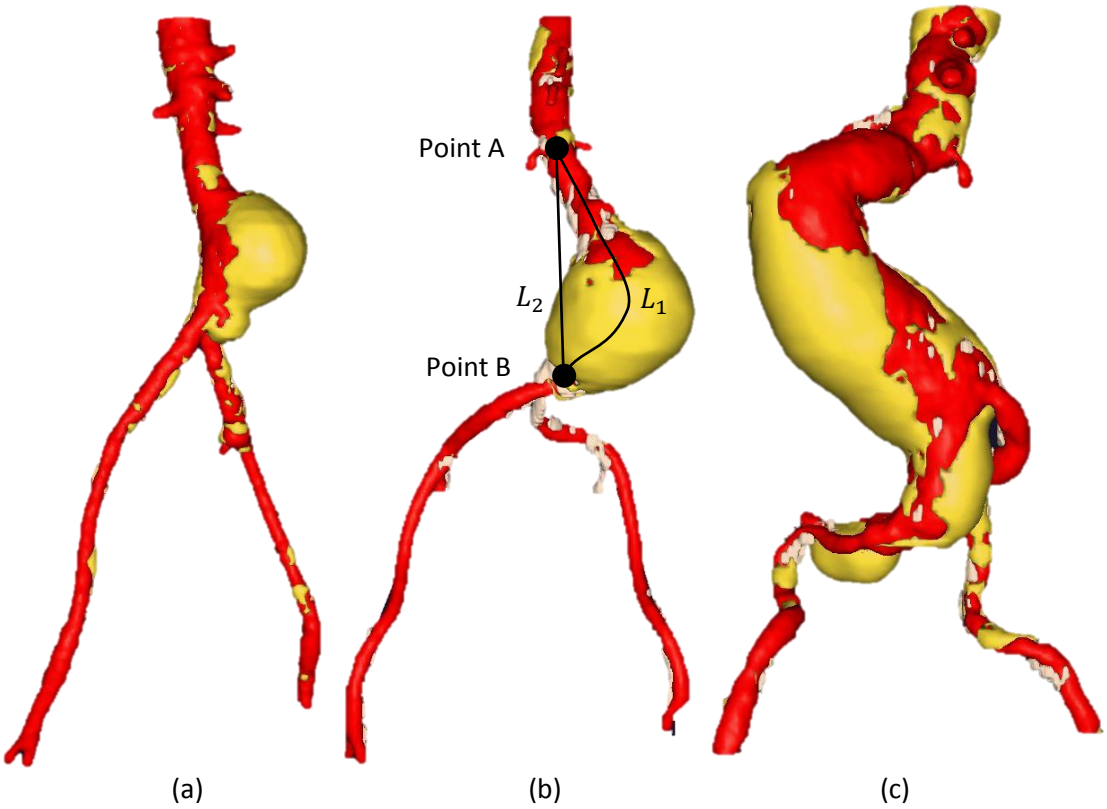

Fig 3.1 Low (a), average (b) and high (c) tortuosity cases of AAAs. The lower renal artery (Point A) and the femoral bifurcation (Point B) are connected with a centreline (L_1) and a straight line (L_2) that allows tortuosity to be defined according to the MLC–straight line ratio approach, as L_1/L_2. The blood lumen (red), the calcified regions (white) and the thrombus (yellow) are visible.

Looking at the AAA reporting list, another interesting point to be made is the emphasis on the iliac arteries' morphology. Iliacs are included in all reports because when ill-shaped they can be an exclusion criteria for EVAR. As discussed in Section 2.1, adverse anatomical characteristics of the iliac arteries are responsible for access-related complications of the delivery system of the endograft and combined with short aneurysmal neck are the leading causes of conversion to open aortic surgery

[118]. The overall most common factor for disqualification for EVAR is regarded to be the length and anatomy of the proximal neck of the AAA [45,50], yet it is calcification, occlusion and tortuosity of the iliac arteries that are responsible for the majority of access complications during EVAR procedures [118]. According to Henretta et al. [119], the difficult anatomy of the iliac arteries can result in some form of complication (injury of the arteries, misalignment of the stent-graft during deployment etc.) in up to 47% of patients whereas according to Clough et al. [93], up to 17% of all EVAR cases can result in significant problems.

Clinical practice has shown that anatomy influences technical success, endoleak rate, migration, as well as the need for secondary procedures [116]. Despite the fact that in clinical routine quantitative measurements are rarely done [118], it is important to identify average values and extremes for tortuosity, angulation and cross sectional dimensions of AAAs so as to establish common and worst case topologies to be used in simulations for stent graft design.

In this section, a series of measurements and statistical analyses are made based on a dataset of patients who underwent EVAR. All results presented derive from the investigation of these data.

3.1.1 Introduction

A series of data provided by m2s, Inc. West Lebanon, NH, USA were used to examine a range of aortic characteristics (Fig. 3.2). CTA scans were originally collected during the "Vascutek Anaconda stent graft system phase II IDE study" in the period May 2009 to July 2011 in various sites in the United States and Canada. The data were supplied anonymised, with age and gender being the only descriptors of the patient. The subsequent analysis took place in m2s Preview v4.0.1 software.

The study included 258 patients (222 (86%) men, 34 (13%) women and 2 (1%) unspecified) aged between 51 and 88 years old. It was a non-randomized, continuous enrolment study that included patients treated with the Anaconda^{TM} stent graft. Patients provided their consent for the use of their data and the inclusion criteria for them were:

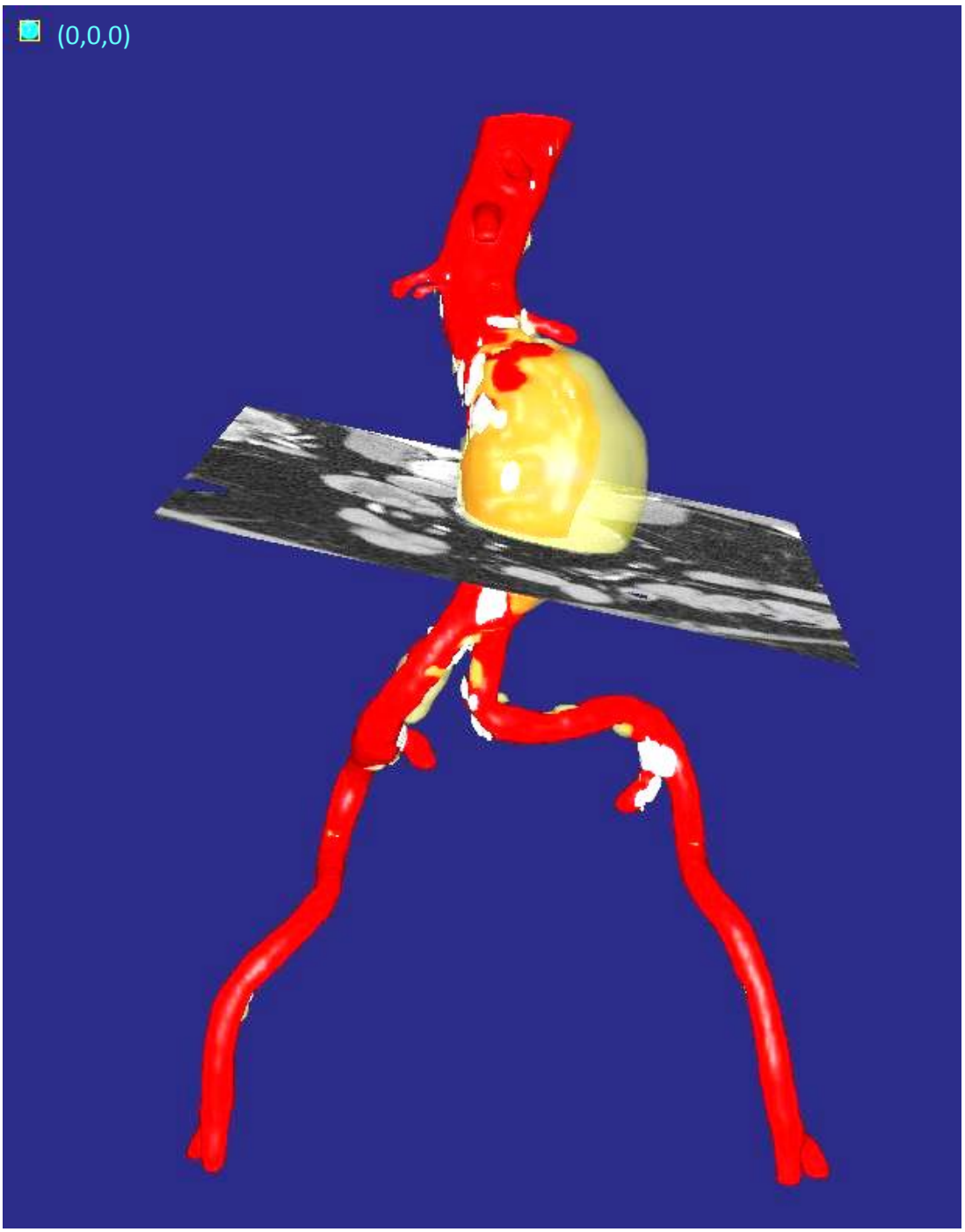

Fig. 3.2 3D reconstruction of the aortic geometry from 2D CT scans in the m2s Preview. The blood lumen (red), the calcified regions (white) and the thrombus (transparent yellow) are visible. The dot at the top left corner corresponds to the (0,0,0) point of the coordinate system, used for all subsequent measurements. It is located at the posterior right corner of the 1st axial CT scan.

- Infrarenal AAA ≥ 4.0 cm in diameter, or AAA growth ≥ 1.0 cm/year
- Iliac artery distal fixation sites ≥ 20 mm in length
- Ability to preserve at least one internal iliac artery
- Femoral/Iliac artery's size and morphology should be compatible with the appropriate delivery system (18F[1], 20F or 23F)

Pregnant patients, or patients with thrombus, calcification and/or plaque ≥ 2 mm in thickness and/or 50% continuous coverage of the vessel's circumference in the intended fixation site were excluded. Among the exclusion criteria were also aneurysms that extended above the renal arteries, significant (> 80%) renal artery stenosis not readily treatable, previous AAA repairs and ruptured or leaking AAAs.

The follow up period of the study was 5 years but herein only pre-op data were used.

3.1.2 Aortic angles

Despite the fact that the geometrical complexity of the aneurysmal site is highly influenced by the angles of the aorta, the renal arteries and the iliacs, documentation of them is extremely rare in the literature. In this section, the aim is to identify all major angles involved in an AAA so as to be able to describe and reproduce its shape. This capability will allow us to establish representative and worst case geometries of AAAs that can be an aid to stent graft design. The data produced herein can be used to characterize patient specific AAAs (e.g. as extreme, treatable, or treatable with a specific stent graft) or allow the creation of various computer-aided design (CAD) aortic models for virtual deployment and testing of endografts.

Commonly used metrics of shape, such as tortuosity and angulation (usually referring to the most acute angle on a vascular path), can only provide a vague perception of the aneurysm. This means that given the value of such a metric there is no

[1] The French scale is commonly used to measuring catheters' size. A round catheter of 1 French has an external diameter of 1⁄3 mm.

mechanism to recreate the AAA, while two completely different aneurysms may very well have the same metric value. Herein a set of 10 angles is proposed for the characterization of the AAA's geometry.

In the traditional set-up, vascular angles are measured by trained clinicians; nevertheless, the amount of uncertainty that lies in such assessments is worth noting. Quite often, clinicians approximate the angles of arteries on 2D images with two straight lines that somehow follow the trajectory of the vessel (with questionable accuracy), while only sometimes specialized software is being used. No matter the strategy, variability between different observers as well as variation in the responses of the same observer at different times (interobserver and intraobserver variability respectively) is always present [114,120]. Although this challenge is inherent to the process of human measurement and cannot be totally eliminated, it is fair to assume that a 2-line definition of an angulated vessel on a 2D plane is particularly prone to errors, especially when the 3D angle is of interest (rather than its projection to the plane in use). For that, a different strategy has been developed herein that allows for a clearer angular definition. According to this process, the investigator needs only to recognize critical points in axial CT slices and an in-house algorithm built by the author is left to calculate the angles between those points. The same process has been identified to be used in specialized software as well (e.g. EndoSize®, Therenva SAS, France), yet only for a couple of angles.

In more detail, following the centreline of the vascular tree (as defined by the algorithms of m2s Preview), 14 points were identified as critical to describe the AAA's geometry (Fig. 3.3). After qualitatively studying a series of AAAs, these points were considered both strategic and adequate to "depict" the overall AAA shape. Points were manually selected on the CT scans for all patient datasets and their assigned coordinates were based on the inherent coordinate system of each scan set (see Fig. 3.2). The points used are explained in Table 3.1.

Although most of these points correspond to anatomic landmarks, because of the versatility of the arterial shape, some of them (P8, P11) relate to locations that characterize best each particular AAA. Note also that point P14, contrary to the rest,

Table 3.1 The 14 critical points used to describe the AAA's geometry.

P1	At the centre of the aorta, a few centimetres above the renals, usually at the superior mesenteric region.
P2	At the centre of the aorta, at the origin of the proximal renal artery.
P3	At the centre of the proximal renal artery, a few centimetres further from its origin (P2), at a suitable distance away from the junction.
P4	At the centre of the aorta, at the origin of the distal renal artery.
P5	At the centre of the distal renal artery, a few centimetres further from its origin (P4), at a suitable distance away from the junction.
P6	At the centre of the aorta, at the proximal end of the aneurysm.
P7	At the centre of the aortic bifurcation.
P8	At the centre of the right common iliac artery, at the most acute curve point.
P9	At the centre of the right femoral bifurcation.
P10	At the centre of the right external iliac artery, a few centimetres further from the bifurcation.
P11	At the centre of the left common iliac artery, at the most acute curve point.
P12	At the centre of the left femoral bifurcation.
P13	At the centre of the left external iliac artery, a few centimetres further from the bifurcation.
P14	The midpoint between points P2 and P4.

was not measured on the scans; instead it was calculated as an average of points P2 and P4.

Finally, using these 14 points, 10 angles were defined, able to describe the AAA (see Fig. 3.3 and Table 3.2).

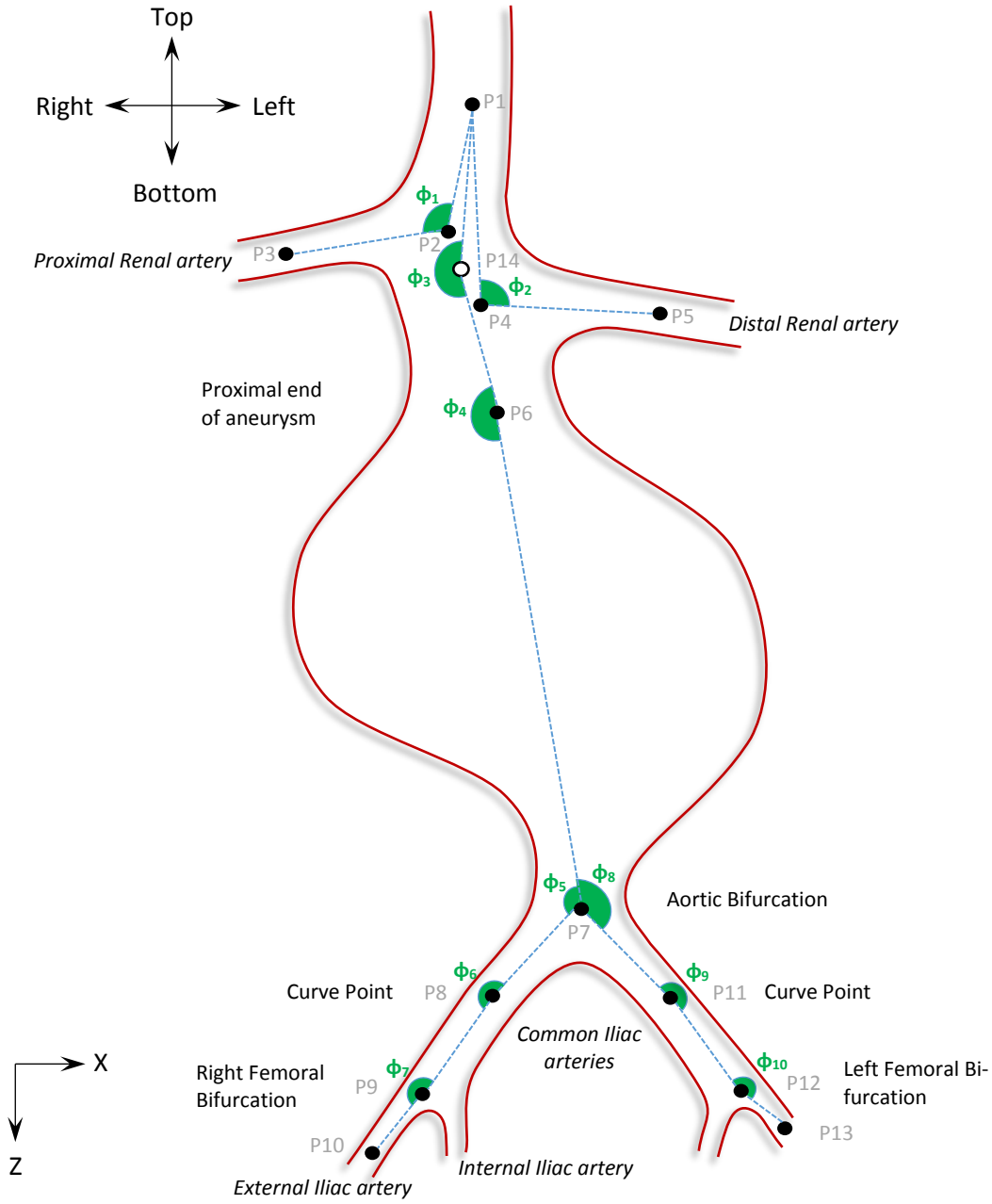

Fig. 3.3 Schematic of the front view of an AAA. Frontal plane. 14 points are identified on the centreline of the aneurysm that allow the definition of 10 angles. Positive angles are illustrated with green. The left-right notation follows the patient's perspective convention.

Table 3.2 The 10 angles used to specify the AAA.

ϕ_1	from the triad of points (P1, P2, P3)
ϕ_2	from the triad of points (P1, P4, P5)
ϕ_3	from the triad of points (P1, P14, P6)
ϕ_4	from the triad of points (P14, P6, P7)
ϕ_5	from the triad of points (P6, P7, P8)
ϕ_6	from the triad of points (P7, P8, P9)
ϕ_7	from the triad of points (P8, P9, P10)
ϕ_8	from the triad of points (P6, P7, P11)
ϕ_9	from the triad of points P7, P11, P12)
ϕ_{10}	from the triad of points (P11, P12, P13)

The advantage of this strategy lies at the ease of identifying the points of interest on the CT scans. Rather than allowing the user to directly measure the angles, the observer is limited to measuring points; then, an automated Matlab algorithm (version R2015b, MathWorks) calculates the angles in space as well as the projections of these angles on 3 different planes (perpendicular to each other) that are commonly used in medical applications (i.e. the frontal, the sagittal and the transverse).

Given the uniqueness of each AAA, it is meaningless to report the coordinates of the identified points. Instead, the angles for all patients in the study have been calculated and the median and range of them are documented. Note that in accordance to the literature, when calculating the angles in space, angles are always $\leq 180^o$. The same is not true though for the projected angles. The projections of the angles on the frontal, sagittal and transverse planes may be $> 180^o$; Fig. 3.3 – 3.6 help to define their positive direction.

The results of the study are presented in Tables 3.3 – 3.6 where the median and range of all angles in their 3D and 2D manifestations are reported. For the readers interested in a more detailed overview, histograms of all angles are provided in Appendix A.

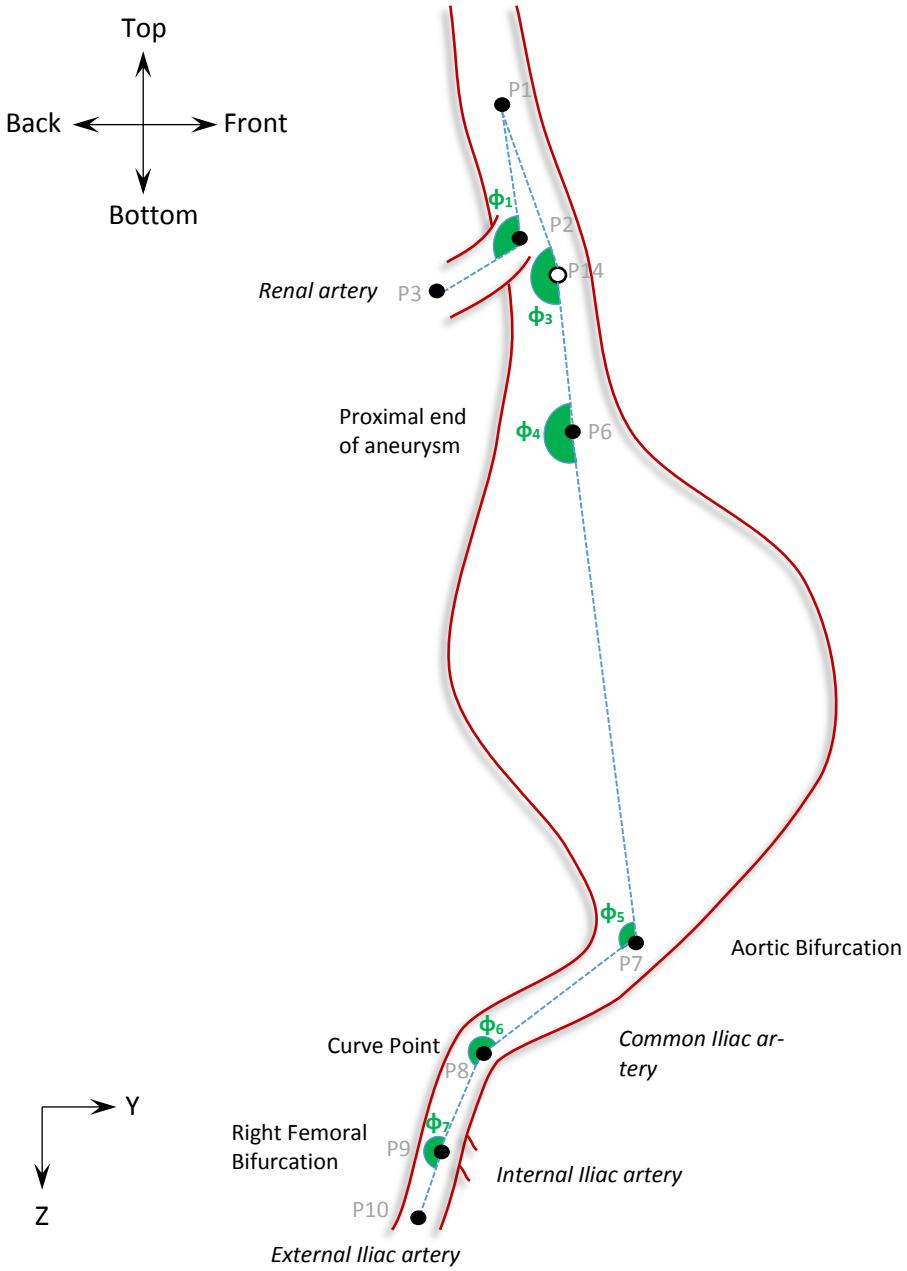

Fig. 3.4 Schematic of the right view of an AAA. Sagittal plane. Positive angles are illustrated with green.

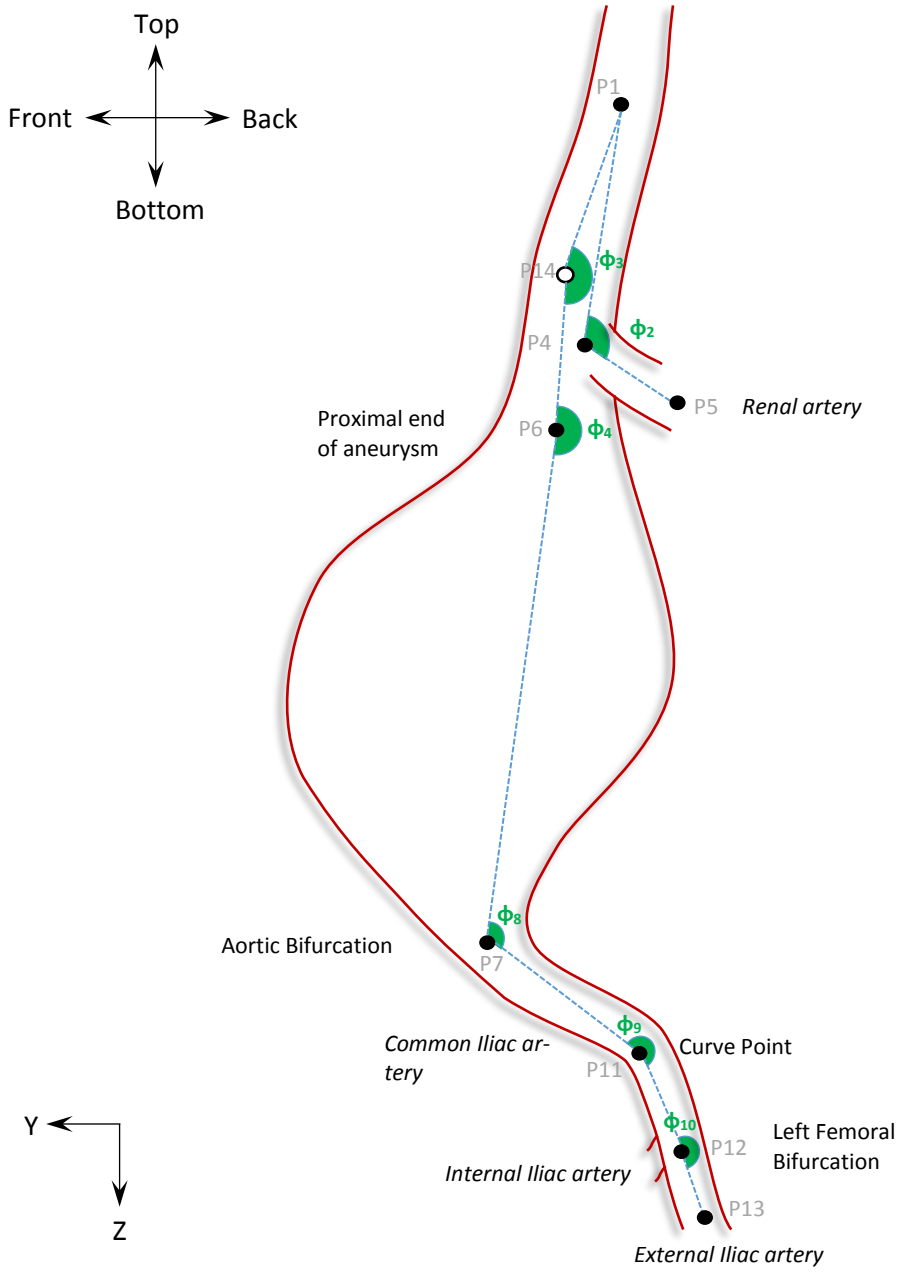

Fig. 3.5 Schematic of the left view of an AAA. Sagittal plane. Positive angles are illustrated with green.

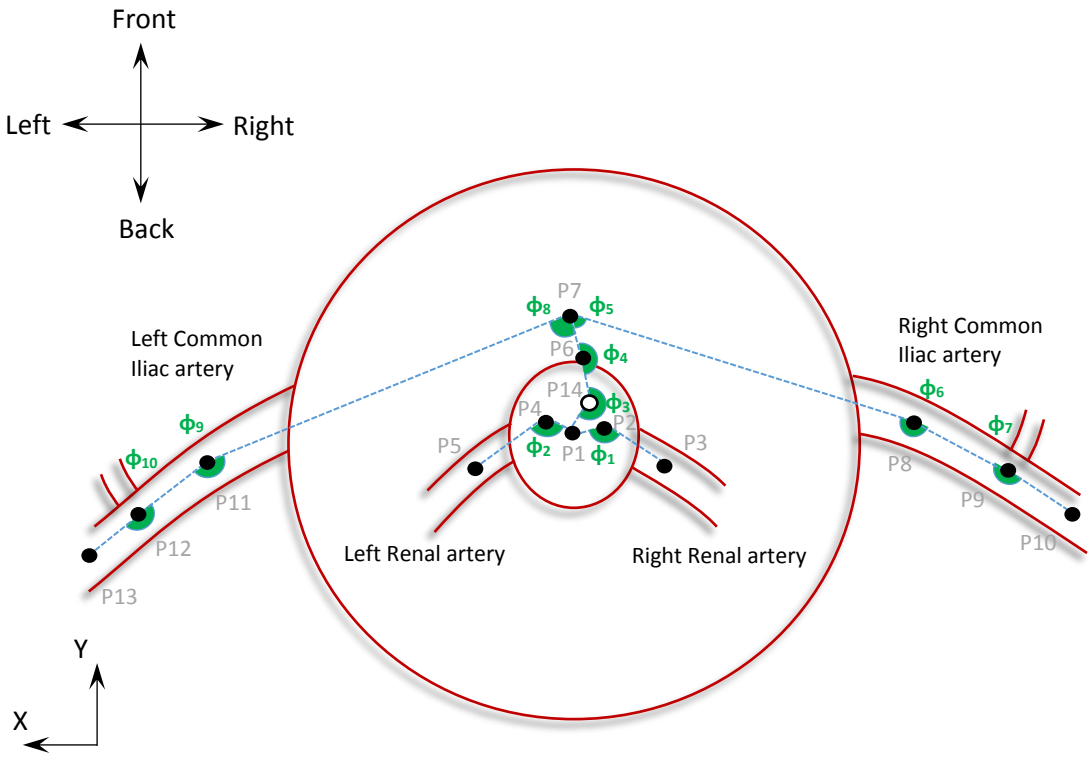

Fig. 3.6 Schematic of the top view of an AAA. Transverse plane. Positive angles are illustrated with green.

Table 3.3 The median and the range of all measured angles in 3D space.

Angles in 3D space	Median	Range
ϕ_1 (deg)	106	31 – 165
ϕ_2 (deg)	98	26 – 155
ϕ_3 (deg)	159	68 – 179
ϕ_4 (deg)	120	31 – 177
ϕ_5 (deg)	115	31 – 173
ϕ_6 (deg)	136	60 – 180
ϕ_7 (deg)	134	45 – 178
ϕ_8 (deg)	100	35 – 156
ϕ_9 (deg)	149	47 – 178
ϕ_{10} (deg)	134	31 – 175

Table 3.4 The median and the range of the projected angles on the XZ-plane.

Angles on the XZ-plane	Median	Range
ϕ_1 (deg)	107	26 – 180
ϕ_2 (deg)	105	23 – 163
ϕ_3 (deg)	178	54 – 293
ϕ_4 (deg)	168	61 – 339
ϕ_5 (deg)	121	23 – 212
ϕ_6 (deg)	190	79 – 336
ϕ_7 (deg)	168	22 – 238
ϕ_8 (deg)	115	32 – 313
ϕ_9 (deg)	179	10 – 330
ϕ_{10} (deg)	180	25 – 270

Table 3.5 The median and the range of the projected angles on the YZ-plane.

Angles on the YZ-plane	Median	Range
ϕ_1 (deg)	164	92 – 341
ϕ_2 (deg)	259	4 – 340
ϕ_3 (deg)	174	112 – 231
ϕ_4 (deg)	224	129 – 305
ϕ_5 (deg)	225	100 – 302
ϕ_6 (deg)	201	88 – 338
ϕ_7 (deg)	143	13 – 360
ϕ_8 (deg)	246	130 – 310
ϕ_9 (deg)	175	9 – 310
ϕ_{10} (deg)	120	1 – 357

Table 3.6 The median and the range of the projected angles on the XY-plane.

Angles on the XY-plane	Median	Range
ϕ_1 (deg)	147	66 – 350
ϕ_2 (deg)	209	6 – 296
ϕ_3 (deg)	192	125 – 309
ϕ_4 (deg)	242	3 – 358
ϕ_5 (deg)	143	1 – 357
ϕ_6 (deg)	140	21 – 240
ϕ_7 (deg)	210	5 – 331
ϕ_8 (deg)	260	0 – 359
ϕ_9 (deg)	174	33 – 327
ϕ_{10} (deg)	139	45 – 341

With the exception of a few variables (ϕ_1, ϕ_2, ϕ_4, ϕ_8, in 3D space and ϕ_4 in YZ plane as well as ϕ_6 in XY plane), no angles were found to follow the normal distribution according to the Shapiro-Wilk test. As will be evident in the following sections, this was true for all other variables of the analysis as well. It was this observation that lead to the decision to study the medians instead of the means of each variable for a more representative quantification since medians are resistant to outliers, meaning that are not easily affected by them.

From a clinical perspective, not all variables are equally significant for EVAR. Angles ϕ_1 and ϕ_2 relate to the renals and become relevant only when the aneurysmal neck is too short and a fenestrated endograft needs to be used. On the contrary, angles ϕ_3 and ϕ_4 are always important since greater neck angulation increases endoleak flow [121]. Li et al. [82] suggest that when the aortic neck (herein ϕ_3) is lower than 145^o, devices with high fixation forces should be used. They also mention that the anterior-posterior neck angle (ϕ_3 on the YZ-plane) influences the migration force of the stent graft significantly.

Both the Clinical Practice Guidelines for EVAR by the Society of Interventional Radiology [115] and Elliot et al. [116] have created a 4-scale scoring system to describe the severity of an aneurysm. The variables that were taken into account were dimensional, angular and clinical (presence of thrombus, disease etc.), and the common variables between their study and the current one are examined. In these studies, grade 0 was assigned to an optimal value of the variable in question, grade 1 to a mild one, grade 2 to a moderate and grade 3 to a severe. Table 3.7 presents the results of the neck angles in accordance to their grading system.

The lower angles studied (i.e angles $\phi_5 - \phi_{10}$) refer to the iliac arteries and are critical for the successful delivery of the endograft. If too acute, the physician will perform open aortic surgery instead of EVAR. Yet, usually these angulations are only qualitatively examined. Through the current study, extreme values have been identified (see for example the very challenging values of ϕ_5 and ϕ_8 in the XZ-plane) and can serve as worst case scenarios for manufacturers.

Table 3.7 Percentages of patients with optimal, mild, moderate and severe neck angulation. The patients refer to the analysis carried herein while the criteria to the ones developed in [115,116].

Variable	Grade	Criteria (deg)	% of patients
Aortic Neck Angle, correlating to ϕ_3	0	$\phi_3 \geq 150°$	81.7
	1	$135° \leq \phi_3 < 150°$	18.3
	2	$120° \leq \phi_3 < 135°$	8.1
	3	$\phi_3 < 120°$	5.1
Aortic Neck Angle, correlating to ϕ_4	0	$\phi_4 \geq 150°$	11.7
	1	$135° \leq \phi_4 < 150°$	16.7
	2	$120° \leq \phi_4 < 135°$	21.8
	3	$\phi_4 < 120°$	49.8

Because tortuosity at the aneurysmal region is very rare [122], no points in the aneurysmal sac were considered. Furthermore, even if the aneurysm does exhibit such an angle, the endograft is unlikely to follow it, making it, therefore, irrelevant for the current study.

Ideally, the existence of an equivalent set of angle values corresponding to the healthy population would serve as reference for the reported results. Moreover, it would allow a more holistic view of the pathology and its effect on the aorta. Unfortunately, though, no such data could be identified in the literature. In future, a comparison between the healthy and the aneurysmal aortic shape should be conducted and possibly shed light into the development of the disease.

Finally, utilizing the current analysis, a patient's aortic shape could be concisely reported as a 1x10 matrix $\boldsymbol{\Phi}$:

$$\boldsymbol{\Phi} = (\phi_1, \phi_2, \phi_3, \phi_4, \phi_5, \phi_6, \phi_7, \phi_8, \phi_9, \phi_{10}) \tag{3.1}$$

in clinical practice, using 3D space angle values. Similarly, a 3x10 matrix that reports the projections of these angles in 3 planes could be used to describe the aortic tree shape for CAD modelling in bioengineering applications.

These angles are a major extension to the angle set commonly used. Both in literature and specialized software attention is given to the neck angles alone, herein called ϕ_3 and ϕ_4. By mapping the entire AAA region though, a unique insight into the pathology has been achieved. Stent graft manufacturers could use the angle definitions and results presented to build AAA case studies identifying the operating range of their endografts. Subsequently, surgeons could perform measurements on patient CT scans and decide which EVAR device could tackle best a specific geometry according to the guidelines of each manufacturer. It is highly hoped that the approach and results of this section will be utilized in the clinical practice.

3.1.3 Aortic dimensions

Contrary to the angles present in an aneurysm, many dimensions of the aneurysmal site are documented prior to EVAR, hence are easier to find in the literature. Herein, 9 dimensional variables were considered per patient. The measurement of these variables, opposite to the ones presented already, were conducted by trained technicians of m2s Preview as part of the initial clinical investigation "Vascutek Anaconda stent graft system phase II IDE study". As a result, the analysis presented in this section is based upon the raw data provided by m2s (9 variables x 258 patients).

To address possible limitations of the study, deriving from the fact that different people were involved in the previous measurements (angles) and the current ones (dimensions), several CT cases were examined and it was ascertained that the author can reproduce the dimensional measurements provided, in the accuracy level established by m2s (see below).

It should also be noted that a few missing values were present in the original dataset due to limitations in the CT scan images; these values were not included in the analysis. The examined variables are reported in Table 3.8 (note that centreline distance refers to the length between two points, measured on the centreline curve (Fig. 3.7)).

Table 3.8 The dimensional variables examined in the AAA geometry.

Average Neck Diameter	The mean value of two neck diameters, one at the distal renal artery (P4) and one at the most distal extent of the proximal neck (P6).
Neck Length	Centreline distance of the proximal aortic neck (length between points P4 and P6).
Max Diameter	Maximum diameter of the aneurysmal sac.
Distal Diameter	Diameter of the minimum cross section of the aorta below the aneurysm and above the aortic bifurcation (around P7).
Renal to Bi Length	Centreline length from most distal renal artery (P4) to the aortic bifurcation (P7).
Volume	Volume of contents of AAA (calculated from the axial slices), from distal renal artery (P4) to the aortic bifurcation (P7).
Average Tortuosity Index	Tortuosity index T is defined as $T = \frac{L_1}{L_2}$ with L_1 being the distance along the centreline between 2 points and L_2 being the straight-line distance between these points. Herein, the mean value of two tortuosity indexes is calculated, one between the lowest renal artery (P4) and the right femoral bifurcation (P9) and one between the lowest renal artery (P4) and the right femoral bifurcation (P12).
Right Iliac Landing Diameter	The average diameter of the right iliac artery (section of interest: from the aortic bifurcation (P7) to the right femoral bifurcation (P9)).
Left Iliac Landing Diameter	The average diameter of the left iliac artery (section of interest: from the aortic bifurcation (P7) to the left femoral bifurcation (P12)).

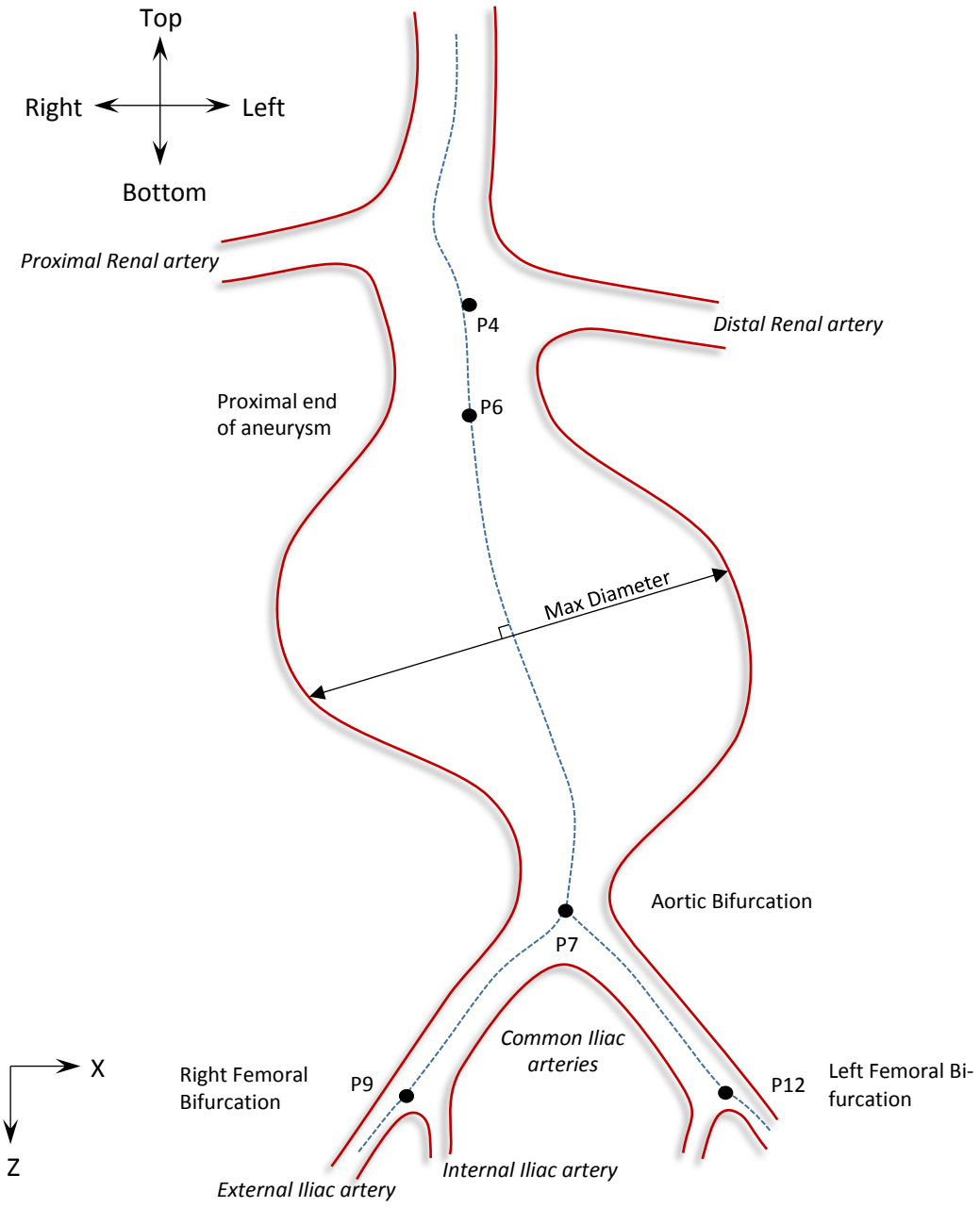

Fig. 3.7 Schematic of the frontal view of an AAA. 5 points are identified on the centreline of the aneurysm (dotted line). The maximum diameter is also identified (black line).

All diameters were measured on CT slices orthogonal to the centreline of the vessel and were calculated to the intima (i.e. diameter of the lumen). It should also be noted that diameters have an accuracy of ±1 mm apart from the maximum one (±1.5 mm). The neck length has an accuracy of ±1.5 mm and the renal to Bi length ±2.5 mm. Finally, the volume is expressed in a 5% maximum range error. These values represent the acceptance criteria for each measurement, yet it is commonly found that the inter-measurer variability for qualified measurers is routinely less than half of that.

The median and range of all dimensional variables examined is reported in Table 3.9. Yet, for the readers interested in a more detailed overview, histograms of all variables are provided in Appendix A.

No dimensional variable follows a normal distribution according to the Shapiro-Wilk test. Frank et al. [122] reported a similar finding when examining the maximum AAA diameter.

AAA size is usually established by the use of ultrasound at the anteroposterior direction [2]. It has been identified, though, that the technique used to acquire the maximal AAA diameter affects the measurements considerably, with CT providing significantly and consistently larger diameters than ultrasound does [123]. Herein, the aortic aneurysm's maximum diameter was measured on CTs as the maximum diameter of the lumen. Nevertheless, the maximum external diameter in any direction, the maximum length of the shorter axis and the average of the anteroposterior and lateral diameters have also been used as valid metrics [122].

Regarding the rest of the variables, distal diameter is usually non-important since, even in the absence of a distal aortic neck, EVAR can be performed. The iliacs, however, are required to have a minimum diameter of usually 7 mm for the delivery of the endograft [115], a requirement that herein is fulfilled since all of the examined patients underwent EVAR. Finally, similar to Table 3.7, Table 3.10 presents the results of the overlapping variables between the current analysis and the studies [115,116].

Table 3.9 The median and the range of dimensional variables.

Variable	**Median**	**Range**
Average Neck Diameter (mm)	23.1	16.8 – 34.2
Neck Length (mm)	22.0	2.0 – 50.0
Max Diameter (mm)	52.0	40.3 – 86.5
Distal Diameter (mm)	18.0	10.5 – 46.5
Renal to Bi Length (mm)	123.9	93.4 – 181.1
Volume ±5% (cm^{-3})	127.0	54.1 – 454.6
Average Tortuosity Index	1.22	1.07 – 1.65
Right Iliac Landing Diameter (mm)	13.5	7.6 – 28.7
Left Iliac Landing Diameter (mm)	13.0	6.7 – 36.1

Table 3.10 Percentages of patients with optimal, mild, moderate and severe neck dimensions. The patients refer to the analysis carried herein and the criteria to the ones developed in [115,116].

Variable	**Grade**	**Criteria (mm)**	**% of patients**
Average Neck Diameter (*AND*)	0	$AND \leq 24$	60.1
	1	$24 < AND \leq 26$	17.8
	2	$26 < AND \leq 28$	15.1
	3	$AND > 28$	7
Neck Length (*NL*)	0	$NL \geq 25$	44.2
	1	$15 \leq NL < 25$	24.8
	2	$10 \leq NL < 15$	11.2
	3	$NL < 10$	19.8

3.1.4 Proximal neck cross section

As mentioned in Chapter 2, the main reasons for EVAR failure are stent migration, endoleaks and stent mechanical failure. For all these to be thoroughly examined with FEA though, the interaction between the vessel and the proximal section of the stent has to be understood in depth. Towards this end, in this section, the

common idealization of the circular cross-section of the aorta is questioned and closely investigated.

Although evidence can be found in the literature for the non-circularity of the aorta [20,29,124], to the authors' knowledge, no thorough investigation has been conducted to quantify either the cross-sectional shape variations of the human abdominal aorta (examined herein) or its effects on stent graft deployment (examined in Section 4.4).

Similarly to the previous section, measurements are once again conducted at a plane perpendicular to the centreline. The importance of such a tactic derives from the fact that the original (axial) scans are not necessarily transverse to the axis of the vessel. This can make cross sections appear non-circular or asymmetric even if they are not, and tortuosity can very often enhance such effects.

Nevertheless, axial scans are sometimes used in clinical practice [125]. In such cases the smallest measurement of the luminal diameter is considered an appropriate approximation of the true vascular diameter [114,126]. Yet the errors introduced with this approximation are not minimal. It has been shown that the use of axial scans leads to statistically significant overestimations of the aneurysmal size when compared to scans transverse to the lumen [127]. Furthermore, the identification of true asymmetries is important. A study showed that AAAs with a significantly asymmetric cross section of the aneurysmal sac are more prone to rupture [126]. Herein, the neck section of the aneurysm is examined because of its importance to the endograft.

As has been mentioned already, the effect of ILT on the AAA is controversial. Similarly, calcification's effect on AAA's stresses has been a topic of debate. The rupture risk of an aortic aneurysm has been hypothesised to both increase in the presence of calcification because the pathology acts as a stress concentrator [128] and decrease since calcification exhibits load-bearing capabilities [129]. For these reasons and because the irregularity of ILT and calcification is vast and random, as well as because deployed stents crush ILT and part of the calcified layer, thrombus and calcification were not included in the analysis.

For all patients, 2 cross sections perpendicular to the centreline were acquired, one at the proximal and one at the distal end of the AAA's neck (Fig. 3.8). For each one of them, a boundary that included the lumen, the calcified as well as the thrombotic region was manually drawn. This allowed the definition of the intima wall's inner border. The images of these borders alone were then manipulated with a Matlab script, turned into binary format and filled to create a 1-colour 2D surface. In each final surface two metrics were applied to quantify their divergence from circularity.

The first metric used was the circularity factor (CF, mentioned further on as circularity), defined as:

$$CF = 4\pi \frac{A}{P^2} \tag{3.2}$$

where A = area and P = perimeter of the examined surface. This metric is affected by ovality as well as irregular (i.e. jagged or rough) edges and for a circle gets a maximum value of 1.

The second metric was the elliptical ratio (ER, mentioned further on as ellipticity) and for the calculation of it, as a first step, the evaluation of an ellipse equivalent to the examined surface was necessary. For the calculation of it, an ellipse with the same second moment of area as the original shape was constructed. Given the ellipse, ellipticity is defined as:

$$ER = \frac{R_1}{R_2} \tag{3.3}$$

where R_1= semi-minor axis of the ellipse and R_2= semi-major axis of the ellipse (Fig. 3.8 c2).

By averaging the values of each metric for the proximal and the distal cross section, average circularity and average ellipticity can be acquired to represent each AAA neck. The analysis was conducted in Matlab and the results are summarised in Table 3.11 while histograms are provided in Appendix A. Note that since both these metrics have an upper limit of 1, they do not follow a normal distribution either.

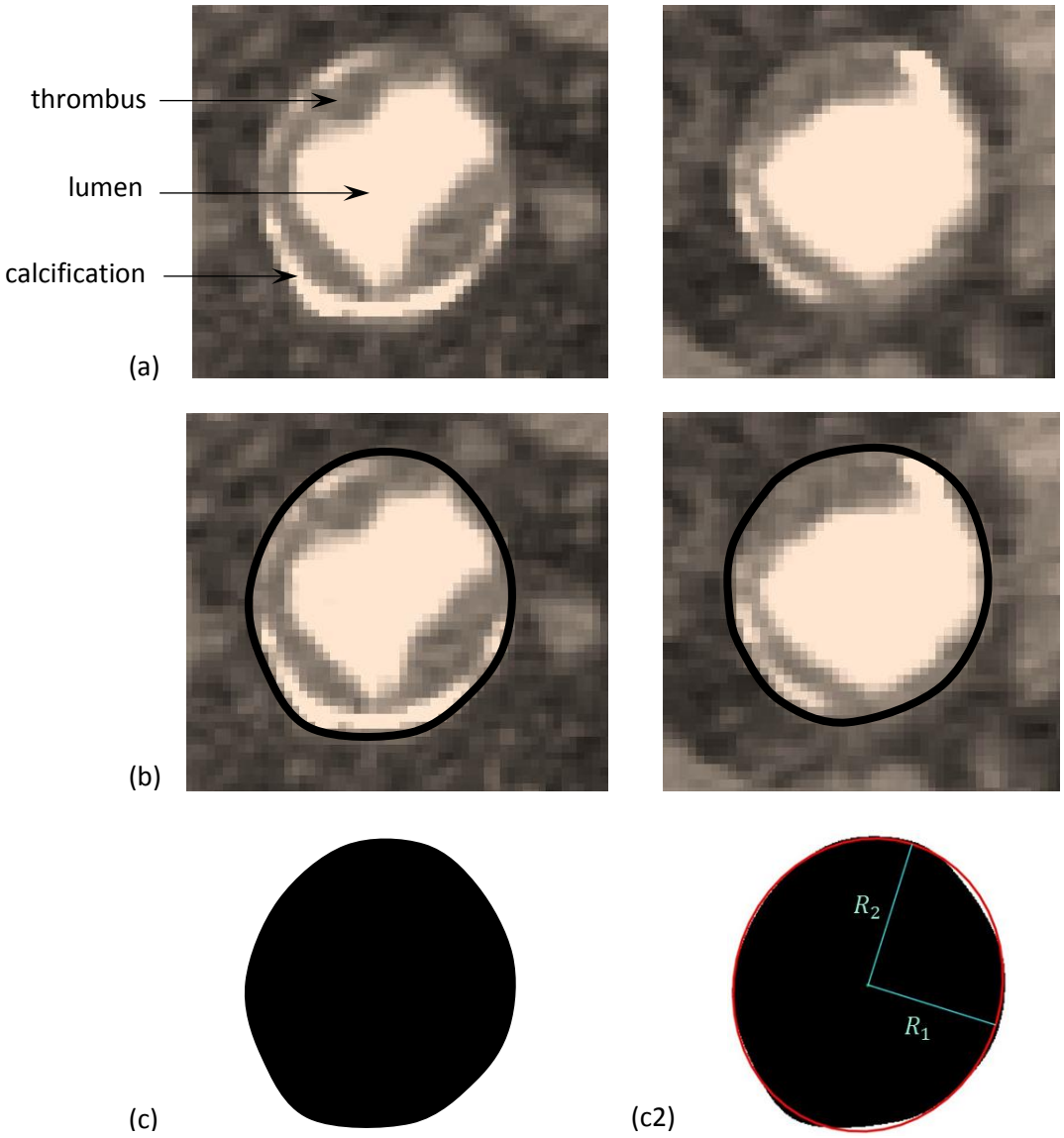

Fig. 3.8 The proximal (left column) and the distal (right column) cross section of a patient's AAA neck. For every image (a) an intima wall border was manually drawn (b) before turned into a binary image (c). Figure (c2) shows the distal cross section of a patient with the equivalent ellipse superimposed on top of it. R_1 and R_2 are the major and minor axes of the ellipse respectively.

Table 3.11 The median and extreme values of the metrics quantifying the shape of the AAA's neck. The first two rows result from the averaging of the cross sections while the bottom two refer to any cross section of the dataset.

Variable	**Median**	**Min**	**Max**
Average Circularity	0.996	0.975	1.004
Average Ellipticity	0.940	0.829	0.992
Circularity	_	0.970	1.005
Ellipticity	_	0.765	0.999

Table 3.11 demonstrates a case were circularity was greater than 1. This is a computational error, produced by the representation of a circle by pixels. The error is small, yet it implies that only 2-decimal spaces should be used for that metric.

In general, circularity is high, suggesting the smoothness of the intima. And while the median average ellipticity is also high (closely resembling a circle), in instances, ellipticity can get as low as 0.765. This highlights the need for special attention when designing and modelling stent grafts, since this is the region of sealing. The effect of such a cross section on the deployment of an endograft will be examined in Section 4.4. For now, Fig. 3.9 offers a visualization of the ellipticity values acquired.

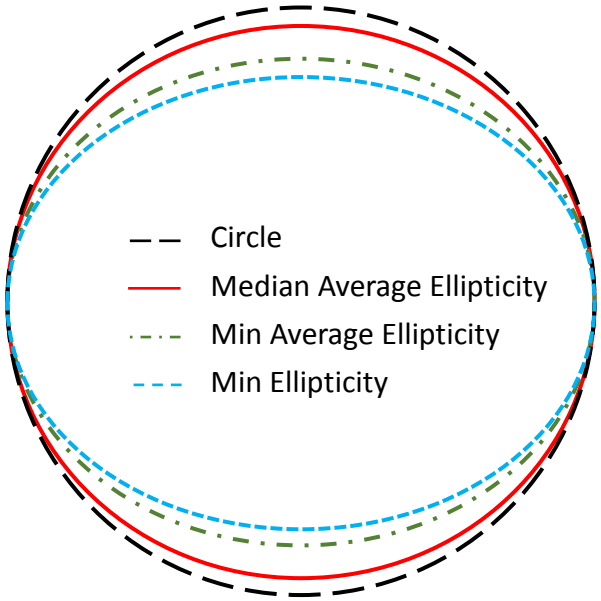

Fig. 3.9 Visualization of ellipticity results.

3.1.5 Secondary statistical analysis

The conducted study was not primarily designed to identify correlations and differences of medians between various subgroups of patients. Nevertheless, further statistical analysis has been performed (with the use of SPSS, version 25) in the belief that the sample of patients, since it was created via a continuous enrolment study, is representative of the patients currently treated with EVAR.

The first proposition to be tested was the lateral and anterior-posterior symmetry of the AAA. In general, AAAs appear to be significantly asymmetric and herein, the medians of the pairs of angles $\phi_1 - \phi_2$, $\phi_5 - \phi_8$, $\phi_6 - \phi_9$, $\phi_7 - \phi_{10}$ were compared. The analysis showed that only $\phi_7 - \phi_{10}$ in 3D space, and $\phi_1 - \phi_2$ and $\phi_5 - \phi_8$ on the XZ-plane have statistically insignificant differences. For all other angles and angle projections, the left side of the AAA was different to the right one. This should not come as a surprise. As Li et al. [82] mentions:

> *Some AAAs become anterior-posterior asymmetric because of the vertebra support. However, as aneurysms get larger, they get longer and therefore must be compensated with angulation because they are fixed in the renal and femoral regions. The neck is usually angled to the left, but not always. As a result, the AAA becomes laterally asymmetric.*

Herein, ϕ_4 on the YZ-plane has a median of 224^o, showing a greater anterior expansion, as mentioned by other researchers in the past [2]. On the XZ-plane, ϕ_3 and ϕ_4 have medians $< 180^o$ creating a slight, general trend of neck angulation to the right.

Correlations of the angles in 3D space were also examined with a 2-tailed Pearson correlation test and a few angles appeared to have weak linear correlations with coefficients ranging between 0.1 and 0.3 at the 0.01 significance level. The only pair with a moderate correlation was $\phi_1 - \phi_2$ with a correlation value of 0.542, suggesting that when the angle of one renal increases, the angle of the other will have a tendency to increase as well. From an AAA design perspective, the lack of strong correlation between angles suggest that an investigator is free to construct any extreme

aortic geometry case study with the values provided in Tables 3.3 – 3.6 in a mix and match manner. This strategy can have a powerful effect in EVAR stent graft designing.

Subsequently, a series of correlations were tested for the dimensional variables of the study. Moderate correlations emerged between the pairs Volume – Average Tortuosity Index (coefficient ρ=0.299), Age – Average Tortuosity Index (coefficient ρ=0.399), Volume – Aneurysmal Length (coefficient ρ=0.590) and Right Iliac Landing Diameter – Left Iliac Landing Diameter (coefficient ρ=0.612). Finally, the variables Volume – Maximum Diameter were strongly correlated (coefficient ρ=0.814). All comparisons were conducted with 2-tailed Pearson correlation tests at the 0.01 significance level.

Wolf et al. [117] have also reported a positive correlation of age and tortuosity and an absence of connection between age and size of the aneurysmal sac. In their study, though, the size of the aneurysm was also unrelated to tortuosity, a result that is not confirmed herein. A similar disagreement is raised with results of Bayle et al. [46] who reported that the bigger the diameter of the aneurysm, the shorter the aneurysmal neck length becomes. No such correlation was observed herein. Both studies, though, had significantly less patients enrolled (75 and 86 respectively).

The effect of gender was also examined. Neck length was statistically significantly bigger in males (23.0 mm vs 16.0 mm for females) as well as the average neck diameter (23.5 mm vs 21.25 mm). The same was also true for the right iliac landing diameter (13.5 mm vs 11.5 mm) and the left one (13.2 mm vs 11.5 mm). The larger diameters present in the male aorta are expected. Furthermore, the absence of correlation between shape metrics (like tortuosity) and gender has been documented in the literature [117]. Regarding the angles in 3D space, ϕ_2 appeared different between the genders (99^o vs 88^o for males and females respectively), similarly to ϕ_4 (119^o vs 109^o) and ϕ_6 (132^o vs 145^o). All the reported values are medians and the significance level of the non-parametric test was 0.05.

For the cross sectional study, average circularity and average ellipticity were compared to each other. The metrics had a Pearson's correlation value of 0.684, suggesting that the shape factors are producing similar values to each other and hence

no significantly rough boundaries are present in the intima. More interestingly, neither of the two metrics correlated to any of the dimensional variables and only circularity presented a weak correlation of 0.161 with ϕ_3 in 3D space. Unfortunately, this means that separate attention needs to be taken for the cross sectional geometry of the aortic neck in a case by case manner.

When comparing the values of the metrics on the two planes of the cross section of the aortic neck (i.e. the relation between the proximal and the distal cross section), only a weak correlation appears (ρ=0.237 for circularity and ρ=0.206 for ellipticity). Nevertheless, according to the Mann-Whitney U test, the medians of both variables are equal for the two planes. As a consequence, the study of only one cross section in the aortic neck's region can provide a reasonable estimate of the cross section of the neck, yet, two cross sections can add more information and are suggested if possible.

As a last remark, it should be noted that CTA scans cannot provide credible information regarding the thickness of the vascular wall; that being the reason this variable was not examined herein. Despite that, its significance has been mentioned in the literature with Romo et al. [130] suggesting that the location of rupture can coincides with the thinnest vascular region. Moreover, wall thickness is known to vary significantly on any given AAA with wall remodelling being an important reason for it [58]. Nevertheless, no correlation between wall thickness and AAA size has been found [131] and reported thickness values can be as low as 0.23 mm at the rupture site and as high as 4.26 mm at the calcified regions of the aneurysm [132].

Closing this section, it is important to highlight that the CT scans obtained for this study reflect a specific group of AAA patients, i.e. those who undergo EVAR. As a result, the conclusions drawn should be generalized to the general AAA population with caution. As has been already mentioned, AAA incidents are four to six times more frequent in men than in women. In the present study, the number of male patients was 6.5 times greater than the number of females, implying that males might have been slightly overrepresented. Having said that, the amount of variables exam-

ined and the extent of statistical analysis performed is believed to improve the understanding of the geometry of the AAA anatomy and bring new insight to the topic. The framework built for the angular characterization of the aneurysmal aorta along with the demonstration that the AAA angles do not, in general, correlate with each other, allows endograft investigators and manufacturers to create representative and worst case geometries for virtual stent graft deployments. The same is true for the cross section study of the AAA neck. All further dimensional analysis assists towards that end too. To the author's knowledge, this is the most extensive geometrical study of the AAA shape.

3.2 FEA Vessel Modelling

Further to the intricacies of the geometrical shape of the AAA, the material of the aorta is no less complex. The highly sophisticated mechanical behaviour of the abdominal aorta has been studied for over a century. Yet, the anisotropic and viscoelastic nature of this vessel has posed major difficulties to researchers who tried to model it. Herein, many of these challenges are discussed and the creation of a material model that simulates the Pressure-Radius response of the aorta is presented.

3.2.1 The mechanics of the abdominal aorta

Elastic arteries are the largest arteries in the body, they are located close to the heart and have a large number of collagen and elastin filaments. Instead of merely providing a conduit for the blood though, elastic arteries are themselves significantly affected by the bloodstream, changing their shape in every pulse and thus creating a complicated fluid/wall interaction system.

Although the material characterization of arteries is still a topic of research, the mechanical exploration of them is more than a century old. In 1881, Roy [133] performed a series of tests on cow, sheep and human aortic samples to find, among other things, that arteries display a thermoelastic and viscoelastic behaviour, they are

anisotropic and heterogeneous and they change properties according to location, disease and post-mortem time. Since then, an abundance of studies has confirmed his findings and closely investigated the characteristics of these behaviours for different sections of the human vascular tree.

As with all elastic arteries, the mechanical behaviour of the aorta is highly complex. The three-layered structure, described in Section 2.1, is still under investigation but it has been shown that when separated, the aortic layers have different mechanical responses [134]. As a whole, though, this structure allows for the artery to be distensible and assist blood propagation while smoothening its flow. Thanks to the Windkessel effect, the aorta stores an excess of blood during the systolic phase of the heart cycle and during the diastolic phase turns this stored dynamic energy into kinetic, pushing the extra blood forward, aiding through this mechanism the damping of pulsation (Fig. 3.10 a).

Moreover, the aorta is pre-stretched in both the axial and the circumferential direction and will retract upon excision and open wide upon axial cutting (Fig. 3.10 b). Axial pre-stretch enables the artery to transmit the pulse pressure without significantly varying its length [135], whereas circumferential pre-stretch has shown to transfer the peak wall stresses to the exterior of the aorta [136].

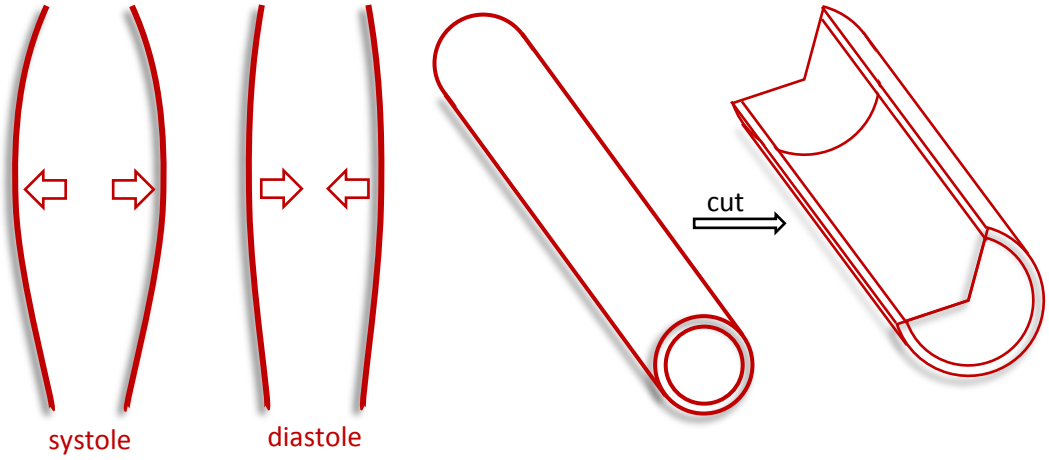

(a) (b)

Fig. 3.10 The vessel demonstrates the Windkessel effect (a). Furthermore, if cut longitudinally and circumferentially, it retracts and opens, because of pre-strains built into the structure (b).

The mechanical characteristics of the aorta depend on age, gender and health condition. Axial pre-stretch of the abdominal aorta is reduced with age [135,137] and this correlation is so strong that it has been utilized as a metric for forensic applications when the identity of a cadaver is unknown and estimation of its age is needed [138]. Also correlated to the increase of age is the enlargement of the diameter of the artery and the increase of stiffness.

Furthermore, health conditions alter the mechanics of the aorta which, nevertheless, can remodel itself through elastin reduction and collagen production [139]. Geest et al. [140] used biaxial tests to show that abdominal aortic aneurysmal tissue is stiffer than the healthy one and Pierce et al. [141], via histological analysis, observed a reduction in the amount of elastic fibres and smooth muscle cells and an increase of collagen fibres in AAA samples.

Despite the common assumption of incompressibility, arteries are, in fact, compressible [142]. Although accurate estimation of the compressibility ratio might be difficult, Yosibash et al. [143] analysed 10 porcine arteries and calculated a compressibility ratio of 2-6% when pressurising vessels from 50 up to 200 mmHg. Furthermore, the aortic wall is also susceptible to pre-conditioning [144] and exhibits hysteresis as well as the Mullins effect [145].

All of the above lead to a very complicated mechanical structure, yet too often in the literature, isotropic, homogeneous and/or 1-layered models are adopted favouring simplicity and ease of application over fidelity.

3.2.2 Overview of aortic models

The mathematical representation of the mechanical behaviour of the aortic wall has challenged researchers for decades. One of the earliest and most influential work was conducted by Fung [146] who studied the mesentery of rabbits and identified an exponential relationship between the Young's modulus and strain which in turn led him to propose an exponential form of the strain energy density function U. This has been generalized into $U = c(e^{Q(E)} - 1)$ with Q being a polynomial equation

and E the Green strain. A few years later, Vaishnav et al. [147] examined the canine aorta and suggested the use of polynomial functions for the description of the stain energy function, while Hoppmann and Wan [148] used the first and second invariant of the right Cauchy-Green deformation tensor to formulate the equation.

These studies, along with most early analyses, assumed the aorta to be isotropic. Despite the fact that the anisotropy of the aorta was known, isotropic models were popular because of their simplicity. Moreover, they were based on either uniaxial or pressure-diameter experiments which could provide no insight into anisotropy, hence allowing for good data-model agreement [1].

Many of the early analyses also used simplified models of the theory of linearized elasticity to describe AAAs [149], yet this practice has been drastically reduced. Despite the fact that the aneurysmal aorta exhibits 50% reduction in the yield and ultimate strength compared to the healthy one [79], aneurysmal tissue can still undertake significant strains. He & Roach [150] reported those strains to be between 10%-20% while Raghavan et al. [79] measured them in the range of 20-40% prior to failure, highlighting the necessity of using hyperelastic constitutive models.

In an effort to create a finite strain constitutive model for AAAs, Raghavan et al. [79] examined 61 specimens of AAA patients in both the longitudinal and the circumferential direction which reanalysed a few years later [149] to fit the strain energy function:

$$U = \alpha(I_B - 3) + \beta(I_B - 3)^2 \tag{3.4}$$

with I_B being the first invariant of the the left Cauchy-Green tensor. They concluded that the use of population mean values for the material parameters α and β (17.4±1.5 N/cm^2 and 188.1±37.2 $\mathrm{N/cm^2}$ respectively) can be used with reasonable sufficiency to any individual, minimizing the need for patient-specific data. The ages of the populations from which they extracted their specimens, though, were 69±2 and 76±2 years (for the longitudinal and the circumferential direction respectively) reducing the confidence of the results due to the small age range.

An interesting finding of Vande Geest et al. [151] on the topic, was that the mechanical response of young specimens was fitted best using a polynomial function

while older specimens were fitted best by exponential ones, highlighting the different response very young compared to older specimens exhibit.

In 2000 Holzapfel, Gasser and Ogden [152] proposed a histological rather than a phenomenological model which took into account the structure of the aortic wall. The model, commonly referred to as HGO, tried to incorporate the complex structure of the vessel described in Chapter 2 and quickly became popular, especially due to its implementation into commercially available FEA software.

The strain energy potential Abaqus uses for the HGO model is based on [152,153]. In more detail, the model assumes that each arterial layer can be expressed as a fibre-reinforced composite with an isotropic ground matrix and two families of collagen fibres embedded into it. Starting with the deformation gradient F and the local volume ratio J ($J(X) = detF(X) = \lambda_1\lambda_2\lambda_3$), the following decomposition is proposed

$$F = (J^{1/3}I)\bar{F} \tag{3.5}$$

splitting F into a purely dilatational part $(J^{1/3}I)$ and a distortional one ($\bar{F}$). Based on that and after a series of calculations, the strain energy potential is described as:

$$U = \frac{1}{D}\left(\frac{(J^{el})^2 - 1}{2} - lnJ^{el}\right) + \frac{c}{2}(\bar{I}_1 - 3) + \frac{k_1}{2k_2}\sum_{a=1}^{N}\left\{e^{k_2\langle\bar{E}_a\rangle^2} - 1\right\} \tag{3.6}$$

where the first two terms refer to the isotropic ground matrix (the first one represents its dilatational contribution and the second one its distortional one) and the third term corresponds to the (distortional) contribution of collagen fibres. Although not all variables will be discussed, it is useful to mention that $\bar{E}_a$ serves as a measure of strain of the fibres and in its definition uses κ, the normalized dispersion parameter of the fibres (κ=0 corresponds to perfect fibre alignment while κ=1/3 corresponds to random distribution so the material then becomes isotropic – for fibre visualization refer to Fig. 2.1 b) and c, k_1, k_2, D are temperature-dependent material parameters that should ideally be specified separately for each one of the 3 aortic layers.

Despite the knowledge that the arterial wall is a layered structure, the shortage of experimental data leads researchers to use a homogeneous, 1-layer model

(e.g. [154] for an HGO model). Adding to the difficulty of implementing the HGO model, the dispersion of its material parameters in the literature is vast:

- c value varies from $7.64 \cdot 10^{-3}$ MPa [153] to $2.02 \cdot 10^{2}$ MPa [154]
- k_1 varies from $9.97 \cdot 10^{-4}$ GPa [153] to 4.07 GPa [154]
- k_2 varies from 107.1 [154] to 524.6 [153]
- κ varies from 0.16 [154] to 0.226 [153]

Although Gasser's study [153] refers to the Iliac artery while Haskett's [154] to the abdominal aorta, the difference in the order of magnitude is indicative of the scattering of values reported.

HGO has also been shown to be too sensitive to Poisson's ratio. Arteries are slightly compressible; however, acquiring the true value of ν with great accuracy is almost impossible and small changes in it (from 0.475 to 0.5) seem to drastically affect stress [155]. At the same time, the data for the HGO model are taken from uniaxial and biaxial tests which cannot take into account residual stresses and strains; thus, the resulting state of the tissue will suffer from inaccuracies [156].

In 2013 Annaidh et al. [155] suggested that the initial decoupling of the HGO strain energy function is wrong since the dilatational component of the strain energy function cannot take into account the anisotropy of volumetric deformations.

In response to that, Vergori et al. [157], mentions that indeed, decoupling the strain energy function of a nonlinear hyperelastic anisotropic material into a dilatational and a distortional part leads to an unphysical response at low strains (where the isotropic nature of the material prevails), however, physiological deformations will be acquired at higher strains. According to HGO theory, a sphere when hydrostatically compressed will deform into a sphere, an expected result since fibres (according to the model's assumption) do not hold compressive loads and hence, their anisotropic contribution disappears. On the contrary, when an orthotropic sphere of the HGO material is homogeneously dilated, theory unnaturally suggests an initial

spherical dilatation until the expected ellipsoid response comes into play at higher strains due to the presence of fibres.

Despite that, and despite all the advancements in the theory of HGO, the initial model in which finite codes like Abaqus are based upon [153] is found to produce unphysical results not only at low but at high strains too, since the unnatural spherical dilatation is present even at the finite deformation regime [155,157].

On a similar note, Gilchrist et al. [158] used the additive decomposition of the strain-energy function into a dilatational and a distortional part to examine a Mooney-Rivlin strain-energy function of a transversely isotropic material (introduced by Weiss et al. (1996)) under hydrostatic tension, and found that finite element codes predict the same unnatural responses. Moreover, they showed that the decoupling proposed by Merodio and Ogden [159], where strain-energy function is split into an isotropic and an anisotropic part, proves to be equally problematic.

Based on Gilchrist et al. [158], Pierrat et al. [160] wrote user defined Abaqus subroutines to implement a new material model. This work seems very promising and manages to capture the behaviour of slightly compressible materials under both hydrostatic tension and compression; nevertheless, the identification of new constitutive parameters is needed before the accurate use of it.

The constitutive modelling and FEA implementation of the aorta (both aneurysmal and healthy) is a rapidly developing research area. Unfortunately though, many problems still remain. A 2018 study [142] examined analytically and experimentally three popular incompressible constitutive models (exponential, angular integration exponential and angular integration piecewise) and concluded that all three are unreliable in predicting Poisson's effects. At finite strain, Poisson ratio is non-constant; as a result, investigators defined it through logarithmic strains:

$$\nu_{ij} = \frac{ln\lambda_j}{ln\lambda_i} \tag{3.7}$$

and they calculated that the theoretical models could predict unrealistic Poisson's ratios (even with negative values), something not supported by experimental observation.

Because of all these challenges and uncertainties, researchers still use quite often simplified arterial models when simulating stent grafts. Table 3.12 offers a collection of vascular models used in the literature when stenting procedures are simulated. Note that some of these analyses assumed a 1-layer and others a 3-layer vascular wall.

Table 3.12 Indicative vessel models used in literature while simulating stenting procedures.

Paper	Location	Constitutive Model	Number of Layers
[81]	aorta	2nd order polynomial	1
[161]	coronary artery	Mooney-Rivlin	1
[83]	coronary artery	Mooney-Rivlin	1
[162]	coronary artery	6th order polynomial	3
[90]	coronary artery	HGO	3
[92]	cerebral vessel	2nd order polynomial	1
[84]	coronary artery	6th order polynomial	1
[163]	coronary artery	6th order polynomial	3
[164]	aorta	Mooney-Rivlin	3
[165]	aorta	linearized HGO	1
[166]	iliac artery	Mooney-Rivlin	1

3.2.3 Acquiring P-R data

The main objectives of the thesis involve the accurate estimation of the strains present in the stent rings, the COF extraction and the prediction of the deployed position of the endograft. As a consequence, when it comes to vessel modelling, the vessel's overall response is of greater interest than the stress field locally present at the arterial wall. More specifically, the main characteristic that needs to be correctly modelled for a stent analysis is the Pressure-Radius (P-R) curve of the vessel at the physiological pressure range (Fig. 3.11) so as to imitate accurately the boundary conditions present *in vivo* around the endograft. This, combined with the

uncertainties that are still present in the constitutive modelling of the artery, lead us to prefer a phenomenological model over a histological one. P-R data, though, for human abdominal aortas are surprisingly infrequent in the literature.

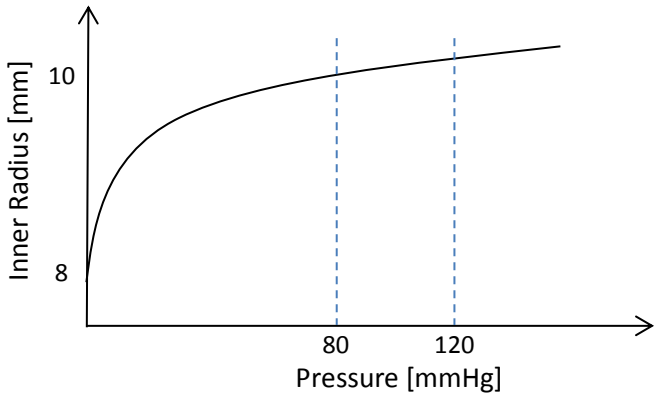

Fig. 3.11 Schematic of a typical Pressure-Radius curve. The dashed lines delimit the physiological pressure range of the human aorta.

While uniaxial tests are common because they can cope with the small samples usually available and while biaxial tests are more adequate to mimic the physiological conditions of a loaded vessel, both tests fail to take into account the residual strains present in the vessels. Pressure tests can offer such an insight, however, due to the larger samples they require, they are extremely rare.

The final objective of this Chapter is to create a material model that will simulate the overall response of the vessel and replicate the way the artery inflates.

One early and very detailed analysis that produced P-R curves of human abdominal aortas was the work of Langewouters et al. [167]. Herein, though, data from the much more recent work of Labrosse et al. [156] have been utilized because of the information available regarding both axial and circumferential stretch responses and the consideration of pre-strains, factors not present in the study of Langewouters.

In the original analysis of Labrosse et al., 4 abdominal segments were examined from females aged 49-65, 7 from males aged 38-66 and 6 segments from males aged 67-77. A cannula was introduced at one end of each specimen and applied stepped pressure up to 21.3kPa (=160 mmHg) while the other end of it was capped. Each segment was free to move axially and both the longitudinal stretch ratio and the change in radius were monitored. The experiment took place at room temperature,

less than 24 hours from harvesting and preconditioning was applied before recording the measurements. Subsequently to pressurization, vessel rings were longitudinally cut in order to release their residual stresses and the opening angle, α, was measured.

In their work, no P-R data were published directly; instead, an analytical model was used to fit the results and the strain energy function along with the fitting variables were reported. Unfortunately, Abaqus does not feature the strain energy function used by the study, so the model parameters cannot be used directly. The analytical model, though, fits the experimental data extremely well (coefficients of determination typically ranged between 0.96 and 1 [168]) and hence, it can be confidently used to recreate the experimental P-R data.

Herein P-R graphs were reconstructed for each one of the 3 aortic categories using the reported strain energy function and material constants. The underlying idea is that for every set of fitted variables, P-R curves can be created and used as "experimental" data that can then be utilized to fit a new strain energy function that is available in Abaqus.

At first, a Maple script was written in order to calculate the necessary pressure, P, to be applied on the vascular wall so as to achieve a given inner radius r_i and a longitudinal stretch λ_θ. For all calculations presented below, the mean values of [156] where used (mean material coefficients, radius, thickness and opening angle per vessel category) unless stated differently. The variance of each parameter ranged

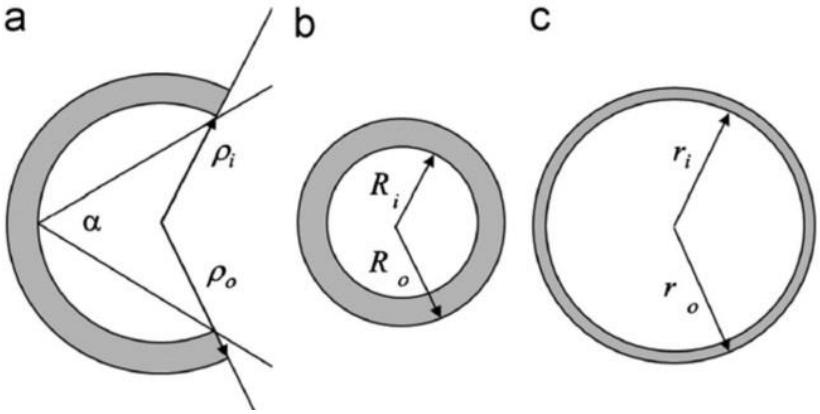

Fig. 3.12 The stress-free (a), the unloaded (b) and the pressurized state (c) of a vessel tube. In the first two states the thickness is assumed to be unchanged and equal to t; similar assumption is made for the original length L. In the pressurized state, the thickness reduces and the length changes to l. From [156] with permission.

from 1-5% for the material coefficients and up to 40% for the opening angle. Fig. 3.12 introduces the nomenclature originally used in the study and followed herein as well.

In the original study [156], the strain energy function is:

$$U = \frac{c_1}{2}\left(e^{\left(c_2 E_\theta^2 + c_3 (E_z^2 + E_r^2)\right)} - 1\right) \tag{3.8}$$

where c_1, c_2, c_3 are the reported material parameters and E_i for $i = r, \theta, z$ are the Green strains. By assuming incompressibility we acquire:

$$E_r = \frac{1}{2(2E_\theta + 1)(2E_z + 1)} - \frac{1}{2} \tag{3.9}$$

so only two strains are independent:

$$E_i = \frac{1}{2}(\lambda_i^2 - 1) \text{ for } i = \theta, z \tag{3.10}$$

The circumferential and longitudinal stretches are respectively defined as:

$$\lambda_\theta = \frac{\pi}{\pi - \alpha} \frac{r}{\sqrt{\frac{\pi}{\pi - \alpha}\lambda_z (r^2 - r_i^2) + \rho_i^2}} \text{ and } \lambda_z = \frac{l}{L} \tag{3.11}$$

so as to take into account the circumferential residual stresses. Regarding nomenclature, r is the radius at the deformed configuration with $r_i \leq r \leq r_o$ and l is the deformed length.

Furthermore, by demanding the mid-line length of the circumference to be the same before and after the axial cut, we also get:

$$\rho_i = \frac{2R_i + t\frac{a}{\pi}}{2(1 - \frac{a}{\pi})} \tag{3.12}$$

The variables $R_i, t, \alpha, \lambda_z$ and λ_θ (evaluated at the inner radius of the vessel) were all experimentally measured. Similarly to the original work, all radii in the current analysis are inner radii as well.

For the construction of P-R graphs, F_z is defined as the force necessary to keep the sample at constant length while under pressure. Then:

$$F_z = \pi \int_{r_i}^{r_o} (2\lambda_z^2 \frac{\partial U}{\partial E_z} - \lambda_\theta^2 \frac{\partial U}{\partial E_\theta}) r dr \tag{3.13}$$

and since the closed end of the vascular section is free to move axially, we demand $F_z = 0$. Nevertheless, because the analytical solution of this equation is impractical to use, $F_z = 0$ is solved for various r_i, calculating the respective λ_z.

Subsequently, for each pair of (r_i,λ_z), pressure is calculated from:

$$P = \int_{r_i}^{r_o} \frac{1}{r} \lambda_\theta^2 \frac{\partial U}{\partial E_\theta} dr \tag{3.14}$$

These (r_i,λ_z, P) sets will serve as the experimental data to be used later on.

An interesting outcome from this analysis is that since residual stresses have been taken into account, $\lambda_\theta < 1$ at R_i, id est, at the closed yet unpressurised state, the vessel at the inner radius is under compression. As a result, $\lambda_\theta = 1$ for a radius greater than the initial one. At the pressurized point where the vessel meets $\lambda_\theta = 1 =$ the same as in the unstressed-open state, the vessel also satisfies $\lambda_z = 1$.

As an effect of that, when examining the initial part of the P-R graph, one can see that the radius at $P = 0$ is greater than R_i. This type of behaviour at the very start of the graph (well before the physiological range) can also be observed in other studies [136] and is explained by the analytical inclusion of residual stresses. Note that if $\alpha = 0$, this effect is not present since the problem becomes equivalent to pressurizing a vessel with no residual stress.

However, even when abnormal initialization is present, it is very quickly compensated by the overall response of the equation and the graph eventually behaves as expected. To validate the analytical results obtained from Maple, the data at $P = 13.3\ kPa = 100\ mmHg$ were compared to the corresponding experimental data provided by Labrosse et al. The analytical values lie always inside the 95% confidence level of the mean experimental values and the predictions are very satisfying (Table 3.13).

In the original study [156], material coefficients are reported with variations at the 95% confidence level. In order to evaluate the sensitivity of the model to c_1, c_2, c_3, a study was performed and it was found that in the given range, alteration of the coefficients alters the plateau of the P-R curve insignificantly. It was noted that increase of c_1 moves the plateau upwards, whereas increase of both c_2 and c_3 moves the plateau downwards. Hence, as far as the coefficients are concerned, less vessel distensibility will involve the lowest value of $c_1$and the highest values of c_2, c_3. Even then, though, the plateau differs by less than 0.5% from the mean case, justifying our choice to use the mean values of the material parameters.

Table 3.13 Discrepancy between the analytical solution and the values reported in [156].

Vessel category	Stretch at 13.3 kPa	Experimental value at 95% confidence level	Analytical value	Discrepancy from the exp. mean
Females 49-65	λ_θ	1.27 ± 0.09	1.27	0.0%
	λ_z	1.11 ± 0.03	1.11	0.0%
Males 38-66	λ_θ	1.35 ± 0.16	1.32	2.2%
	λ_z	1.10 ± 0.09	1.11	0.9%
Males 67-77	λ_θ	1.15 ± 0.03	1.14	0.9%
	λ_z	1.05 ± 0.04	1.05	0.0%

3.2.4 Fitting a new strain energy function

Having recreated the experimental data (later seen in Fig. 3.13), a fitting analysis was performed in Matlab. First though, the aforementioned ill-position of the P-R data at the initial state had to be tackled, hence, alteration of the dataset at low values of pressure was performed to provide a smooth start of the curve and satisfy $P(r = R_i) = 0$. This alteration was conducted from the initial point of zero pressure $(0, R_i)$ up to a predefined, arbitrary point (P', r') which laid well before the start of the physiological range of pressures which is of interest. The physiological range is assumed to be [80 , 120]mmHg which is equivalent to [10.7 , 16.0]kPa.

The values of P, r_i, λ_z calculated on Maple were used as an input for $P > 0$ and the alteration of the initial part of the dataset was conducted by using the logarithmic function:

$$r_i = ln(\beta P + 1) + R_i \tag{3.15}$$

where $\beta = \frac{e^{r'-R_i}-1}{P'}$. Fig. 3.13 illustrates the original and the altered datasets.

By using the altered dataset – which behaves identically to the original one at the range of interest – fitting was performed by minimizing the equation:

$$\int_{r_i}^{r_o} \frac{1}{r} \lambda_\theta^2 \frac{\partial U}{\partial E_\theta} dr - P \tag{3.16}$$

(where the integral corresponds to the new function U and P refers to the calculated values of the previous section) through the use of the non-linear least square subroutine lsqnonlin. After testing several polynomial functions for the strain energy density function U, a 6th order reduced polynomial (also named the Yeoh model) was found to fit the data best:

$$U = \sum_{i=1}^{6} c_i (I_1 - 3)^i \tag{3.17}$$

c_i are the material parameters to be fitted and I_1 is the first strain invariant (i.e. $I_1 = trC$ with C being the right Cauchy-Green tensor of the deformation gradient F) for which I_1=$\lambda_r^2 + \lambda_\theta^2 + \lambda_z^2$. This function allowed for a perfect fit since in all cases the coefficient of determination was 1.0. Given the fact that the fitted data originated from a function, the acquisition of such a high coefficient should not come as a surprise.

Later on, this polynomial function will allow a successful implementation in Abaqus, as it has been reported to be used in numerous cases for the modelling of the coronary artery [84,162,163]. The fitted coefficients produced from the Matlab analysis are reported on Table 3.14.

Table 3.14 Fitted coefficients for the 6th order reduced polynomial strain energy function. c_i are reported in MPa.

Category	c_1	c_2	c_3	c_4	c_5	c_6	R^2
Females aged 49-65	0.0028	0.0209	-0.0463	0.2100	-0.2985	0.2254	1.00
Males aged 38-66	0.0019	0.0195	-0.0091	0.0378	-0.0414	0.0358	1.00
Males aged 67-77	0.0048	0.0911	-1.0600	9.5292	-31.7421	46.3921	1.00

Finally, it can be noted that a smaller P' (i.e. shorter intervention to the original data) stiffens the initial slope of the P-R curve but, as expected, leaves the rest of the graph unaffected.

3.2.5 Validation of the strain energy function

The last stage of the analysis involved the implementation of the isotropic, 6th order reduced polynomial strain energy function along with the fitted parameters c_i, $i = 1 \dots 6$ into the FEA solver. In Abaqus this function takes the form:

$$U = \sum_{i=1}^{6} c_i (\bar{I}_1 - 3)^i + \sum_{i=1}^{6} \frac{1}{D_i} (J^{el} - 1)^{2i} \tag{3.18}$$

where $\bar{I}_1$ is the first distortional strain invariant, J^{el} is the elastic volume ratio defined as the total volume ratio (current volume/original volume) over the thermal volume ratio (herein=1) and D_i are material parameters. The model was assumed almost incompressible with Poisson's ratio being over 0.4999 (leading to D_1=0.004593 and $D_i = 0$ for i=2,..,6) and density = $1.16 \cdot 10^{-9}$ $tonne/mm^3$.

Video 3.1 FEA results of Abaqus/Explicit. Displacement (in mm) of a vascular section (Females aged 49-65) simulating the experiment of Labrosse et al. For the video, refer to the pdf version.

Since the experimental data of Labrosse et al. were acquired for pressures up to 160 mmHg = 21.3 kPa, this was the maximum pressure used in Abaqus as well. For this purpose, a vascular tube was constructed in the FEA environment, fixed in one end and pressurized while leaving the other end capped and free to move axially. The

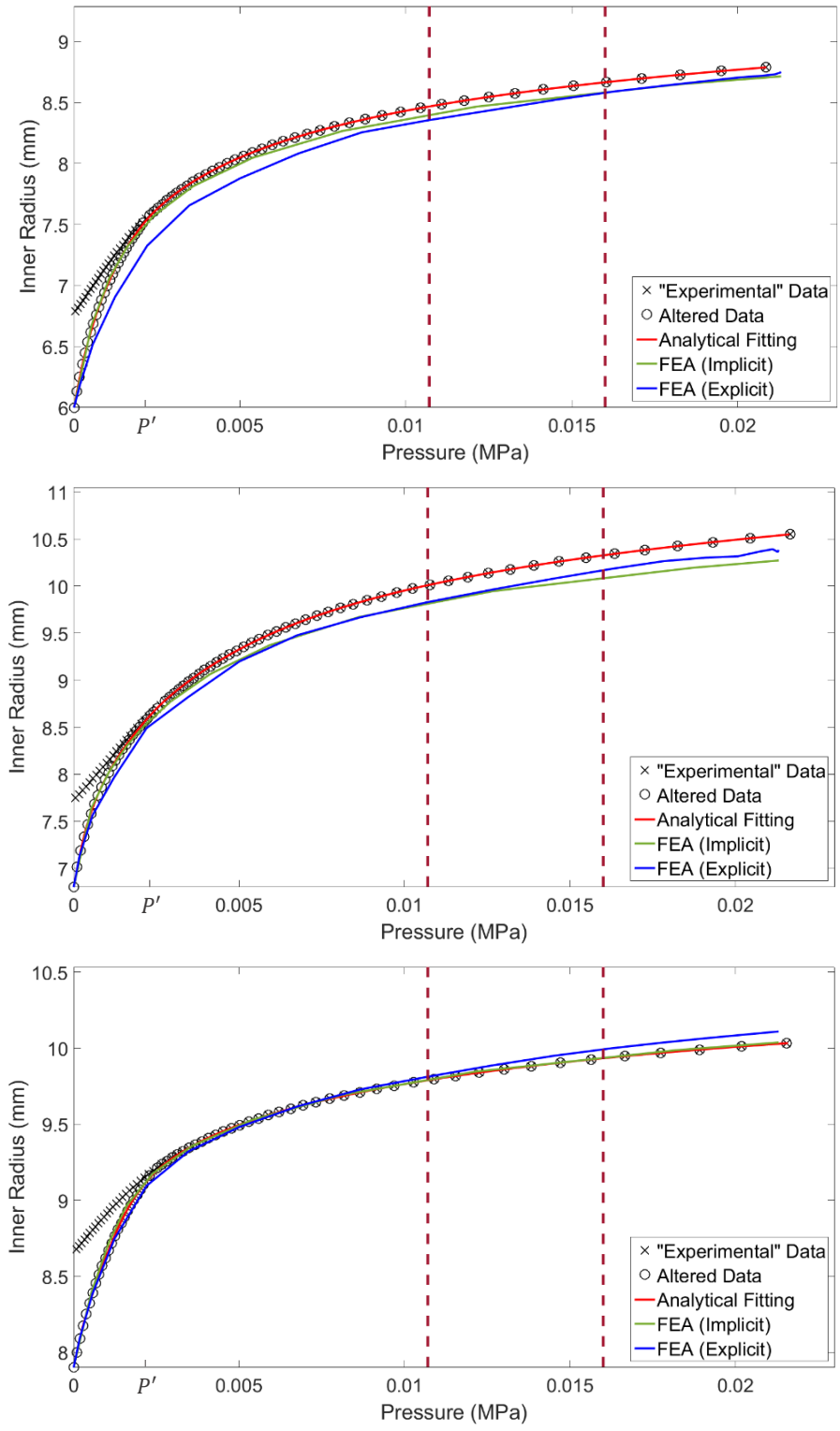

Fig. 3.13. Pressure – Inner Radius curves for the three cases studied. From top to bottom are the results for Females (49-65), Males (38-66) and Males (67-77). The original "experimental" results (crosses) were altered at the initial pressurization region, i.e. before point P' (circles) and according to the latter, analytical fitting was performed (red line). The coefficients produced through this procedure were validated using implicit (green line) and explicit (blue line) FE analysis. The region between the dotted vertical lines signifies the physiological range.

analysis was performed for all 3 vessel categories using both an implicit and an explicit solver (Abaqus/Standard and Abaqus/Explicit respectively). In all cases, continuum elements were used (C3D10H and C3D4 tetrahedral elements respectively) under the same meshing (Video 3.1), although it was observed that mesh density affected the P-R curve insignificantly. Additionally, for the Abaqus/Explicit analyses, the time step was 5 times the 1st natural period of the vessel.

As can be seen in Fig. 3.13, the models closely follow the behaviour of the original P-R curves. The agreement is very satisfying for both solvers and can be confirmed by the maximum discrepancy identified at the pressure range of interest (Table 3.15), validating the entire modelling process.

This material model will be used in Chapter 4.

Table 3.15 Maximum error for the P-R curve between the FEA and the analytical solution at the physiological pressure range.

Category	**Maximum Error Abaqus/Standard**	**Maximum Error Abaqus/Explicit**
Females aged 49-65	-1.0%	-1.3%
Males aged 38-66	-2.4%	-1.8%
Males aged 67-77	0.0%	0.6%

3.2.6 Identification of the unloaded vessel size

In clinical reality, vascular dimensions are monitored in a loaded rather than an unloaded state. Since patient specific data can only be acquired via screening modules like CTA, the patient geometry imported to any numerical analysis will inevitably refer to an *in vivo*, already pressurized configuration. As a result, the classical FEA approach in which the initial condition of a structure is thought to be unloaded and stress-free is challenged.

Efforts to alleviate the problem focus on computing the unloaded geometry of the vessel by utilizing both its deformed configuration and the known boundary

conditions during screening (primarily, arterial pressure). This process can be performed prior to all other analysis steps and can provide the reference configuration for subsequent calculations.

Towards this end, Govindjee and Mihalic, successfully created a FE formulation in finite hyperelasticity for compressible [169] and later on quasi-incompressible materials [170]; they did so by re-parameterizing the standard equilibrium equations after interchanging spatial and reference coordinates. Putter at al. [171], used a backward incremental method and a neo-Hookean material to compute the wall stress of an AAA on the true diastolic geometry while Chandra et al. [172] used a Mooney-Rivlin model; in their work, they pressurized the vessel, plotted the pressure-displacement response of each node and then through extrapolation identified the location of the nodes at zero pressure. Based on a different approach, Gee et al. [173] used an inverse design analysis to calculate a stress-free reference configuration, a method that yielded poor results when geometry was complex. On the same study, though, researchers also developed a method based on a modified updated Lagrangian formulation in which a multiplicative split of the deformation gradient was executed to generate a pre-stressed configuration. This idea was further developed by Weisbecker et al. [174] to a generalized pre-stressing algorithm in which the iteration process updated the deformation gradient field instead of the displacement one.

All the techniques above seek to establish the correct stress state of the loaded arterial wall at the initiation of the FE analysis. Herein, however, the phenomenological model has not been developed to predict the stress field of the aorta, hence such aim is out of the scope of this work. Since, what is of interest here, is the correct vascular response at the application of pressure, no computationally expensive analysis is needed. Instead, analytical tools can be utilized for the identification of the initial geometry as described below.

For a given set of inner radius r_m, and thickness, t_m, that can be observed via clinical screening at pressure P_m, we are looking for the original inner radius, R_i, and thickness, t, that upon inflation will result at the observed set $(P_m,\ r_m, t)$, given the vessel category (Fig. 3.14).

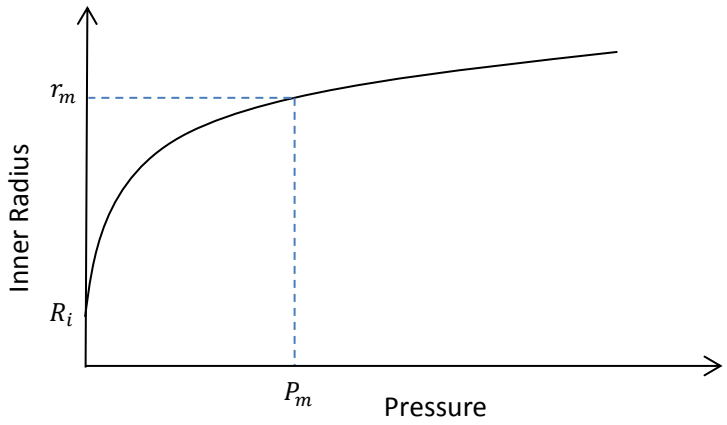

Fig. 3.14 Pressure-Radius curve that starts from R_i and satisfies $r(P_m) = r_m$.

In more detail, by using one of the examined vessel materials, hence a specific set of $c_i, i = 1,..,6$ coefficients, we can treat the original radius, R_i, as an unknown and identify it by equating the equation (3.14) of the specified strain energy function with P_m.

Note that P_m is not straightforward to extract in the clinical setting and a mean value of pressure during the cardiac cycle might be the most realistic choice. Since the ventricles spend approximately one-third of the cardiac cycle in systole and two-thirds in diastole, a commonly used approximation (see for example [175]) for the time-weighted arterial blood pressure in large system arteries is:

$$P_m = P_d + \frac{1}{3}(P_s - P_d) \tag{3.19}$$

where P_d is the diastolic pressure and P_s the systolic one. When considering $P_d = 80\ mmHg$ and $P_s = 120\ mmHg$, then $P_m = 93.3\ mmHg = 12.44\ kPa$. This value will be used as the reference pressure in various cases examined in the thesis.

After acquiring the R_i value, the original thickness, t, can also be calculated by utilizing incompressibility, via the equation:

$$t = \sqrt{t_m(t_m + 2r_m) + R_i^2} - R_i \tag{3.20}$$

thus providing complete information for the creation of the original, unloaded vascular section. Note that for this procedure, $\lambda_z = 1$ is used since it is assumed that the vessel cannot deform axially *in vivo*.

Using this approach, when examining cylindrical vascular sections, we can model the original vessel with the specified R_i and t and result in the correct P-R plateau. With a similar rational, when examining complex patient specific aortas, the initial vascular radius that upon pressurization will satisfy the CTA configuration can also be identified; however, for such vessels, CAD software requires to be used to efficiently shrink non-straight geometries into the unloaded ones.

3.3 Discussion and summary

Tortuosity and kinking are major contributors to the topological uniqueness of AAAs. Herein, 10 angles were identified as adequate for the description of the AAA region while their 3D values, along with their projection values, were calculated for 258 patients treated with the Anaconda stent graft. The calculation of the median and extremes of these angles helps quantify and understand the geometrical landscape of the abdominal aortic aneurysms. For a vessel to be fully described, distances of the points that define these angles are also needed, nevertheless, this information was not taken into account in the statistical analysis as it would unnecessarily complicate the clarity of the outputs. In a clinical set-up, where the geometry of a specific patient is of interest, these values could be included.

Along with the angle analysis, 9 dimensional variables were also considered, further assisting to the identification of the norms and extremes of AAAs. This knowledge can help clinicians categorize patients according to the severity of various geometrical characteristics and can assist manufacturers in building case-study aneurysms for stent design assessments. To the author's knowledge, this is the most extensive study on the geometry of AAAs.

In addition, for the first time, the cross section of the AAA neck was extensively examined, challenging the assumption of circularity. Results showed that the median average ellipticity doesn't lie far from a circle, yet aneurysmal necks with very elliptical cross sections were identified. Furthermore, the lack of correlation between

the shape metrics used and other geometrical characteristics of the aneurysm, indicate that special attention needs to be taken in a patient by patient manner. The existence of significantly non-circular cases could prove alarming for the endograft performance.

Regarding the material model of the vessel, although it has been shown that the aortic wall is anisotropic, isotropic models for the aorta are widely used in the literature for their simplicity and the close-to-isotropy response of the vessel at the physiologic pressure range [176]. A critical review of the literature showed that despite modelling advances, problems in the implementation of anisotropy and compressibility are still present and negatively influence FEA results.

The use of a material model of high fidelity that can capture local strain effects was initially considered and yet eventually abandoned as no reliable P-R vessel responses could be identified in the literature. On the contrary, studies that tried to use such models in inflating tests have reported significant discrepancies between the experiment and the numerical model results. For example, the HGO model has been reported to consistently under-predict the P-R response of the vascular tissue by up to 35% due to the exclusion of residual stresses [97].

In order to emphasize on the correct global response of the vessel, a phenomenological model of the aortic wall was created; that way, the inflation of arterial sections under pressure was correctly represented providing accurate boundary conditions for the stent graft analyses to follow. The model described herein can be easily implemented in most FEA codes and the technique presented for identifying the unloaded vessel size is quick and reliable.

Pressurizing a cylindrical section of an artery poses essentially a 1D deformation, hence, anisotropy does not add extra information in cases like these. For that reason, all results reported in Chapter 4 (that implements the material model in vascular tubes) do not suffer from the assumption of isotropy. When more complex geometries are introduced, though, limitations might arise. As a result, the technique presented herein should be used with caution for (patient-specific) 3D geometries that incur high curvature variations.

Another limitation is that the data used are based on a small number of specimens and constrain vessels to fit into one of 3 available categories. Furthermore, the experiments of Labrosse et al. [156] were conducted at room temperature, a condition that is likely to have an effect on the mechanics of the aorta [167]. The scarcity of P-R data regarding human specimens in the literature, however, is worth noting and currently restricts attempts of more accurate material modelling.

Chapter 4

Ring Model

As it has already been established, EVAR has become extremely popular in recent years, yet mechanical aspects of the endografts often affect the outcome of the intervention. In this Chapter we examine a novel way to model the basic unit of a stent graft by trying to acquire computationally efficient FEA solutions without sacrificing precision. A model like that has an end in itself, as it can allow the mechanical study of the basic building block of the endograft, yet at the same time, serves as a step towards the creation of full stent graft models as well.

During the last decade a variety of stents have been developed followed by the advancement of computational techniques to better understand their effects and improve their overall performance. Stent design optimization [84], sensitivity studies for their geometrical parameters [85,177], fatigue life analysis [69,70], investigation of the vessel-artery interaction [178,179] and patient specific simulations [163,165] have been conducted providing insight for both the clinicians and stent device designers. As has been mentioned already though, most of these studies have been primarily conducted on similarly designed Z-shaped stents since these geometries are the most dominant in the market. Even comparative studies between different stents have used devices with related shapes [180]. Another common characteristic of these stents is that the production process usually involves laser cutting of Nitinol tubes

and in some cases annealing, leading to a stress free stent when undeformed. Nevertheless, the behaviour of alternative geometries has rarely been examined. An interesting exception is the work of Demanget et al. [88] where eight commercially available endograft limbs (the iliac legs of Z-stents, a spiral stent and the Anaconda^{TM} endograft) were simulated, underlining the importance of the global design on the mechanical performance of such devices.

Herein, a computationally efficient numerical model of a bundle of Nitinol wires, the basic structural unit of the commercial stent graft Anaconda^{TM} (Terumo Aortic), has been developed. In recent studies, when bundle rings were to be modelled, researchers often adopted the 'equivalent beam' approach [88,94,95]. This technique assumes that a multi-turn bundle can be represented by a 1-turn model as long as the 2nd moment of area for both of them is the same. Although its simplicity is tempting, the drawback of this approach is significant since such a model exaggerates material strain magnitudes because the radius of the wire is increased. Moreover, the bending stiffness of the bundle is correctly represented only at low deflections; since Nitinol is non-linear, in high deflections, the equivalent structure will inevitably behave different from the true one due to the false stress/strain levels developed. As a result, altering the wire thickness will affect both the strain and the stiffness of the structure making the model inadequate for most structural analyses. Such sacrifice is not made herein.

Furthermore, and contrary to most other modelling attempts, the approach presented here can take into account the pre-strains induced in the wires during manufacturing, a feature proven to be of great importance to the characterization of the behaviour of the structure. Finally, because the goal of the modelling technique is to be easily extendable into multiple bundle rings, hence simulating the metallic scaffolding of the whole device, the symmetry that the circular structure exhibits was not utilized (as, for example, in the works of [76,97]). In such a way, patient-specific devices will be able to be built without altering the fundamental basis of the method. To the best of the author's knowledge, currently, there is no model available that can correctly capture the mechanical characteristics of the Anaconda^{TM} ring and at the

same time produce results in no more than a few hours, making it computationally efficient enough for research and development purposes. This is the void the current model aims to fill.

4.1 Development of the Ring Model

The Anaconda™ stent graft device consists of a series of circular bundle rings which are sutured to a tubular polyester fabric (Fig. 4.1). Each one of these bundles is constructed from multiple turns of a Nitinol wire. The wire is originally straight and is formed into a bundle by being turned onto a mandrel; then its two ends are crimped to form a closed ring. The first proximal bundle ring of the device is considered to be the most important since it is the first the bloodstream meets and, having the greatest stiffness, is primarily responsible for ensuring sealing and, in conjunction with the hooks, anchoring.

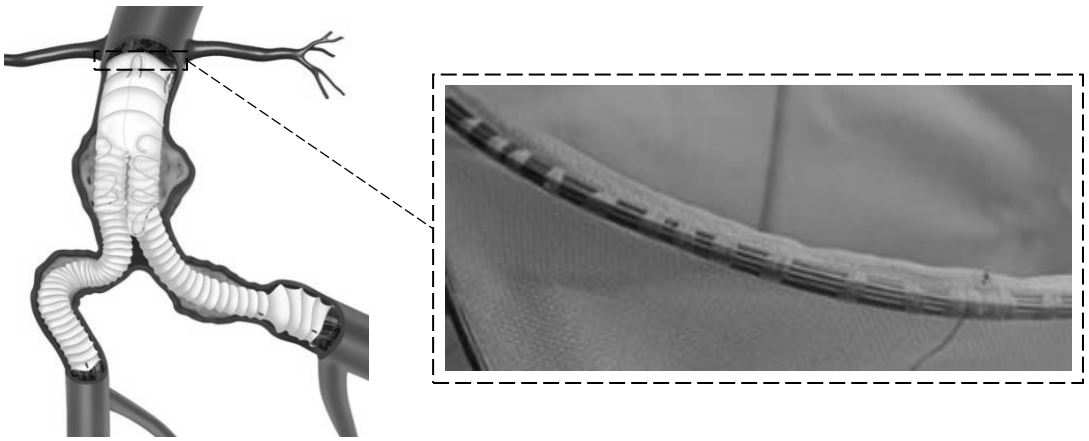

Fig. 4.1 The Anaconda™ stent graft (Terumo Aortic) placed inside an AAA [207]. The 1st proximal bundle ring is shown in detail illustrating the multiple turns of Nitinol wire sutured onto the fabric.

To model an *n*-turn bundle ring, *n* straight superimposed wires of Timoshenko beam elements (B32H, hybrid quadratic functions that allow for transverse shear deformation) were formed into a circle and subsequently joined start-to-end. In other words, instead of turning 1 Nitinol wire *n* times (as in manufacturing), *n* overlapping (i.e. occupying the same space) wires were considered, joined together so that the

bundle would behave as a single entity, and then turned once (Fig. 4.2). After that, the *n* wires were tied start-to-end to remain circular. Because the whole bundle behaves as one, boundary conditions need only to be applied to a single wire, a feature that will prove useful for the reduction of computational cost.

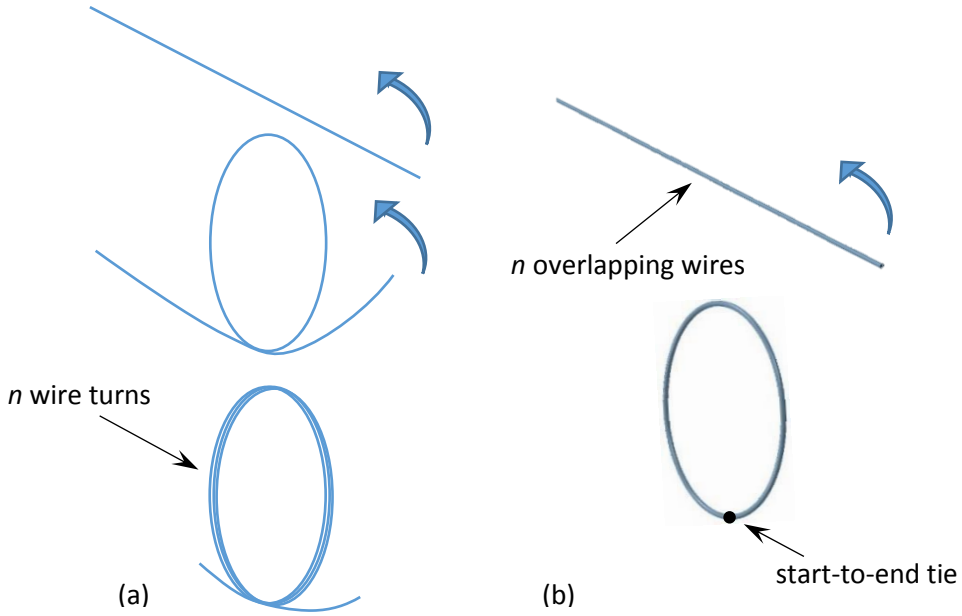

Fig. 4.2 During manufacturing, a wire is turned *n* times to create a bundle (a); yet herein, *n* wires that occupy the same space are turned once (b).

Although beam elements can capture the mechanical response of the bundle ring, they cannot fully represent its cross sectional geometry, especially because of the wire superposition. This aspect is important since correct topological representation means that once the ring is deployed into the artery it will be correctly deformed and hence, acquire an accurate global shape which will lead to an accurate strain state.

For that reason, surface elements (SFM3D4R, quadrilateral with reduced integration and no inherent stiffness) were used to create a circular shell representing the bundle surface (later seen in Fig. 4.4). These elements do not add any stiffness to the structure nor would capture strains; however, by tying them to the beam elements at the beginning of the analysis, they provide the model with a satisfactory approximation of the bundle size and as a result, the global deployed shape of the

ring. The identification of the appropriate bundle diameter, though, brings some complications.

In reality, the cross section of the bundle consists of tightly arranged wires that stay in place due to sutures. These ties, though, are manually created during manufacturing and result in the inconsistent arrangement of the Nitinol turns through the circumference of the rings. As a result, there is no straightforward way to calculate the diameter of each bundle. In order to acquire an estimator of the cross sectional diameter of the bundles, results from circle packing theory have been utilized. Packing theory is a branch of mathematics that, in the most general sense, provides optimal arrangements of geometrical shapes inside other geometrical shapes. Herein, the results regarding arranging a specific number of circles (Nitinol turns) inside the smallest possible circle (bundle approximation) are used (Fig. 4.3).

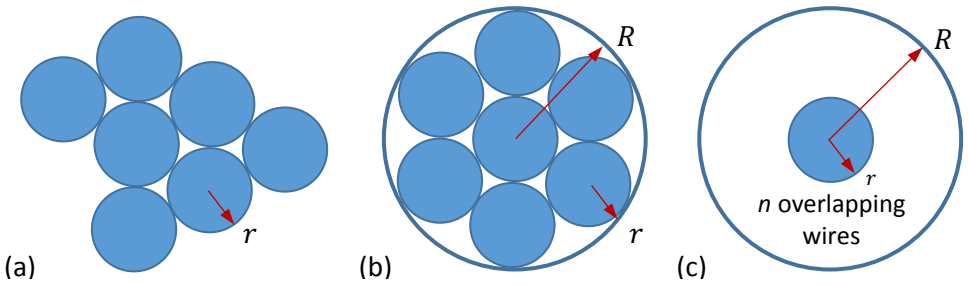

Fig. 4.3 Cross section of a realistic bundle configuration possibility (a) and of a configuration according to the circle packing theory (b). The model (c) has a bundle diameter equal to the one calculated by the circle packing theory and hosts all the turns overlapped at the centre of the bundle.

Table 4.1 reports the ratio,

$$BW = \frac{Bundle_{Radius}}{Wire_{Radius}} \tag{4.1}$$

for n=1,…,14, were n is the number of wire turns inside the bundle. For these and greater values of BW, the reader is referred to [181,182]. Note, though, that currently no Anaconda™ device has a ring which accommodates more than a 14-turn wire.

Table 4.1 The ratio BW allows the construction of a bundle with the smallest possible cross section to accommodate *n* wires of a given radius.

$\boldsymbol{n}$	$\boldsymbol{BW}$	$\boldsymbol{n}$	$\boldsymbol{BW}$
1	1.000	*8*	3.304
2	2.000	*9*	3.613
3	2.154	*10*	3.813
4	2.414	*11*	3.923
5	2.701	*12*	4.029
6	3.000	*13*	4.236
7	3.000	*14*	4.328

By combining beam and surface type elements, a ring model that closely approximates both the stiffness and the topology of the bundle was created (Fig. 4.4). Moreover, due to the superposition of Nitinol turns, neither computationally expensive wire-to-wire interactions needed to be modelled, nor case-specific cross-sectional arrangements depending on the number of turns each ring is constructed from.

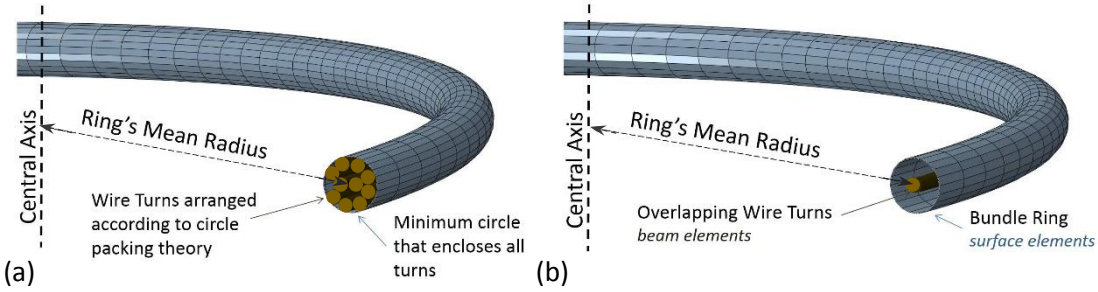

Fig. 4.4 The bundle model. Arranging the *n*-turns of a single wire according to circle packing theory allows the circle of minimum diameter that can enclose all of them to be calculated (a). This circle serves as the bundle ring's diameter while the *n* wires are superimposed at the centre of it (b).

In order to build a ring, the wire diameter, the ring's inner diameter and the number of wire turns need to be known; and all of these parameters greatly affect the overall structural stiffness of the bundle as has been seen in sensitivity studies not presented herein. Contrary to the number of turns that is strictly defined, though,

small manufacturing errors do exists for the considered diameters. Furthermore, examination of typical stent rings showed that the wire diameter is more consistent to its mean value than the ring diameter is. However, evaluation of several bundles showed that the theoretical inner diameter of the ring (i.e. the diameter of the mandrel upon which the wire is being turned onto) and the physical one, produce a discrepancy of less than 1%, giving confidence in the use of mean values for all variables.

The construction of the bundle ring constitutes only the first step of the analysis. Following that, each ring is compacted into a catheter with the use of a cylindrical sheath (SFM3D4R elements) of varying diameter which serves as a compacting tool (Fig. 4.5 a,b). Furthermore, an internal cylindrical surface is modelled (as a rigid surface) representing the inner tube present in the physical delivery system, referred to as the braided stiffener. Modelling the full compaction of the ring is necessary because of the path-dependent nature of Nitinol. If excluded, the final stress/strain state of the material will not capture the *in vivo* state of the device.

After compaction, the bundle ring can be subsequently deployed into a vascular section (Fig. 4.5 c). The deployment occurs via the inflation of the compaction cylinder and the boundary conditions for both compaction and deployment are:

- $\text{Rotation}_x=0$ for points B, D
- $\text{Rotation}_y=0$ for points A, C
- $\text{Rotation}_z=0$ for points A, B, C, D
- $\text{Displacement}_x=0$ for points A, C
- $\text{Displacement}_y=0$ for points B, D
- $\text{Displacement}_z=0$ for points B, D

(4.2)

with points identified in Fig. 4.5. These conditions are straightforward in order to secure the stability of the ring.

After deployment, the vessel is pressurized for the ring to experience a pulsating loading according to the requests of the analysis. For that step, in addition to equations (4.2), the following restriction is applied as well:

- $\text{Rotation}_y=0$ for point B (4.3)

This condition secures that the ring will not experience a “full body rotation” around its tangential axis while it enhances the ring/vessel contact and increases the stability of the interaction.

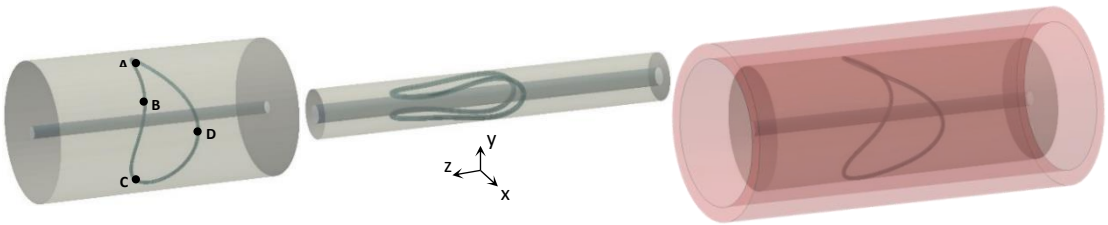

(a) (b) (c)

Fig. 4.5 After the ring formation, the ring is compacted with the help of a shrinking cylinder (a) that collapses the ring into the sheath diameter (b) before the final deployment through the cylinder’s inflation (c). The innermost cylinder represents the braided stiffener.

Initial tests using equation (4.3) from the compaction stage, revealed that the resultant compacted shape of the ring differed from the shape acquired from micro-CT scanned devices inside their sheaths. The reason being that during compaction, the potential energy of the ring increases dramatically and the ring, in its effort to minimize the stored energy, causes changes in its twist despite the suture and friction restrictions; as a result, the rotational restriction imposed by equation (4.3) seems unrealistic in the early stages of the analysis. It is hypothesized, though, that after vessel/ring equilibrium is reached, no further rotation takes place.

Because of geometrical, material and contact non-linearities, implicit dynamic steps with a quasi-static formulation are used both for the compaction and the deployment of the ring as well as the pressurization of the vessel. For this formulation, Abaqus uses a Backward Euler scheme which has a viscous effect that increases stability. Because of inertial effects though, the time scale of the analysis becomes relevant and needs to be sufficiently large so that dynamic effects are damped out, allowing the solution to approach steady-state. The period of each step that was used herein is 0.01 seconds and the kinetic energy was checked throughout all analyses to be a small fraction (<5% and usually <1%) of the internal energy. Lastly, to further enhance stability and aid convergence, a non-symmetric Jacobian matrix was chosen.

This helps to deal with the unsymmetric terms that are created in the stiffness matrix during the analysis (particularly at contact).

All cases presented in this Chapter were performed using Abaqus/Standard. For simulating the Nitinol alloy, a user defined subroutine (UMAT) that follows the constitutive model proposed by Auricchio [65] was used. The density was set to 6.45 g/cm^3 and the material parameters employed were calibrated specifically for the Anaconda™ wires at 37 °C during the development of the PhD thesis of Boukis [77] (Table 4.2).

Table 4.2 Parameters for the constitutive model of Nitinol (refer to Fig. 2.5).

Austenite elasticity E_A (GPa)	59
Austenite Poisson's ratio ν_A	0.33
Martensite elasticity E_M (GPa)	26.5
Martensite Poisson's ratio ν_M	0.33
Transformation strain ε^L (MPa)	0.05
Start of transformation loading σ_L^S (MPa)	636
End of transformation loading σ_L^E (MPa)	740
Start of transformation unloading σ_U^S (MPa)	430
End of transformation unloading σ_U^E (MPa)	302
Start of transformation stress in compression (MPa)	965

4.2 Validation and further exploration

After the creation of the Ring Model, assessment and validation is needed before applying it to any trustable stent analysis. This section presents a series of tests and comparisons made to ensure the credibility of the model. Note that all vascular sections in this Chapter have been modelled with the phenomenological model developed in Chapter 3. Apart from Section 4.2.2, all analyses use an arterial model corresponding to males aged 67-77 (material parameters provided in Table 3.14). Section 4.2.2 uses the aforementioned as well as the model corresponding to males aged 38-66.

4.2.1 Integration points

The use of beam elements for stent modelling, although widespread, is not always the choice of researchers; there are plenty of studies which have used continuum finite elements (e.g. [84,163,177]). However, apart from the obvious advantages of beam elements when it comes to computational efficiency, another merit is the existence of integration points at the outer perimeter of them, a characteristic not present in continuum elements. This feature is helpful in bending dominated problems such as stent compaction, since the maximum stresses occur in the circumference of the structure, and a more accurate calculation of them can be performed.

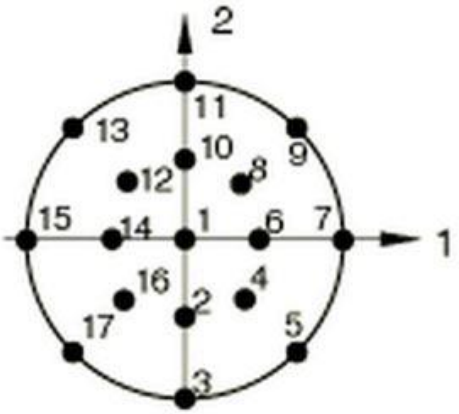

Fig. 4.6 Default section points at the cross section of a beam element [183].

More specifically, in order for Abaqus to calculate the variables of interest, numerical integration is executed at multiple points of each finite element, namely its section points. The default number of section points of a beam element is 17, and are distributed over its cross section according to Fig. 4.6. As can be seen, 3 points are used in the radial direction and 8 over its circumference allowing for the notation (3,8). Nevertheless, according to Abaqus Documentation [183],

> *the default number of section points is adequate for monotonic loading that causes plasticity. If reversed plasticity will occur, more section points are required.*

Since the Ring Model is built to compact and then deploy into a vessel (i.e. enter superelasticity and then unload its strains), the first parameter that needed to be specified was the adequate number of section points of the beam elements. Towards that end, a 4-turn ring with a diameter of 35.9 mm and 0.28 mm wire thickness (later on mentioned as Case 5) was used for the investigation. The vascular section was modelled as a straight tube and the interaction between the ring and the vessel was modelled with a friction coefficient of 0.05. The variables of interest were:

- Maximum strain, ε, at systole
- Maximum delta strain: $\Delta\varepsilon = \varepsilon_{Diast} - \varepsilon_{Syst}$
- Maximum mean strain: $M\varepsilon = \frac{\varepsilon_{Diast}+\varepsilon_{Syst}}{2}$
- Chronic outward force (COF), at systole

and were all evaluated after 30 loading cycles (between diastolic and systolic pressure). It should be mentioned that COF is calculated by summing the radial component of all (nodal) forces, F_R, produced by the ring on the vascular surface (later seen in Fig. 4.17). Note also that each one of the strain variables was examined independently of the rest; for example, maximum $\Delta\varepsilon$ is calculated after examining the difference of strain values developed in every node of the ring and identifying the largest one, hence, it may not be related to the node of maximum diastolic (or systolic) strain. As a result, the location of each one of the variables does not need to coincide with the location of the others. Finally, all strains are logarithmic, since the investigations performed involve large deformation analyses.

The number of section points was progressively increased from (3,8) to (3,10), (3,16), (3,20), (3,24), (3,30), (5,10), (5,16), (5,20), (5,24), (5,30), (7,10), (7,16), (7,20), (7,24), (7,30), (9,30) and finally to (11,36). The latter configuration was considered to be the most accurate one and as section points increased, the results of the models were found to more closely fluctuate around its solution.

Video 4.1 along with Fig. 4.7 display a representative analysis result.

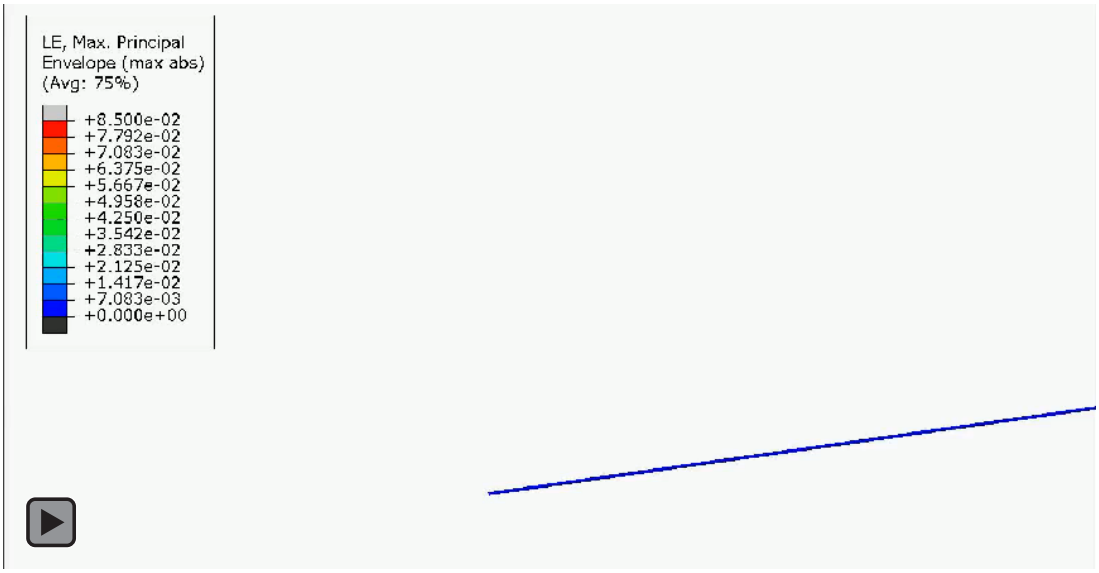

Video 4.1 Maximum principle strains developed at the ring during the simulation. The bundle shell and the braided stiffener have been supressed to allow for better visualization. For the video, refer to the pdf version.

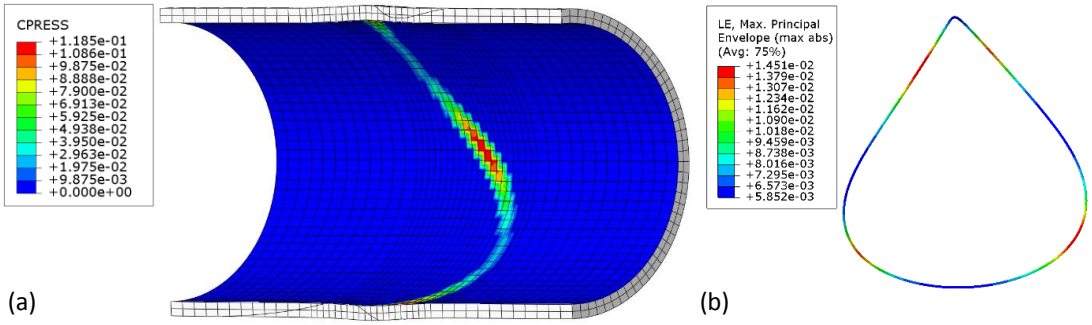

Fig. 4.7 Contact pressure (N/mm^2) on the inner surface vessel wall (a) and maximum principle strain on a wire of the ring.

The number of section points that was finally decided to be used in all further analyses was (5,20) as it provided a low runtime for the simulation and at the same time its results varied 2% at the most from the (11,36) reference configuration.

4.2.2 Mesh convergence studies

In FE analysis, mesh sensitivity studies are necessary to establish mesh independent solutions. Because the current project, though, wishes to create a tool for

any bundle ring, an extensive mesh study needed to be conducted to take into account a variety of combinations of wire and ring diameters.

Seven rings with 4-turns each were fully compacted and deployed inside a vascular section. Large systolic (150 mmHg) and small diastolic (60 mmHg) pressure was applied on the vascular wall in order to create a significant pulse variation. For the ring/vessel system to reach a steady state, a number of loading cycles were implemented.

For the current spectrum of ring configurations, the available range for the ring diameter is 7.5 to 50 mm and for the wire diameter 0.1 to 0.28 mm. However, not all combinations are relevant (e.g. the thickest wire will not be used with the smallest ring). As a result, the $WR = {}^{Wire\ diameter}/_{Ring\ diameter}$ ratio was considered and was identified to range from 0.004 to 0.013 in existing devices. As a consequence, the bundle rings that were chosen incorporated these extreme ratios, unless the result for the wire diameter was outside the wire thickness range, in which case the thinnest/thickest wire was chosen (Table 4.3). Note that the wire diameter relates always to a wire in use.

Table 4.3 Configuration of the mesh study analysis. The extreme ratios were to be used for the establishment of the wire diameter unless the result was outside the wire thickness range, in which case the thinnest/thickest wire was chosen.

Case Number	**Ring diameter (mm)**	**Wire diameter (mm)**
Case 1	7.5	0.1
Case 2	21.7	0.1
Case 3	21.7	0.26
Case 4	35.9	0.14
Case 5	35.9	0.28
Case 6	50.0	0.2
Case 7	50.0	0.28

Because the highest stresses and strains are being developed in the region of the peaks (points A and C of Fig. 4.5) and valleys (points B and D) of the ring, the mesh

is constructed to be denser there. In the analysis, the element size on the peaks and valleys was controlled while the elements between them were allowed to have sizes up to twice longer. In each successive mesh refinement, element length was scaled down by a factor of 2 and, like before, four variables were considered: Maximum Strain ε at Systole, Maximum Delta and Mean strain and COF.

In order for a mesh to be accepted, all variables needed to remain below a 5% threshold change. If, for example, the maximum strain ε is considered along 3 consecutive meshes *n*-1, *n* and *n+1*, we control:

$$\frac{|\varepsilon_{n+1}-\varepsilon_n|}{|\varepsilon_{n+1}|} \leq e \qquad (4.4)$$

to be true for e = 5%. If it is, then the final value ε_{n+1} is considered to be the converged strain, ε_0; if not, a denser mesh is produced and the above process is repeated. The mesh to be used, eventually, is the mesh that for all variables produces values that differ 5% at the most from the mesh of convergence (Fig. 4.8). In the example mentioned, that mesh would be the *n*-th one. This is considered to be the optimal mesh in the sense that it uses as few elements as possible to predict strains and forces with an acceptable error.

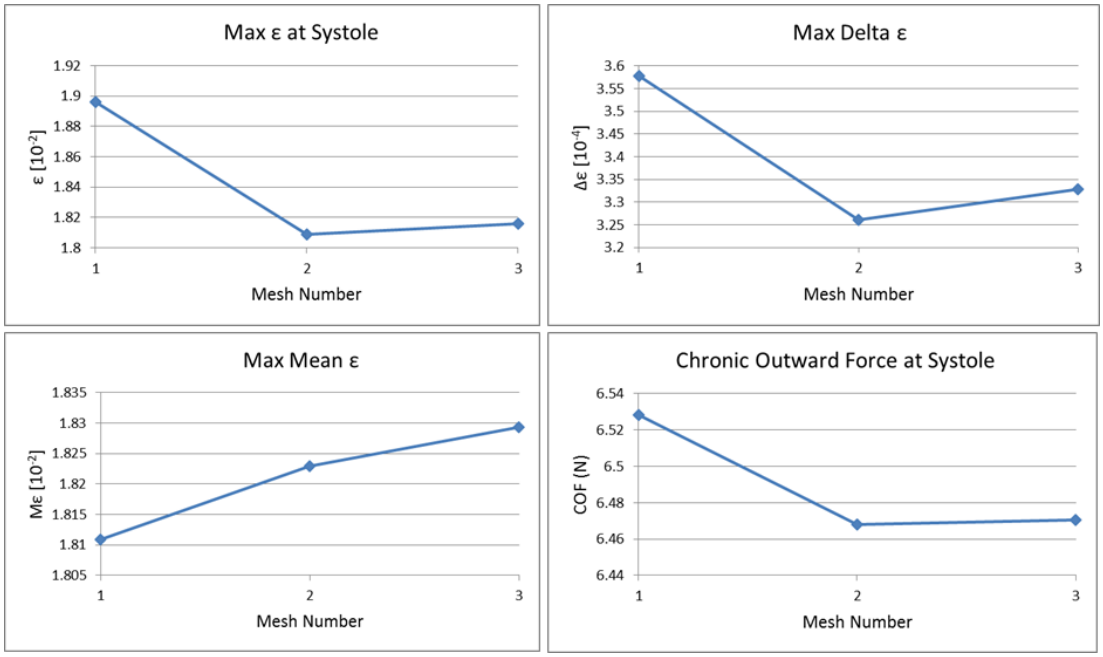

Fig. 4.8 Representative mesh converging (Case 3). The variables of interest converge below the threshold e = 5% as the number of elements in the wire increase (higher mesh number).

Through this procedure, the optimized value of the aspect ratio, where:

$$Aspect\ ratio = \frac{Wire\ diameter}{Element\ size} \tag{4.5}$$

was identified to be 0.52 for all ring configurations.

With this value, the number of elements per Nitinol turn ranges from 60 to 300 depending on the ring size. Regarding the bundle, the same meshing result is being used along its length, while for its cross sectional circumference 20 elements are used to capture circularity. As a consequence, if x is the number of beam elements per turn, the bundle shell of the respective ring has $20 \cdot x$ surface elements.

Lastly, through the mesh study, it was highlighted that pressure cycling has an effect on all variables and especially the maximum value of $\Delta\varepsilon$, because of small reconfigurations between the ring and the vessel. More specifically, as the vessel pulsates, the ring adopts its shape through bending and micro rotations, and a few cycles are necessary for these motions to become repetitive. The minimum number of cycles necessary for a converged result ranges from 5 for the rings with the lowest WR to 15 for the ones with the highest WR. Note that despite the 5% threshold, almost all variables in all cases exhibited errors of ~2%.

For all cases discussed, the vessel model had 2 elements in thickness (Video 4.1). Furthermore, the smallest beam element was not longer than the vessel's elements so as to keep meshes in a similar scale. Nevertheless, a proper mesh convergence study of the vessel needed to be conducted as well. For that, the same convergence criteria were used but with an e =2% threshold error. For this analysis, only the total radial force was considered.

The vessel consisted of cubical continuum elements (C3D8RH, reduced integration scheme and hybrid formulation; these options are good for incompressible materials and distorted meshes while they are cost efficient compared to other 3D elements). For the study, 3 cases of arteries were tested:

- one narrow and stiff (representing an iliac artery)

[Diameter = 9.1 mm and thickness = 1.4 mm at 120 mmHg, vessel material: male aged 67-77]

- one big and distensible (representing a large aorta)
  [Diameter = 31.7 mm and thickness = 1.4 mm at 120 mmHg, vessel material: male aged 38-66]
- one ordinary (representing a common aorta)
  [Diameter = 24.3 mm and thickness = 1.6 mm at 120 mmHg, vessel material: male aged 38-66]

For all models, the global size of the elements was gradually reduced and COF was checked once equilibrium was established after cycling.

The resulting optimum mesh was an inhomogeneous mesh which separated the vessel into an inner and outer layer. The boundary between the two layers was set at 60% from the inner surface and allowed a denser mesh closer to the vessel/ring contact interface. The outer wall had 1 element in thickness and the inner had multiple. For the 1st case, 4 elements were needed while for the other two, 2. This reflects on the dimensions of the vessel rather than its distensibility. The need for a denser mesh in the 1st vessel is the result of a bigger $^{thickness}/_{diameter}$ ratio. In the following simulations the number of elements has been adjusted accordingly between 2-4 elements on the inner vascular layer. Lastly, the central region of the vessel, which corresponds to the ring deployment region, was also denser, with the axial length of the elements being equal to their radial dimension.

Both meshes are illustrated in Fig. 4.9.

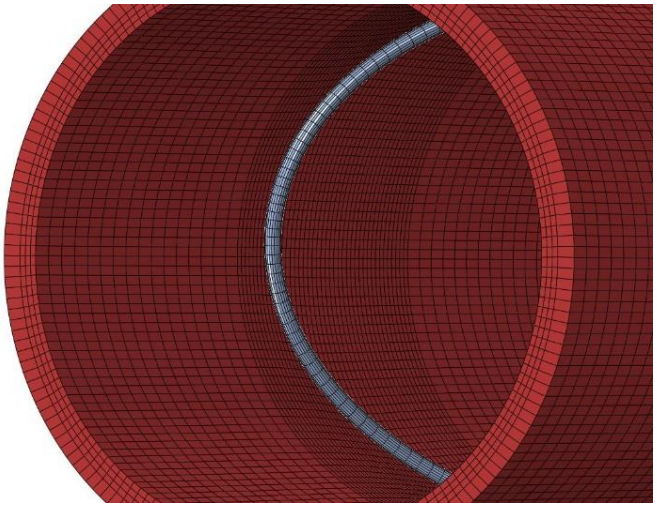

Fig. 4.9 The converged meshes. The elements at the saddles are shorter as well as at the vessel's inner and central region. Note that the wires and bundle share the same meshing along the circumference of the ring.

4.2.3 Analytical validation

As already mentioned, an important feature of the Anaconda™ device is that due to the manufacturing process of bending the wire into a circle, pre-strains are present even in the undeformed configuration of the stent (i.e. before compaction). As a result, one major objective of the current work is to correctly represent those effects by the inclusion of a pre-strain load step. This process was analytically validated by comparing the strain ε of several bundle rings at the end of the circular forming phase with the analytical values of the formula:

$$\varepsilon = \frac{Wire_{Radius}}{Ring_{Radius}} \tag{4.6}$$

which refers to the maximum strain of a Bernoulli beam under pure bending.

As the available devices cover a wide range of dimensions, four rings were used as representative from the variety of combinations of wire thickness and bundle diameter (Table 4.4). These rings will also be used later in the study.

Table 4.4 Configuration of the 4 bundle rings used in the validation process (see Fig. 4.4 for the variable definitions).

Variables	**Ring 1**	**Ring 2**	**Ring 3**	**Ring 4**
Wire Diameter (mm)	0.180	0.160	0.220	0.200
Ring Mean Diameter (mm)	27.02	33.16	39.25	48.09
Number of Turns	10	8	14	9
Bundle Diameter (mm)	0.69	0.53	0.95	0.72

After bending the straight wires into a circular ring, the magnitude of the strains was found to be significant, generally in the order of 0.4-0.7 · 10^{-2} and the FEA model predictions varied less than 0.1% from the analytical solution (4.6) for all four rings. This response offers great confidence regarding the accuracy of the initial load step in the capturing of pre-strains.

4.2.4 Saddle pull test validation

In the literature, different experiments have been used to evaluate the total radial force produced by the stent in the form of the radial resistive force (RRF) or the chronic outwards force (COF). Gong et al. [73] used a crimping loop both in a laboratory and FEA environment, García et al. [177] simplified the process using compressive plates only on a numerical model, while others have used a homogeneously shrinking outer surface [85,180] or even a single-strut compression set-up [69] to simulate the overall radial compression.

Nevertheless, in this study, an alternative experimental configuration was deemed more appropriate for the Ring Model validation because of the uniqueness of the bundle geometry that can easily lead to instabilities. Towards that end, the results of a test conducted by Terumo Aortic in May 2013 were used.

The four rings mentioned in section 4.2.3 were tied at four equidistant points along their circumference and were loaded in such a manner that the deformed shape *in vivo*, termed 'saddle shape', was replicated (Fig. 4.10). This setup will be referred to as the 'saddle pull test'.

Apart from providing a stable configuration, this test has the additional advantage of being separated of any radial contact, hence allowing the bending process within the bundle to be independently evaluated, something not true for the majority of other radial force testing approaches.

During the experiment, each bundle was attached to four pairs of polyethylene strings (each pair had one descending and one ascending fibre) with an average stiffness of 7.41 N/mm per 100 mm length. The strings were connected to a Tinius Olsen H5KS tensile testing machine with a 50 N load cell calibrated in the range of 0.5-50 N. The force accuracy was 0.5% of the applied load and the displacement accuracy was in the range of 0.002 mm. After preconditioning, the bundle was pulled to an extreme (to simulate the strains developed during compaction) before being partially unloaded and cycled for 100 cycles, between a position of high *in-vivo* deflection and a position of low *in-vivo* deflection (representing two extreme EVAR sce-

narios). Cycling between these positions resulted in capturing the entire range of saddle shapes possible for that ring in any target vessel. In reality, any particular ring motion range will be far smaller as it will be governed by the motion of one vessel.

Every bundle configuration was tested with three samples at 37 °C and the average values for their dimensions are the ones reported in Table 4.4 [184]. Note

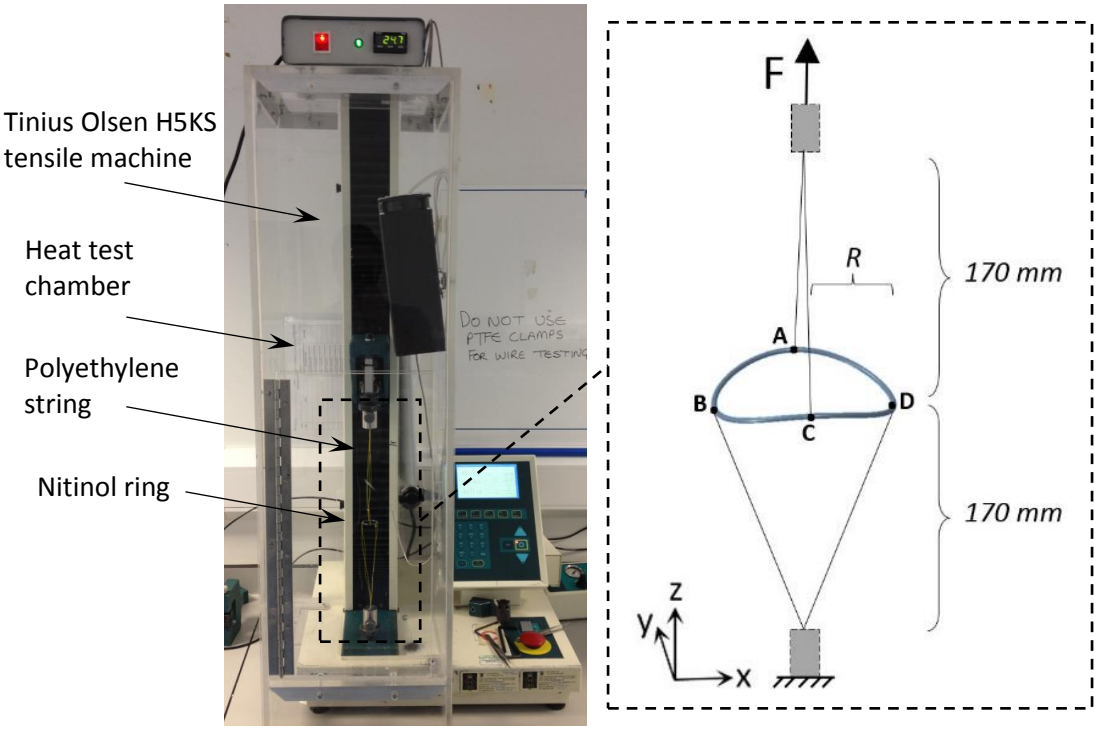

Fig. 4.10 The experimental set-up of the saddle pull test. In the schematic, pairs A,C and B,D represent the peaks and valleys of the ring bundle.

that the uniaxial cycling of the machine induced a radial deformation to the tested rings; this deformation replicated the pulsatile movement of the endograft inside the aorta. As a result, the experiment offers an insight into the overall structural stiffness of the bundle in its operational state, allowing the general response of the structure to be quantified.

This set-up was replicated in Abaqus for the conduction of the validation. Each string was simulated with the use of an Axial Connector, a special type of element that provides a connection between a pair of nodes without restricting any component of relative motion. Instead, the relative displacement is measured and stiffness is added along the line separating the nodes. It should be noted that in the FEA model

only four connections were used for each polyethylene string with double the aforementioned stiffness, hence:

$\frac{1482}{total\ length}\frac{N}{mm}$, where $total\ length = \sqrt{170^2 + R^2}$ as shown in Fig. 4.10.

All strings were attached to one turn of the bundle while a reference point served as the load cell. The peaks and valleys of the bundles were fully restricted rotationally considering that the strings used to pull the bundles greatly restrained the wire's rotation. Although, in reality, the tangential restriction ($Rotation_x$=0 for points A, C and $Rotation_y$=0 for points B, D – see Fig. 4.10 for locations) may not be equal to zero, a value close to zero is reasonable to assume since the rotation of the saddles is severally restrained due to the sutures, the friction of the string ties and the wire to wire interaction (Fig. 4.11).

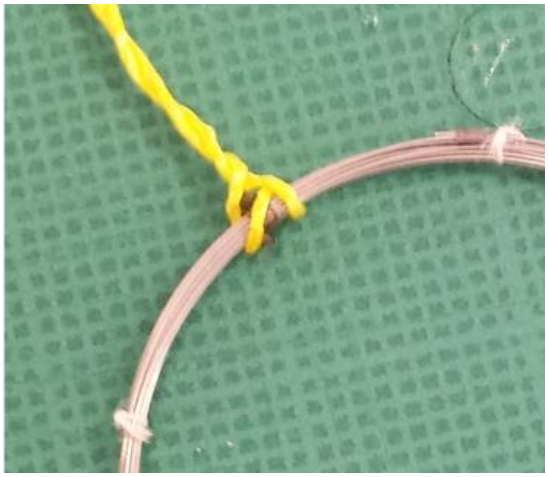

Fig. 4.11 The sutures (white ties) and the polyethylene strings (yellow fibres) attached to a bundle ring to be tested.

Through the FEA results (Video 4.2), force-displacement data were acquired to perform the validation. As can be seen in Fig. 4.12, the computational results of the force-displacement curves follow the trend of the experimental graphs and at the region of interest (i.e. the cycling part of the loading which corresponds to the *in vivo* conditions of the stent graft inside the aorta), are in good agreement with the experimental values. Discrepancy of the FEA analysis when compared to the experimental load cell measurements at the cycling region for each bundle is reported in Table 4.5.

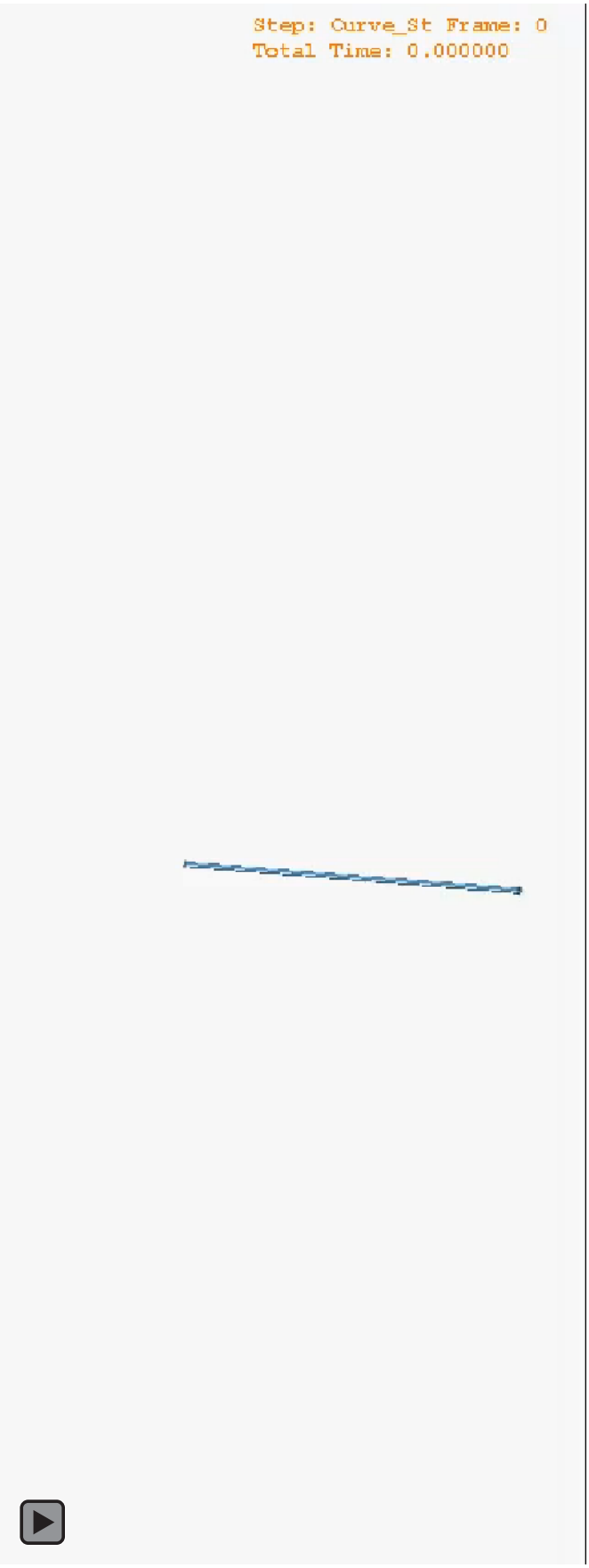

Video 4.2 The saddle pull test simulated in Abaqus/Standard. For the video, refer to the pdf version.

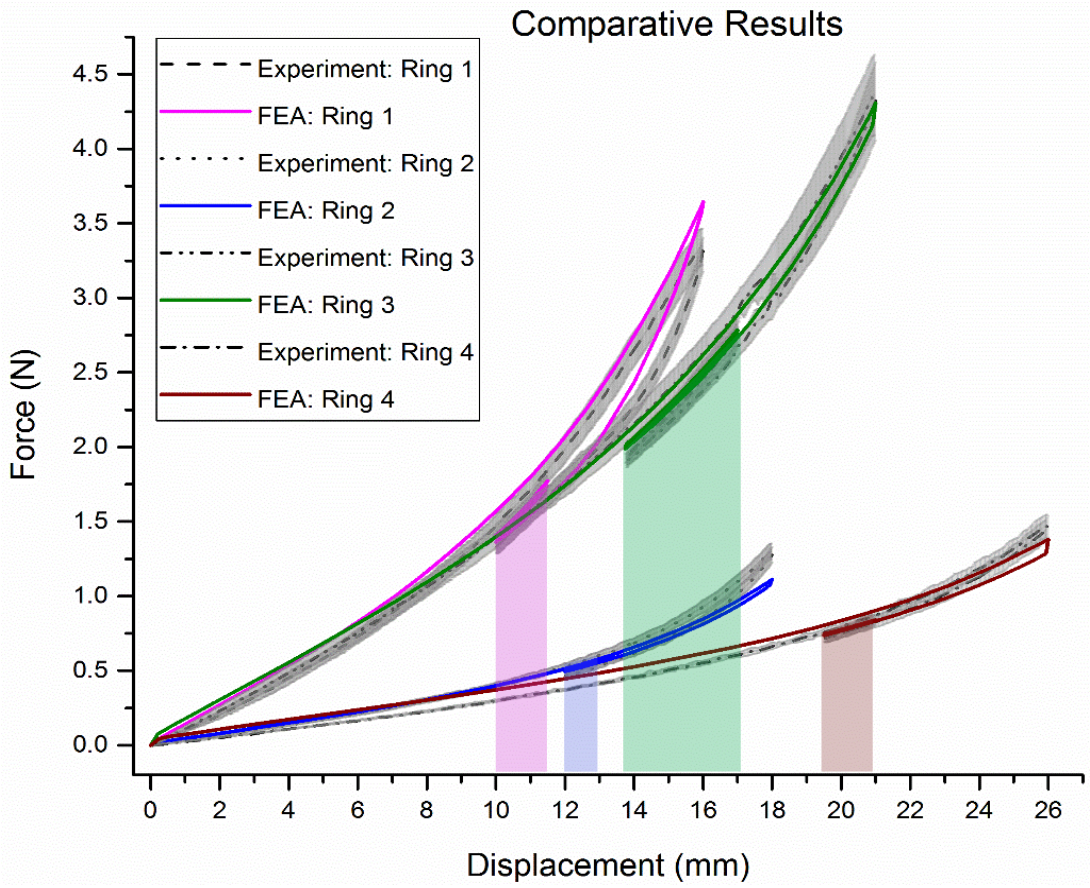

Fig. 4.12 Comparative results of all four rings tested. The grey area corresponds to the standard deviation of the experiments while the coloured regions represent the regions of interest for each bundle ring.

Table 4.5 Deviation of the FEA force-displacement response from the corresponding experimental results for each bundle ring at its operational region.

Ring	**FEA deviation in force from the experimental mean values**
Ring 1	3.2 – 5.4 %
Ring 2	1.5 – 7.0 %
Ring 3	1.2 – 3.3 %
Ring 4	0.0 – 4.1 %

The three samples of each bundle configuration produced a noteworthy standard deviation during the experimental testing. This variation can be associated with small dimensional discrepancies of the samples (referring to the bundle ring diameter in particular) and the non-standardized way of tying the turns of each bundle together. Despite this, it is evident that FEA predictions closely lie in the experimental result regime. The model predictions for Ring 3 and 4 are inside the standard deviation margin of the experiments while the predictions for Ring 1 and 2 differ by 0.6% and 1.1% from the upper limit, respectively.

These discrepancies were directly related to the diameter of the wire; the thinner the wire, the greater the difference from the experimental values. The fact that the wire diameter greatly affects the results comes as no surprise since the testing evokes primarily bending and it is well known that the radius of a wire dominates its bending moment.

Moreover, it is interesting to note that in all cases the model is stiffer than the experimental bundle; hence, the reported values can infer a force overestimation resulting from the strict confinement of the rotational degrees of freedom at the peaks and valleys of the bundle ring.

In order to quantify the effect the manufacturing process has on the global stiffness of the bundle ring, a second set of Nitinol bundles that did not account for the manufacturing strains was compared against the experimental results. Repeating the previous analysis while excluding pre-strains (rings were not created from straight wires but instead, considered initially as circles) can illustrate the importance of this modelling approach (Fig. 4.13 and Table 4.6).

In the case where the ring forming manufacturing process of wire bending has not been taken into account, the structure is stiffer. The reason for this is that before the pulling forces are applied, the material of the bundle is zero stressed and as a result can undertake greater strains before entering Nitinol's plateau (for example Fig. 4.13 suggests that Ring 4 has not yet entered the martensitic region since no hysteresis is observed). Since the bundle spends more time in the elastic region, it

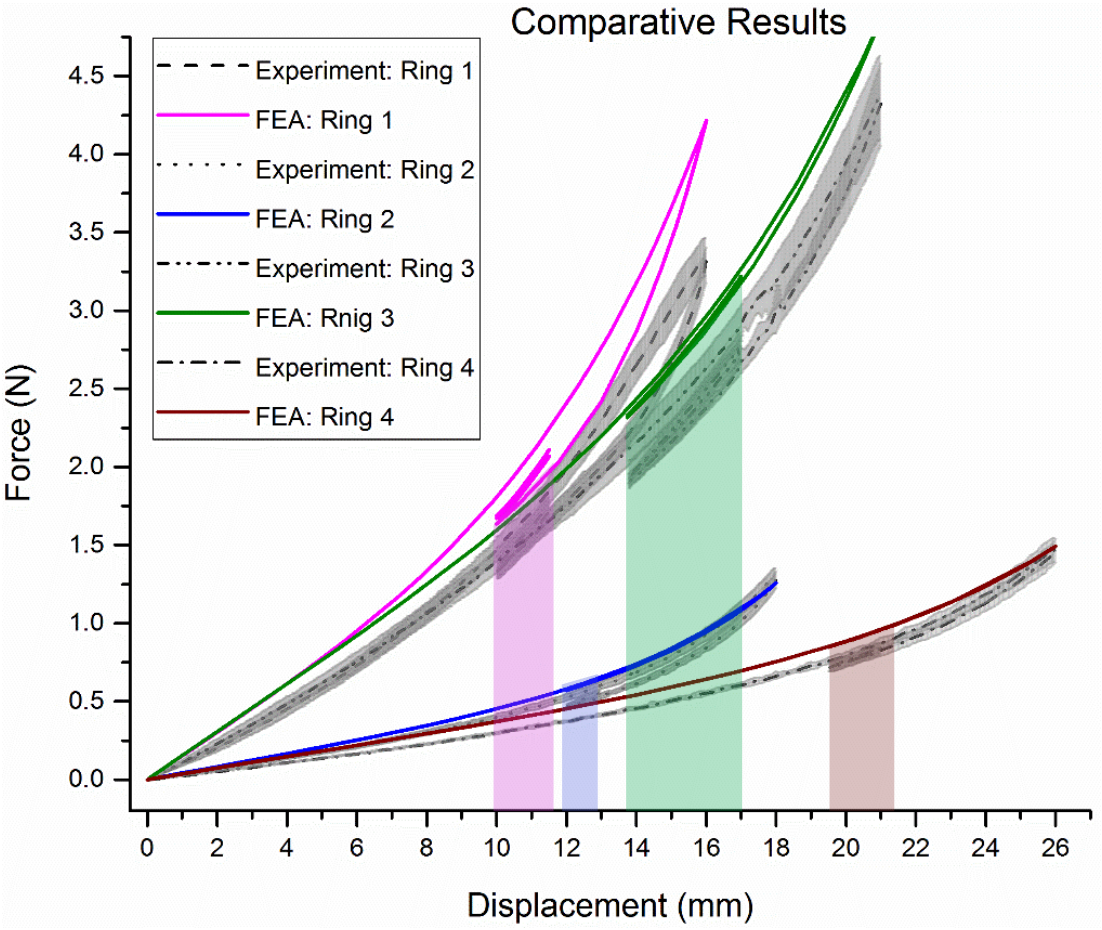

Fig. 4.13 Comparative results of all four bundles. No manufacturing pre-strains applied. The grey area corresponds to the standard deviation of the experiments while the coloured regions represent the regions of interest for each bundle ring.

Table 4.6 Deviation of the FEA force-displacement response from the corresponding experimental results for each bundle at its operational region. Model with no manufacturing pre-strains.

Ring	**FEA deviation in force from the experimental mean values**
Ring 1	22.7 – 26.3 %
Ring 2	16.8 – 22.8 %
Ring 3	17.0 – 20.0 %
Ring 4	14.0 – 18.8 %

can exhibit greater stiffness when compared to the superelastic response the pre-strained bundle ring presents. It is noted that for the material parameters being used herein, the strain limit of the linear region of austenite Nitinol for 37 ^{o}C is 1.08%.

Lastly, it is mentioned that the analysis time of the saddle-pull validation was less than 4 minutes per case.

4.2.5 Comparison with a continuum model

A further exploration of the validity of the model lead to a comparison against another FEA model that makes use of continuum elements. After Hall and Kasper [185] showed that beam elements can produce similar results with continuum elements with respect to radial force estimations, many studies have taken advantage of the reduced computational cost of the former. Nevertheless, continuum elements are considered the standard for accurate FEA representation and herein a comparison with such a model is conducted to evaluate not only COF but maximum ε_{Diast}, ε_{Syst}, $\Delta\varepsilon$ and $M\varepsilon$ as well.

The continuum model that was employed for the comparison was developed in the PhD studies of Bow and details can be found in [76]. The model used double symmetry to describe the ring bundle and contrary to the superposition used herein, all the Nitinol turns were explicitly modelled, allowing for a cross sectional wire distribution (Fig. 4.14). This lead the wire turns to have different initial lengths with each other and different curvatures during the analysis. Other dissimilarities between that model and the one developed herein include differences in the contact formulation against the vessel and necessary boundary restrictions for stability. Apart from that, the two models were set up to simulate the four rings used in the previous section (Table 4.4) in full compaction, deployment and pulsation under the same conditions.

Because the continuum model distributes the wire turns in space, direct modelling of the bundle rings used above (i.e. multi-turn rings) brings more variability to the comparison than the mere differences of the finite elements in use. For that, each

bundle ring was modelled both in a multi-turn and a 1-turn version. The former corresponded to the real bundle and the latter served as a 1 on 1 comparison of the models. Note that the 1-turn version of Ring 4 was severely slender and unstable, hence it was excluded from the analysis.

As can be seen in the results, the individual turns of the continuum model act separately and each one experiences both tension and compression due to bending (Fig. 4.15 a). Likewise, the overlapping turns of the beam model experience a very similar strain state to the distributed turns of the continuum model (Fig. 4.15 b,c); some section points of the beam are under tension and some under compression, supporting the modelling choice of superimposing the Nitinol wires (illustrated in Fig. 4.3 c).

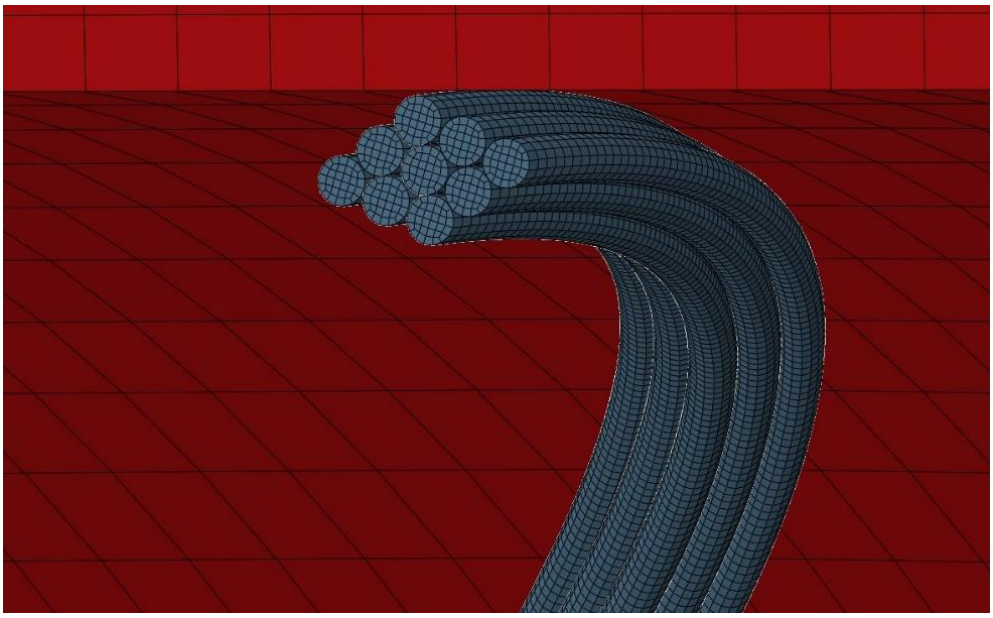

Fig. 4.14 The continuum element model of Ring 4, as developed in [76]; with permission.

To quantify the difference between the modelling approaches, the % variation between the turn(s) of the continuum model and the beam model were measured on the parameters of interest; we call this quantity Var (baseline is considered to be the continuum model). For the 1-ring cases, Var was a single value, but for the multi-turn cases it was an array, and averaging was conducted ($\overline{Var}$). The mean and standard deviation of the 4 ring cases were calculated either on Var or on $\overline{Var}$ and results are reported in Table 4.7.

(a)

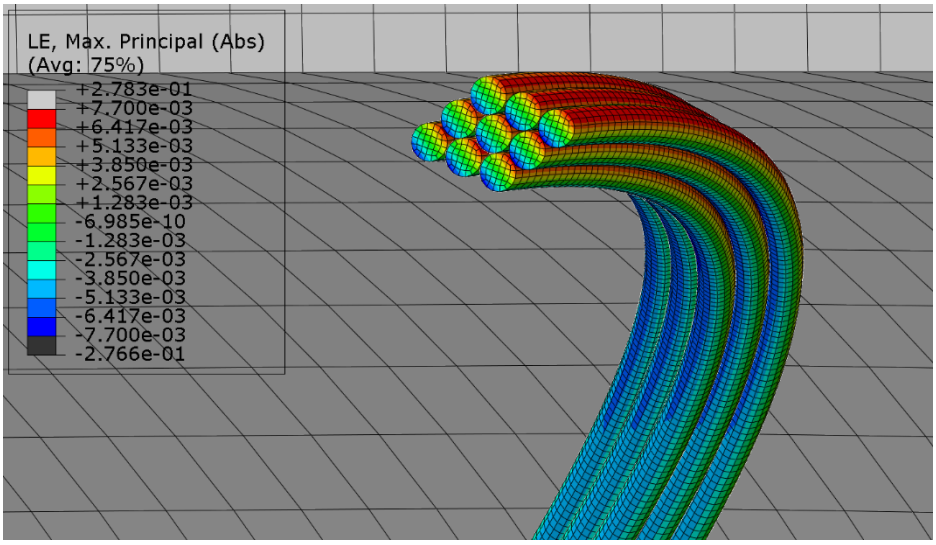

(b)

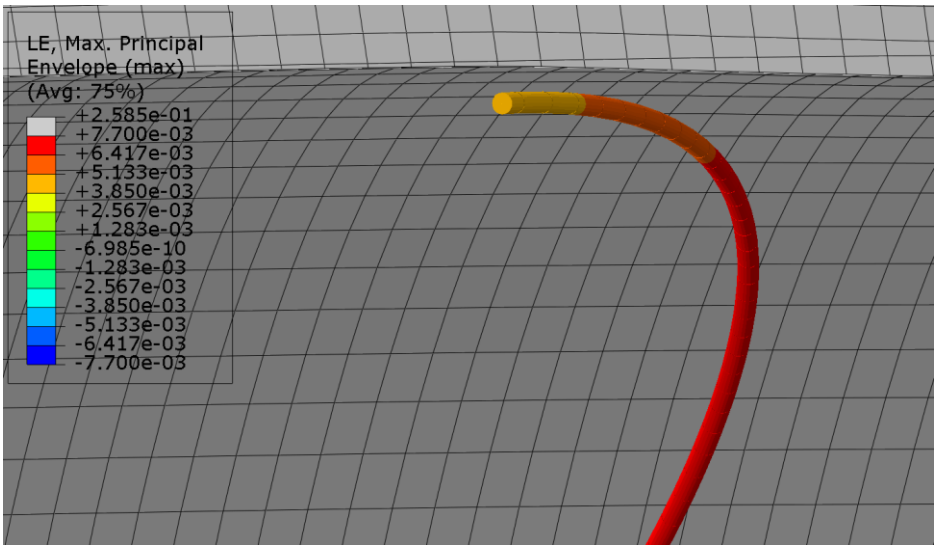

(c)

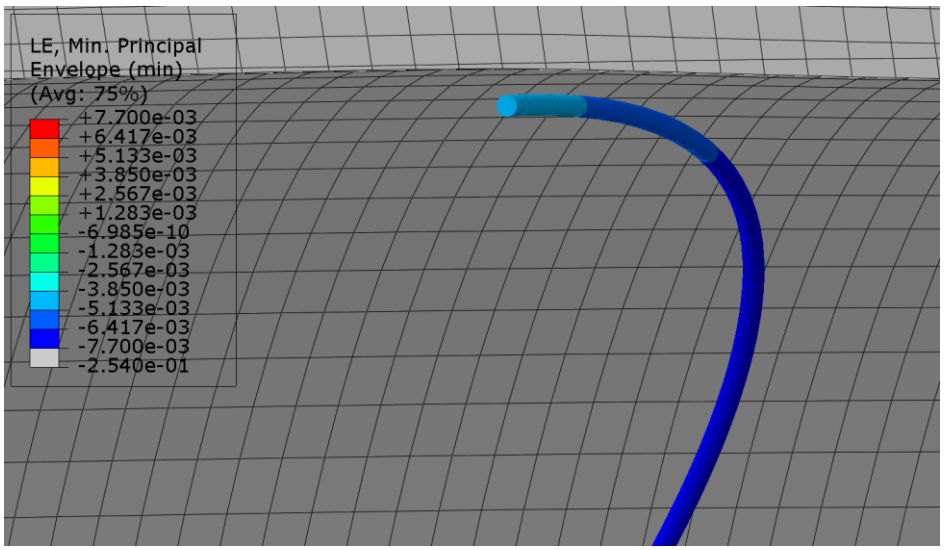

Fig. 4.15 Each turn of the continuum model experiences tension and compression (a). Similarly, the overlapping turns of the beam model have some integration points under tension (b) and some under compression (c).

Table 4.7 Mean ± standard deviation of the % variation between the turn(s) of the continuum model and the beam model. Negative values signify beam model's under-estimation when compared to the continuum model. For the 1-turn model, Ring 4 has been excluded from the results.

Variables	**1-Turn Model**	**Multi-Turn Model**
Maximum ε_{Diast}	-2.2 ± 1.1	-5.3 ± 2.7
Maximum ε_{Syst}	-0.9 ± 1.6	-3.4 ± 2.5
Maximum $\Delta\varepsilon$	29.0 ± 11.9	23.1 ± 17.6
Maximum $M\varepsilon$	-3.2 ± 1.1	-5.2 ± 1.9
COF (N)	0.0 ± 1.1	2.2 ± 1.1

As can be seen in the 1-turn cases, there is a small underestimation of the beam model prediction of the maximum ε_{Diast}, ε_{Syst} and $M\varepsilon$ in the order of 1-3% when compared to the continuum model's results. Nevertheless, $\Delta\varepsilon$ discrepancy is significantly higher and consistently positive meaning that the beam model captures a worst case scenario of fatigue. Given that delta strains are an order of magnitude smaller than the rest of the strains, it is expected to be more sensitive to small variations of the ε outputs. It is hypothesized that the differences in the boundary restrictions of the two models primarily explain this discrepancy.

For the multi-turn cases, the standard deviation of the results increases as expected and for $\Delta\varepsilon$ reaches 17.6%. The rest of the variables remain similar for the two models. Note that no trend was observed between Var (or $\overline{Var}$) and the ring size, or the number of wire turns present in each case.

Regarding the beam model, strains were higher in the 1-turn versions because the ring was less stiff, so it stayed more compacted (for ε measurements) and hence more affected by the vessel pulsation (for $\Delta\varepsilon$ measurements). The latter observation was also true for the continuum model, yet regarding maximum strains, the opposite was detected: the multi-turn cases of the continuum model produced higher maximum ε than their respective 1-turn models probably because their turns are distributed, i.e. the turn with the highest curvature in the multi-turn case it is believed to be under more severe bending than the turn of the 1-turn versions. Note that in all

cases, the maximum strains were developed in the saddles and were in the range of 0.7 – 1%.

Since the shell bundle of the beam model occupies the same space as the real bundle, the positioning of the ring inside the vessel is captured correctly. However, because all wire turns are lying in the centre of the bundle, they all share the same stress and strain state. This is a limitation of the model developed in this study; from a fatigue perspective, the worst-loaded ring (i.e. the ring in which the greatest $\Delta\varepsilon$ is produced) will most probably be missed by the analysis. Nevertheless, whether a continuum model can do that accurately is equally questionable.

The high value of standard deviation of $\Delta\varepsilon$ reported in Table 4.7 reflects the significant intra-variance present in the continuum model. In more detail, it was observed that the turn with the highest $\Delta\varepsilon$ exhibited anywhere from 8% (for Ring 2) to 45% (for Ring 3) higher delta strains than the turn with the lowest $\Delta\varepsilon$ on the same continuum ring; these values seem surprisingly large for turns that share so similar conditions and raise the need for further investigation.

As already mentioned, the continuum model is a quarter ring model and unavoidably has symmetry constraints; these are different from the beam model's which is not totally symmetrical. On the contrary, and in agreement to the physical bundle, the beam model has a weld connection to link the two ends of the wire, breaking the symmetry of the circle. Furthermore, the last boundary condition of the (4.2) set of equations, which prevents the axial rigid body movement of the ring, also imposes non-symmetric conditions separating the saddles into peaks (which are axially constrained) and valleys (which are free to move axially). This feature lead the maximum $\Delta\varepsilon$ to be consistently developed in the valleys of all the beam bundle rings. For the continuum bundle rings though, which were axially restricted from a midpoint (allowing both the peaks and valleys to move axially), maximum $\Delta\varepsilon$ was developed not only on but close to the saddles as well. Whether the actual location of the maximum $\Delta\varepsilon$ resides exactly in the saddles of the bundle ring or not has not been

shown experimentally given the difficulty of such experiment. In all cases, the maximum $\Delta\varepsilon$ of both models was around 0.1%, well below the 0.4% value which has been reported in the literature as threshold for Nitinol fatigue fracture [69].

When examining the strain distribution along the entire length of the wires, the models produce similar results as well (Fig. 4.16). The boundary conditions already discussed, result in a symmetric quarter continuum model that is repeated along the circumference, something not true for the beam model in which peaks and valleys are distinguishable. The variance of the models, though, minimizes when examining the strain of greatest interest, i.e. the maximum one.

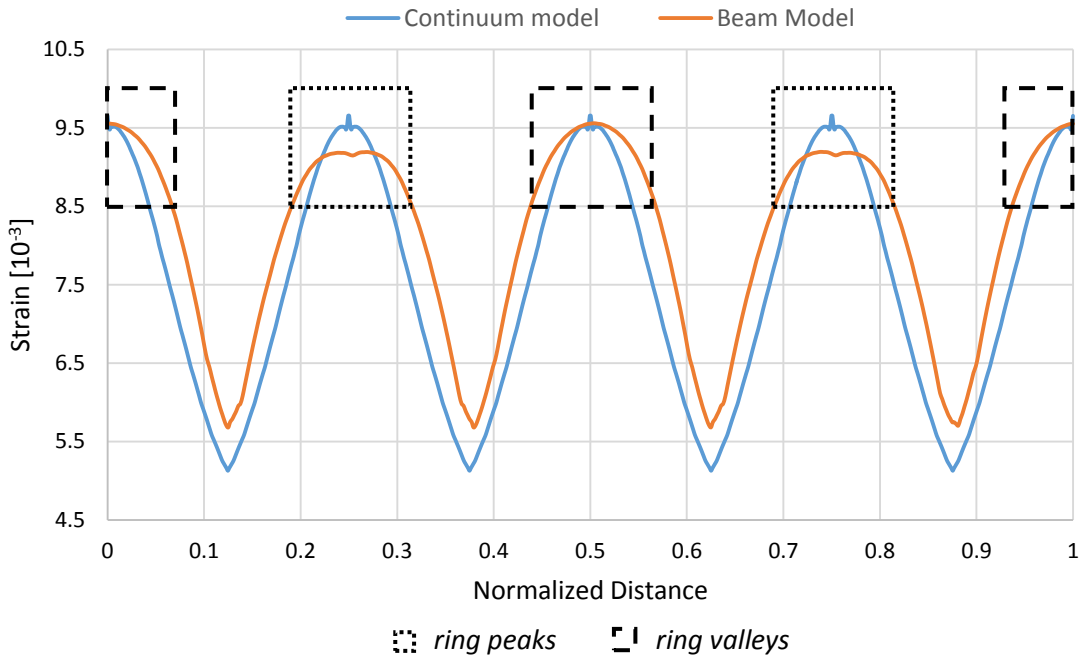

Fig. 4.16 Maximum principle strain along the length of wire. Ring 1 in the 1-turn case is being illustrated, at diastole. The peaks of the graph correspond to the peaks and valleys of the ring, while the lows correspond to the midsections between the saddles.

The COF was the variable with the least variation between the models, having no practical difference in the 1-turn cases and varying by 2.2% at the multi-turn ones. And this, despite the unavoidable difference in the second moment of area between the two models. As a result, and in accordance with previous studies on different

stent designs [180,185], it can be concluded that beam and continuum elements are equally capable of predicting the COF of the Anaconda™ stent graft.

Overall, the models are in very good agreement with each other, despite their inherent differences. Unfortunately, no experimental values are available for the strains (and especially the delta strains) the bundle ring exhibits, hence the true value of the tested variables is unknown. The small variation between the two models, though, provides confidence for the range in which the results lay.

The runtime for the 1-turn cases slightly favoured the continuum model. However, in the multi-turn cases, the continuum model was 7-23 times slower than the beam one. Furthermore, it should be noted that the addition of turns at the beam model did not add any measurable computational cost; on the contrary, runtime for most cases was reduced when the number of turns increased thanks to a stiffer, and as a result more stable, ring. This suggests that the model is very adequate for scaling, i.e. the simulation of the full device.

4.3 Effects of oversize and friction coefficient

With the 1-ring model validated, radial forces and strains can be examined under conditions similar to the EVAR approach. In this section, the oversize and friction coefficient effects between the stent and the vessel are investigated, since both variables impose uncertainties in clinical practice.

As stent oversize, we define the percentage by which a stent is larger than the target vessel:

$$oversize = \left(\frac{Ring_{Diameter}}{Vessel_{Diameter}} - 1\right) \cdot 100\% \tag{4.7}$$

This practice is common in EVAR as it enhances sealing and anchoring, yet no optimum oversize value is specified in the literature. Herein, a sensitivity study was performed to allow stent responses to be explored. On a similar basis, the friction coefficient μ, defined as:

$$\mu = \frac{F_{shear}}{F_R} \tag{4.8}$$

at the Nitinol-vessel interface (Fig. 4.17) is not well understood and few studies have tried to explore the interaction. Therefore, the present work considers a range of values of the coefficient μ allowing for the variation in the response of the deployed stent to be revealed.

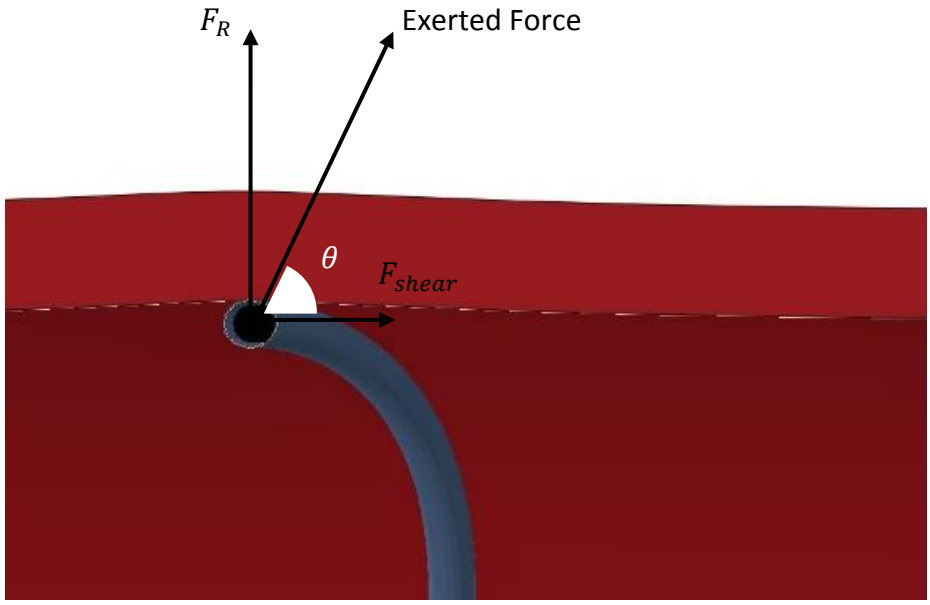

Fig. 4.17 Analysing the exerted force.

The stiffest bundle ring validated, i.e. Ring 1, was used for the study. The ring was fully compacted into a sheath of 6.7 mm and deployed into seven straight tubes of length equal to 1.9 · ring diameter – so as to be long enough to leave the ends unaffected. The diameter of the vessel was each time chosen so as to produce the desired stent/vessel oversize at a mean arterial pressure $P_m = 93.3\ mmHg$. Each of these sections had a different wall thickness so that each vessel, despite its size, would have the same radial stiffness i.e. the same pressure-radius response. The vessel was cycled 10 times between a diastolic (80 mmHg) and a systolic (120 mmHg) pressure to establish equilibrium before any result was exported. The variables in question were the COF of the ring (at systole), responsible for sealing and (partly) anchoring and the $M\varepsilon$ developed in the ring between diastole and systole.

The friction coefficient, μ, for all the examined cases, is reported in Table 4.8 and covers a spectrum of practically frictionless (Case 1) up to high friction conditions (Case 5). These values are in the range of values commonly found in the literature

[94,163–165,178,186]. Finally, the stent oversize ratios stepped from 10%-40% in 5% increments.

All simulations were run on 4 Xeon© cpus of a desktop computer (3.40GHz, 64GB) and the analysis time was between 150 to 470 minutes depending on the vessel size.

Table 4.8 Friction coefficients for all cases tested.

$\boldsymbol{\mu}$				
Case 1	Case 2	Case 3	Case 4	Case 5
0.005	0.05	0.1	0.3	0.5

For all cases examined, the lower the friction coefficient was, the greater the COF became for a given oversize (Fig. 4.18 top). Moreover, at some friction coefficient value below 0.3, the COF started to be practically constant, so that for coefficients less than 0.1, the COF was almost unaffected by oversize. The proximity of the results acquired when using friction coefficients 0.05 and 0.005 suggests that the whole COF line converges for low coefficient values.

Friction coefficient affects COF because COF takes into account only the radial component, F_R, of the exerted stent force (Fig. 4.17). When friction coefficient reduces, the ring becomes flatter and the angle θ of the exerted force increases, increasing the chronic outward force.

Looking at the whole friction range, an increase of the coefficient from 0.005 to 0.5 results in a COF decrease anywhere from 40% to 16% depending on the oversize. It may also be noticed that the difference between all cases reduces at higher oversize ratios.

Contrary to COF, maximum $M\varepsilon$ (Fig. 4.18 bottom) increases linearly with the increase of oversize. Moreover, friction coefficient has a minimal effect on $M\varepsilon$, with higher values of μ producing higher ring strains. The rationale of this effect is the same as above. Lower friction coefficients lead to a flatter ring which induces smaller bending on the bundle, leading to lower $M\varepsilon$. This effect, though, is small compared

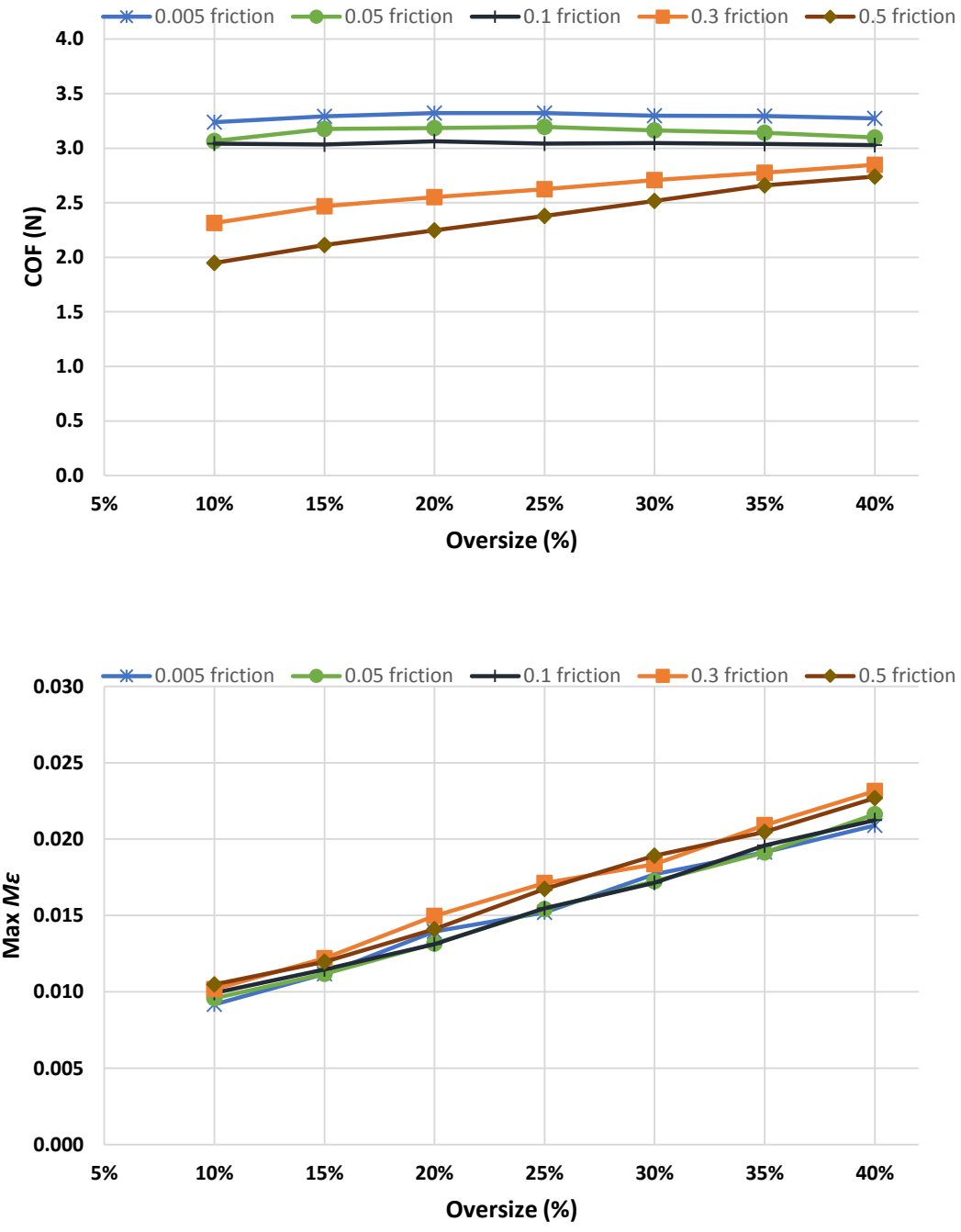

Fig. 4.18 COF (top) and maximum $M\varepsilon$ (bottom) versus bundle ring oversize for Ring 1, examined under various friction coefficients.

to the effect oversize has on strains. An increase of the coefficient from 0.005 to 0.5 increases $M\varepsilon$ by an average of 8% while an increase of the oversize from 5% to 40% raises strains by an average of 122%. The different behaviour of COF and $M\varepsilon$ is a result of Nitinol's superelasticity. Since the high strain regions of the bundle operate in the martensitic plateau, changes in the shape of the ring will result in changes in the developed strains without an equally strong effect on the exerted forces.

In the literature, it is common for numerical models to use both low and high friction coefficients such as 0.06 [163], 0.1 [178] or even 0.4 [94,165]. Following a more sophisticated route, Mouktadiri et al. changed the friction coefficient of the interaction according to the degree of calcification of the internal layer of the artery from 0.05 to 0.5 [164]. Very few of the available studies, though, support the choice of their friction coefficient with experimental data. One tribological, laboratory study which examined the topic was conducted by Dunn et al. [187] and the friction coefficient between bovine aortic endothelial cells and a polished glass surface was measured to be in the range of 0.01-0.07. In addition to the fact that these values may not reflect the Nitinol-artery interaction though, it was also noted that hypertension as well as pressure from the deployed stent may result in cell death or removal, leading to alteration of the underlying friction. All of the above reflect the need for more tests in order to explore the vessel/stent interaction experimentally.

On a different approach, despite the common practice of considering one fixed value of μ for the stent/vessel interface, Vad et al. [186], reported that the friction coefficient depends on the oversize ratio of the stent in an inversely proportional way. Their methodology involved performing experimental pull-out tests of stent graft devices from polymer tubes, and using the pull-out force results, they derived friction coefficients for the device-vessel interaction using both an analytical method and FEA simulations. Although their analytical results differed by one to three orders of magnitude from their simulation ones, the trend of the coefficient with oversize was similar in both. Their results should, however, be used with caution: considerable assumptions were made in order to model the device-vessel interactions with no validation provided. Nevertheless, during our preliminary studies, a series of tests were

conducted according to the assumption that friction coefficient decreases with increasing oversize. Although not presented herein, the results showed that a variant friction coefficient had minimal effect on COF when compared to the major influence the friction magnitude itself had on the results.

The values of COF produced herein are in the range found in the literature [70,178,186]. Furthermore, the plateau of COF, strongly present in the lower friction coefficient cases, can be attributed to both the geometrical non-linearities of the deployed bundle ring and the material non-linearities of Nitinol which operates in its plateaued region. Moreover, a gradual reduction of the contact area of the stent/vessel interaction was noticed at increased oversizes, probably the result of the distribution of radial forces. As the oversize increases, the magnitude of F_R at the saddles decreases (Fig. 4.19).

In the study of Sternbergh et al. [188], 351 AAA patients treated with Z-stents were examined and it was reported that those with stent oversize above 30% experienced a 14-fold increase in migration events compared to those with oversize below that threshold. Similarly, Kratzberg et al. [189] noted that for barbed stent grafts, higher oversizing leads to a decrease in attachment strength. These results show that an increase in oversize might bring unwanted phenomena some of which could possibly be explained by a rearrangement of the radial forces.

Similarly, neck dilation has also been linked to migration [57]. It is interesting to note, though, that if neck dilation is independent of the EVAR execution, as some studies have suggested [25,190], this might explain why surgeons prefer larger stents: if the treated vessel dilates post-operatively no matter the endograft, a larger stent is not chosen to produce greater COF but to ensure sealing in the new, enlarged vessel configuration (which will lead to lower final oversize and different F_R distribution).

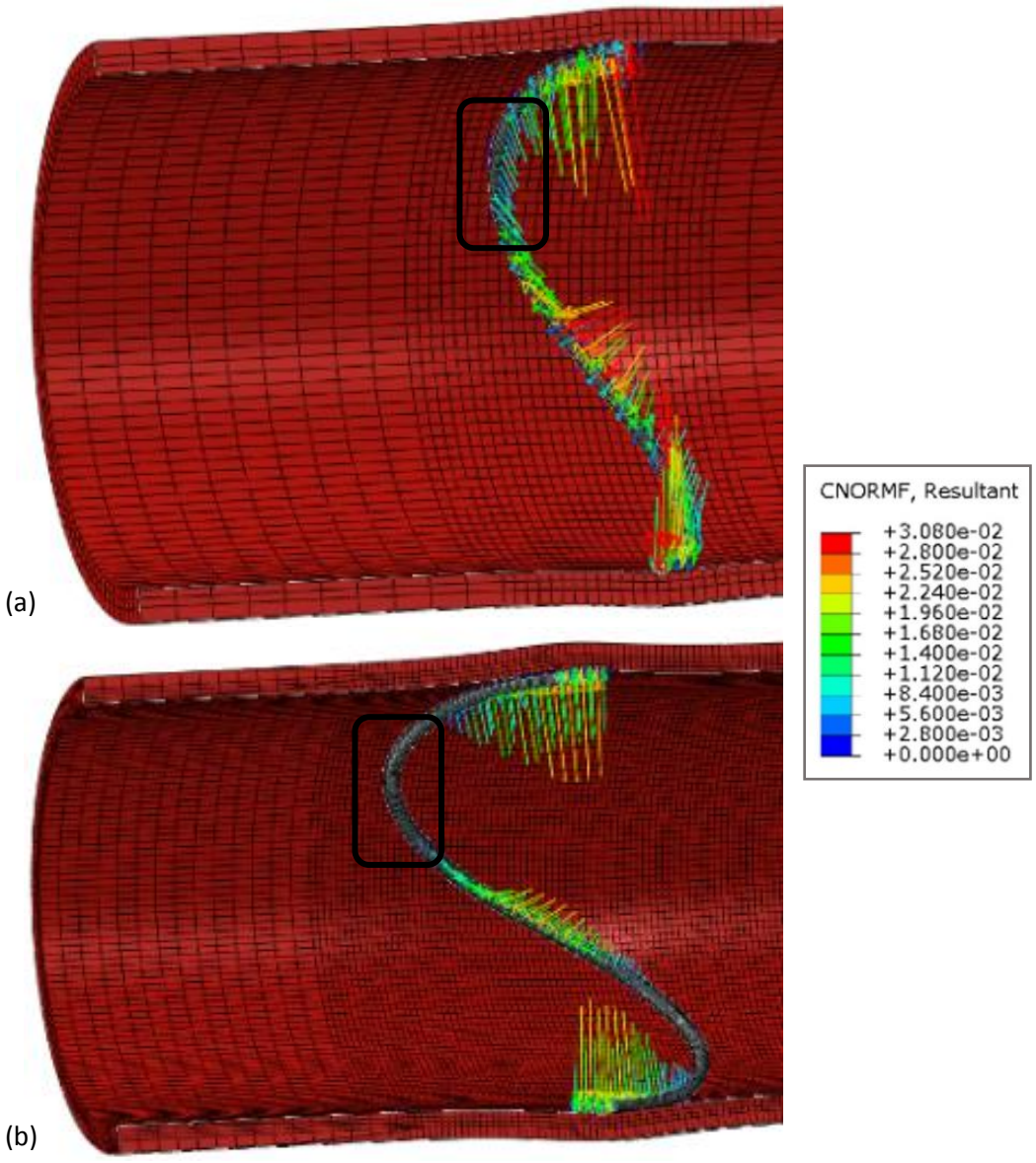

Fig. 4.19 COF distribution at the 10% (a) and 40% oversize configuration (b) for Ring 1 at 0.05 friction (force in N). The saddle region highlighted experiences a significant reduction in radial forces as the oversize increases.

4.4 Cross section study

In most numerical analyses of endografts, vessels are treated as circular tubes, yet the assumption of circularity does not always hold true when examining CTA scans of the aorta, as demonstrated in Section 3.1.4.

Apart from the fact that vessels do not always come in circular shapes, the existence of calcification can further affect the shape of the lumen and as a result, the boundaries of the deployed device. Furthermore, even when the cross-section is circular, it's possible that some of the rings of the endograft may not deploy perpendicularly to the axial direction of the vessel, leading them to experience elliptical boundary conditions (Fig. 4.20).

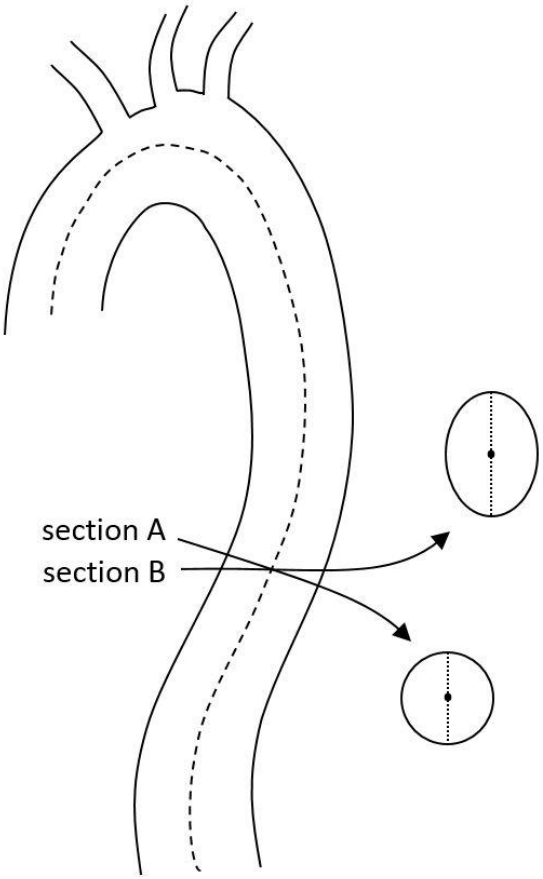

Fig. 4.20 The circular cross section of the aorta when examined in a plane perpendicular to its centreline (section A) appears to be elliptical in a tilted plane (section B).

Despite these observations, almost every investigation of the mechanical response of stent deployment is carried out assuming circular boundary geometries (for some recent examples refer to [84,162], [178,191]). Even where analysis of plaque is attempted [83,161,177] or patient specificness in taken into account [163], the assumption of a circular luminal cross section is maintained. Some researchers [192] have proposed the development of tools to take into account all geometrical irregularities of vessels, while others have developed such algorithms [193] when reconstructing the aortic geometry from 2D data. However, no stent deployment was taken into account in these studies. It should be mentioned that when investigators use non-idealized patient specific data to reconstruct the aorta, they do encounter non-circular cross sections [164,165], yet, to the author's knowledge, no detailed study has been reported regarding the effect this aspect may have on the endograft.

Because fatigue life as well as anchoring and sealing of the stent may by compromised by the ovality of the cross-section of the vessel, the issue was investigated further. In this section, an idealised approach of the non-circularity of the artery has been followed by assuming a series of elliptical vessels in the range of ellipticity values identified in Section 3.1.4. In each vascular section, Ring 1 was deployed assuming μ = 0.3 (as the smallest friction coefficient that is not constant over the oversize range). The vessel was pressurised between diastole (P_{Diast} = 80 mmHg) and systole (P_{Syst} = 120 mmHg) and the maximum ring strain and COF were examined at the end of the systolic phase. The delta strain between systole and diastole was also examined but no direct results will be presented for commercially sensitive reasons; instead, qualitative remarks will be made.

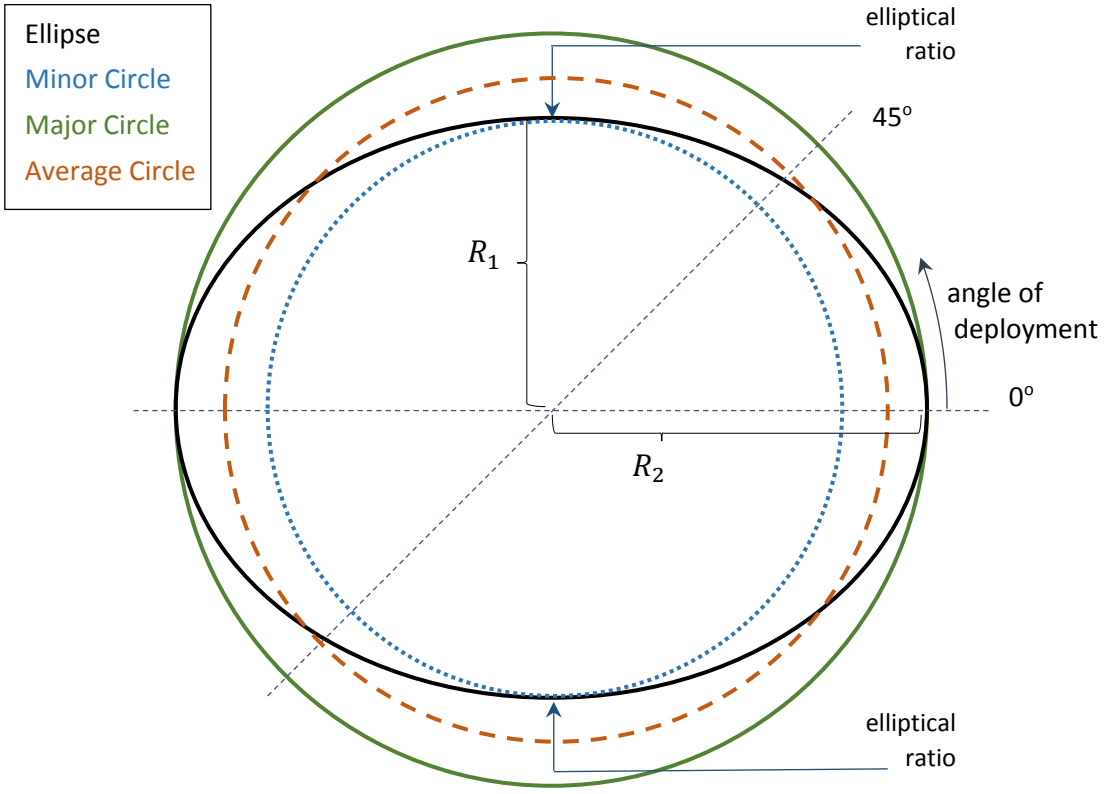

Fig. 4.21 The elliptical ratio changed from 1 (green circle) up to 0.77 (black ellipse). For every one of the ellipses, a circle with diameter equal to its minor axis (blue dotted circle) and an average diameter circle (brown dashed circle) were examined. Additionally, 3 angles of deployment were studied for each elliptical section.

A straight tube of original thickness of 2 mm was constructed to represent the neck of the aneurysm. By altering the semi-minor axis, R_1, of the cross section, the elliptical ratio was adjusted according to the equation (3.3), where R_1 = semi-minor axis of the ellipse and R_2 = semi-major axis (Fig. 4.21).

Starting from the value of 1, representing a circle, 4 more equidistant ratios were examined down to the value of 0.77, the most extreme ratio identified in the patient dataset of Chapter 3. Because of the geometry of the ring, for each ellipse, 3 cases regarding different deployment positions were studied: (i) with the peaks and valleys of the ring being aligned with the axes of the cross-section, (ii) with the ring peaks at 22.5^o angle and (iii) with the ring peaks at 45^o (refer to Fig. 4.21) For symmetry reasons, the 0^o and 45^o are the extreme cases of rotation about the axial direction of the vessel. Additionally, two more cases were examined for each ratio different to 1; these were the circular cross-sections of a vessel with radius equal to R_1, hereafter called minor circle, as well as a circular vessel with an average diameter of $\frac{R_1+R_2}{2}$.

The reason for examining the circular cases was to compare the ellipses with the results that would occur if common circular approximations were followed. The original circle represents the case of approximating the ellipse with its major axis, the minor circle corresponds to the minor axis approximation and the average circle lies in between.

A 5% oversize of the ring at mean pressure of $P_m = 93.3\ mmHg$ was initially assumed. It should be highlighted, though, that this value relates only to the initial circular vessel. Since the same ring is used for all vessel models, greater oversize ratios will be acquired for all cases but the first (for the smallest minor circle oversize is 37% while for the smallest average circle 19%). By altering the thickness, all vessels exhibited the same stiffness.

The total number of models was 21 (9 cases of circles + 4 cases of ellipses · 3 deployment angles) and the specifications for each one are summarized in Table 4.9. All simulations were run on 6 Xeon© cpus of a desktop computer (3.40 GHz, 64 GB) and the analysis time was between 80 to 226 minutes depending on the vessel size.

Table 4.9 Cross-section specifications of the vascular section. Values are reported in mm at 0 Pa.

Ellipses			Circles	
Elliptical Ratio	R_2	R_1	**Minor Circle R**	**Average Circle R**
1.00	9.98	9.98	9.98	9.98
0.94 (average)	9.98	9.38	9.38	9.68
0.89	9.98	8.88	8.88	9.43
0.83 (min average)	9.98	8.28	8.28	9.13
0.77 (min)	9.98	7.68	7.68	8.83

In all models examined, the maximum strain of the Nitinol wires increased while the elliptical ratio decreased (Fig. 4.22). The reduction of one axis of the cross section lead to a steady rise in strains. However, when considering the minor circle, it becomes apparent that a symmetrical shrinkage results in a much faster increase of strain.

The worst case ellipse had 1.91% maximum strain and if the major axis approximation was followed, the strain would be underestimated by 51.2%. In contrast, the minor axis approximation would result in a 64.2% overestimation. Regarding the average circle, an underestimation is also observed but it is insignificant (1.3%). If we consider the average elliptical ratio ($ER = 0.94$), the major axis approximation underestimated strains by 18.7% and the minor axis approximation overestimated them by 16.5%. The average circle was once again very close, just 3.3% above the elliptical value.

During the analysis, delta and mean strains were also acquired and the trends observed were the same as in the maximum strain. At the extreme ratio of 0.77, the average circle underestimated delta strains by 7.8%, while the minor circle overestimated them by 26.8%.

A similar variation was observed for the total radial force (Fig. 4.23). The major axis approximation underestimated COF by 13.7% at the 0.77 ratio and by 2.4% at the 0.94 ratio. In contrast, the minor circle overestimated COF by 6.1% at the 0.77 ratio and by 6.3% at the 0.94 ratio. The average circle laid 3.2% below the extreme elliptical value and 2.4% below the average one.

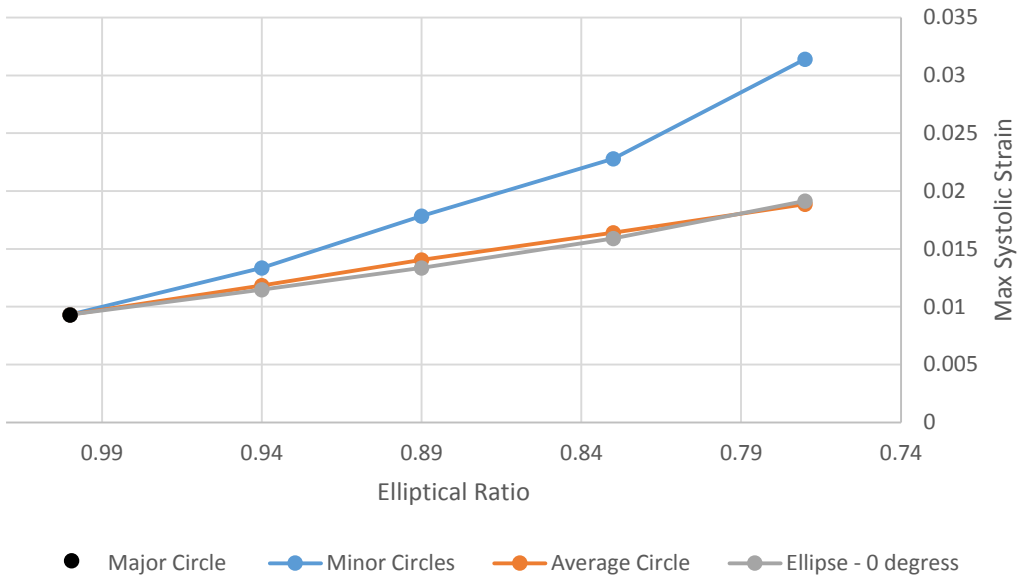

Fig. 4.22 Maximum strain developed on the ring at systole. Ring deployed in all circles and the ellipses at 0° degrees.

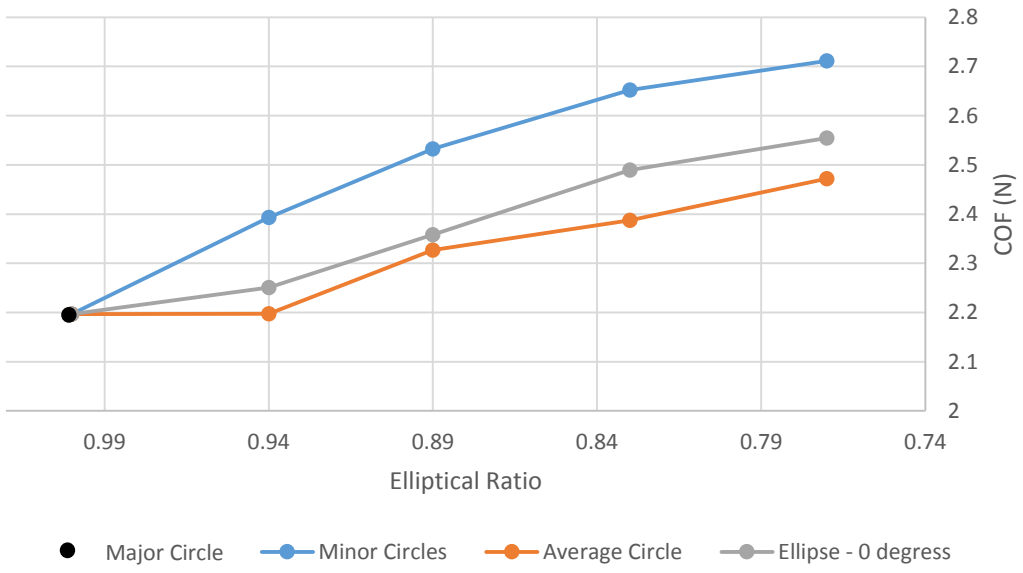

Fig. 4.23 Chronic outward force of the ring at systole. Ring deployed in all circles and the ellipses at 0° degrees.

When examining the differences that arise once the deployment angle changes, results are less sensitive. COF does not change more than 1.5% at any configuration (Fig. 4.24) while maximum strain stays below a 2% variation (Fig. 4.25). Delta strain, though, appears more sensitive, especially below the 0.83 elliptical ratio and it reached a minimum at 45°. The reason is that a non-circular cross section under

homogeneous pressure will inflate inhomogeneously, meaning that the positioning of the device will have an effect in the fatigue life of the stent. The stent ring was observed to develop its maximum $\Delta\varepsilon$ at the valleys, and it was concluded that the saddles are better not to align with the axes of the ellipse, given that the major diameter difference occurs at the major axis of the cross section.

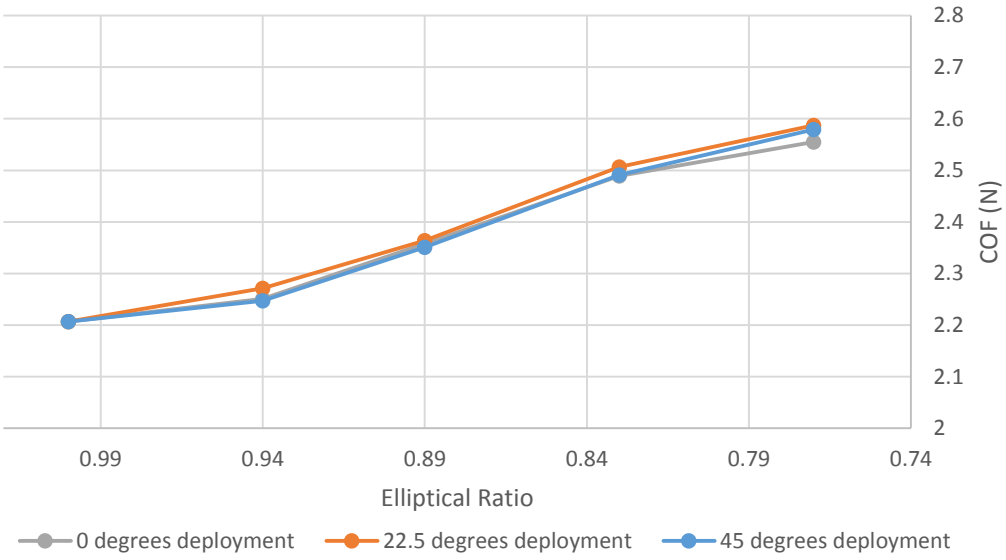

Fig. 4.24 Chronic outward force of the ring at systole. Ring deployed in the ellipses at various angles.

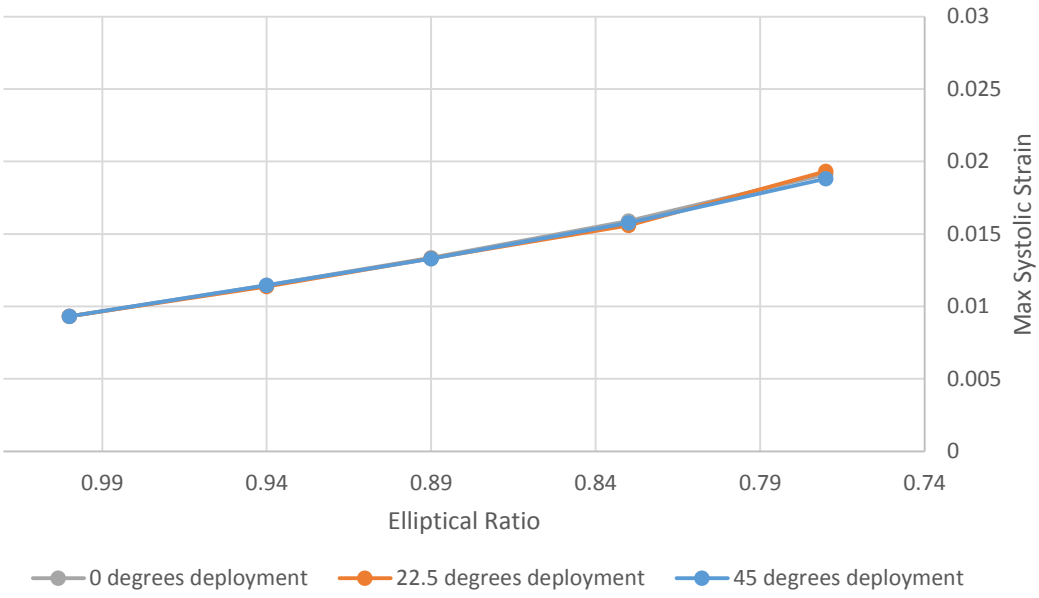

Fig. 4.25 Maximum systolic strain developed on the ring at systole. Ring deployed in the ellipses at various angles.

4.5 Moving towards multiple rings

The development of the 1-ring model has proven to be very useful in the investigation of critical parameters for the success of EVAR. In addition though, it has opened the way for multi-ring modelling. The creation of Anaconda™ sections (i.e. multiple connected rings) can be seen as an initial step towards a full device model. It can help understand the challenges present in the complete endograft modelling and allow the examination of ring-to-ring interactions.

Perhaps not surprisingly, the main challenge for such a transition lies in the connection between the rings themselves. In reality, the fabric of the device serves not only as a boundary for the blood flow but also as the structural element that unites the endograft. Nevertheless, initial analysis showed that the geometrical non-linearity of the fabric imposes great instabilities to the system impeding the advancement of the model. The issue was eventually addressed with the development of a separate model discussed in Chapter 5. Herein, though, the use of alternative connectors was investigated.

In order to model the scaffolding of the device (i.e. the metallic part only), consecutive rings were connected with Axial Connectors at their peaks and valleys (Fig. 4.26 a). In general, connector elements implement kinematic constraints between the nodes they are assigned to and Axial Connectors, as has already been mentioned in the saddle pull test, provide a connection between two nodes where the relative displacement is along the line separating the two nodes (it is a spring-like behaviour).

The connectors were assigned non-linear properties to account for the slack, i.e. the excess of fabric, between the rings. Particularly in extension, it is evident that the rings have an initial ease to move apart before the fabric becomes fully extended. The fabric examination presented in Section 5.2 was used to assist the definition of these connectors. Each connector had stiffness k = 0.5 N/mm for the first 13.5% of the distance between the rings and then stiffness was increased considering the longitudinal elastic modulus E_L of the fabric. In more detail, if F represents the tensile forces acting on a fabric tube of radius R and thickness t, then:

$$F = \sigma A = \varepsilon E_L A = \frac{x}{RD} E_L 2\pi Rt \tag{4.9}$$

for an x displacement of the initial distance RD, which is the distance between two consecutive rings. Hence, the stiffness, k, can be obtained from:

$$k = E_L \frac{2\pi Rt}{4RD} \tag{4.10}$$

for E_L = 225 MPa and t = 0.15 mm. Note that the 4 in the denominator exists because four connectors are being used.

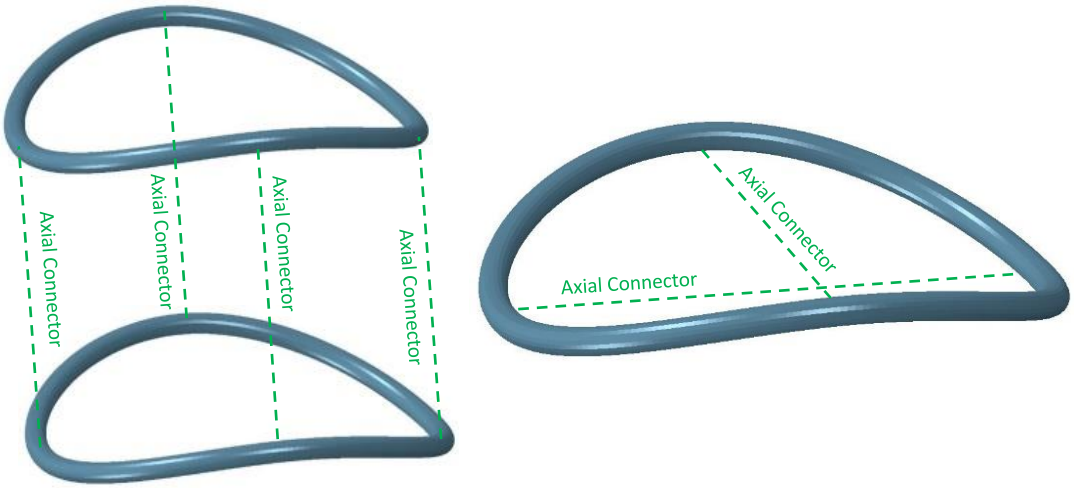

(a) (b)

Fig. 4.26 Axial Connectors linking the rings (a) and a cross pair of connectors modelling the saddle shape of a ring (b).

The existence of the fabric also restricts rings from flattening out. Each ring, even at rest, has a characteristic saddle shape when sutured to the device. To recreate this effect, the peaks and the valleys of each ring were connected to each other with Axial Connectors, creating a cross pair (Fig. 4.26 b). These connectors had non-linear stiffness and a reference length equal to the saddle radius of the ring (which is smaller than the original flat ring radius). As a result, they can aid the ring into keeping its saddle shape even if no vascular boundaries are present (e.g. in the aneurysmal region).

In addition to the fabric, in reality, the two most proximal rings of the device are connected with hooks. The hooks enhance the anchoring of the Anaconda™ and increase the columnar stiffness of the upper section of the endograft. The way in

which the hooks connect with the bundle rings though, is very complex, with all degrees of freedom being impeded yet none being fully restricted. Modelling this part of the device is very challenging and it is something generally avoided in the literature. Herein, multiple combinations of boundary conditions were tried and the final configuration can be seen in Fig. 4.27. The peak of each hook (point A) is connected

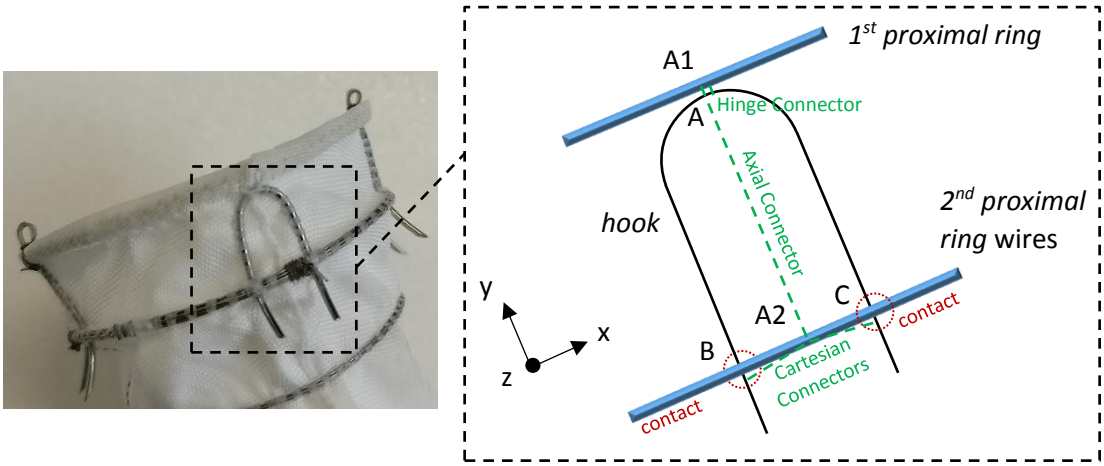

Fig. 4.27 A hook of the Anaconda™ with a schematic of the developed model illustrating the connectivity assigned.

to the 1st proximal ring (point A1) with a Hinge Connector which only allows rotations around the x-axis. The legs of the hooks (points B and C) are connected to the 2nd proximal ring (point A2) with Cartesian Connectors that provide stiffness in all spatial directions. At the same time, frictionless contact is used between the hooks and the 2nd proximal ring. Note that the A1-A2 Axial Connector (as shown in Fig. 4.27) is the connector that simulates fabric and is independent of the hooks.

This configuration allows for all degrees of freedom to be controlled and adjusted according to reality and works well in non-excessively tortuous anatomies. The latter cases are problematic because the coordinate systems of the connectors cannot follow the rotations of the nodes during the analysis; as a result, they will eventually impose restrictions at wrong directions if the final position of the stent differs significantly from the original. This issue is further explored and resolved in Chapter 5.

The challenge of using non-straight arterial geometries arises only with multiple rings. For a 1-ring model, alterations in the geometry and orientation of the vascular section (before the initiation of the analysis) can provide all the necessary variability regarding the positioning of the bundle ring. The same is not true, though, for two rings or more. Furthermore, when multiple rings are considered, appropriate delivery of the scaffolding needs to take place prior to deployment (if the vessel is not straight). Towards that end, a series of quadrilateral shell element (S4R, reduced integration scheme) cylinders can be used to translate and rotate the stent. Details of this technique will also be discussed in Chapter 5 as is the same for the two models. Meanwhile, it is useful to mention that the braided stiffener is no longer rigid but deforms in accordance to the rest of the cylinders.

Note that if the vascular section is created in Abaqus, the developed algorithm can automatically extract its centreline points and allow for an easy delivery, without the need for any user input. Furthermore, the vessel is rotated and translated so as to match the orientation of the stent before the start of the analysis, reducing the computational cost of the solution.

As with the 1 ring models, contact is enforced using the penalty contact algorithm which approximates hard pressure-overclosure behaviour in a way that the contact force is proportional to the penetration distance. Frictionless contact is assigned between the rings as well as between the rings and the compaction cylinder. Adequate friction coefficients are used for the remaining interactions and friction is activated and deactivated in various stages of the process to ensure realism and stability. A result of the multi-ring model deployed in a curved vascular section is demonstrated in Fig. 4.28. For this analysis, 4 rings were considered in order to simulate the scaffolding of the Anaconda™ body module and the runtime was less than 10 hours on 12 Xeon© cpus of a desktop computer (3.40 GHz, 64 GB).

The idealization of the ring-to-ring connection with four saddle links alone proved to be computationally efficient, yet needs fine-tuning to produce reliable results. The exploration of these optimum/most realistic values for the connector variables though, is left for future work. Given the fact that the Axial Connectors can only

partially represent the effects of fabric and cannot provide the framework for CFD analysis, the development of a full device model from a different starting point was deemed more appropriate to pursue herein. This model is presented in Chapter 5.

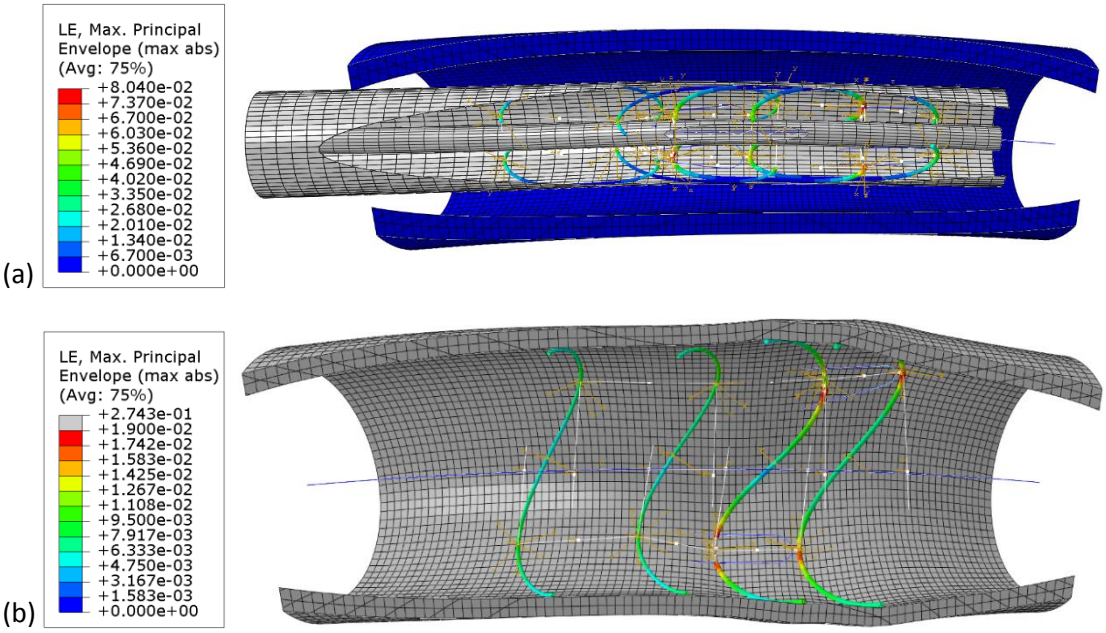

Fig. 4.28 The maximum principle strain of the scaffolding of the body of the Anaconda™ when compacted into a delivery sheath (a) and when deployed into a vascular section (b). The hooks, the Axial Connectors, the braided stiffener and the vascular centreline are visible. The bundles have been supressed to allow wire visibility.

4.6 Discussion and summary

Although FEA has become a major tool for stent analysis, the studies conducted in the literature are not too often compared against experimental results, sometimes making the conclusions less robust. This, in combination with the fact that the stent type significantly affects the structural response of the device [87], has triggered the in-depth study presented here. A bundle ring stent technology has been modelled with a combination of beam and surface finite elements. With the approach developed herein, the shape, the global stiffness and the strains of the structure can all be well predicted while at the same time, with overlapping the Nitinol turns, no

computationally demanding wire-to-wire interactions need to be included. This allows for the development of bigger scaffolding sections as well as the inclusion of generally omitted endograft components like the hooks, in simulations that are not too time consuming. A full, computationally efficient stent device for design optimization purposes or patient-specific applications could be built upon this modelling approach.

Regarding validation, comparison of four physical rings with their equivalent FEA models produced similar force-displacement responses while the discrepancies from the experiment always appeared as force overestimations. This effect reflects the exclusion of multiple aspects of the physical bundle such as the wire-to-wire interactions, the change of wire positioning along the length of the bundle, the assumption that the centre of mass of the strand always lies at the centre of the cross section of the bundle and the use of a constant value for the stiffness of the polyethylene strings despite the slightly non-linear response produced during the uniaxial testing of the material. Most importantly though, the models reflect the replacement of friction with total restriction of rotation along the wire's direction (at the connection points of peaks and valleys) and hence account for the inability to impose the real boundary conditions in every detail. It can be postulated that it is for this overestimation of the friction constraint that the model consistently appears stiffer. Nevertheless, the model produces results inside the standard deviation of the experiment or very close to this range.

The model developed herein has been shown to be cost effective. The solution time of minutes needed for the saddle-pull test and several hours for the full bundle ring's compaction, deployment and cycling through systole and diastole is deemed to be low enough to allow a viable, accurate tool for the bundle ring assessment. The respective continuum model, for the same analysis, needed anywhere from 7 to 23 times more time to produce results. In their analysis, Hall et al. [185] reported that factor to be 15, making their continuum model lie in the middle of the current results. Direct runtime comparison with other studies in the literature is not trivial since differences in stent geometries, material parameters, the amount of

crimping as well as the exclusion of the cycling steps will inevitably affect the computational cost; reported times from hours to days though can be found in the bibliography [94,98].

Previous simulations of the Anaconda device (the reader is referred to [88,94,95,194]) used 'equivalent beam' models sacrificing the accuracy of the outputs, while also considered the undeployed configuration of the bundle to be unstressed, a strategy proven herein to add significant errors into the results, not only for strain but for radial stiffness as well. The exclusion of the initial load step leads to high divergences from the saddle-pull experiments in the order of 26%.

After validating the model, a parametric study was conducted in order to explore the effect of both stent oversize and friction, on the COF exerted by the bundle ring and the mean strain, $M\varepsilon$, developed in it. For μ values below 0.3, COF remained stable from 10% up to 40% oversize. This suggests that if the real value of the friction interaction is medium or low, the oversize is not a crucial factor for the success of EVAR, as far as migration is concerned. The same cannot be said, though, in the case of high friction coefficients. Unfortunately, few results are available in the bibliography to give confidence to one case over the other, while the existence of calcification and thrombus can further affect the interface. It should also be mentioned that a preliminary study was conducted to examine the effect the normal contact force formulation has on the COF (i.e. different numerical implementations of the normal contact definition were considered) and results showed that change of this characteristic affects the stability of the solution rather than the force values themselves.

The plateau of COF, strongly present in the lower friction coefficient cases, can be attributed to both the geometrical non-linearities of the deployed bundle ring and the material non-linearities of Nitinol which operates in its superelastic region. Moreover, a gradual reduction of the contact area of the stent/vessel interaction was noted at increased oversizes, probably the result of the distribution of radial forces. The rearrangement of the radial forces can possibly explain unwanted phenomena such as migration and type I endoleaks.

Regarding $M\varepsilon$, results showed that friction coefficient had a minor effect on them with lower values of μ leading to lower values of strains by a small percentage. Yet the increase of oversize linearly increased the developed $M\varepsilon$ from an average of 0.001 at 10% oversize to an average of 0.022 at 40% oversize.

In clinical practice, specialists make use of approximate diameters of target vessels to decide upon the most suitable endograft. Utilizing the cross sectional analysis of Chapter 3, a thorough examination was conducted exploring the effects the cross sectional shape of the vessel has on the Ring Model and both the chronic outward force and (especially) the strains were found to be significantly affected.

The major axis approximation was found to underestimate the maximum strain by 51% at the most extreme ellipticity and the total radial force by 14%. In contrast, the minor axis approximation overestimated the maximum strain by up to 64% and the total radial force by up to 6%. These two approaches represent the most common approximation of the vascular cross section. On the other hand, the average circle produced a much better estimation of the maximum strain and underestimated the chronic outward force by just 3.2% when compared to the respective elliptical shapes. As a result, the average circle can be safely used to calculate these variables. However, even with this approach, poorer results would be produced if delta strain was of interest (underestimation by up to 7.8%).

Regarding the axial angle of deployment, the most sensitive variable was delta strain, particularly below the 0.83 elliptical ratio. This variable was minimized at a deployment angle of 45^{o} due to the asymmetric inflation of the vessel. Note that with more complicated cross sectional shapes, the optimum direction from a fatigue life point of view will be different and case specific. Nevertheless, the study showed that COF and maximum strains will be practically unaffected by the deployment angle.

In conclusion, the Ring Model presented herein has the ability to capture the strains developed on the Nitinol wire for any further fatigue testing, as well as the chronic outward force for sealing and anchoring evaluation. The friction coefficient of the stent-vessel interaction has been shown to affect COF, while oversizing could be a non-critical parameter on stent migration; in highly oversized cases though, the

developed strains need to be carefully examined. Finally, it is recommended that future stent graft analyses should take variations in target vessel geometry into account since the use of non-idealized cross sections may have an important effect on the functional performance of the devices.

Chapter 5

Full Device Model

The final objective of this thesis is to develop a computationally efficient Anaconda^{TM} model. Such a model will be able to simulate the full stent graft device and deploy it into any random (that is, patient specific) geometry. The prediction of the deployed endograft positioning will allow the clinical and biomechanical assessment of EVAR prior to surgery. The conduction of such analyses can serve as a powerful tool that will allow clinicians to examine the deployment of different endografts (on the market or tailor-made) inside patient specific AAAs, given the readily available CTA scans of the patient. The examination of a variety of clinical scenarios, such as deployment in different proximal regions or usage of multiple iliac leg modules at the distal site of the endograft, will further help clinicians to decide the optimum intervention. The key outcomes that are prioritized herein are the prediction of the deployed shape of the endograft below the 5 mm error which has been reported as a commonly accepted limit practitioners use when incorporating simulations in their clinical workflow [195], and the ability of the simulation to be used for hemodynamic analysis. These capabilities can provide an insight on migration forces, possible endoleak risk and fabric occlusion that may lead to thrombosis; all treasured features in the medical and medical device manufacturing community.

Preliminary studies of endograft deployment involved both an idealized stent graft and an idealized AAA (see for example [82,196]). Despite the merits such analyses may bring though, they can only reveal gross trends and features of the surgical technique since they fail to include key mechanical and geometrical characteristics.

Perhaps the first study on virtual deployment of a bifurcated stent graft in a non-idealized AAA was published in 2012 [179], where the numerical model developed was compared against an experimental stent deployment inside a silicone aneurysm. The study is significant because it showed the capabilities of FEA and a global agreement between the two. Nevertheless, the simulated device was under-expanded during deployment and at the bifurcation of the aorta produced significant errors when compared to the experimental images. Unfortunately, the distance (i.e. error) between the deployed struts and the predicted ones was not reported. Similarly, the runtime of the FEA analysis was not disclosed either.

When studies create full stent simulations to predict the deployed stent position and at the same time try to accurately capture the mechanical state of the underlying materials, they inevitably produce computationally expensive models. A model of this type was developed by Morlacchi et al. [163] to simulate a coronary stent made out of a cobalt-chromium alloy. The model required 60 hours to run on two nodes of a high computing cluster; and yet, coronary stents have no fabric.

The existence of fabric on the EVAR endograft poses significant difficulties for simulation and if included, it increases the runtime dramatically. Due to its physical dimensions, fabric buckles and folds naturally, making the analysis extremely non-linear, with very large deformations and complex self-contact conditions.

In 2015, Perrin et. al [165] presented an integrated approach to delivering and deploying an EVAR stent graft inside a patient specific geometry reporting anywhere from 55 to 100 hours of runtime. The technique was further developed and the following year was used to simulate the Anaconda^{TM} stent graft [195].

To date, the paper of Perrin et. al [195] is the best full Anaconda^{TM} simulation that exists in the literature. Their full device model was validated against one *in vitro* and two *in vivo* deployments and the comparative results were very satisfactory, with

the maximum error between the virtual and the experimental stents being generally below 5 mm. The major draw-back of the study was its computational cost. Despite the simplifications employed using an 'equivalent beam' model, the reported runtime was over 40 hours. This is nowhere near the timeframe that can be useful for clinical practice while it can be challenging even for product developing purposes.

In this Chapter, common simplifications have been used as well, both for feasibility and efficiency reasons. Nevertheless, the time frame of solving full device simulations has been drastically reduced, giving this study an advantageous position in the FE analysis of EVAR.

5.1 Development of the Full Device Model

Section 4.5 demonstrated the feasibility of the Ring Model to scale into multiple rings and simulate sections of the Anaconda^{TM} scaffolding. For the full device model, though, fabric is too important to be dismissed. The Axial Connectors that were developed in Chapter 4 can only grossly represent the graft's connective effects since they only connect peaks to peaks and valleys to valleys. Experimental evidence shows that tension lines in the fabric are more complex than that and very often manifest themselves in diagonal directions. As a result, if large sections of the device need to be modelled, the inclusion of fabric becomes crucial in order to capture the overall behaviour of the structure [166]. What is more, only the addition of fabric can allow the model to be useful for detailed hemodynamic analyses, making its presence of utmost importance in the current framework.

As already mentioned, preliminary efforts to add fabric into the scaled Ring Model made the simulation too unstable (and time consuming) to run until the end of the analysis. To overcome the stability challenge, the explicit solver of Abaqus was used instead of the implicit one employed so far, a choice that is in agreement with the literature when the graft is simulated. However, this decision pushed towards the creation of a new model altogether, since not all modelling features employed until now are available in both Abaqus/Standard and Abaqus/Explicit.

5.1.1 Explicit versus implicit solver

Abaqus has two different solvers for tackling different FEA problems. The implicit solver (Abaqus/Standard) is the modelling choice when simulating static or quasi-static problems with smooth non-linear behaviour (e.g. no material wrinkling involved). On the other hand, the explicit solver (Abaqus/Explicit) can be used to simulate dynamic analysis such as wave propagation or impact. Nevertheless, thanks to its robustness, the latter is often employed to model static problems as well if the non-linearities involved make the implicit solver too slow or non-convergent.

Another advantage of the explicit procedure regards scaling. As the model size increases, solution cost for the explicit solver increases slower than for the implicit one, making it more attractive for large analyses. For the method to be efficient, though, the time scale is important.

The explicit solver is conditionally stable allowing, as a result, only short time advancements per iteration in order to keep the solution realistic. This means that the total time to be simulated needs to be small enough to make the explicit solver advantageous. However, for small time frames inertia effects arise. Hence, since herein we want to acquire static solutions, the aim is to model the process in the shortest time period in which inertial forces remain insignificant. For that to be achieved, the period of the lowest mode of the structure (which is the one usually dominating its response) needs to be calculated and used as an indicator for the time frame of the simulation. The ratio of kinetic over internal energy is also monitored to be kept low, ensuring the negligibility of inertia.

One could argue that the deployment of the endograft is not a static procedure in the first place. The pulling of the sheath that releases the device certainly generates dynamic effects and each ring creates a small impact with the vascular wall during deployment. These effects, though, are usually disregarded in favour of analysing the long term state of the device. And while is true that after deployment, dynamic effects also exist due to the pulsating loads of pressure, as an initial modelling attempt, the exclusion of such complexities is deemed reasonable. As a result, the

presented work assumes that a static analysis is sufficient in order to explore the main characteristics of EVAR.

Leaving its stability advantages aside, a considerable drawback of Abaqus/Explicit is that it does not currently offer certain modelling features of importance for the developed analysis. At present (version: Abaqus 2018), the software does not support necessary features to model the initial load step of the Ring Model, and in particular the 'Model Change' technique which allowed the crimping of the ring after the circular formation. As a result, the manufacturing strains (i.e. pre-strains established by the forming of the ring), whose importance has been illustrated in Chapter 4, cannot be included when using Abaqus/Explicit. The consequence of this is significant. If manufacturing strains are excluded, the final state of Nitinol will be inaccurate, questioning the very reason of taking such a complex material into account. And if strains cannot be predicted accurately, there is no need for multiple turns to be modelled either. As a result, due to current software limitations and in order to favour computational efficiency, in the Full Device Model that predicts positioning, no pre-strains, no Nitinol and no multiple-turns are included.

It is meaningful to note that since the analysis is displacement driven for the greatest part of the EVAR simulation (endograft is compacted inside a sheath, the sheath is delivered to the artery and dilated to allow the expansion of the device inside the vessel), the final shape of the rings is marginally affected by their underlying material. As a result, this choice is not expected to affect significantly the outputs of interest.

The alternative modelling approach that has been taken, is presented below.

5.1.2 Building the scaffolding

The Anaconda^{TM} stent graft device consists of 3 separate pieces (or modules) as shown in Fig. 2.3, the main body and the two iliac legs. During EVAR, the surgeon deploys the main body of the endograft and soon after the two legs, which lock inside the body and stay fixed relative to each other from then on. To avoid the computational cost of simulating the interaction between those pieces as well as the separate

stages of deployment, the virtual device developed herein is modelled as one piece. Yet, as it will be shown, the relative position of the three modules is taken into account at the building stage of the device, prior to the initiation of the analysis.

Given the complexity of the problem and the large number of variables involved, significant effort has been put into making the process as automated as possible. As a result, given a vascular geometry, the user decides upon the number of rings and ring characteristics that should be used to accommodate it, the position of the legs relative to the body (how low and under which angle does the lock happen) and the position of the device relative to the vessel (i.e. the proximal region of deployment). Once the choice of the Anaconda™ device design and its position has been made, the in-house algorithm built by the author creates the endograft, compacts it and deploys it inside the vessel without any further user input.

The building process of the device starts with the scaffolding, and in particular, with the creation of circular rings. These rings are made of beam elements that are enclosed with surface elements similarly to the Ring Model of Chapter 4, yet they are modelled as circles right from the start of the analysis. Furthermore, since computational efficiency is an important feature of this model, an 'equivalent beam' approach has been used to represent it.

The standard approach for creating 'equivalent beam' models is based on the fact that bending forces are dominating the endograft. As a result, the aim is usually to create 1 wire (instead of *n*) that has the same second moment of area as the bundle, ensuring the same bending stiffness. Herein, though, we are looking for equating directly the bending stiffness product EI. This means that apart from changing radius, we also allow for the alteration of the material of the wire. By assuming that initially all circles are overlapping in the centre of the bundle, and after assigning a random radius r_2 per ring that is marginally smaller than its bundle radius (Fig. 5.1), we get:

$$E_1 I_{overlapping} = E_2 I_2 \Rightarrow E_2 = E_1 \frac{n r_1^4}{r_2^4} \tag{5.1}$$

The advantage of this approach derives from the fact that thicker wires lead to coarser converged meshes (see Section 4.2.2) and less stiff materials result in larger

stable time increments in the explicit approach. Following the above strategy, both effects take place and both reduce the overall solving time.

Note that the modulus E_1 is the stiffness of the linear austenitic region of Nitinol and is equal to 59 GPa (refer to E_A of Table 4.2). As a result, the material to be used is linear elastic with ring-dependent stiffness E_2, Poisson's ratio v = 0.33 and density 6.45 g/cm^3.

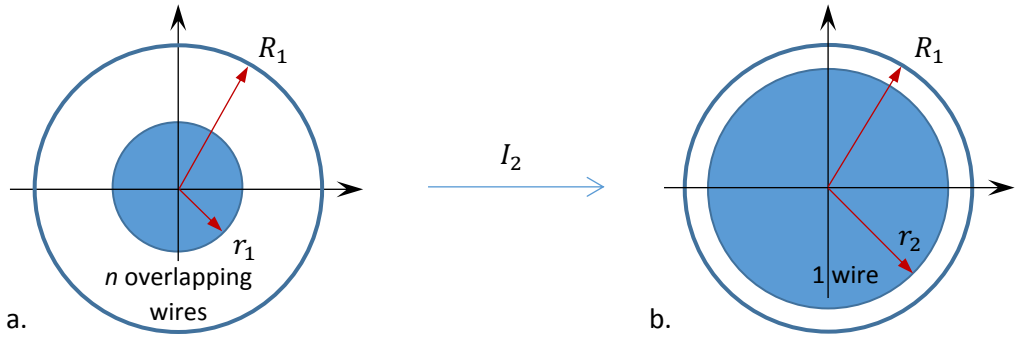

Fig. 5.1 The overlapping turns of the Ring Model (a) and the beam with an equivalent radius (b).

As had been noted in Chapter 4, the bending stiffness equivalency is just a rough approximation of the final stiffness of the ring and is not expected to accurately predict the true mechanical response of the scaffolding. It should be mentioned though, that an exploratory analysis was conducted to quantify this error by re-simulating the saddle pull test of Section 4.2.4. It was observed that the discrepancies from the experiment were similar to the Ring Model behaviour for Ring 2 and 4, yet for the stiffer rings they were significantly larger. Especially for Ring 1, the error increased to 15.0 – 18.5 % for the case where manufacturing strains where included and 30.0 – 34.1 % for the case where pre-strains were not taken into account (compare with Table 4.5 and 4.6 respectively). The reason for this non-uniform increase is that stiffer rings develop greater strains under the *in vivo* deformation hence enter the martensitic plateau earlier, leading to a greater difference against the equivalent (linear) model. This, once again, demonstrates that for analyses that aim to capture the stiffness and even more so, the strains of the bundle, bending moment equivalency is not sufficient.

Apart from the bundle rings, the scaffolding of the Anaconda^{TM} includes several S-shaped metallic supports located at the distal end of the body module (Fig. 2.3). These regions are important in clinical practice since they keep the lumen of the body open during the deployment of the legs, yet they would serve no functional purpose *in silico*. Furthermore, their design complexity is significant, as they do not follow a specific mathematical curve. As a result, inclusion of them was not performed herein.

Hooks were also excluded from the analysis. Their challenging degrees of freedom, as explored in Section 4.5, increase the computational cost of the simulation due to the introduction of instabilities. The omission of hooks also simplifies the contact condition since no damage models need to be implemented to simulate the penetration of them into the vessel.

Finally, meshing of the rings follows the rules of Chapter 4.

5.1.3 Building the fabric

In reality, the Nitinol bundles are hand-sewn onto a tubular fabric following the lines of a pattern. This process results in a graft shape that is very difficult to reproduce numerically and at the resting state of the device, create folds that are not perfectly repeatable (Fig. 5.2 d). As a result, the approach followed herein to model the graft is idealized.

The fabric of the device is developed in two phases. The first phase involves the main tubular sections of the body and leg modules (Fig. 5.2 a). These parts have straight regions with lengths equal to the saddle height of each ring, i.e. the longitudinal distance between its peaks and valleys. Their curved regions are allocated to the spaces between the rings and allow the excess of graft present between the bundles of the Anaconda^{TM} to be modelled (Fig. 5.2 d).

The second phase of the fabric development regards the distal region of the body module. This section splits the original lumen into 2 lumens so as to account for the aortic bifurcation. This division, however, is very challenging to model in Abaqus,

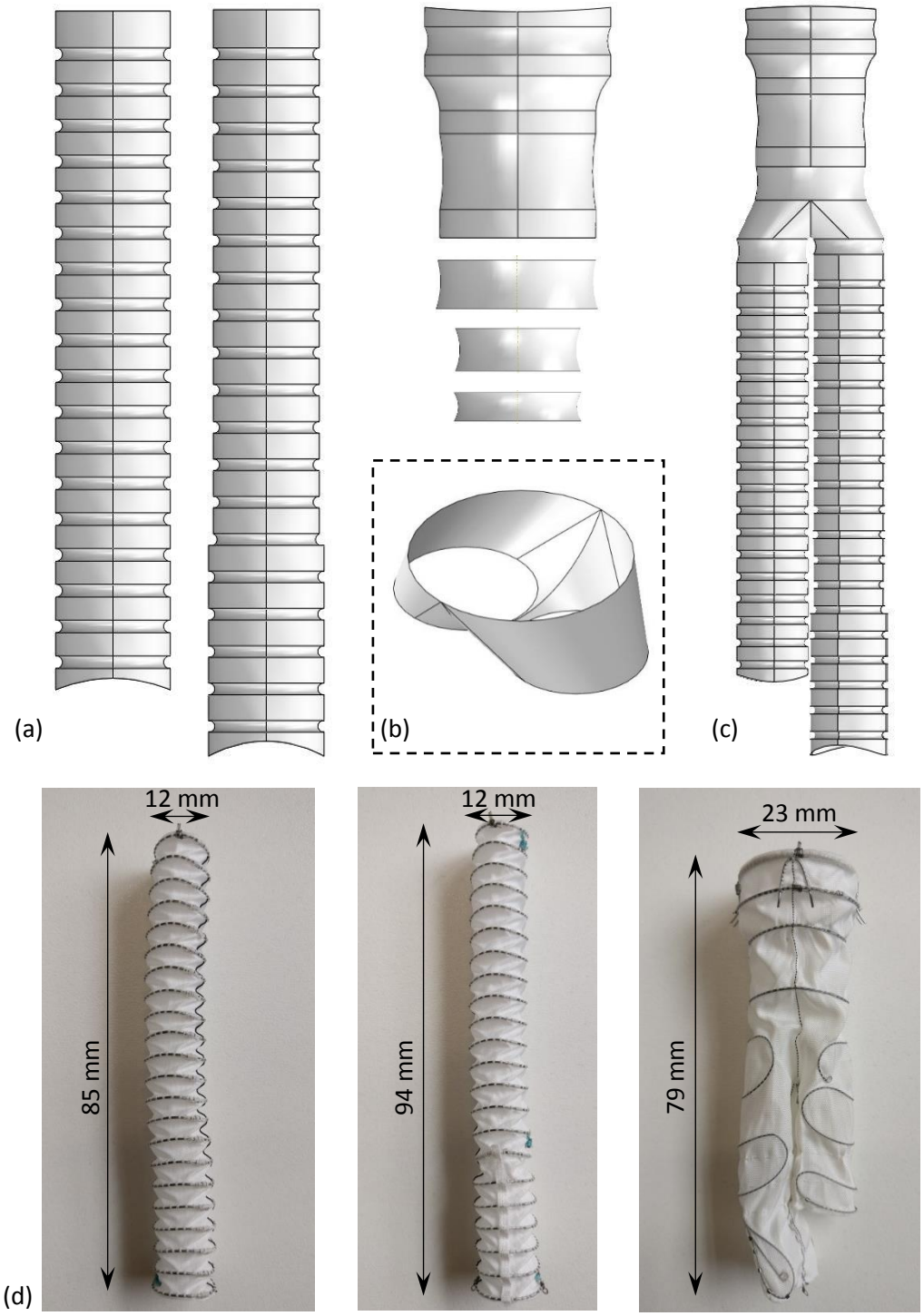

Fig. 5.2 The tubular parts of the fabric are created using Abaqus (a). The distal end of the body module is imported from SolidWorks (b) and then connected to the remaining parts to form the entire graft. A real device is also shown for comparison (d).

hence the 3D CAD software SolidWorks 2017 (Dassault Systèmes SolidWorks Corp) was used (Fig. 5.2 b). This section is then imported into Abaqus and connected with the other fabric parts to create the final graft (Fig. 5.2 c).

The Anaconda^{TM} device uses a woven polyester fabric with 0.14 mm thickness for the body module and 0.12 mm for the legs. Herein, though, a simple elastic material was used with constitutive parameters taken from the literature [70,196] (Table 5.1). The use of a more complex fabric material [87] was also examined, but no obvious advantage was noticed. In that study, Demanget et al. [87] loaded a fabric sample with tensile forces in various directions to establish an orthotropic plane stress model for the in-plane behaviour of the graft. Nevertheless, as Geest et al. [151] observes, an anisotropic constitutive model cannot be produced from uniaxial tensile data, even if multiple uniaxial directions are considered. Hence, Demanget's more elaborate model has yet to prove its advantage.

Lastly, fabric is modelled using Kirchhoff thin shell elements (S4R, reduced integration scheme with enhanced hourglass control and finite membrane strain formulation) with 0.25 mm length size. These elements are adequate for large-strain analysis and can tackle high distortions, while the hourglass control adds bending stiffness to the system, which aids stability.

Table 5.1 Parameters of the fabric model [70,196].

Elastic modulus (MPa)	55.2
Poisson's ratio	0.46
Thickness (mm)	0.14

5.1.4 Building the model

The initial configuration of the endograft is dictated by the position of the iliac legs relative to the body. These parameters are provided by the user and allow the algorithm to build the rings and fabric of all the modules in the desired orientation, before the initiation of the analysis. Furthermore, while in reality the scaffolding is

attached to the fabric using a series of polyester sutures, in the FE model, instead of using an abundance of discrete connecting points, a continuous connection is used along the length of the rings. Both these strategies enhance the computational efficiency of the simulation.

In the model, the connection between the fabric and the scaffolding occurs in the first two steps of the analysis. In the initial step, a sinusoidal displacement is assigned to the rings to acquire the saddle shape the rings have at their rest state (Fig. 5.3 b). At this stage, frictionless, no separation contact (at the tangential direction and normal direction respectively) is used to establish the fabric-ring contact. After that, the rings are compacted and the contact is changed to “rough”, which is a Coulomb frictional model with infinite friction, hence preventing slippage between the involved surfaces regardless of the contact pressure. This condition remains for the rest of the analysis. Note that the first step of the process is in essence part of the second step (i.e. the fabric-ring contact occurs during a “monotonic” ring compaction), hence the computational cost of it does not burden the total runtime.

The scaffolding and the fabric are the main building blocks of the endograft, yet a series of additional features and structures are needed to perform an EVAR simulation. Perhaps the most obvious parts to be discussed are the delivery catheters which have already been briefly mentioned in Section 4.5. Each module (i.e. body and two legs) has its own pair of cylindrical catheters (shell elements, S4R), one with a rigid wall (Catheter A) and one inflatable (Catheter B). The two catheters of each pair have the same radius and are tied to each other for the initial part of the analysis. Catheter A is tied to a beam that resides in its centre and can help with delivery, while Catheter B has no centreline and aids deployment.

In more detail, since in this model the material of the rings is linear elastic, full compaction is not needed, as a result, no cylindrical surface is used to crimp the endograft to its most extreme state. Instead, the rings are pulled by the peaks and valleys to reduce their diameter enough to fit inside the catheters; these loads resemble the saddle pull test of Section 4.2.4 (Fig. 5.3 c). Additionally during compaction, the

rings are slightly pulled apart from each other with a displacement $L_{unstheath}$. In reality, this elongation takes place during unsheathing (deployment) of the device inside the AAA, yet, since the computational deployment performed herein is via the inflation of catheters (i.e. application of pressure at the inner cylinder wall), pulling of the device is simulated earlier for convenience.

Once the rings are inside the catheters, the forces used to pull them are released and the rings come into contact with Catheter A. Delivery follows, as boundary conditions are applied to the centreline of Catheter A forcing both catheters to move accordingly (Fig. 5.3 d). Once delivery is completed, the endograft switches its contact from Catheter A to B, the tied contact between the catheters is supressed and pressure is applied to the inner wall of Catheter B making it expand, thus allowing the endograft to deploy inside the vessel (seen later on in Video 5.1).

The overview of the analysis can be described in the following steps:

Fabric initialization	Rings are assigned a sinusoidal deformation that imitates the resting state of Anaconda™.
⇩	
Compaction	Pulling forces compact the rings.
⇩	
Release	Rings are released inside Catheter A.
⇩	
Delivery	Catheters move the device at the centreline points of the vessel.
⇩	
Initial pressurization	The vessel is inflated from 0 MPa to its systolic pressure.
⇩	
Deployment	Catheter B is inflated and the endograft is deployed inside the vessel.
⇩	
Pressurization	Diastolic and systolic pressure are interchangeably applied at the vascular wall.

Transition steps have also been included in different stages of the described analysis to minimize inertia effects and increase stability.

As can be seen in Fig. 5.3, the original and the final orientation of the rings do not coincide. What is more, the final orientation of each ring is unknown prior to the import of the vascular geometry. This poses a challenge in the definition of boundary conditions at the final stage of the simulation. In Abaqus, apart from very specific exceptions, no coordinate system can follow the rotation of nodes during the analysis, meaning that if a boundary condition is maintained throughout the analysis, the original orientation of it will be maintained as well, despite the movement of the structure. At the same time, no node can have boundary conditions expressed in more than one coordinate system, even if they are applied in different steps of the

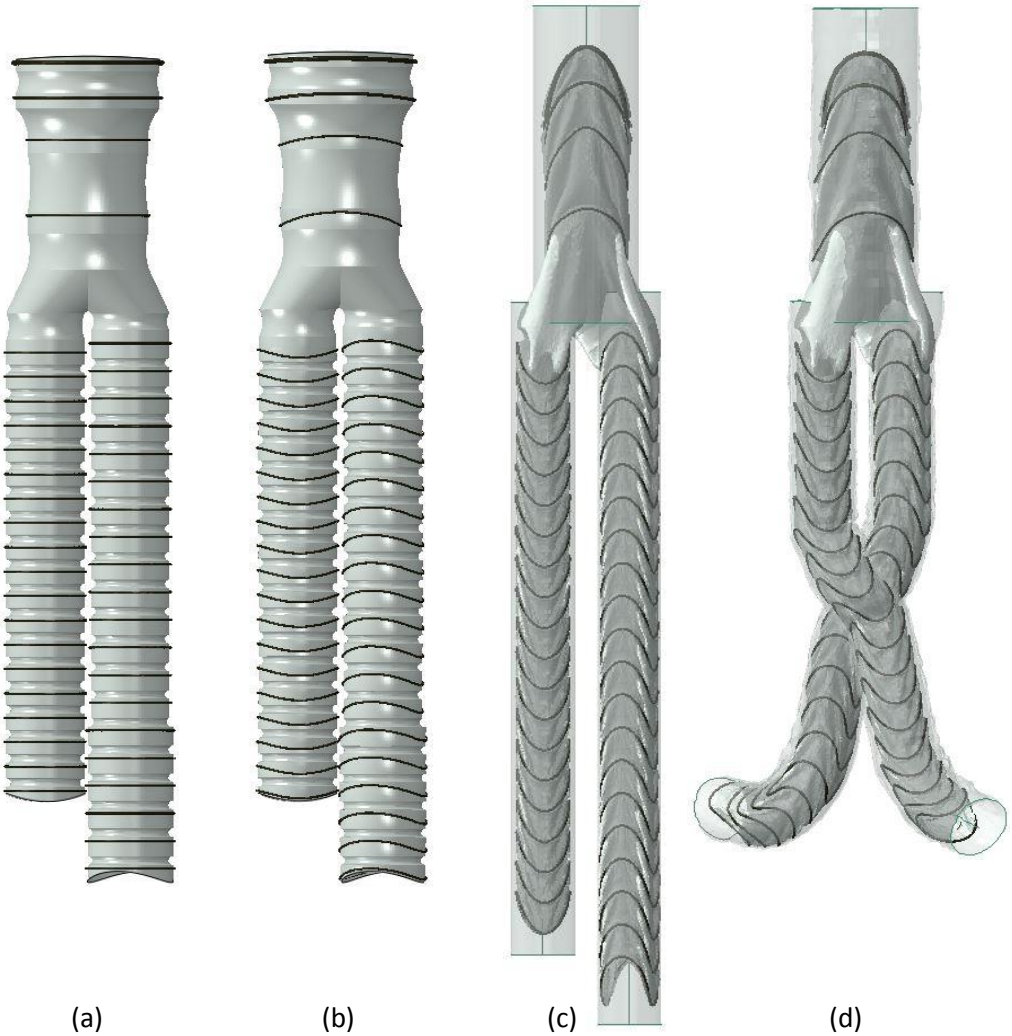

Fig. 5.3 The Anaconda™ model at the beginning of the analysis (a) and after fabric initialization (b). Pulling forces fit each module inside its corresponding pair of catheters (c) which are then moved during delivery according to the vessel's centre points (d).

simulation. As a consequence, the simple definition of boundary conditions, as expressed with equations (4.2), is not possible.

To address the issue, reference points were created at the peaks and valleys of each ring and were connected via weld connectors with the respective saddles (Fig. 5.4). This way, the reference points and the ring's peaks/valleys shared all translational and rotational degrees of freedom from the beginning of the analysis. During compaction, boundary conditions were applied at the peaks and valleys of each ring (points A, B, C, D) making use of local coordinate systems oriented according to the original stent graft positioning. After delivery, though, boundary conditions were applied at the reference points of each ring (points A', B', C', D') making use of coordinate systems oriented according to the centreline of the vessel.

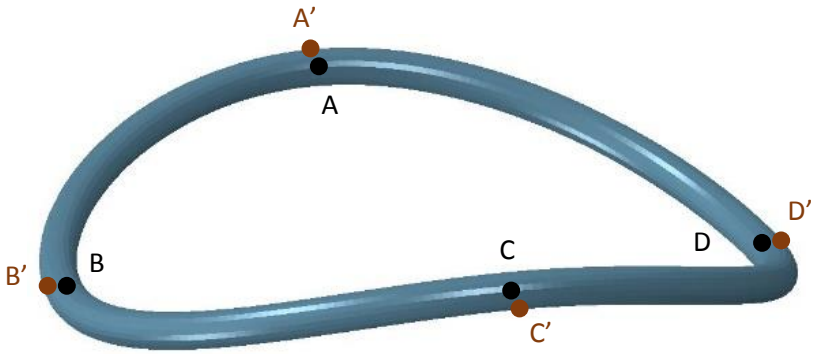

Fig. 5.4 In each saddle point of the wire (black dots), a corresponding reference point is created (brown dots). In the model, the points are overlapping and connected with weld connectors. Here, space is applied between them for visualization purposes.

Via these manipulations, equations (4.2) were defined in the appropriate orientations during compaction, release, deployment and pressurization; note, though, that the axial constraint $\text{Displacement}_z=0$ is applied only at the proximal ring of each module. Note also that during delivery and initial pressurization, the rings are constrained only by the movements of the catheters and not implicitly by boundary conditions.

From deployment onwards, $\text{Rotation}_y=0$ is also applied to points B, D and during pressurization, $\text{Rotation}_x=0$ is demanded for points A, C (refer to Fig. 4.5 for point definitions). These are stricter conditions than those applied in the Ring Model and correspond to an overconstrained arrangement. They are chosen herein only for their

efficiency and increase of stability and not for their accuracy. Since their application does not affect the shape of the rings, the effect they have on the stress/strain field is not important. Appropriate boundary conditions are also applied to the catheters throughout the analysis to prevent rigid body motion.

Another important feature of the model is the existence of Axial Connectors, similar to the ones introduced in Chapter 4. Herein, the cross connectors of Section 4.5 are used to replicate the reduced diameter of the docking zone of the Anaconda^{TM} body (Fig. 2.3), i.e. the region in which the legs connect to the body. These connectors have minimal compressive stiffness and 0.1 N/mm tensile stiffness above the reference docking zone diameter, which is 11.6 mm and 10 mm depending on their longitudinal position. Additionally, Axial Connectors are being used between the 1st and the 2nd proximal ring to approximate the restrictions applied by the hooks. The connectors are also non-linear with 0.05 N/mm compressive stiffness and 10 N/mm tensile stiffness. As it was mentioned in Chapter 4, the fine-tuning of these values requires meticulous experimental testing that was not pursued in the current body of work. The values reported herein are the product of trial and error, as well as the visual validation that will be discussed in Section 5.3.

Various contact conditions are used throughout the analysis. Apart from the "rough" contact between the fabric and the rings, as well as between Catheters A and B, self-contact is assigned to the fabric (with a friction coefficient of 0.005) and the rings (frictionless). In addition, appropriate contact is assigned to various steps of the analysis to release the rings inside the Catheters and perform delivery. At deployment, contact is assigned between the vessel and both the rings (friction coefficient of 0.5) and the fabric (friction coefficient of 0.005).

The technique developed herein is very easy to use in patient specific geometries and most importantly, it is an automatic procedure. More specifically, given a random vessel geometry with a set of centre points, the algorithm creates a second set of points along the centreline at the location in which each ring will be deployed. Thanks to the latter set, correct coordinate systems can be created to define post-

deployment boundary conditions. The centreline of Catheter A is also partitioned according to the second set. This allows catheters to be displaced to the exact vascular location, hence deliver the endograft to the chosen position inside the vessel. Note that part of the delivery happens before the start of the analysis with the vessel being rigidly translated and rotated to the orientation of the stent graft, hence further reducing the computational cost.

The schematic of Fig. 5.5 demonstrates the critical steps of delivery.

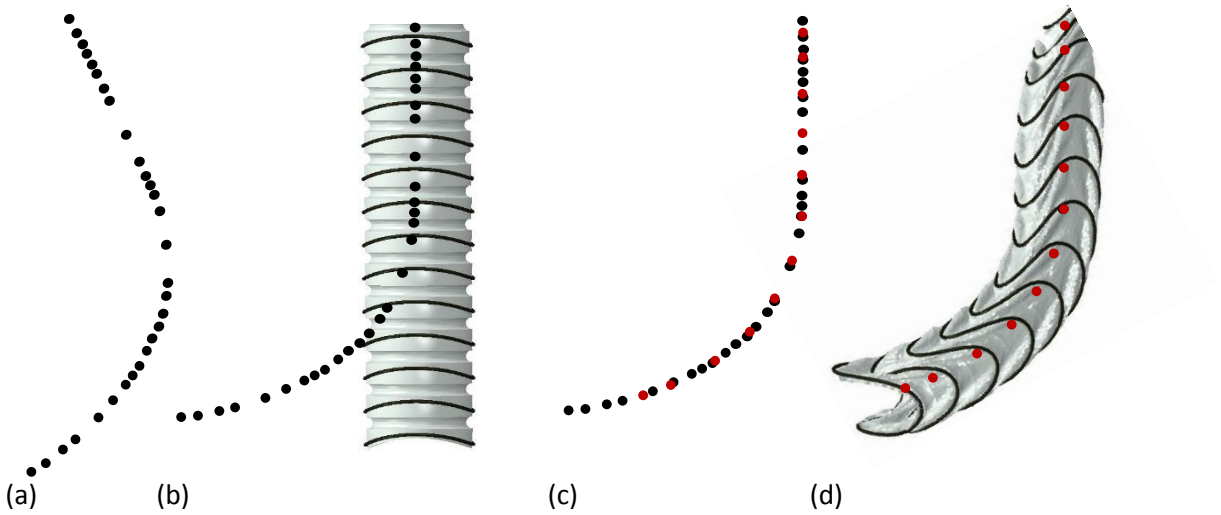

Fig. 5.5 The imported set of centre points (a) is rigidly moved (along with the vessel) to be oriented according to the stent before the initiation of the analysis (b). Using these points (black dots), a new set of points is defined (red dots). By taking advantage of the user inputs (stent specs, position of the legs relative to the body and deployment position of the most proximal ring), this set can be placed at the location where the centre of the deployed rings will eventually lie (c). Using the red set, Catheter A (along with Catheter B and the endograft) can be moved inside the vessel. Finally, new coordinate systems can be defined through that set so that boundary conditions can be applied to the correct post-delivery orientation (d).

5.2 Experimental fabric testing

It has already been mentioned that the way Anaconda™ is manufactured differs from the way the model is set up. As illustrated, the approach followed herein involves the displacement of the rings in a sinusoidal path onto the fabric which already has an excess of material between the rings. To calculate the amount of extra

fabric needed though, which corresponds to the size of the curves present in the tubular section of the graft (Fig. 5.2 a), a series of measurements were conducted in different endografts.

The body of 6 Anaconda™ devices which covered the range of sizes available in clinical practice were considered for the test. For each body, the distance between its four rings was measured at the four saddles (Fig. 5.6 a). Rings are named as R1, R2, M1, M2 in the order of the most proximal to the most distal. Each device was considered at rest (Fig. 5.6 b), at two different deployments representing two different oversize ratios (Fig. 5.6 c) and at full extension (Fig. 5.6 d). Note that the oversize ratio was not constant among the devices as the test was limited by the available tubes used for deployment (Table 5.2). Nevertheless, all the imposed oversizes were in the operational range of the endograft.

(a) (b) (c) (d)

Fig. 5.6 The distance between the four body rings was measured at the peaks and the valleys of six stent grafts (a). For each one of them, the resting state (b), a deployed state (c) and the full extension state (d) were considered.

Measurements of the full extension states were conducted during the experiment while the rest of the lengths were calculated later on via images (similar to Fig. 5.6 b and c). All measurements have an observational error of ± 0.1 mm.

Table 5.2 The devices measured, along with the imposed oversizes.

Device Name	Device Outer Diameter (mm)	Oversize 1 (%)	Oversize 2 (%)
OLB23	23.2	5.5	20.2
OLB25	25.2	14.5	19.4
OLB28	27.4	13.2	24.5
OLB30	29.5	6.1	13.0
OLB32	31.6	13.7	21.1
OLB34	33.6	14.7	20.9

The detailed results of the analysis have been summarized with the use of graphs and are reported in Appendix B. Herein, only a few important trends and values are discussed.

Because the devices are hand-sewn, there is a significant variability in the amount of fabric present between the anterior and posterior peaks and the left and right valleys of each section (Fig. 5.6 a). Nevertheless, some consistent behaviours were observed. First of all, at deployment, the valleys are primarily under compression while the peaks are under tension, signifying that the device does not experience double symmetry. Regarding the different oversize ratios, variabilities are less clear. It appears that with greater oversize, valleys are under greater compression but peaks are less affected. Furthermore, the R2-M1 distance changes the most both in compression and in tension, possibly because it involves a significant component perpendicular to the length of the device. Regarding the full extension state, the peaks of R2-M1 are the ones which extend the most, reaching distances of up to 435% more than the rest state.

By comparing the full extension state with the rest state we can approximate the available fabric slack. This serves not only this model but the Ring Model as well, thanks to a more accurate definition of the Axial Connectors that approximate the effects of fabric. The average extension between R1-R2 and M1-M2 of all devices was

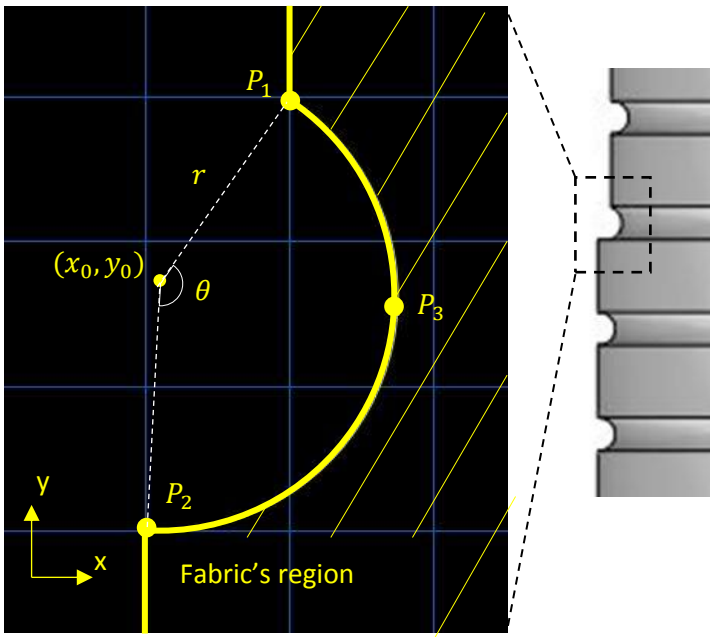

Fig. 5.7 Detail of the fabric definition. The linear sections of the graft are connected by curves.

13.5% when compared to the rest state, a value that was used in Section 4.5. These distances are mainly axial (parallel to the axis of the stent), hence allow for a reasonable slack approximation, whereas the R2-M1 distance has a large transverse component and was not taken into account for the calculation of the average extension.

To make use of the fabric measurements in the Full Device Model, the slack observed has to be connected to the curves at the fabric definition (Fig. 5.2 a). Each one of these curves is designed as a section of a circle defined by 3 points (Fig. 5.7). And since the points at the linear region of the fabric are fixed, only 1 point controls the excess of fabric between the rings (P_3 at Fig. 5.7).

In more detail, assume the 3 points $P_1(x_1, y_1)$, $P_2(x_2, y_2)$ and $P_3(x_3, y_3)$ with P_1, P_2 given and:

$$y_3 = \frac{y_1 + y_2}{2} \tag{5.2}$$

Then, the length L of the circular section is controlled by x_3 alone.

If we solve the standard equation of the circle:

$$(x - x_0)^2 + (y - y_0)^2 = r^2 \tag{5.3}$$

for the points P_1, P_2, P_3, we get for the centre (x_0, y_0) and the radius r:

$$x_0 = \frac{(x_1^2 + y_1^2)(y_2 - y_3) + (x_2^2 + y_2^2)(y_3 - y_1) + (x_3^2 + y_3^2)(y_1 - y_2)}{2(x_1(y_2 - y_3) - y_1(x_2 - x_3) + x_2 y_3 - x_3 y_2)} \quad (5.4)$$

$$y_0 = \frac{(x_1^2 + y_1^2)(x_3 - x_2) + (x_2^2 + y_2^2)(x_1 - x_3) + (x_3^2 + y_3^2)(x_2 - x_1)}{2(x_1(y_2 - y_3) - y_1(x_2 - x_3) + x_2 y_3 - x_3 y_2)} \quad (5.5)$$

$$r = \sqrt{(x_1 - x_0)^2 + (y_1 - y_0)^2} \quad (5.6)$$

All three quantities are functions of x_3.

In addition, the angle θ between the points P_1, P_2 and the centre can be found by the dot product of the vectors $(x_1 - x_0\ ,\ y_1 - y_0)$ and $(x_2 - x_0\ ,\ y_2 - y_0)$, i.e.:

$$\theta = Arccos\left(\frac{(x_1 - x_0)(x_2 - x_0) + (y_1 - y_0)(y_2 - y_0)}{\sqrt{(x_1 - x_0)^2 + (y_1 - y_0)^2}\sqrt{(x_2 - x_0)^2 + (y_2 - y_0)^2}}\right) \quad (5.7)$$

As a result, the length L of the curve section will be:

$$L = \theta r \quad (5.8)$$

and through the use of (5.4) – (5.7) will be a function of x_3. At the same time, the slack, L_s can be calculated as:

$$L_s = L - (y_1 - y_2) \quad (5.9)$$

hence the slack can be expressed as a function of x_3. This allows the algorithm to incorporate the fabric excess as measured (L_s) into the design of the graft (with the appropriate definition of x_3).

5.3 3D printed AAA validation

To assess the performance of the model, a validation test was conducted. Towards this end, an AAA CAD model was designed and 3D printed to be used as a mock artery. Experimental and virtual deployment of a full Anaconda™ device followed and the spatial difference between the two approaches was measured and used as an error indicator for the model. The key locations of interest were the proximal and distal regions of the endograft, the macroscopic shape of the flow lumen and the existence of sharp fabric folds that would impede the flow.

The comparison of the experimental and FEA results was performed by superimposing images of the two in 4 different views. This technique is not the most rigorous, yet it has been used in the literature for its ease of implementation [163,179]. The alternative option of micro-CT scanning the deployed endograft (and then registering it according to the FEA result) requires the entire experiment to take place in a facility with such a scanner; this option was very challenging to pursue and eventually abandoned.

5.3.1 Mock aneurysm

For the construction of the AAA, a CAD model of a healthy aorta was initially provided by Terumo Aortic (Fig. 5.8 a). This file was imported to Abaqus where necessary manipulations took place: the aortic section above the renals was removed as well as a large part of the iliac arteries; in addition, an aneurysm was added (Fig. 5.8 b). The 3D printing of the aorta was conducted by Malcolm Nicholls Limited (Warwickshire, UK) and in order to be transparent, an essential characteristic for visual post-processing, it was necessary after manufacturing to be hand polished. Because of that, the CAD model was further cut in half to allow access to the technicians in both the exterior and the interior surfaces of the printed structure (Fig. 5.8 c1, c2). After printing and polishing, the pieces were glued together to reconstruct the vessel and delivered to us for the experiment.

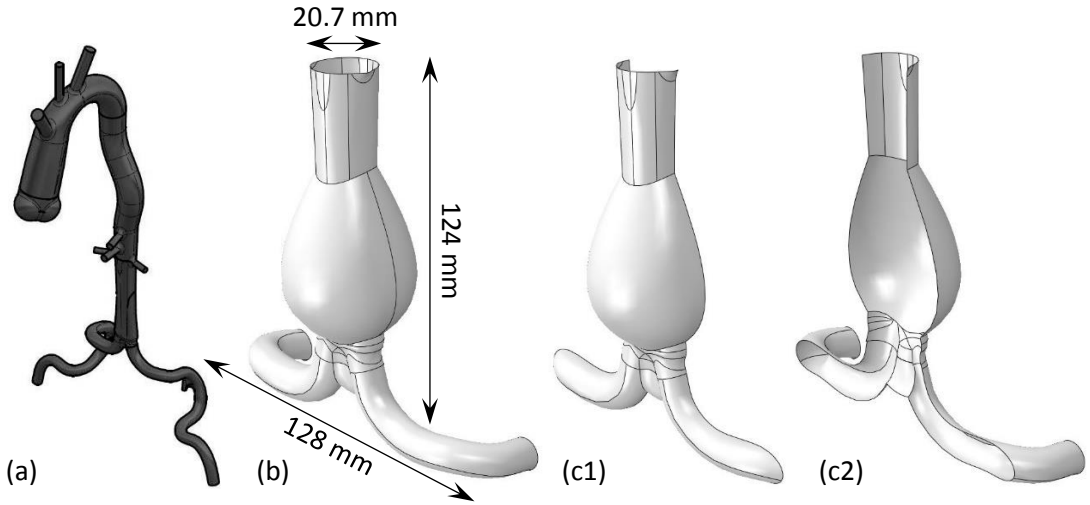

Fig. 5.8 The process of creating the CAD AAA model. The design model of a healthy aorta (a) was turned into a case-study AAA (b) and split in half to allow for hand polishing (c1, c2).

The size and angulation of the vessel was in the values observed in Chapter 3. The neck was 31.3 mm in length and its diameter was 20.7 mm while the maximum diameter of the aneurysm was 43.3 mm. Table 5.3 reports the relevant angles. Note that because the artery was modelled in a CAD software, some points were collinear, making a few angle projections impossible to measure.

Table 5.3 Angles of the mock artery in degrees (refer to Section 3.1.2 for definitions).

Angle	**Frontal plane (XZ-plane)**	**Sagittal plane (YZ-plane)**	**Transverse plane (XY-plane)**
ϕ_3	180	180	_
$\phi_5 = \phi_8$	140	180	_
$\phi_6 = \phi_9$	128	180	180

The material of the developed AAA was WaterShed® XC 11122, a resin with elastic modulus E ≈ 2 GPa. The thickness was set to 3 mm towards the outward direction of the CAD surface and the polishing finish achieved a 99% transparency.

The AAA print was cable-tied to a peg board to be held upright and the deployment was conducted in the manner surgeons perform the EVAR: first the body was deployed and then the two legs (Fig. 5.9). The body of the Anaconda™ device used has the catalogue number OLB23 (resulting in 13% oversize at the neck region) while the legs were L12x100 (Fig. 5.9, right-side leg) and FL1213x110 (Fig. 5.9, left-side leg). The legs were chosen to be different for variability; the former has 22 rings with a mean diameter of 12.25 mm while the latter accommodates 16 rings of 12.25 mm and 6 of 13.31 mm. All three modules are illustrated in Fig. 5.2 d. Furthermore, the end sections (spikes) of the hooks were removed from the endograft as they could not penetrate the resin and would pose unnatural restrictions to the deployed geometry of the rings.

Because of the stiffness of the resin, the vessel behaved as a rigid structure, and that proved to be a challenge for the delivery of the device. The sharp (90^o) turn at the iliacs was very tight for the delivery system to move upwards and unusual force

was needed to introduce the catheter. All three delivery systems (for the three modules) were twisted and pushed to make the initial turn and the body section experienced minor “jumps” at the time of deployment. The result of this strenuous delivery was the twist of the device, with the left leg being connected to the right iliac and the right leg to the left. Nevertheless, such a stent graft position can also occur in clinical practice if the iliacs are too tortuous. Because of that, the validation was pursued with this set-up, which can be thought of as a model of a challenging EVAR deployment. Pictures from the anterior, the posterior and the left and right views were taken to be used for the FEA assessment.

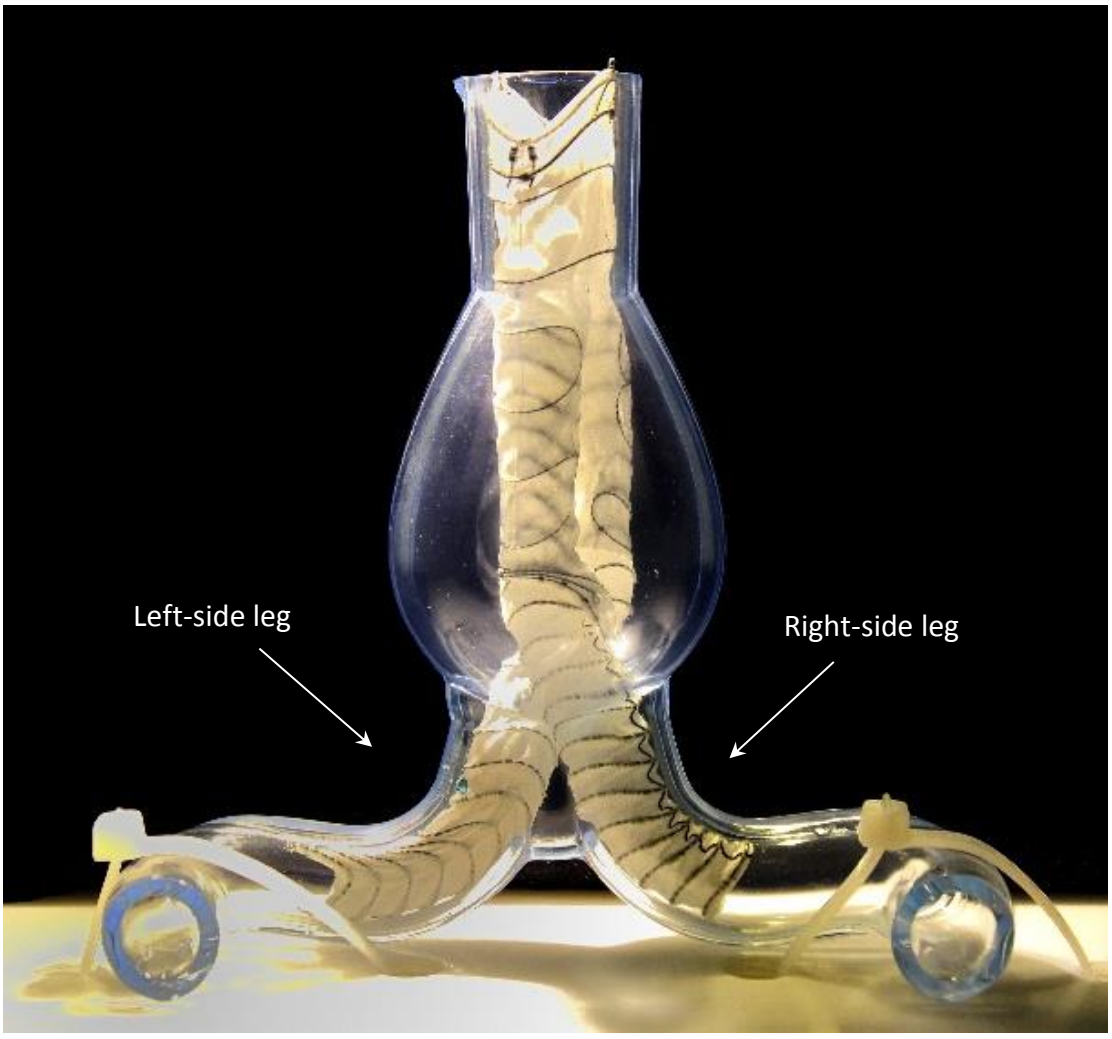

Fig. 5.9 The Anaconda^{TM} device deployed inside the mock artery.

5.3.2 FEA model and validation

Since the geometry of the AAA was built in Abaqus, making use of it in the FEA environment was trivial. Nevertheless, for the analysis to run, centreline points needed to be identified as well. For that purpose, the open source software vmtk 1.3 [197] was used and centrelines were extracted in the form of a vector of points. These points were imported into Abaqus, yet final adjustments were necessary. Since the vessel and the centreline were imported into the FEA platform separately, the centreline set needed to be rigidly translated and rotated in order to align with the vessel. Furthermore, at the aneurysmal region, the points were laterally displaced to allow for the legs to be positioned correctly (if unmoved, the legs would overlap each other at the centre of the AAA). All these manipulations occur with minor user input which is related to the initial orientation of the vessel.

For the ring modelling, the endograft specifications of the manufacturer were used rather than measurements of the sample itself. It should also be noted that because of the way the model is built, no ring of the iliacs can be placed more proximal than the bifurcation of the body module. In other words, if the leg deployment occurs high enough to surpass the graft bifurcation (as in the current set-up, where the top iliac ring has almost reached the most distal body ring (Fig. 5.9)), then no iliac ring above the bifurcation will be modelled.

Before the analysis, the shortest non-dynamic time period needed to be identified as well. For that, Abaqus offers an eigenfrequency extraction procedure which computes the natural frequencies of a structure. Using this process, the period, $T_0 = 0.0135$ s, of the lowest mode of the endograft was calculated and a time period of $1.5T_0$ was used for most FEA steps. The stages of the analysis follow the steps described in Section 5.1 with the exception of the pressurization steps, which were omitted since the vessel is rigid.

Mass scaling was used throughout the analysis to increase the minimum stable time increment, thus speeding up the solution process. The kinetic energy (ALLKE) of the deformable structures though, was monitored to not exceed 10% of their internal energy (ALLIE) for most of the simulation process. This ratio was significantly

increased only during delivery, yet that did not raise a problem since, at the delivery step, the analysis is displacement driven and the endograft is confined inside the catheters, hence the inertia effect on the rings is minimized. The ratios of ALLKE/ALLIE at the end of the simulation was 2.4%, securing a static solution.

The analysis run on 12 cpus (Intel® Xeon®, 3.4 GHz) with 64 GB RAM and the analysis time was 4h 14m, a result much faster than the times reported in the literature. A video of the analysis is presented in Video 5.1.

Video 5.1 The Full Device Model during simulation. The endograft in reference to the vessel (left) and with the meshing being visible (right). The catheters have been supressed to allow for better visualization. For the video, refer to the pdf version.

With the solution in place, the FEA output was rotated in space to correspond to the views captured in the mock artery deployment. It should be noted that the identification of the visualization plane that corresponds to the plane of the photographs was conducted manually, using the AAA outline as guidance. This process, though, has inevitably introduced errors since it is practically impossible to identify a plane in space through trial and error. This challenge most likely exaggerated the maximum distance error between the model and the experimental rings.

The following figures (Fig. 5.10 – 13) demonstrate the superposition of the experimental and the FEA results. The maximum error is reported subsequently.

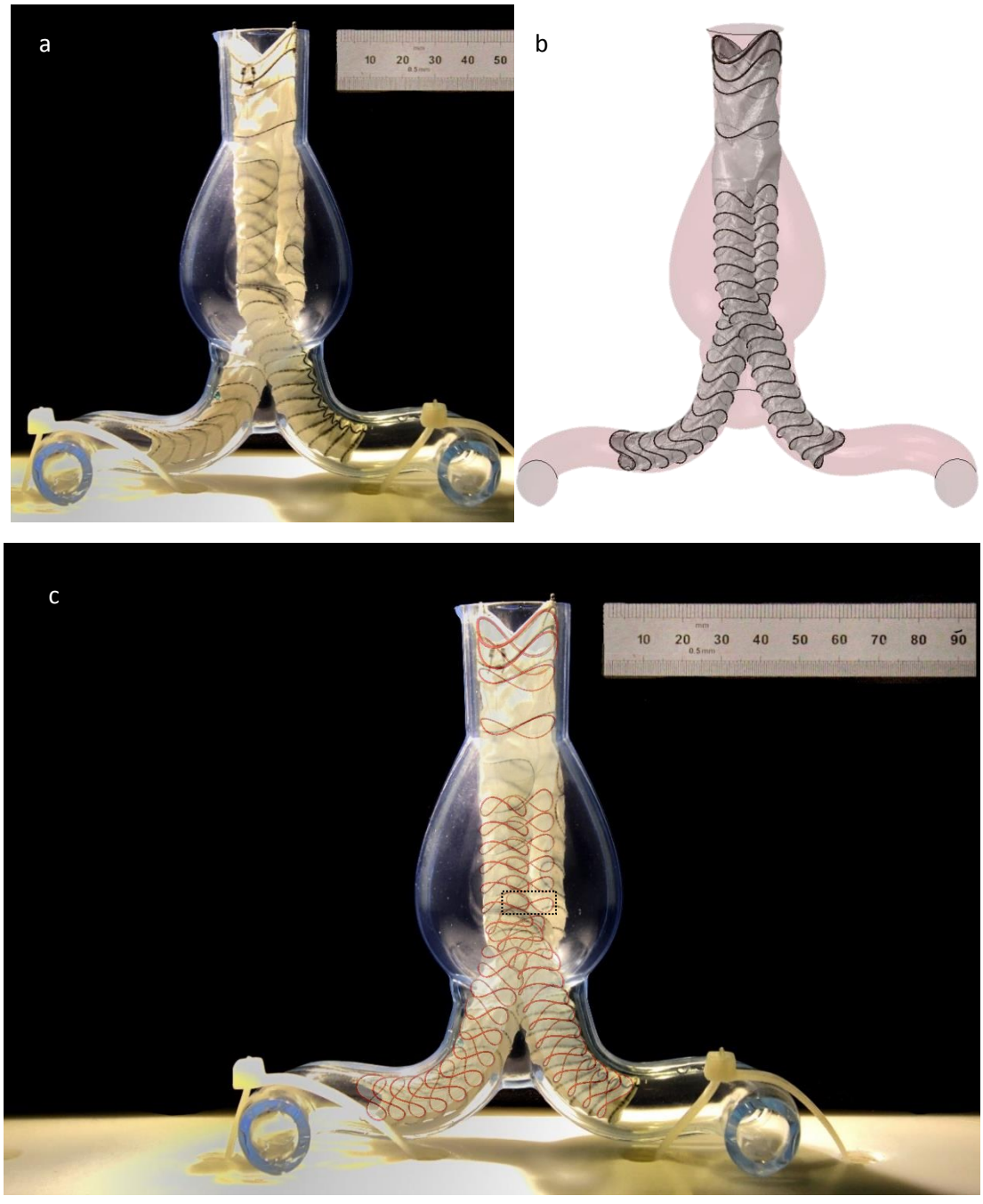

Fig. 5.10 The Anaconda™ device experimentally (a) and virtually (b) deployed inside the mock artery. At the superposition (c), the FEA rings are highlighted in red. Front view.

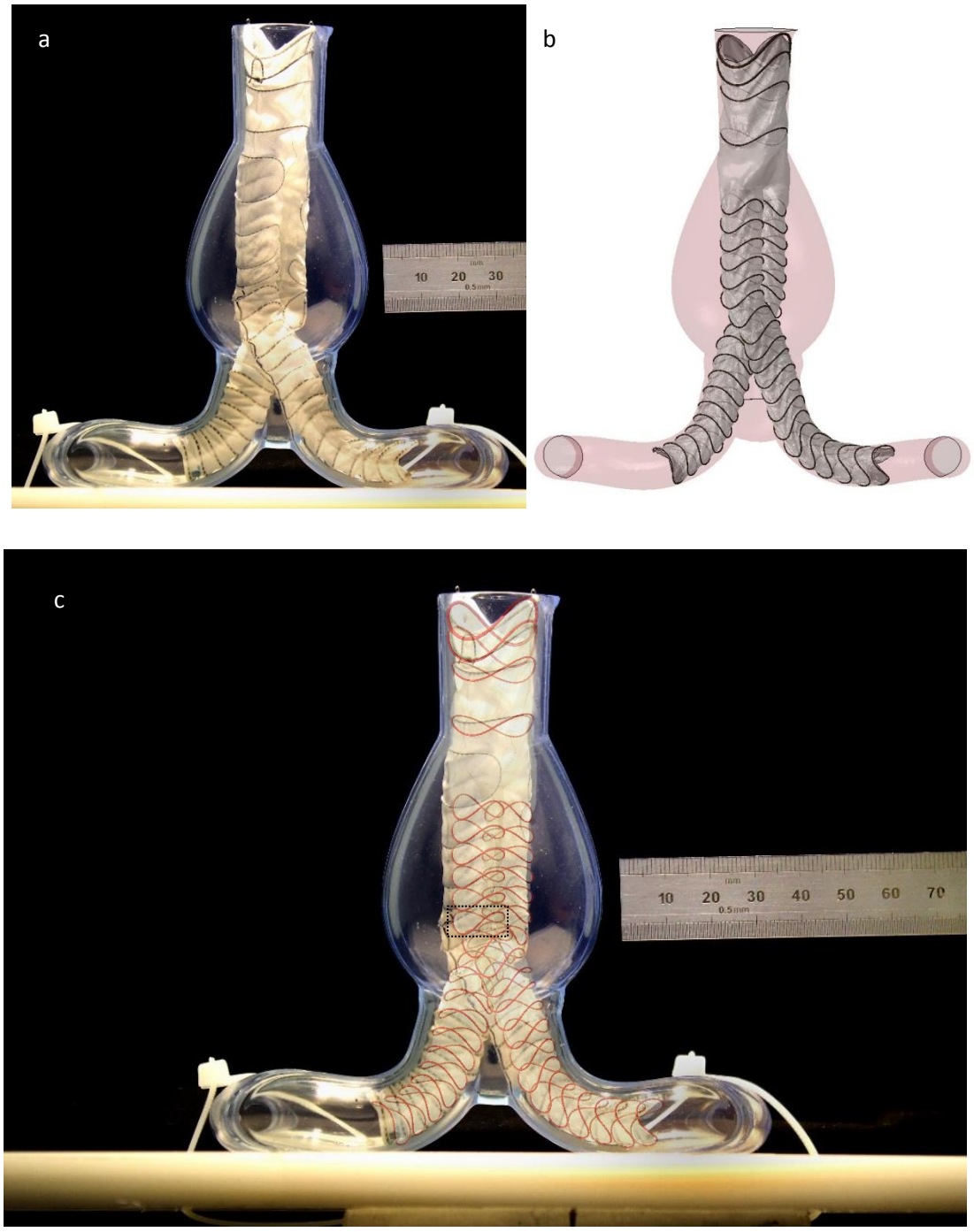

Fig. 5.11 The Anaconda™ device experimentally (a) and virtually (b) deployed inside the mock artery. At the superposition (c), the FEA rings are highlighted in red. Back view.

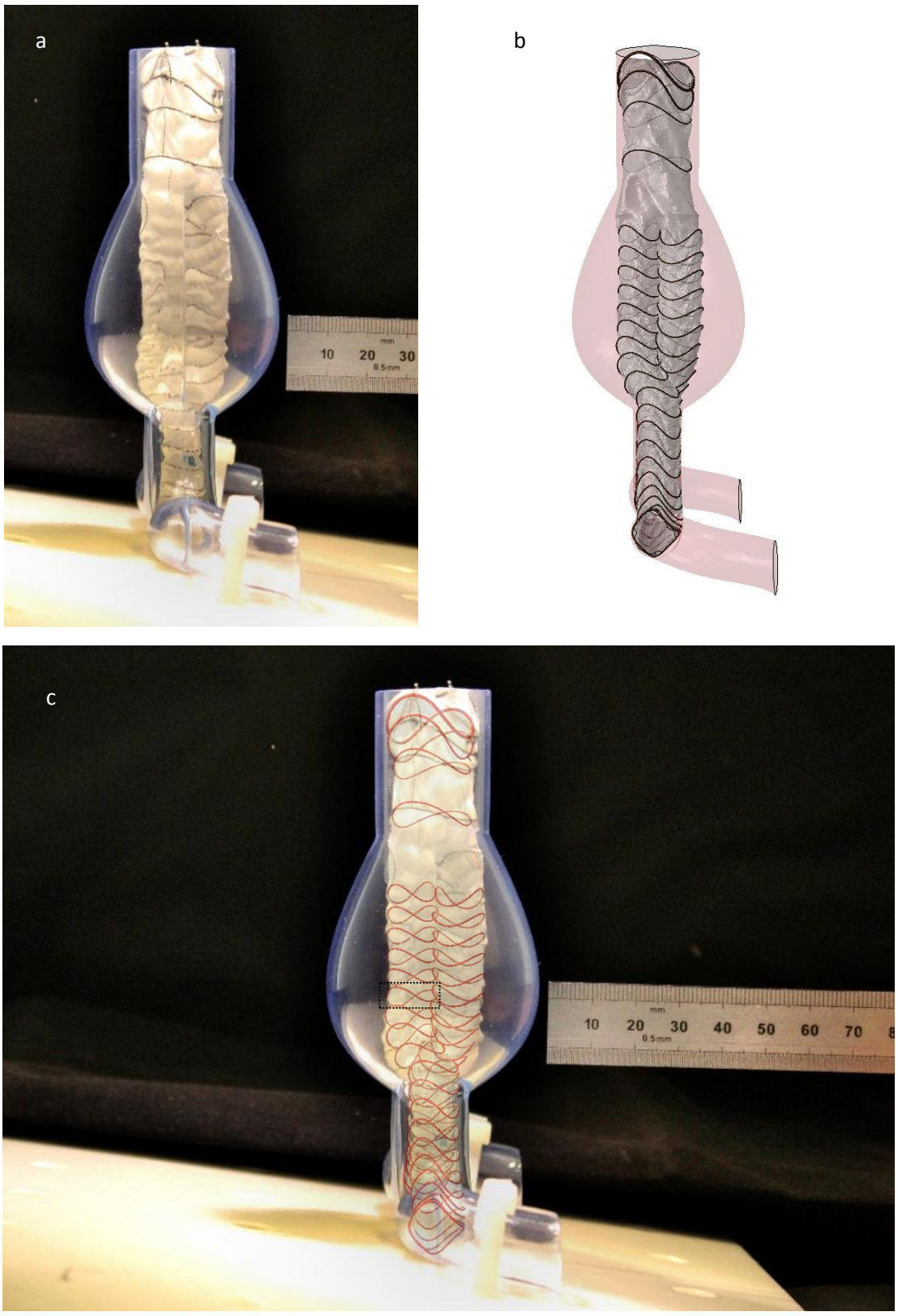

Fig. 5.12 The Anaconda™ device experimentally (a) and virtually (b) deployed inside the mock artery. At the superposition (c), the FEA rings are highlighted in red. Right view.

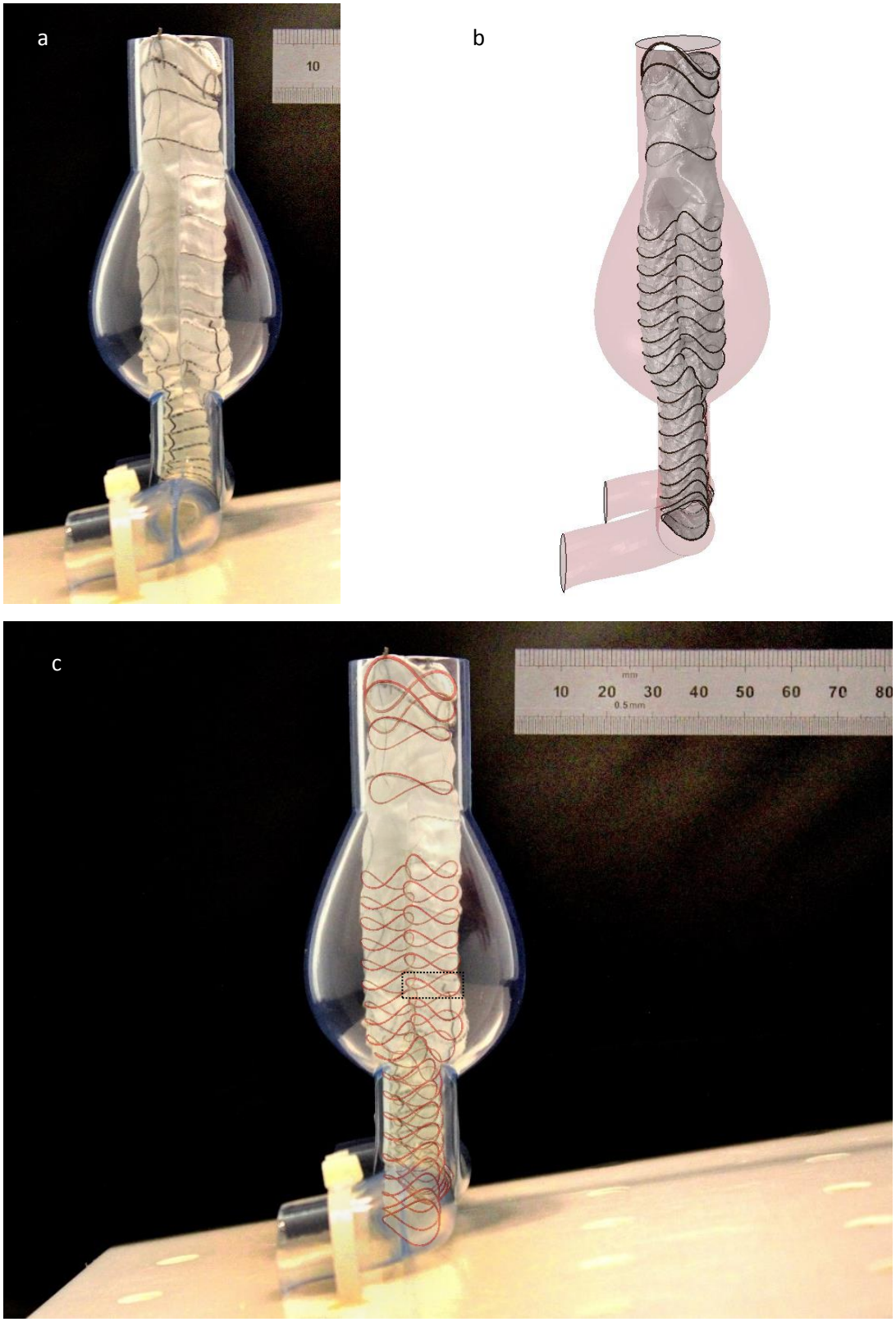

Fig. 5.13 The Anaconda™ device experimentally (a) and virtually (b) deployed inside the mock artery. At the superposition (c), the FEA rings are highlighted in red. Left view.

The maximum error for the FEA model is defined as the maximum 3D distance between the experimentally deployed and the virtually deployed rings and can be calculated from the superimposing images above. Since the pictures are taken from 2 perpendicular planes, the 3D distance between any two locations can be expressed as $L = \sqrt{a^2 + b^2 + c^2}$, with a, b, c being the components of this distance at the x, y and z direction. The a, b, c values can be easily identified in the figures for the areas with the greatest discrepancy.

This analysis showed that the maximum error was located at the anterior peak of the 6th ring of the left iliac leg (the black box in Fig. 5.10 – 13 c highlights the ring). The 3D distance between the FEA peak and the experimental one was identified to be 12.6 mm.

It was generally observed that the aneurysmal region was the area of greatest errors. This comes as no surprise. In reality, during delivery, endografts follow the path of least resistance and not the one described by the centrelines of the vessel. This has obvious implications in the deployed position of the device, and in more tortuous aneurysms will generate even higher errors. Yet because in the aneurysmal region endografts are less restricted, they experience low angulations, hence the accurate prediction of this section is less important from a mechanical point of view.

The discrepancies produced at the high contact regions were much lower. The last ring of the right-side iliac leg was chosen as a representative case of a high error ring in the non-aneurysmal site and the 3D distance between the FEA peaks and the experimental ones was measured to be 3.4 mm. This value is well below the 5 mm threshold that has been set as target for the accuracy. It is interesting to note that part of this error corresponds to the inability of the model to capture the rotation along the longitudinal direction of each module. For example, the FL1213x110 iliac leg twists along its length as can be seen in Fig. 5.11. This is most probably the result of unsheathing and cannot be replicated by the FEA model.

Regarding the behaviour of the fabric, folds have been reproduced. The accuracy of them is not quantified but it can be seen that in most cases, folds tend to occur in the same regions for both the experiment and the simulation. Furthermore,

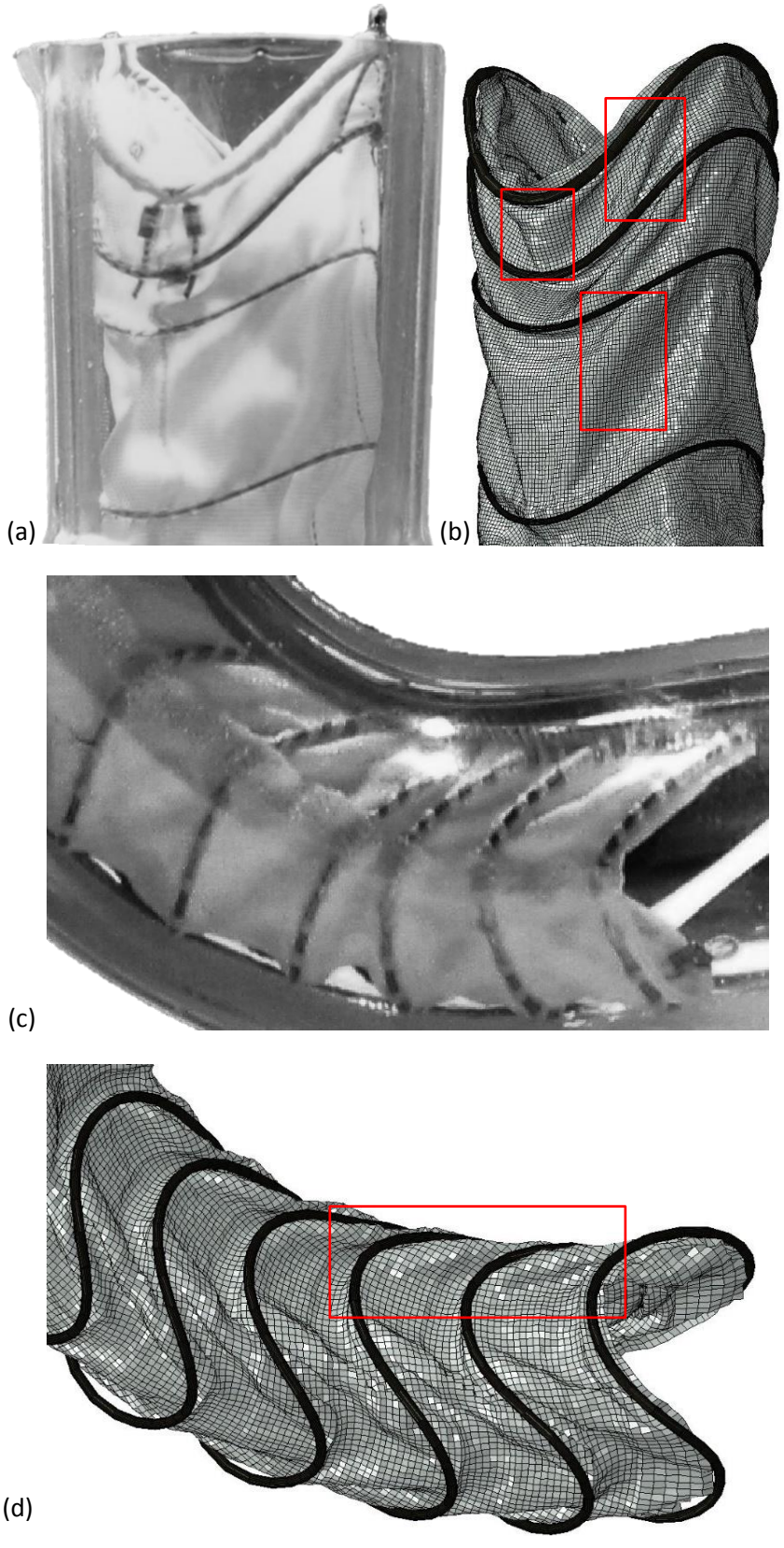

Fig. 5.14 Detail of the proximal (a & b) and distal (c & d) regions of the endograft. The fabric folds are visible both for the body and the left-side iliac leg modules while the highlighted regions are well predicted regions of high wrinkling. In (c) & (d) the axial twist mismatch is also visible.

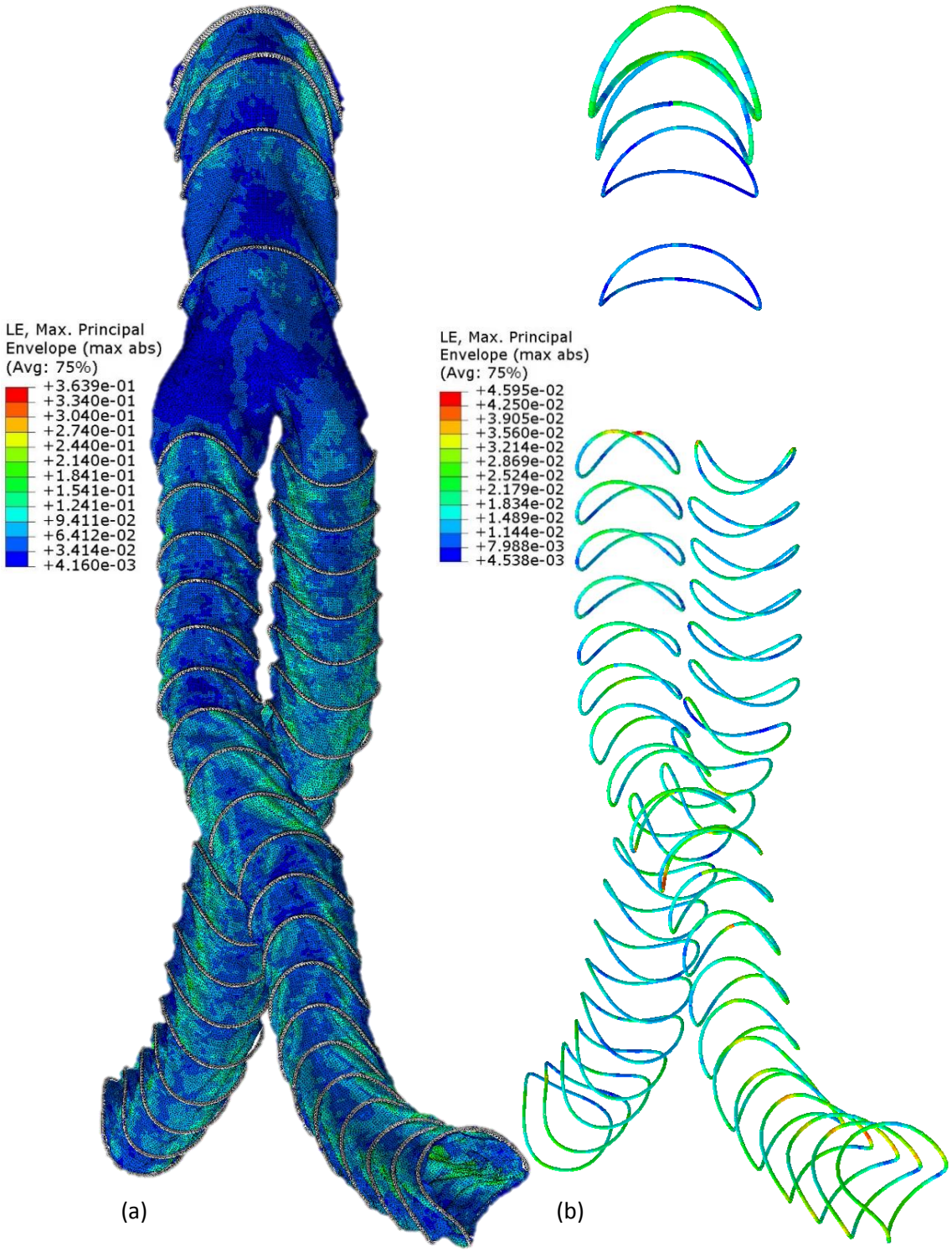

Fig. 5.15 Maximum principle strain of the fabric (a) and of the equivalent wire rings (b). Because of the simplifications followed, the magnitudes are not accurate, however strain distribution can highlight the areas that have the highest risk of failure.

intense wrinkles that can affect flow have been modelled correctly as can be seen in the highlighted areas of Fig. 5.14.

In general, the simulated locations of greatest interest (proximal and distal regions of the endograft) demonstrate good agreement with the experimental regions, while the macroscopic shape of the flow lumen has been accurately captured for the entire length of the device.

For completeness, the strains developed in the model are also reported (Fig. 5.15). It has already been discussed that the simplifications adopted do not allow for the accurate prediction of strains; nevertheless, strain distribution can still be of value, as it may be able to highlight the areas that need special attention due to an increased risk of failure. These areas could be examined more closely, later on, using the Ring Model developed in Chapter 4.

This analysis illustrates that the Full Device Model can deliver a valuable approximation of the deployed position of the Anaconda^{TM} device in a quick time frame. The analysis cannot serve as a robust validation as more cases would be necessary for that, yet the capabilities of the developed algorithm are evident and the cost effectiveness quantifiable.

5.4 CFD: proof of concept

As already mentioned, the simulation of a full device deployment can serve as an initial stage towards a hemodynamic analysis. And although the current body of work is not focused on such a study, it is very tempting to use the model in a CFD simulation, as a proof of concept.

Herein a CFD analysis is attempted in order to capture the effect graft wrinkles have on the flow field. To achieve that, the analysis presented on the previous section (5.3.2) was repeated and after the endograft deployment, the fabric was pressurized at $P_m = 12.44\ kPa$. The deformed graft geometry was exported from Abaqus and introduced to a series of software for smoothening and preparation.

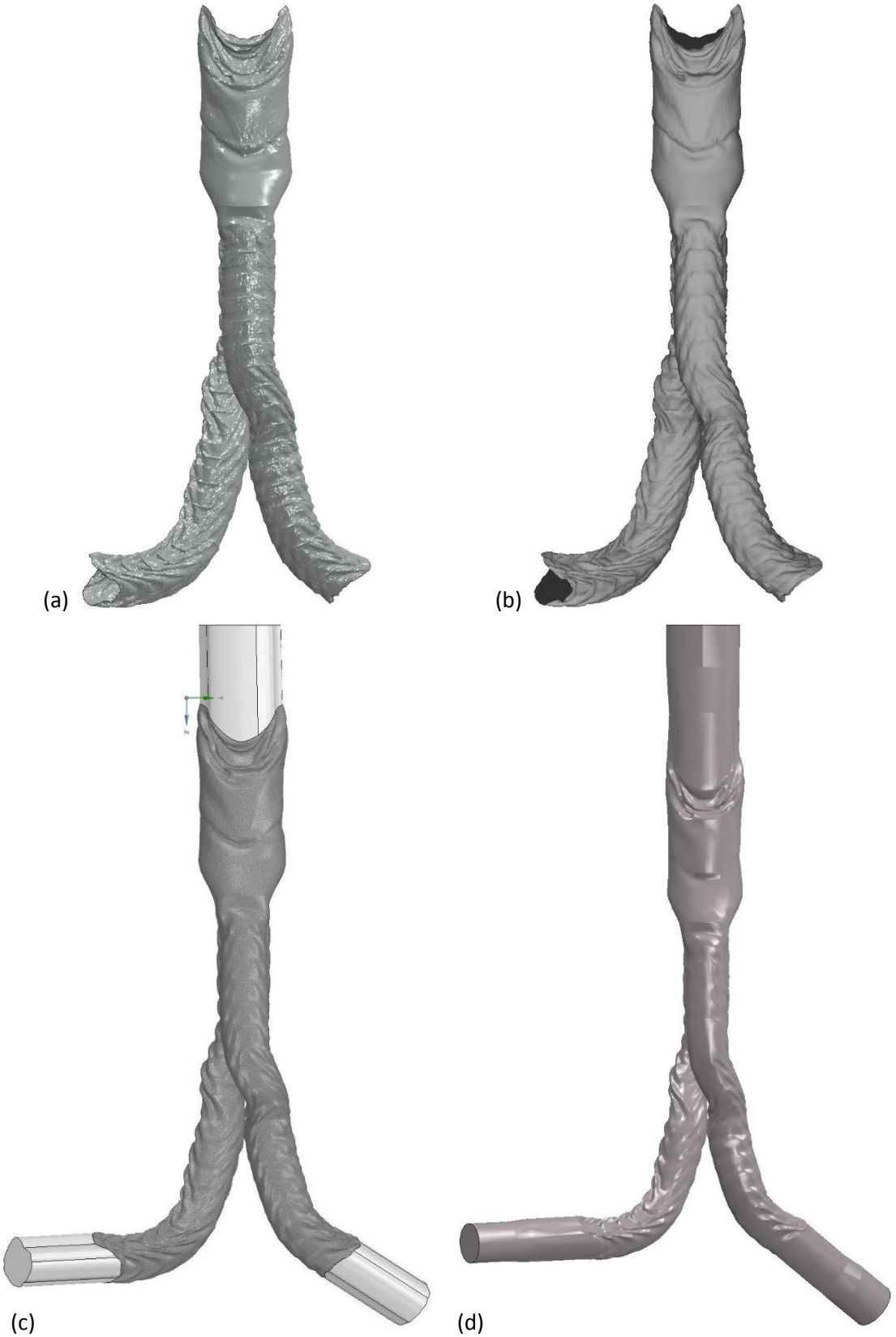

Fig. 5.16 The deformed fabric geometry exported as an FEA result (a), smoothened (b), attached to straight tubes (c) and reintroduced to Abaqus for CFD analysis (d).

Following the technique developed by Maclean (Terumo Aortic), the exported geometry (Fig. 5.16 a) was introduced to the open-source mesh processing software MeshLab for mesh simplification and smoothing (Fig. 5.16 b). Subsequently, the geometry was introduced into Materialise 3matic (Materialise NV, Leuven, Belgium) where an inwards offset of 0.2 mm was applied to the fabric to resolve small penetrations existing at the crossing of the legs while straight tubes were connected to the inlet and outlets to improve the boundary condition implementation (Fig. 5.16 c). Finally, the structures were merged together and re-introduced into Abaqus for the CFD analysis (Fig. 5.16 d).

The flow was assumed to be incompressible and the blood non-Newtonian with density ρ = 1060 kg/m^3 and dynamic viscosity described by the Carreau-Yasuda model:

$$\mu = \mu_\infty + (\mu_0 - \mu_\infty)[1 + (\lambda\dot{\gamma})^{0.64}]^{\frac{n-1}{2}} \tag{5.10}$$

where $\dot{\gamma}$ denotes the scalar shear rate. The shear viscosity at low shear rates, μ_0 = 0.16, the shear viscosity at large shear rates, μ_∞ = 0.0035 and material coefficients λ and n were equal to 8.2 s and 0.2128 respectively, following common values found in the literature [105,106].

For the analysis, 3 cardiac cycles were simulated for pulse cycle independency with a parabolic velocity inlet (flowrate = 2.5 L/min for 60 bpm) and pressure outlet (83 – 122 mmHg) that followed the waveforms of Fig. 5.17. These conditions represent only one scenario of the possible boundary conditions present in the human aorta. Additionally, a no slip condition was applied at the walls. 7 million 4-node linear

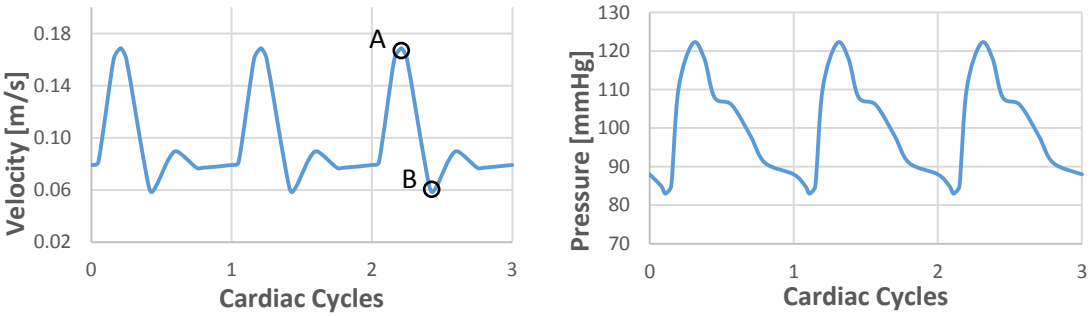

Fig. 5.17 The velocity (left) and pressure (right) waveforms as implemented in the inlet and outlet of the aneurysm respectively. The black marks refer to time-points of output.

tetrahedron (FC3D4) elements were used for the simulation and the analysis time was 12 hours on the same computing set-up as the one used in the previous section.

Results for the velocity field, the vorticity and the time averaged wall shear stress (TAWSS) were computed because of their medical importance. Particularly the last two variables have been linked to ILT formation [198,199], an unwanted phenomenon, especially when developed in the narrow regions of the endograft (i.e. the iliac legs). Note that TAWSS is defined as the integral of the magnitude of wall shear stress, $\overrightarrow{\tau_W}$, over one (herein the 3rd) cardiac cycle T:

$$\text{TAWSS} = \frac{1}{T}\int_0^T |\overrightarrow{\tau_W}| dt \tag{5.11}$$

and was calculated using the trapezoid rule of integration. For the rest of the variables, output was retrieved at the moment of the maximum or minimum inlet velocity of the 3rd cardiac cycle (encircled points A and B of Fig. 5.17, respectively).

Examining the velocity field output macroscopically, the result appears unaffected by the existence of fabric wrinkles (Video 5.2), while the overall flow looks smooth, perhaps because endograft devices with crossed legs might promote a favourable hemodynamic effect [105,200]. The peak velocity appears at the iliac legs, as reported in previous studies as well [201].

When closely examining the folds though, the effect of the wrinkles becomes evident. Especially in large folds, the velocity of the blood decreases dramatically leading to areas of almost stagnant flow even when the inlet flowrate maximizes (Fig. 5.18 c). Moreover, when the velocity of the inlet reaches its minimum, flow recirculation occurs (Fig. 5.18 d). A similar behaviour can be observed in smaller fabric folds too, yet the effect is less strong.

When investigating the TAWSS and the vorticity, the impact of the folds also becomes evident (Fig. 5.19). The pattern of both variables closely matches the pattern of the fabric's creases, highlighting the effect these geometrical characteristics might have in the drag forces developed in the endograft and as a consequence, in its ability to resist migration. In addition, the areas of low TAWSS should be closely monitored as they are prone to thrombus formation.

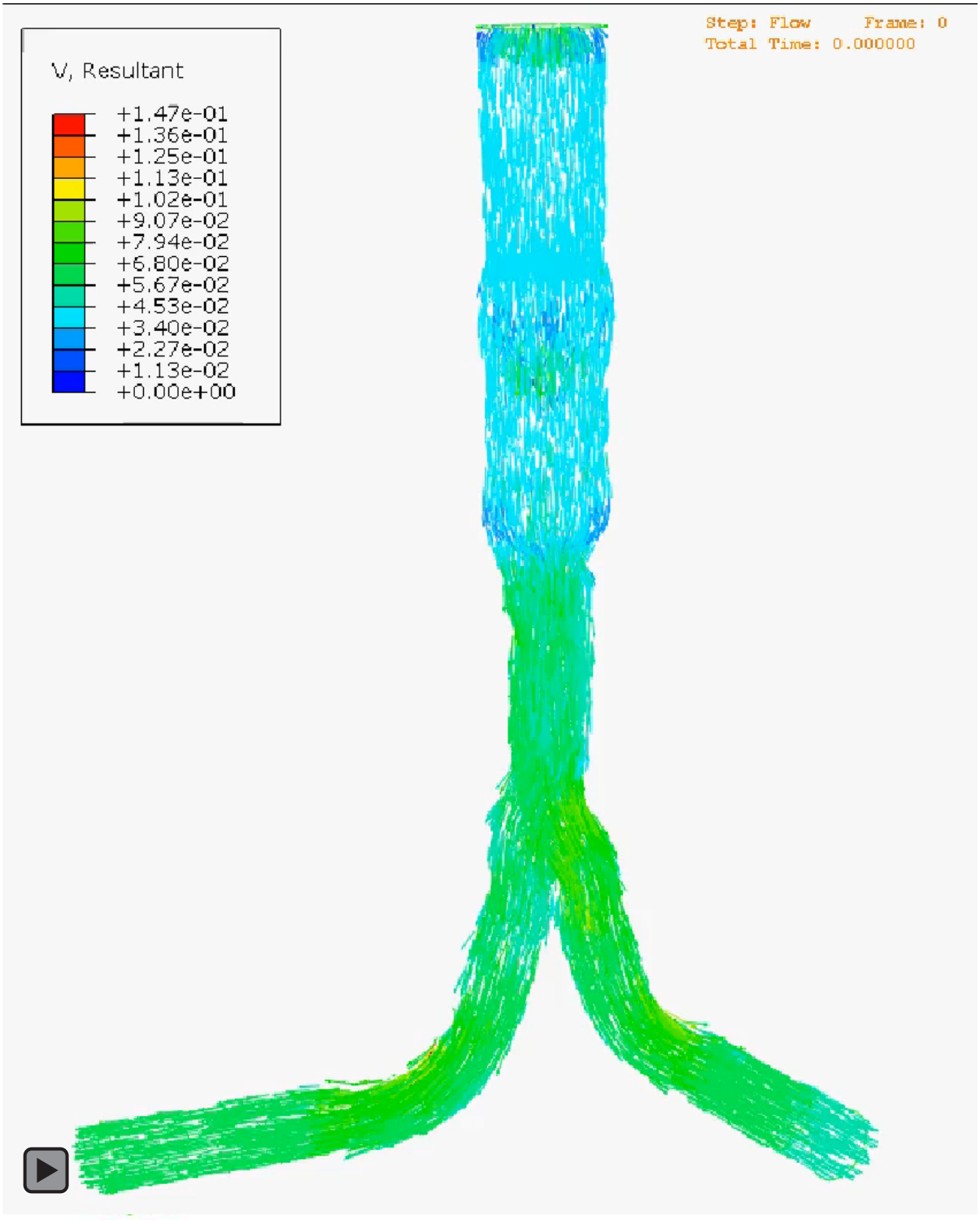

Video 5.2 The velocity field during all 3 cardiac cycles (in m/s). For the video, refer to the pdf version.

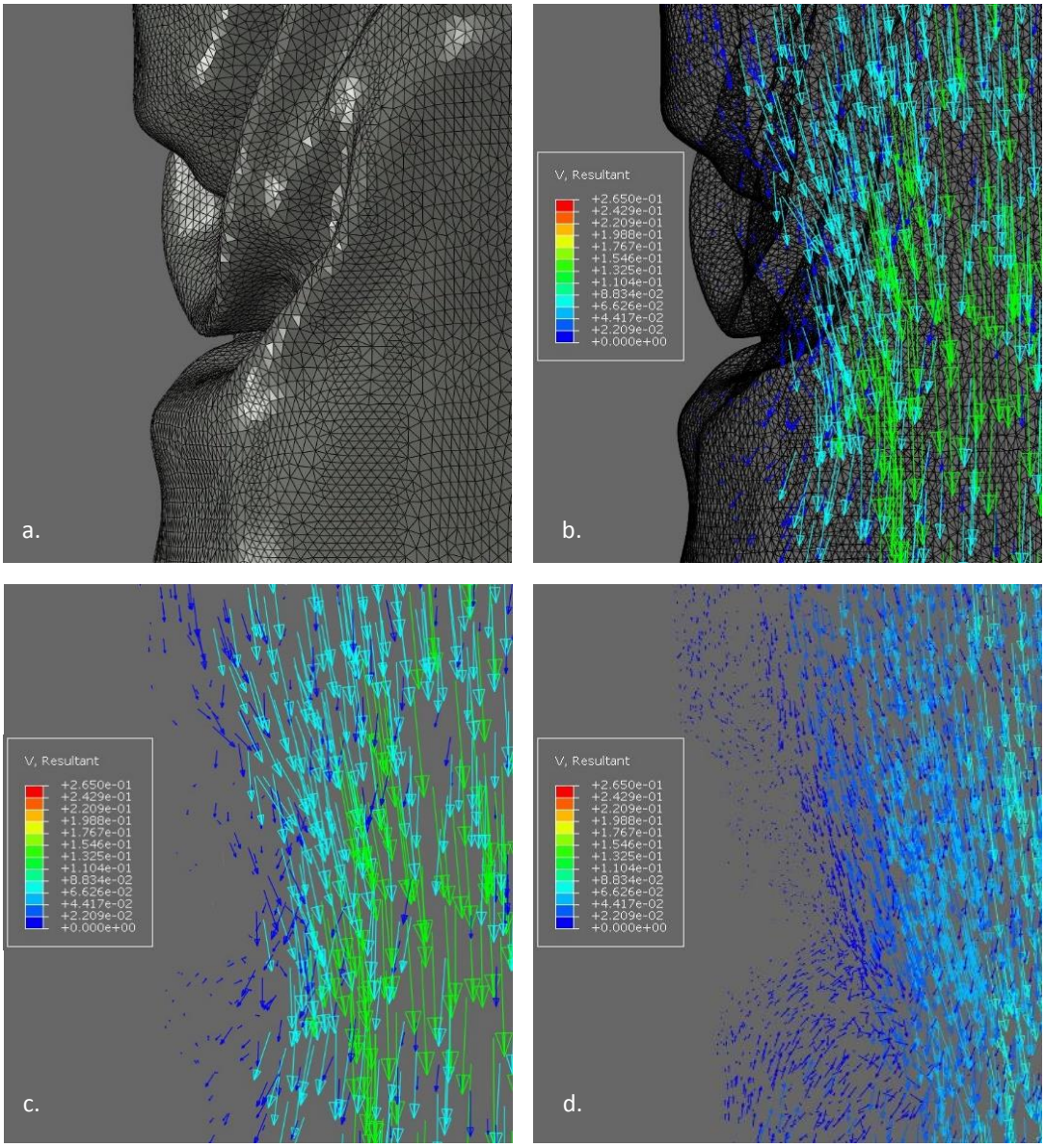

Fig. 5.18 Detail of the fabric folding between the 2nd and 3rd proximal ring of the endograft. The mesh (a), the mesh with the velocity vectors superimposed at time point A (b) and the velocity vectors at time point A (c) and point B (d) are visualized. Recirculation can be observed at the bottom left part of image d. Unit is m/s.

In summary, the inclusion of fabric folds has been shown to affect the hemodynamic fields of the stented AAA with the major wrinkles posing threats to the success of EVAR by disturbing the flow pattern and causing low wall shear stresses that can result in thrombus formation and occlusion. As it is apparent, only a high fidelity geometrical model of the deployed endograft has the ability to capture these effects. As a result, the capability of the developed model to be used for such meticulous CFD

analyses highlights its strengths and merits while it also concludes the final objective of the thesis.

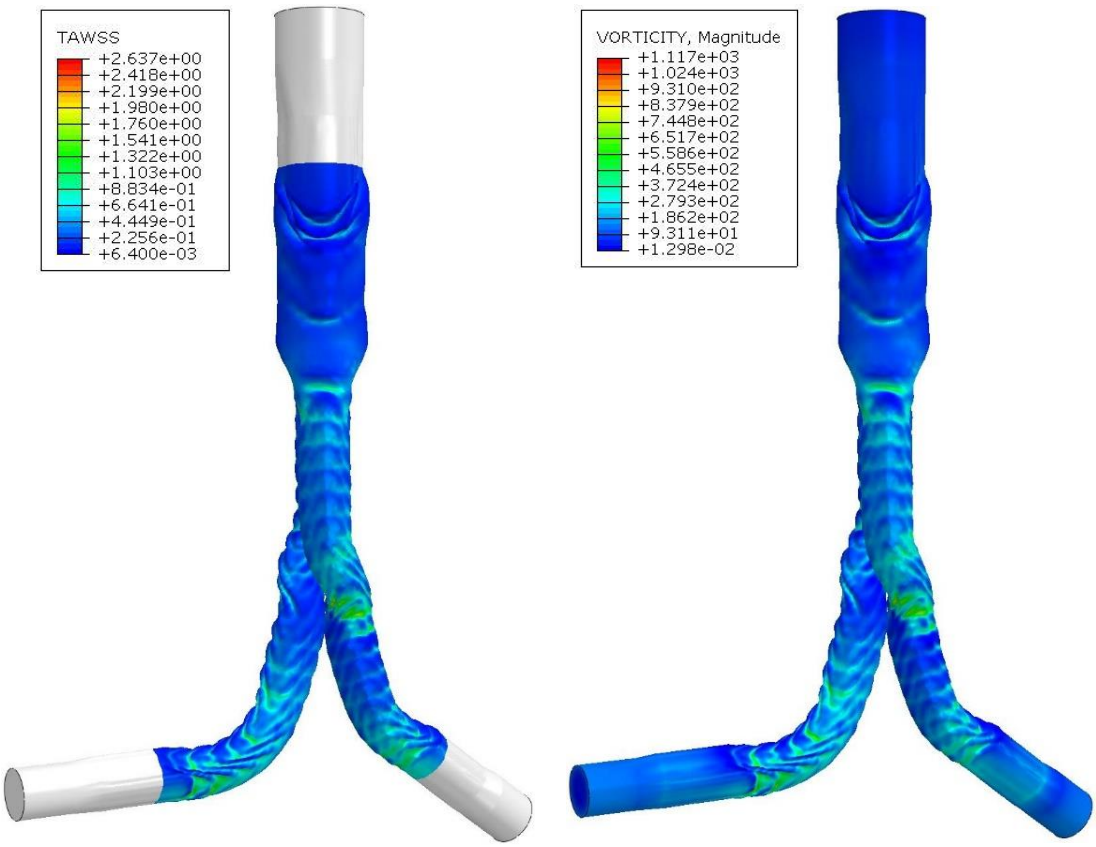

(a) (b)

Fig. 5.19 The TAWSS (a) and the vorticity (b) at time point A (units are Pa and s^{-1} respectively), as developed on the boundary layer of the fabric.

5.5 Discussion and summary

A computationally efficient Anaconda™ model was set as a goal of most importance in the current body of work. The aim was to develop the numerical framework for full device deployment into patient specific geometries, able to predict the post-op position of the stent graft as well as allow its output to be used for hemodynamic analyses. Such a model can be a powerful tool in EVAR planning and assessment as well as endograft development and patient-specific designing.

Driven by the severe geometrical and contact non-linearities of the problem, the explicit solver of Abaqus was utilized. In that framework, the 'equivalent beam' approach was used to model the scaffolding of the device without the inclusion of the manufacturing process. To further favour the efficiency of the model, the graft was constructed with regions of excess fabric already embedded to its design; that way there was no need to perform the ring/fabric tying on a straight graft tube followed by an equilibrium step that would prolong the analysis, as demonstrated in other approaches [195]. The appropriate size of the excess fabric areas was shown to be easily calculated from experimental measurements and these measurements were conducted in a series of fabric tests that can feed both the Ring Model and the Full Device Model. Finally, the graft design incorporated all three endograft modules into one, omitting the computational cost of the interaction between the different parts of the device.

Following the endograft construction, delivery and deployment of it needed to be addressed. The relevant strategies that can be found in the literature range from simple stent deployment inside straight vessels [70,84] up to excessively pressurizing curved vessels to a point where they can host originally-straight stent devices [83], and from moving stents along a guidewire [90] up to using thick, rigid vessel centrelines as quasi-guidewires to follow [163]. Yet herein, a different approach was chosen due to its computational efficiency and robustness when dealing with complicated vessel geometries.

As already mentioned in other works [165,179], a catheter can be used to move a stent graft inside a vessel and capture its curvature faithfully. The strategy developed here involves 3 sets of catheters, one for each stent module, which can be prescribed the appropriate boundary conditions so as to follow the aortic centrelines. One cylinder of each set is responsible for the delivery and one for the deployment of every stent part. With this delivery technique, there is no need to follow analytical curves as other studies have suggested (e.g. [92] used circular arcs to approximate the vascular shape). As a result, the endograft can faithfully follow the path of the

aorta and subsequently be deployed inside the artery in a quick and automatic manner, no matter its geometry.

The next challenge identified was the prescription of boundary conditions in the deployed endograft configuration and it was addressed with the creation of reference points linked to every saddle of the model. These entities, in conjunction with the peaks and valleys of each ring, allow the use of different coordinate systems that adequately describe both the pre and post deployment stent graft orientations.

In order for the model to be validated, a transparent mock artery was 3D printed and a full stent device was deployed inside it. The aortic wall was chosen to be rigid so as to minimize the impact of the material model of the vessel into the analysis. The experiment was then reproduced numerically with a shell vessel that had the same surface as the inner surface of the printed aneurysm and the difference between the two deployments was used as a metric of the simulation error.

Superimposed visualization of the experimental photos and simulation is usually used only for a qualitative assessment (see for example [110,179]), yet herein measurements were taken in different image planes to determine the error. The maximum 3D distance between the FEA and the experimental device was 12.6 mm yet the average error was significantly lower. Because of the technique followed, the precise identification of the mean error is impossible, yet the calculation of specific rings in the non-aneurysmal region showed that the error is much less than the 5 mm threshold.

The Anaconda^{TM} deployment performed by Perrin et al. [195] demonstrated similar accuracy. For comparative reasons, only the errors of the *in vitro* case of their study is considered here, since this case was the one involving a rigid AAA. In that study, the FEA result was registered to the scanned post-deployment endograft geometry and the registration matrix of the simulated device allowed the calculation of the position error vector. That way the distance between the predicted place of each ring and the actual post-deployment position of it were computed. Although the metric could not take into account differences at the axial angle of deployment or the tilt of the plane of deployment, it could measure the longitudinal position error along

the axial direction of each stent and the transverse position error, normal to that. Results showed that the maximum longitudinal error for the rigid phantom case was 11 mm whereas for the transverse direction the maximum error was over 7 mm. Furthermore, the normalized diameter error for each stent was also computed and found to be 35% at the most. In this analysis, like the one presented herein, the average error of the rings was much smaller, generally below 5 mm.

Since the act of stent deployment (even in lab conditions) is not highly repeatable, all models will generate some errors when compared to post-op images. Taking into account that even in simple bending tests, the positional error of stents can reach 4.0 mm [202], one can better appreciate the technical difficulties involved to create an accurate FEA prediction of EVAR.

Equally challenging is to obtain valuable numerical results in a computationally efficient manner. The virtual deployment of FE stents in the literature is reported to take tens of hours making the runtime a significant restriction in design development and patient-specific assessment. Herein, the runtime was significantly reduced with the wall-clock time being slightly over 4 hours in a 12 cpu computer.

The key reasons for the cost effectiveness of the developed model can be summarized below:

1. Effective fabric design that allows for a quick ring/graft tie
2. Efficient 'equivalent beam' approach
3. Quick and robust delivery technique
4. The 3 endograft modules are modelled as one, hence different part interactions and appropriate assembly during the analysis are omitted

Despite the merits described, the model has still some significant challenges to overcome. More specifically, in the deployed set-up, some stent rings did not come in full contact with the vessel, meaning that their deployment was not perfect. The reason might be related to the graft material model which does not represent the real graft as well as the contact conditions between the various shell surfaces (bundles, fabric, catheters, AAA) which are not the most realistic in contact interactions.

The contact between the rings and the fabric was also challenged in some regions (see Fig. 5.14 d), probably, once again, because of the element formulations. In general, 4 node shell elements (fabric and catheters), 4 node surface elements (bundles) and 4 node rigid shell elements (vessel) are not the most suitable for contact definitions, hence the efficiency they provide comes at a price.

Adding to the fabric challenges, the sharp curvature changes of the fabric definition are slightly evident at the deployed configuration as well (Fig. 5.20), causing an unwanted effect; once again, the fabric material should ideally be improved while the addition of a fillet could smoothen the sharp edge transitions.

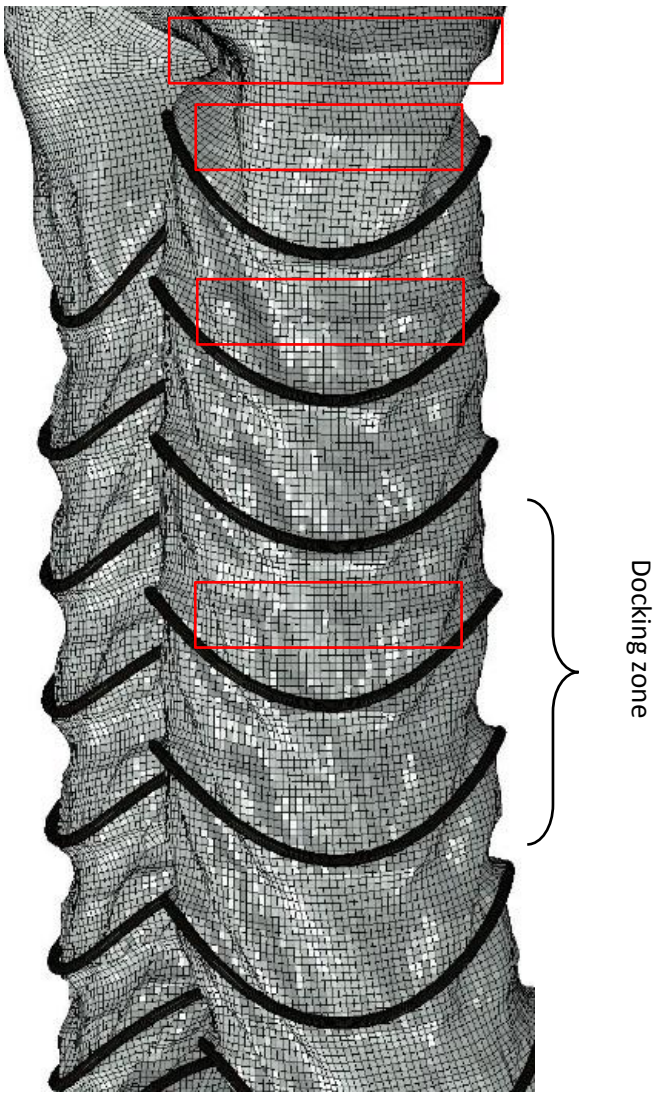

Fig. 5.20 The edges of the original graft design are visible in the deformed configuration (red boxes).

Lastly, the rings of the leg modules that correspond to the docking zone of the Anaconda™ body should be less deployed (Fig. 5.20) replicating the reduced diameter of the region. In the post-processing of the analysis it became evident that the Axial Connectors used for the purpose could not act as intended. Ideally, the connectors should be activated after compaction (similar to the strategy used in the Ring Model), yet the absence of the 'Model Change' option does not allow for that. As a result, connectors were defined with non-linear elasticity to allow for an easy compaction and stiff deployment beyond the docking diameter, yet the results were not satisfactory.

These insights can further guide the development of the framework. Nevertheless, the overall behaviour of the simulation showed that, even in its current state, the model can be used as a preliminary EVAR predictive tool especially for the non-aneurysmal regions, the overall shape of the flow lumen and the existence of major fabric folds that would impede the flow.

To more thoroughly validate the model, more AAA geometry cases should be considered. Ideally, sharp rigid vascular corners (like the ones that were present at the iliacs) should be avoided and micro-CT scanning could be employed. Furthermore, the study of simpler geometries like the deployment of iliac leg modules into simple curve tubes could better illustrate the effect of fabric and could also prove useful for more accurate Axial Connector definitions for the Ring Model. Herein, it was observed that the deployed shape of the device was primarily affected by the fabric geometry (e.g. length of the curved sections of the graft) and the assigned displacement $L_{unstheath}$ during compaction. Finally, it was confirmed that changes in the material of the rings did not lead to any significant variations in the shape of the device, as it was initially hypothesized.

Further to the structural analysis, it was successfully demonstrated that the output of the FEA simulation can be used as input for a CFD investigation. Unfortunately, buckling and kinking incidents are not rare for endograft devices [203], especially in tortuous arteries [166]. Such events can result in flow disturbances, throm-

bosis and eventually to ischemia [204], jeopardizing the health and life of EVAR patients. As a result, the in-depth understanding of the consequences the deployed shape of the stent graft has to the hemodynamic is crucial, yet not trivial to acquire.

Herein, the capability of the developed model to address such questions was presented, with a proof-of-concept implementation of the high fidelity fabric geometry into a blood flow study. It was observed that the fabric fold pattern significantly affects the wall shear stress and the vorticity pattern, while major graft wrinkles were shown to result in flow disturbances, stagnant areas and recirculation. These effects imply that the inclusion of a realistic fabric shape into a hemodynamic analysis could bring new insights into the EVAR prospects of success and eventually lead to improved endograft designs. Since the smooth-graft approximation cannot incorporate those clinically crucial characteristics, it is hoped that the current study will bring more attention to the topic and help for more realistic simulations to be conducted in the future.

Chapter 6

Summary and Conclusions

This thesis presents the development of advanced FEA techniques to simulate a ring stent graft device which can treat patient specific AAAs. Towards that goal, the patient specificness of the abdominal aortic aneurysms had first to be defined and explored. Subsequently, numerical models were developed to study the basic structural unit of the Anaconda^{TM} device as well as the full endograft.

The current Chapter concludes this body of work by providing a summary of all analyses conducted, by discussing the extent to which the thesis objectives were met, by reviewing the limitations present and by proposing future work.

6.1 Summary

The endovascular aneurysm repair treatment for AAAs is a fairly recent medical development that has seen great advancements in the last decades. Yet, the variety of shapes and sizes in which these aneurysms manifest themselves is vast. It is because of this that when a single device is available at a clinical centre, suitability rates of EVAR candidates drop dramatically, suggesting that there is no one device able to be used in all EVAR cases [47]. Furthermore, when devices are custom designed (like fenestrated devices are), they achieve greater contact with healthy artery and are less likely to migrate [25], hence offering better clinical outcomes. These observations, among others, point out the importance of the endograft design and the

benefits a patient could receive if custom devices were more regularly offered in clinical practice.

As a first step towards that end, the present body of work focused on the identification of the patient specific characteristics of the AAA. Dimensional and angular variables were recognized, measured and statistically analysed in a set of 258 patients. The detailed analysis of variations in the aneurysmal shape of AAA patients is important twofold. First, it allows researchers and stent graft manufacturers alike to establish the topological landscape under which medical devices have to operate in. This was the main drive for the current analysis as well. Furthermore, though, it can enhance our understanding of rupture. It has been argued that AAA wall stresses differ from patient to patient primarily due to differences in aneurysmal geometry and secondly due to differences in the aneurysmal material properties [78]. If that is the case, an elaborate yet universal aortic constitutive model combined with a detailed patient specific geometry might be the best way to assess AAAs' risk of rupture and perform FEA stent analysis.

With the boundary framework being set, a FEA model of a bundle ring was developed, able to capture the strains induced to the structure during manufacturing. The novel modelling approach presented allowed the Ring Model to successfully predict the radial forces and the strains developed in its structure while at the same time be computationally inexpensive. Furthermore, the development of an aortic model allowed the stent ring to be examined under various conditions and important conclusions were drawn regarding the oversizing, the friction coefficient between the stent and the vessel and the cross section of the aneurysmal neck.

Lastly, a Full Device Model was generated and compared against an experimental deployment into a 3D printed AAA. The model was able to predict the positional outcome of the EVAR-like set-up in a mock artery. Significant modelling challenges needed to be overcome for such an analysis, yet the model produced errors similar to the ones reported in the literature while it demands an order of magnitude less runtime than its equivalent counterparts. Furthermore, the use of such a model need not be limited to EVAR positional predictions. More specifically, the utilization

of it in CFD analyses can be of great value. As demonstrated in a hemodynamic investigation, a more detailed flow study can be accomplished by taking into account the fabric folds, revealing small scale disturbances that cannot be predicted following the generally used approximation of a smooth graft boundary.

All the Abaqus models presented herein are the result of scripts written in python. Since these codes lie at the core or the thesis, these scripts, along with the in-house algorithms for the aortic angle and the aortic cross section calculations, will be submitted to Pure (pure.strath.ac.uk), Strathclyde's data repository, where they will be kept for at least 10 years after deposit. Nevertheless, access to some of them will be limited due to commercial sensitivity.

The codes are highly automated and require from the user a small amount of necessary inputs, generally limited to the geometrical specifications of the endograft to be simulated. The ease of using these scripts is aligned with the aim of the thesis to provide models that will be used for analysing endografts beyond the completion of the current body of work. The will to produce tools and results of value to the medical practice underlined most decisions taken in the current thesis. It is highly hoped that this was achieved.

6.2 Conclusions

Given the attention AAAs have received in the literature, it is surprizing that no rigorous shape studies have been conducted to document and understand their morphology. To ameliorate the need, the present thesis has proposed a framework under which the angulation of the abdominal aortic tree can be recorded.

By analysing the shape of 258 AAA patients, 10 angles were identified as crucial to describe the geometry of a given aneurysm. Measurements of these angles in the patient dataset allowed the identification of their median and extreme values in different planes. These results allow the characterization of a given aneurysm from representative all the way to worst case for any region of interest driving forward stent design modelling and in the future, maybe, clinical decisions. The absence of

correlation between most of these angles suggest that an investigator is free to construct any extreme aortic geometry case study with the values reported herein in a mix and match manner.

The angular analysis was accompanied by the identification of 9 dimensional variables also significant (and much more commonly examined) for the description of the aortic geometry. If both sets of variables are used, then a given AAA can be described in much detail. Statistical analysis showed that no dimensional variable follows the normal distribution. Furthermore, a positive correlation between age and tortuosity was observed, as well as an absence of connection between age and size of the aneurysm. Gender differences were also identified in the aneurysmal neck.

To the author's knowledge, for the first time a rigorous examination of the cross section of the aortic neck was conducted. Using two different metrics for the perimeter of the intima, the commonly accepted circularity assumption was challenged. The analysis showed that although the median average ellipticity doesn't lie far from a circle, aneurysmal necks with very elliptical cross sections do exist. And since no correlation was found between the circularity metrics and the other variables examined, it is implied that separate attention needs to be taken for the cross sectional geometry of the aortic neck when assessing EVAR suitability and stenting outcomes.

This extended analysis successfully addressed one of the key goals of the thesis, namely to describe and quantify patient specificness. At the same time, valuable knowledge for stent designing was attained via the documentation of the range of geometric variables.

A 2009 study reported that when it comes to an elective AAA operation, patients are over six times more likely to prefer EVAR over open aortic surgery [205]. Given the minimally invasive approach of the former, this should come as no surprise. Yet the failure of EVAR to produce better long-term results than open surgery is an alarming fact for the engineering world that needs to produce more reliable endografts.

FEA can assist this effort either by improving the endograft characteristics in general or by allowing tailor-made stent graft devices to be built on a patient-to-patient basis. Such personalized models are powerful since they can help design endografts that are optimized for the boundary conditions of the host vessel. As a result, the main goal of the thesis was to provide those tools necessary to increase the suitability of EVAR and decrease the complications that come along with it. What that meant is that robust, realistic and computationally efficient models needed to be developed. This target was met in a very satisfactory level.

A rarely modelled stent design was simulated with a novel finite element approach using beam and surface elements, accompanied with experimental validation. A saddle-pull test confirmed that the structural response of the bundle model is realistic while a comparison with a higher fidelity continuum FEA model showed that the prediction of strains is also reliable. Furthermore, the importance of manufacturing pre-strains was establish by demonstrating that exclusion of them quadruples the error of the simulation from a maximum of 7% to over 26%.

Moreover, it was shown that the ratio of stent oversizing does not significantly affect the COF exerted from the rings, given that the friction coefficient between the stent and the vessel is low. As a result, the importance of oversizing is closely linked to the stent/vessel interaction. For example, calcified necks could possibly be more sensitive to oversize than healthy ones are, since they provide a rougher interface. In any case, more experimental tests regarding the Nitinol/artery interface are needed.

Following the cross section analysis of the aneurysmal neck, the effect different clinical approximations have on the ring bundle were examined. The major axis approximation of the perimeter was found to underestimate the maximum strain by up to 51% and the total radial force by 14%. On the other hand, the minor axis approximation overestimated the maximum strain by up to 64% and the total radial force by up to 6%. Contrary to that, the rarely (if at all) used approximation of the average circle produced a much better estimation of the maximum strain and underestimated the chronic outward force by just 3.2% when compared to the respective

elliptical shapes. As a result, the average circle should be preferred as a cross section descriptor.

Apart from its reliability and utilization for the acquisition of useful insights, the Ring Model developed was also shown to be cost effective. The solution time for all cases that involved ring deployments and cycling through systole and diastole was a few hours, making it viable for design studies. The high fidelity continuum model that was used for a comparative analysis needed anywhere from 7 to 23 times more runtime to produce results.

Although the present study was specific to a particular stent design, the modelling technique developed can be used in a straightforward way to similarly designed medical devices like Thoraflex^{TM} Hybrid (Terumo Aortic) or other engineering applications regarding slender structures under large deflections and/or demanding contact interactions. It should be mentioned that the Thoraflex^{TM} Hybrid in particular, was considered during both the mesh convergence study (Section 4.2.2) and the Saddle pull test validation (Section 4.2.4) where apart from the relevant Anaconda^{TM} rings, larger Thoraflex^{TM} rings were also used since they share the same technology.

The thesis has also produced a 6th order Yeoh model able to replicate the pressure-radius behaviour of the healthy abdominal aorta. This model was used throughout this body of work and proved very suitable for ring stent analyses as it can simulate the *in vivo* boundary conditions of a deployed ring, particularly in the healthy neck region. Since the model was validated against P-R data, it is one of the very few models available in the literature that can credibly help with stent graft assessment.

Further to the Ring Model, a Full Device Model was developed. This work met the objective of a complete device model that is able to predict the deployed shape and position of the endograft post-EVAR. The Full Device Model can be run for different geometries, deployment conditions or stent's initial placement and draw helpful conclusions for stent graft manufacturers and surgeons alike. Among other reasons, it can be used to examine challenging arterial topographies, understand the conditions under which stent-vessel contact is compromised and illuminate the effect of fabric wrinkles in the creation of thrombus, leading to design improvements and

clearer rules of dos and don'ts during EVAR. Furthermore, simulations could be run after surgery in a patient specific manner and given post-op images, manage to recreate the exact stent deployment present in the treated person. This can allow tailor made analysis of an implanted endograft leading to personalized alerts. If the deployed stent is prone to migration or flow disturbances, medical treatment can be adjusted accordingly.

The model developed herein was compared to an experimentally deployed Anaconda^{TM} device and managed to capture a challenging, crossed-leg deployment. The maximum error of the simulation was identified to be 12.6 mm, yet the average error in the non-aneurysmal region was significantly smaller, well below the 5 mm threshold of clinical acceptance. Most importantly, the model achieved great computational efficiency providing results in a bit more than 4 hours, making it an order of magnitude faster than respective models in the literature. Furthermore, both the Full Device and the Ring Model require a small amount of user inputs, irrespective of the challenging deliveries that might be required to achieve. That way, the produced tool from this thesis is a user friendly code that can be set-up for any new case study in just a few hours.

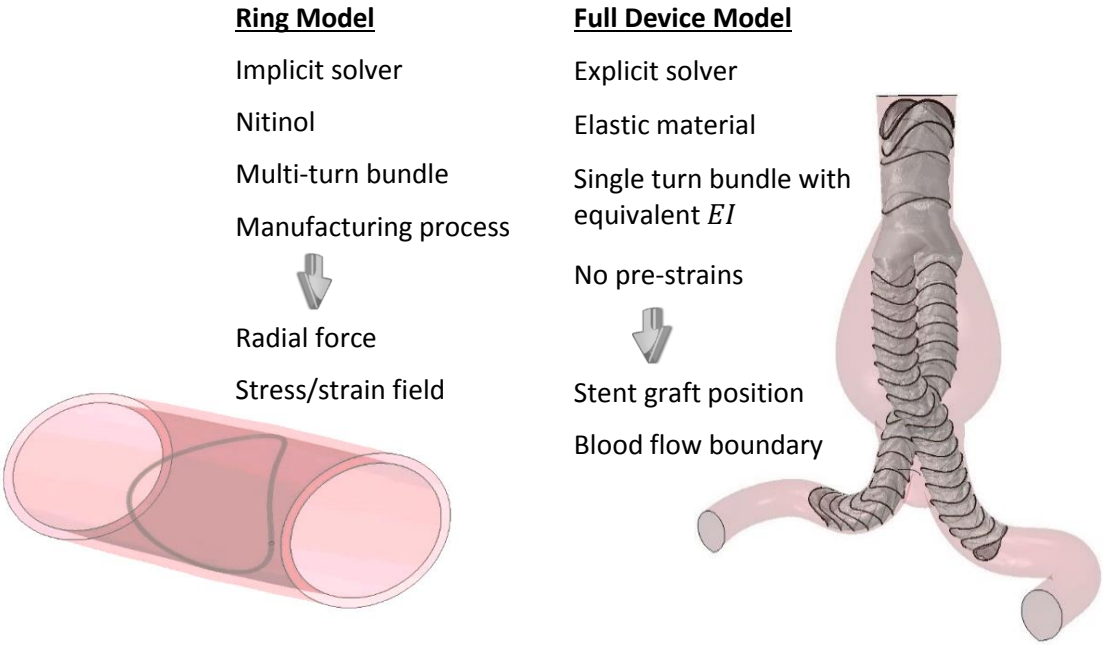

Fig. 6.1 The two stent graft models developed in the thesis.

As a last remark, it should be once again suggested that the Ring Model presented in Chapter 4 should be used for parametric studies or fatigue life analyses of 1 ring (or small scaffolding sections, once the Axial Connectors are validated) because of its accuracy, while the Full Device Model developed in Chapter 5 should be utilized to capture the global characteristics of EVAR, such as endograft positioning or fabric shape. Fig. 6.1 provides a graphical outline of these models.

Concluding this section, the following list can be compiled outlining the key deliverables from the thesis:

- A matrix, $\boldsymbol{\Phi}$, was established to describe the patient's aortic shape
- Representative and worst case AAA geometries were identified
- AAAs can be created for case studies in a mix and match (angle) manner
- Cross sections of the AAA neck can diverge from circularity and need to be examined case-by-case
- Mean aortic diameter approximation should be used for the AAA neck in EVAR simulations
- The $M\varepsilon$ of the ring is strongly affected by oversize, yet COF is mainly influenced by the friction of the vessel/bundle interface
- The inclusion of fabric folds allows a more insightful CFD study

The thesis also delivered:

- a phenomenological model that recreates the P-R response of the aorta
- the most computationally efficient Anaconda™ ring model that can capture the mechanical characteristics of the bundle, to date
- the most computationally efficient full Anaconda™ model that can predict the deployed endograft positioning, to date

These outcomes address the original objectives set out at the end of Chapter 2: the patient specific variability was established and a geometrical framework that

can help endograft advancements in future studies was developed; in addition, realistic yet computationally efficient stent models were created allowing for the mechanical evaluation of the stent rings, the prediction of the post-op shape of the device and the ability of the model to allow highly detailed CFD analyses. And all that for any target geometry, which is to say, for any patient specific host vessel.

6.3 Limitations

The work presented could not have been conducted if a series of approximations and simplifications were not followed.

Regarding the vascular model, it was assumed that the wall was homogeneous and isotropic with constant thickness, while neither thrombus nor calcification were included. These assumptions are commonly made in the literature due to uncertainties and variability of the human tissue as well as on the grounds of efficiency. Moreover, despite the fact that the abdominal aorta is connected to the thoracic aorta and the iliac arteries while at the same time stays in contact with the surrounding tissue and organs, these structures were not considered.

Regarding the Ring Model, it is reminded that plasticity was not included in the Nitinol definition. Nevertheless, the results presented here do not suffer from this simplification since no case study experienced strains at the plasticity strain range (9-10%). It is mentioned, though, that experimental results have shown that some rings do enter plasticity when fully compacted, since permanent deformations are visible when retrieving the ring and unwinding the wire. If such ring configurations are of interest, the Nitinol model should be updated.

Furthermore, as discussed in Section 4.2.5, the overlapping of the Nitinol turns does not allow the identification of differences along the width of the bundle, a limitation that could be important in $\Delta\varepsilon$ analysis. Moreover, the circular shape of the bundle can only grossly approximate the cross section of the bundle ring. If detailed contact conditions between the rings and the vessel are of interest (e.g. for

direct endoleak assessment or accurate description of the contact pressure field on the vascular wall) then this approximation might have significant implications.

Regarding the Full Device Model, the most significant developing constraint was the lack of the 'Model Change' option in Abaqus/Explicit, the technique that would allow a variety of important featured to be turned on and off during the analysis according to the demands of the simulation. This unavailability did not allow for the correct stress/strain Nitinol state to be included and affected the docking zone of the endograft as well. Furthermore, the omission of an appropriate constitutive model for the fabric material may have negatively affected the virtual deployment of the device, creating higher discrepancies from the experiment.

Although some initial work was conducted with the inclusion of the hooks, their complex boundary restrictions made some simulations unstable, leading to the decision to exclude them from most analyses and only somewhat recreate their axial mechanical effect. The metallic supports at the distal part of the body module as well as the sutures were also excluded from the analysis in the basis of efficiency and unnecessary fidelity.

One aspect of the work that has not been highlighted enough is the occurrence of numerous instabilities encountered during the development of the models. Stability issues were present for almost the entire duration of the code development either because of the significant non-linearities of the problem or because of the Nitinol implementation in Abaqus, especially when used in conjunction with beam elements. Unfortunately, Abaqus was found to have some unstable behaviours (bugs?) that given its "black box" solver cannot be thoroughly examined. As a result, from the main aim of creating a robust, realistic and computationally efficient stent model, robustness is currently the most challenging characteristic. Although most models work without problems, every so often some geometry proves to be a challenge and small manipulations are needed.

These limitations, along with opportunities identified during the development of the thesis, drive the future work proposed below.

6.4 Future Work

For an in-depth assessment of the AAA geometry, the study of angles presented in Section 3.1.2 should be repeated for healthy individuals as well as for the general AAA population (i.e. not only for those treated with EVAR) so as to comprehensively reveal the extent of change the aortic tree undergoes in the presence of the aneurysm. Ideally, the same should also happen for the cross section study conducted in Section 3.1.4.

For the Ring Model, the inclusion of plasticity in the Nitinol model should be a priority, particularly if cases of more extreme strains are to be simulated. Furthermore, the cross section of the bundle could remain a shell surface yet with a non-circular shape. Depending on the number of turns per ring, an adequate boundary perimeter could be drawn according to the circle packing theory's optimal configuration. This shell could better approximate the shape of the bundle.

Regarding the Full Device Model, the use of fillet at the sharp curvature changes of the fabric definition would allow for a more realistic graft behaviour. More importantly though, a comprehensive study of the fabric material properties should be conducted and the material in use should be updated. In addition, the separate validation of the graft model and the conduction of experiments on small-length endograft sections would allow an in-depth understanding of the way the scaffolding and the fabric interact; towards that end, the examination of iliac legs in simply curved vascular sections could serve as a helpful set-up. Detailed examination of the ring-to-ring interactions could also help the fine-tuning of the Axial Connectors used in Section 4.5 and progress the reliable scaling of the Ring Model. From a similar analysis, hook connectors could be finely adjusted as well.

Regarding the full device validation, an AAA geometry that will allow a smooth experimental deployment should be preferred. Furthermore, the model should be tested in a deformable vessel as well, where the endograft will experience a more realistic equilibrium. Later on, since the radial forces due to blood pressure from the inner side of the device are partially counteracted by the aortic wall and the aneurys-

mal sac pressure from the outside, the inclusion of more structural components (stagnant blood, thrombus etc.) will allow the model to be assessed against real EVAR cases.

The use of the Full Device Model in CFD analyses should also be a priority. Section 5.4 illustrated the capability of the model to be used in hemodynamic investigations, yet the use of it in a great range of aortic angulations and different fabric slack case studies can provide a deeper understanding of the EVAR procedure and its complications. Such a potential should be utilized.

Once the 'Model Change' option becomes available in Abaqus/Explicit, new possibilities will arise. As already mentioned, improved cross connector definition in the docking zone of the endograft will be feasible and easy to implement. Yet the prospects are far more exciting. With the 'Model Change' option applicable, the manufacturing strains will be able to be captured and as a result, modelling of both Nitinol and multiple turns will be meaningful. In that set-up, all the advantages of Abaqus/Standard will be applicable on the Full Device Model of Abaqus/Explicit, practically leading to the merging of the two models. Note, though, that this would significantly increase the computational cost of the simulation while the full compaction of the endograft might be a challenge because of excessive fabric element warping. Despite this, a model as such is worth perusing as it would be able to deliver all important information in a – all things considered – cost effective framework. As a result, there could be a time where a patient's CTA scans, along with their age, gender and blood pressure, could serve as the geometry, the material and the boundary conditions respectively for personalized FEA EVAR simulations. By calculating the radial forces, the strains and post-op shape and position of the endograft, a model like that could suggest a treatment course to reduce migration, endoleaks and occlusions altogether.

Abaqus also offers a feature of predefining a stress/strain state field. This allows the user to import to the simulation a deformed geometry from another simulation and assign to it the stress/strain state it acquired during its original deformation. This feature, though, is not currently available for beam elements. Once

Abaqus supports this option, all the endograft modules (all the sizes of bodies and iliac legs) could be simulated up to compaction; then, with every new AAA geometry, these pre-run models could be imported to the patient-specific geometry further reducing the solution time cost, since only half the analysis would be necessary (that is, for the delivery and the deployment of the endograft).

Looking into further developing the simulations, a FSI model could be built around the Full Device Model. In such a case, the vascular material model should be updated and ideally take into account viscoelasticity which might alter the frequency response of the aortic wall [139]. A model like this will be able to provide the most holistic evaluation of an AAA patient and assist in crucial medical decisions.

An integrated FEA tool for developing, assessing and virtually deploying the Anaconda^{TM} stent graft in patient specific AAAs will someday, hopefully, be part of the ordinary clinical routine. This thesis has tried to identify and tackle some of the major challenges towards that future. With an improved endograft technology and an enhanced understanding of the challenges associated with the AAA fixation, an extra step was taken on the road to better healthcare. Thanks to this and every other research effort on the field, EVAR suitability will be further increased while the associated complications will be decreased. Thanks to every research effort, lives will be saved.

References

1. Humphrey JD. Cardiovascular Solid Mechanics; Cells, Tissues, and Organs. 1st ed. Springer-Verlag New York; 2002. 758 p.

2. Khan S, Verma V, Verma S, Polzer S, Jha S. Assessing the potential risk of rupture of abdominal aortic aneurysms. Clin Radiol [Internet]. 2015;70(1):11–20. Available from: http://dx.doi.org/10.1016/j.crad.2014.09.016

3. Wanhainen A. How to define an abdominal aortic aneurysm--influence on epidemiology and clinical practice. Scand J Surg. 2008;97:105–9.

4. Johnston KW, Rutherford RB, Tilson MD, Shah DM, Hollier L, Stanley JC. Suggested standards for reporting on arterial aneurysms. J Vasc Surg. 1991;13:452–458.

5. Giannoglou G, Giannakoulas G, Soulis J, Chatzizisis Y, Perdikides T, Melas N, et al. Predicting the Risk of Rupture of Abdominal Aortic Aneurysms by Utilizing Various Geometrical Parameters: Revisiting the Diameter Criterion. Angiology [Internet]. 2006;57(4):487–94. Available from: http://ang.sagepub.com/content/57/4/487.abstract%5Cnhttp://ang.sagepub.com/content/57/4/487.full.pdf%5Cnhttp://ang.sagepub.com/content/57/4/487.short

6. Steinberg CR, Archer M, Steinberg I. Measurement of the abdominal aorta after intravenous aortography in health and arteriosclerotic peripheral vascular disease. Am J Roentgenol [Internet]. 1965 Nov 1;95(3):703–8. Available from: http://www.ajronline.org/doi/abs/10.2214/ajr.95.3.703

7. Lo RC, Lu B, Fokkema MTM, Conrad M, Patel VI, Fillinger M, et al. Relative importance of aneurysm diameter and body size for predicting abdominal aortic aneurysm rupture in men and women. J Vasc Surg [Internet]. 2014 May;59(5):1209–16. Available from: http://www.sciencedirect.com/science/article/pii/S0741521413020259

8. Laughlin GA, Allison MA, Jensky NE, Aboyans V, Wong ND, Detrano R, et al. Abdominal Aortic Diameter and Vascular Atherosclerosis: The Multi-Ethnic Study of Atherosclerosis. Eur J Vasc Endovasc Surg [Internet]. 2011 Apr;41(4):481–7. Available from: http://www.sciencedirect.com/science/article/pii/S1078588410007884

9. Länne T, Sonesson B, Bergqvist D, Bengtsson H, Gustafsson D. Diameter and compliance in the male human abdominal aorta: Influence of age and aortic aneurysm. Eur J Vasc Surg [Internet]. 1992;6(2):178–84. Available from: http://www.sciencedirect.com/science/article/pii/S0950821X05802373

10. Fillinger MF, Racusin J, Baker RK, Cronenwett JL, Teutelink A, Schermerhorn ML, et al. Anatomic characteristics of ruptured abdominal aortic aneurysm on conventional CT scans: Implications for rupture risk. J Vasc Surg. 2004;39(6):1243–52.

11. Joh JH, Ahn H, Park H. Reference Diameters of the Abdominal Aorta and Iliac Arteries in the Korean Population. 2013;54(1):48–54.

12. Nicholls SC, Gardner JB, Meissner MH, Johansen KH. Rupture in small abdominal aortic aneurysms. J Vasc Surg [Internet]. 1998 Nov;28(5):884–8. Available from: http://www.sciencedirect.com/science/article/pii/S0741521498700655

13. Brewster DC, Cronenwett JL, Hallett Jr JW, Johnston KW, Krupski WC, Matsumura JS. Guidelines for the treatment of abdominal aortic aneurysms: Report of a subcommittee of the Joint Council of the American Association for Vascular Surgery and Society for Vascular

Surgery. J Vasc Surg [Internet]. 2003 May;37(5):1106–17. Available from: http://www.sciencedirect.com/science/article/pii/S074152140300421X

14. Ryan R. Davies, MD, Amy Gallo, MD, Michael A. Coady, MD, MPH, George Tellides, MD, PhD, Donald M. Botta, MD, Brendan Burke, BS, Marcus P. Coe, BA, Gary S. Kopf, MD, and John A. Elefteriades M. Novel Measurement of Relative Aortic Size Predicts Rupture of Thoracic Aortic Aneurysms. Ann Thorac Surg. 2006;

15. Wever JJ, Blankensteijn JD, Th. M. Mali WP, Eikelboom BC. Maximal Aneurysm Diameter Follow-up is Inadequate after Endovascular Abdominal Aortic Aneurysm Repair. Eur J Vasc Endovasc Surg [Internet]. 2000;20(2):177–82. Available from: http://www.sciencedirect.com/science/article/pii/S1078588499910511

16. Parr A, Jayaratne C, Buttner P, Golledge J. Comparison of volume and diameter measurement in assessing small abdominal aortic aneurysm expansion examined using computed tomographic angiography. Eur J Radiol [Internet]. 2011 Jul;79(1):42–7. Available from: http://www.sciencedirect.com/science/article/pii/S0720048X09006871

17. Vorp DA, Raghavan ML, Webster MW. Mechanical wall stress in abdominal aortic aneurysm: Influence of diameter and asymmetry. J Vasc Surg [Internet]. 1998;27(4):632–9. Available from: http://www.sciencedirect.com/science/article/pii/S0741521498702277

18. Elger DF, Blackketter DM, Budwig RS, Johansen KH. The Influence of Shape on the Stresses in Model Abdominal Aortic Aneurysms. J Biomech Eng [Internet]. 1996 Aug 1;118(3):326–32. Available from: http://dx.doi.org/10.1115/1.2796014

19. Pappu S, Dardik A, Tagare H, Gusberg RJ. Beyond Fusiform and Saccular: A Novel Quantitative Tortuosity Index May Help Classify Aneurysm Shape and Predict Aneurysm Rupture Potential. Ann Vasc Surg [Internet]. 2008 Jan;22(1):88–97. Available from: http://www.sciencedirect.com/science/article/pii/S0890509607003123

20. de Bruijne M, van Ginneken B, Viergever MA, Niessen WJ. Interactive segmentation of abdominal aortic aneurysms in CTA images. Med Image Anal. 2004;8(2):127–38.

21. Simão da Silva E, Rodrigues AJ, Magalhães Castro de Tolosa E, Rodrigues CJ, Villas Boas do Prado G, Nakamoto JC. Morphology and diameter of infrarenal aortic aneurysms: a prospective autopsy study. Cardiovasc Surg [Internet]. 2000 Dec;8(7):526–32. Available from: http://www.sciencedirect.com/science/article/pii/S0967210900000600

22. Adolph R, Vorp DA, Steed DL, Webster MW, Kameneva M V, Watkins SC. Cellular content and permeability of intraluminal thrombus in abdominal aortic aneurysm. J Vasc Surg [Internet]. 1997;25(5):916–26. Available from: https://doi.org/10.1016/S0741-5214(97)70223-4

23. Vorp DA, Lee PC, Wang DHJ, Makaroun MS, Nemoto EM, Ogawa S, et al. Association of intraluminal thrombus in abdominal aortic aneurysm with local hypoxia and wall weakening. J Vasc Surg [Internet]. 2001 Aug;34(2):291–9. Available from: http://www.sciencedirect.com/science/article/pii/S0741521401594288

24. Schurink GWH, van Baalen JM, Visser MJT, van Bockel JH. Thrombus within an aortic aneurysm does not reduce pressure on the aneurysmal wall. J Vasc Surg [Internet]. 2000;31(3):501–6. Available from: http://www.sciencedirect.com/science/article/pii/S0741521400903112

25. Corbett TJ, Callanan A, Morris LG, Doyle BJ, Grace P a, Kavanagh EG, et al. A review of the in vivo and in vitro biomechanical behavior and performance of postoperative abdominal aortic aneurysms and implanted stent-grafts. J Endovasc Ther. 2008;15:468–84.

26. Lindholt JS, Søgaard R, Laustsen J. Prognosis of ruptured abdominal aortic aneurysms in Denmark from 1994–2008. Clin Epidemiol. 2012 May;4:111–3.

27. Egelho CJ, Budwig RS, Elger DF, Khraishi TA, Johansen KH. Model studies of the flow in abdominal aortic aneurysms during resting and exercise conditions. J Biomech. 1999;32(1999):1319–29.

28. Li Z, Kleinstreuer C. Blood flow and structure interactions in a stented abdominal aortic aneurysm model. Med Eng Phys [Internet]. 2005;27(5):369–82. Available from: http://linkinghub.elsevier.com/retrieve/pii/S1350453305000032

29. Lee K, Johnson RK, Yin Y, Wahle A, Olszewski ME, Scholz TD, et al. Three-dimensional thrombus segmentation in abdominal aortic aneurysms using graph search based on a triangular mesh. Comput Biol Med [Internet]. 2010;40(3):271–8. Available from: http://dx.doi.org/10.1016/j.compbiomed.2009.12.002

30. Silverberg E, Lubera JA. Cancer statistics, 1987. CA Cancer J Clin [Internet]. 1987;37(1):2–19. Available from: http://www.ncbi.nlm.nih.gov/pubmed/3099992

31. National Records of Scotland. Vital Events Reference Tables 2016 [Internet]. 2016. Available from: https://www.nrscotland.gov.uk/statistics-and-data/statistics/statistics-by-theme/vital-events/general-publications/vital-events-reference-tables/2016/section-6-death-causes

32. Starr JE, Halpern V. Abdominal aortic aneurysms in women. J Vasc Surg [Internet]. 2013 Apr;57(4, Supplement):3S–10S. Available from: http://www.sciencedirect.com/science/article/pii/S0741521412023439

33. Tong J, Schrie AJ, Cohnert T, Holzapfel GA. Gender Differences in Biomechanical Properties, Thrombus Age, Mass Fraction and Clinical Factors of Abdominal Aortic Aneurysms. Eur J Vasc Endovasc Surg. 2013;45(4):364–72.

34. investigators I trial. Endovascular or open repair strategy for ruptured abdominal aortic aneurysm: 30 day outcomes from IMPROVE randomised trial. BMJ [Internet]. 2014;348. Available from: https://doi.org/10.1136/bmj.f7661

35. NHS England. NHS public health functions agreement 2016-17 [Internet]. 2016. Available from: https://www.england.nhs.uk/commissioning/wp-content/uploads/sites/12/2016/04/serv-spec-23-abdominal-aortic-aneurysm.pdf

36. Dotter C. Transluminally-placed coilspring endarterial tube grafts: long- term patency in canine popliteal artery. Invest Radiol. 1969;4:327–332.

37. Kim JH, Kang TJ, Yu WR. Mechanical modeling of self-expandable stent fabricated using braiding technology. J Biomech. 2008;41(15):3202–12.

38. Roguin A. Historical Perspectives in Cardiology; Stent: The Man and Word Behind the Coronary Metal Prosthesis. Circ Cardiovasc Interv. 2011;4:206–9.

39. Parodi JC, Palmaz JC, Barone HD. Transfemoral Intraluminal Graft Implantation for Abdominal Aortic Aneurysms. Ann Vasc Surg [Internet]. 1991;5(6):491–9. Available from: http://www.sciencedirect.com/science/article/pii/S0890509606615410

40. Dillavou ED, Muluk SC, Makaroun MS. Improving aneurysm-related outcomes: Nationwide benefits of endovascular repair. J Vasc Surg. 2006;43(3):446–52.

41. Sethi RK V, Henry AJ, Hevelone ND, Lipsitz SR, Belkin M, Nguyen LL. Impact of hospital market competition on endovascular aneurysm repair adoption and outcomes. J Vasc Surg.

2013;58(3):596–606.

42. Schermerhorn ML, O'Malley a. J, Jhaveri A, Cotterill P, Pomposelli F, Landon BE. Endovascular vs. Open Repair of Abdominal Aortic Aneurysms in the Medicare Population. N Engl J Med. 2008;358(5):464–74.

43. The United Kingdom EVAR Trial Investigators. Endovascular versus open repair of abdominal aortic aneurysm - Supplementary Appendix. N Engl J Med. 2010;362:1863–71.

44. Propper BW, Abularrage CJ. Long-term safety and efficacy of endovascular abdominal aortic aneurysm repair. Vasc Health Risk Manag. 2013 Apr;9:135–41.

45. Armon MP, Yusuf SW, Latief K, Whitaker SC, Gregson RH, Wenham PW, et al. Anatomical suitability of abdominal aortic aneurysms for endovascular repair. Br J Surg. 1997;84(2):178–80.

46. Bayle O, Branchereau A, Rosset E, Guillemot E, Beaurain P, Ferdani M, et al. Morphologic assessment of abdominal aortic aneurysms by spiral computed tomographic scanning. J Vasc Surg [Internet]. 1997 Aug;26(2):238–46. Available from: http://www.sciencedirect.com/science/article/pii/S0741521497701848

47. Carpenter JP, Baum RA, Barker CF, Golden MA, Mitchell ME, Velazquez OC, et al. Impact of exclusion criteria on patient selection for endovascular abdominal aortic aneurysm repair. J Vasc Surg. 2001;34(6):1050–4.

48. Elkouri S, Martelli E, Gloviczki P et al. Most patients with abdominal aortic aneurysm are not suitable for endovascular repair using currently approved bifurcated stent-grafts. Vasc Endovasc Surg. 2004;38(5):401–12.

49. Tomee SM, Bastiaannet E, Schermerhorn ML, Golledge J, Hamming JF, Lindeman JH. The Consequences of Real Life Practice of Early Abdominal Aortic Aneurysm Repair: A Cost-Benefit Analysis. Eur J Vasc Endovasc Surg. 2017;54(1):28–33.

50. Wolf YG, Fogarty TJ, Olcott IV C, Hill BB, Harris EJ, Mitchell RS, et al. Endovascular repair of abdominal aortic aneurysms: Eligibility rate and impact on the rate of open repair. J Vasc Surg [Internet]. 2000 Sep;32(3):519–23. Available from: http://www.sciencedirect.com/science/article/pii/S0741521400073602

51. Kristmundsson T, Sonesson B, Dias N, Malina M, Resch T. Anatomic suitability for endovascular repair of abdominal aortic aneurysms and possible benefits of low profile delivery systems. 2014;22(2):112–5.

52. Maleux G, Ph D, Koolen M, Heye S. Complications after endovascular aneurysm repair. Semin Intervent Radiol. 2009;26(1):3–9.

53. Grundmann R, editor. Diagnosis and Treatment of Abdominal and Thoracic Aortic Aneurysms Including the Ascending Aorta and the Aortic Arch. IntechOpen; 2011.

54. Raghavan ML, Kratzberg J a, Golzarian J. Introduction to biomechanics related to endovascular repair of abdominal aortic aneurysm. Tech Vasc Interv Radiol [Internet]. 2005;8(1):50–5. Available from: http://www.ncbi.nlm.nih.gov/pubmed/16098937

55. Sharif MA, Lee B, Lau LL, Ellis PK, Collins AJ, Blair PH, et al. Prosthetic stent graft infection after endovascular abdominal aortic aneurysm repair. J Vasc Surg [Internet]. 2007;46(3):442–8. Available from: http://www.sciencedirect.com/science/article/pii/S0741521407009457

56. Maleux G, Koolen M, Heye S, Nevelsteen A. Limb Occlusion after Endovascular Repair of

Abdominal Aortic Aneurysms with Supported Endografts. J Vasc Interv Radiol [Internet]. 2008;19(10):1409–12. Available from: http://www.sciencedirect.com/science/article/pii/S1051044308006441

57. Conners MS, Sternbergh WC, Carter G, Tonnessen BH, Yoselevitz M, Money SR. Endograft migration one to four years after endovascular abdominal aortic aneurysm repair with the AneuRx device: A cautionary note. J Vasc Surg. 2002;36(3):476–84.

58. Li Z, Kleinstreuer C. Analysis of biomechanical factors affecting stent-graft migration in an abdominal aortic aneurysm model. J Biomech [Internet]. 2006;39(12):2264–73. Available from: http://www.sciencedirect.com/science/article/pii/S0021929005003453

59. Zarins CK, Bloch DA, Crabtree T, Matsumoto AH, White RA, Fogarty TJ. Stent graft migration after endovascular aneurysm repair: importance of proximal fixation. J Vasc Surg [Internet]. 2003;38(6):1264–72. Available from: http://www.sciencedirect.com/science/article/pii/S0741521403009467

60. Najibi S, Steinberg J, Katzen BT, Zemel G, Lin PH, Weiss VJ, et al. Detection of isolated hook fractures 36 months after implantation of the Ancure endograft: A cautionary note. J Vasc Surg [Internet]. 2001;34(2):353–6. Available from: http://www.sciencedirect.com/science/article/pii/S0741521401140334

61. Jacobs TS, Won J, Gravereaux EC, Faries PL, Morrissey N, Teodorescu VJ, et al. Mechanical failure of prosthetic human implants: A 10-year experience with aortic stent graft devices. J Vasc Surg [Internet]. 2003;37(1):16–26. Available from: http://www.sciencedirect.com/science/article/pii/S0741521402751999

62. Katzen BT, MacLean AA. Complications of Endovascular Repair of Abdominal Aortic Aneurysms: A Review. Cardiovasc Intervent Radiol [Internet]. 2006 Dec;29(6):935–46. Available from: https://doi.org/10.1007/s00270-005-0191-0

63. Suzuki K, Ishiguchi T, Kawatsu S, Iwai H, Maruyama K, Ishigaki T. Dilatation of stent-grafts by luminal pressures: experimental evaluation of polytetrafluoroethylene (PTFE) and woven polyester grafts. Cardiovasc Intervent Radiol [Internet]. 2001;24(2):94–8. Available from: http://www.ncbi.nlm.nih.gov/pubmed/11443393

64. How T V, Fisher RK, Vallabhaneni SR, Chong CK. 8 - Vascular implants for peripheral arterial bypass and aortic aneurysm repair. In: Gourlay T, Black RA, editors. Biomaterials and Devices for the Circulatory System. Woodhead Publishing; 2010. p. 217–48. (Woodhead Publishing Series in Biomaterials).

65. Auricchio F, Taylor RL, Lubliner J. Shape-memory alloys: macromodelling and numerical simulations of the superelastic behavior. Comput Methods Appl Mech Eng [Internet]. 1997;146(3–4):281–312. Available from: http://www.sciencedirect.com/science/article/pii/S0045782596012327

66. Duerig TW, Tolomeo DE, Wholey M. An overview of superelastic stent design. Minim Invasive Ther Allied Technol. 2000;9(3–4):235–46.

67. Wadood A. Brief Overview on Nitinol as Biomaterial. Adv Mater Sci Eng [Internet]. 2016; Available from: http://dx.doi.org/10.1155/2016/4173138

68. Committee. ISO 25539-2:2012, Cardiovascular implants -- Endovascular devices -- Part 2: Vascular stents [Internet]. 2012. Available from: https://www.iso.org/standard/60604.html

69. Pelton a. R, Schroeder V, Mitchell MR, Gong XY, Barney M, Robertson SW. Fatigue and durability of Nitinol stents. J Mech Behav Biomed Mater. 2008;1(2):153–64.

70. Kleinstreuer C, Li Z, Basciano CA, Seelecke S, Farber MA. Computational mechanics of Nitinol stent grafts. J Biomech [Internet]. 2008;41(11):2370–8. Available from: http://linkinghub.elsevier.com/retrieve/pii/S0021929008002777

71. Duerig T, Pelton a, Stöckel D. An overview of nitinol medical applications. Mater Sci Eng A. 1999;273–275:149–60.

72. Ng KL, Sun QP. Stress-induced phase transformation and detwinning in NiTi polycrystalline shape memory alloy tubes. Mech Mater. 2006;38(1):41–56.

73. Gong X-Y, Pelton AR, Duerig TW, Rebelo N, Perry K. Finite Element Analysis and Experimental Evaluation of Superelastic Nitinol Stents. Proc SMST. 2003;

74. Tobushi H, Shimeno Y, Hachisuka T, Tanaka K. Influence of strain rate on superelastic properties of TiNi shape memory alloy. Mech Mater. 1998;30(2):141–50.

75. Qidwai MA, Lagoudas DC. Numerical implementation of a shape memory alloy thermomechanical constitutive model using return mapping algorithms. Int J Numer Methods Eng. 2000 Jan;47(6):1123–68.

76. Bow D. Mechanical Analysis and Simulation of the Nitinol Ring Stent: Assessing the Radial Strength, Fatigue and Compaction Strains. University of Strathclyde; 2018.

77. Boukis A. A comprehensive methodology for the experimental characterization and numerical modelling of nickel-titanium wires used in medical devices. PhD [dissertation]. University of Strathclyde; 2018.

78. Vorp DA. Biomechanics of abdominal aortic aneurysm. J Biomech. 2007;40(9):1887–902.

79. Raghavan ML, Webster MW, Vorp DA. Ex vivo biomechanical behavior of abdominal aortic aneurysm: Assessment using a new mathematical model. Ann Biomed Eng [Internet]. 1996;24(5):573–82. Available from: http://dx.doi.org/10.1007/BF02684226

80. VORP DA, RAGHAVAN ML, MULUK SC, MAKAROUN MS, STEED DL, SHAPIRO RON, et al. Wall Strength and Stiffness of Aneurysmal and Nonaneurysmal Abdominal Aorta. Ann N Y Acad Sci [Internet]. 1996;800(1):274–6. Available from: http://dx.doi.org/10.1111/j.1749-6632.1996.tb33330.x

81. Martino ES Di. Wall stresses before and after endovascular repair of abdominal aortic aneurysms. In: Proceedings of IMECE04 [Internet]. 2004. Available from: https://www.researchgate.net/publication/267622817_Wall_Stresses_Before_and_After_Endovascular_Repair_of_Abdominal_Aortic_Aneurysms

82. Li Z, Kleinstreuer C, Farber M. Computational analysis of biomechanical contributors to possible endovascular graft failure. Biomech Model Mechanobiol [Internet]. 2005;4(4):221–34. Available from: http://www.ncbi.nlm.nih.gov/pubmed/16270200

83. Wu W, Wang W, Yang D, Qi M. Stent expansion in curved vessel and their interactions: A finite element analysis. J Biomech. 2007;40(11):2580–5.

84. Azaouzi M, Lebaal N, Makradi a., Belouettar S. Optimization based simulation of self-expanding Nitinol stent. Mater Des [Internet]. 2013;50:917–28. Available from: http://dx.doi.org/10.1016/j.matdes.2013.03.012

85. Hsiao HM, Chiu YH, Lee KH, Lin CH. Computational modeling of effects of intravascular stent design on key mechanical and hemodynamic behavior. CAD Comput Aided Des [Internet]. 2012;44(8):757–65. Available from: http://dx.doi.org/10.1016/j.cad.2012.03.009

86. von Sachsen S, Mohr FW, Senf B, Neugebauer R, Etz CD, Florek H-J. A method for integrating finite element results in a surgical planning software for evaluating stent graft properties in endovascular surgery. 2011 4th Int Conf Biomed Eng Informatics [Internet]. 2011;1343–8. Available from: http://ieeexplore.ieee.org/lpdocs/epic03/wrapper.htm?arnumber=6098637

87. Demanget N, Avril S, Badel P, Orgéas L, Geindreau C, Albertini J-N, et al. Computational comparison of the bending behavior of aortic stent-grafts. J Mech Behav Biomed Mater [Internet]. 2012;5(1):272–82. Available from: http://linkinghub.elsevier.com/retrieve/pii/S1751616111002402

88. Demanget N, Duprey A, Badel P, Orgéas L, Avril S, Geindreau C, et al. Finite element analysis of the mechanical performances of 8 marketed aortic stent-grafts. J Endovasc Ther Int Soc Endovasc Spec [Internet]. 2013;20(4):523–35. Available from: http://www.ncbi.nlm.nih.gov/pubmed/23914862

89. Gupta A, Sett S, Varahoor S, Wolf B. Investigation of interaction between guidewire and native vessel using finite element analysis. Proc 2010 … [Internet]. 2010;1–7. Available from: http://www.simulia-china.com/download/global/2010/Gupta_SCC2010.pdf

90. Mortier P, Holzapfel GA, De Beule M, Van Loo D, Taeymans Y, Segers P, et al. A novel simulation strategy for stent insertion and deployment in curved coronary bifurcations: Comparison of three drug-eluting stents. Ann Biomed Eng. 2010;38(1):88–99.

91. Liao R, Green NE, James Chen S-Y, Messenger JC, Hansgen AR, Groves BM, et al. Three-Dimensional Analysis of in vivo Coronary Stent – Coronary Artery Interactions. Int J Cardiovasc Imaging. 2004;20(4):305–13.

92. De Bock S, Iannaccone F, De Santis G, De Beule M, Mortier P, Verhegghe B, et al. Our capricious vessels: The influence of stent design and vessel geometry on the mechanics of intracranial aneurysm stent deployment. J Biomech [Internet]. 2012;45(8):1353–9. Available from: http://dx.doi.org/10.1016/j.jbiomech.2012.03.012

93. Clough R, Hertault A, Azzaoui R, Sobocinski J, Haulon S. Low-Profile EVAR. Endovasc today. 2016;15(3):72–5.

94. Senf B, von Sachsen S, Neugebauer R, Drossel WG, Florek HJ, Mohr FW, et al. The effect of stent graft oversizing on radial forces considering nitinol wire behavior and vessel characteristics. Med Eng Phys [Internet]. 2014;36(11):1480–6. Available from: http://dx.doi.org/10.1016/j.medengphy.2014.07.020

95. Perrin D, Badel P, Orgeas L, Geindreau C, Roscoat, Albertini, et al. Patient-specific simulation of endovascular repair surgery with tortuous aneurysms requiring flexible stent-grafts. J Mech Behav Biomed Mater. 2016;63:86–99.

96. McCummiskey E. The development of an analysis tool for the design of endovascular devices. University of Strathclyde; 2008.

97. Van Zyl M. The development of an integrated modelling framework to aid with the design of endovascular devices. University of Strathclyde; 2015.

98. Frischkorn J, Reese S. Solid-beam finite element analysis of Nitinol stents. Comput Methods Appl Mech Eng [Internet]. 2015;291:42–63. Available from: http://linkinghub.elsevier.com/retrieve/pii/S0045782515001139

99. Strbac V, Pierce DM, Rodriguez-Vila B, Sloten J Vander, Famaey N. Rupture risk in abdominal aortic aneurysms: A realistic assessment of the explicit {GPU} approach. J Biomech [Internet]. 2017;56:1–9. Available from:

http://www.sciencedirect.com/science/article/pii/S0021929017301197

100. Chong CK, How T V. Flow patterns in an endovascular stent-graft for abdominal aortic aneurysm repair. J Biomech. 2004;37(1):89–97.

101. Kandail H, Hamady M, Yun X. Patient-specific analysis of displacement forces acting on fenestrated stent grafts for endovascular aneurysm repair. J Biomech [Internet]. 2014;47(14):3546–54. Available from: http://dx.doi.org/10.1016/j.jbiomech.2014.08.011

102. Morris L, Delassus P, Grace P, Wallis F, Walsh M, McGloughlin T. Effects of flat, parabolic and realistic steady flow inlet profiles on idealised and realistic stent graft fits through Abdominal Aortic Aneurysms (AAA). Med Eng Phys. 2006;28(1):19–26.

103. Suess T, Anderson J, Danielson L, Pohlson K, Remund T, Blears E, et al. Examination of near-wall hemodynamic parameters in the renal bridging stent of various stent graft configurations for repairing visceral branched aortic aneurysms. J Vasc Surg [Internet]. 2016;64(3):788–96. Available from: http://www.sciencedirect.com/science/article/pii/S0741521415009842

104. Ou J, Tang AYS, Chiu TL, Chow KW, Chan YC, Cheng SWK. Haemodynamic Variations of Flow to Renal Arteries in Custom-Made and Pivot Branch Fenestrated Endografting. Eur J Vasc Endovasc Surg. 2017;53(1):133–9.

105. Stefanov F, Mcgloughlin T, Morris L. A computational assessment of the hemodynamic effects of crossed and non-crossed bifurcated stent-graft devices for the treatment of abdominal aortic aneurysms. Med Eng Phys [Internet]. 2016;0:1–16. Available from: http://dx.doi.org/10.1016/j.medengphy.2016.09.011

106. Morris L, Stefanov F, McGloughlin T. Stent graft performance in the treatment of abdominal aortic aneurysms: The influence of compliance and geometry. J Biomech [Internet]. 2013;46(2):383–95. Available from: http://www.sciencedirect.com/science/article/pii/S0021929012006781

107. Polanczyk A, Podyma M, Stefanczyk L, Szubert W, Zbicinski I. A 3D model of thrombus formation in a stent-graft after implantation in the abdominal aorta. J Biomech [Internet]. 2015;48(3):425–31. Available from: http://www.sciencedirect.com/science/article/pii/S0021929014006873

108. Resch T, Malina M, Lindblad B, Malina J, Brunkwall J, Ivancev K. The Impact of Stent Design on Proximal Stent-graft Fixation in the Abdominal Aorta: an Experimental Study. Eur J Vasc Endovasc Surg. 2000;20(2):190–5.

109. Papaharilaou Y, Ekaterinaris JA, Manousaki E, Katsamouris AN. A decoupled fluid structure approach for estimating wall stress in abdominal aortic aneurysms. J Biomech. 2007;40(2):367–77.

110. Larrabide I, Kim M, Augsburger L, Villa-uriol MC, Rüfenacht D, Frangi AF. Fast virtual deployment of self-expandable stents : Method and in vitro evaluation for intracranial aneurysmal stenting. Med Image Anal [Internet]. 2012;16(3):721–30. Available from: http://dx.doi.org/10.1016/j.media.2010.04.009

111. Spranger K, Ventikos Y. Which spring is the best? Comparison of methods for virtual stenting. IEEE Trans Biomed Eng. 2014;61(7):1998–2010.

112. Spranger K, Capelli C, Bosi GM, Schievano S, Ventikos Y. Comparison and calibration of a real-time virtual stenting algorithm using Finite Element Analysis and Genetic Algorithms. Comput Methods Appl Mech Eng [Internet]. 2015;293:462–80. Available from:

http://www.sciencedirect.com/science/article/pii/S0045782515001322

113. Ahn SS, Rutherford RB, Johnston KW, May J, Veith FJ, Baker JD, et al. Reporting standards for infrarenal endovascular abdominal aortic aneurysm repair. J Vasc Surg [Internet]. 1997 Feb;25(2):405–10. Available from: http://www.sciencedirect.com/science/article/pii/S074152149770363X

114. Chaikof EL, Blankensteijn JD, Harris PL, White GH, Zarins CK, Bernhard VM, et al. Reporting standards for endovascular aortic aneurysm repair. J Vasc Surg. 2002;35(5):1048–60.

115. Walker TG, Kalva SP, Yeddula K, Wicky S, Kundu S, Drescher P, et al. Clinical Practice Guidelines for Endovascular Abdominal Aortic Aneurysm Repair: Written by the Standards of Practice Committee for the Society of Interventional Radiology and Endorsed by the Cardiovascular and Interventional Radiological Society of Europe. J Vasc Interv Radiol [Internet]. 2010;21(11):1632–55. Available from: http://dx.doi.org/10.1016/j.jvir.2010.07.008

116. Chaikof EL, Fillinger MF, Matsumura JS, Rutherford RB, White GH, Blankensteijn JD, et al. Identifying and grading factors that modify the outcome of endovascular aortic aneurysm repair. J Vasc Surg. 2002;35:1061–6.

117. Wolf YG, Tillich M, Lee WA, Rubin GD, Fogarty TJ, Zarins CK. Impact of aortoiliac tortuosity on endovascular repair of abdominal aortic aneurysms : Evaluation of 3D computer-based assessment. :594–9.

118. Kristmundsson T. A Novel Method to Estimate Iliac Tortuosity in Evaluating EVAR Access. J Endovasc Ther [Internet]. 2012;157–64. Available from: https://doi.org/10.1583/11-3704.1

119. Henretta JP, Karch LA, Hodgson KJ, Mattos MA, Ramsey DE, McLafferty R, et al. Special iliac artery considerations during aneurysm endografting. Am J Surg [Internet]. 1999 Sep;178(3):212–8. Available from: http://www.sciencedirect.com/science/article/pii/S0002961099001567

120. Isselbacher EM. Thoracic and abdominal aortic aneurysms. Circulation. 2005;111(6):816–28.

121. Albertini J-N, Macierewicz JA, Yusuf SW, Wenham PW, Hopkinson BR. Pathophysiology of Proximal Perigraft Endoleak Following Endovascular Repair of Abdominal Aortic Aneurysms: a Study Using a Flow Model. Eur J Vasc Endovasc Surg [Internet]. 2001;22(1):53–6. Available from: http://www.sciencedirect.com/science/article/pii/S1078588401913851

122. Frank A. Lederle, MD, Samuel E. Wilson, MD, Gary R. Johnson, MS, Donovan B. Reinke, MD, Fred N. Littooy, MD, Charles W. Acher, MD, Louis M. Messina, MD, David J. Ballard, MD, PhD, and Howard J. Ansel M. Variability in measurement of abdominal aortic aneurysms. J Vasc Surg. 1995;945–52.

123. Sprouse LR, Meier GH, LeSar CJ, DeMasi RJ, Sood J, Parent FN, et al. Comparison of abdominal aortic aneurysm diameter measurements obtained with ultrasound and computed tomography: is there a difference? J Vasc Surg [Internet]. 2003;38(3):466–71. Available from: http://www.sciencedirect.com/science/article/pii/S0741521403003677

124. Duquette AA, Jodoin PM, Bouchot O, Lalande A. 3D segmentation of abdominal aorta from CT-scan and MR images. Comput Med Imaging Graph [Internet]. 2012;36(4):294–303. Available from: http://dx.doi.org/10.1016/j.compmedimag.2011.12.001

125. Flachskampf FA. How Exactly Do You Measure That Aorta?: Lessons From Multimodality Imaging. JACC Cardiovasc Imaging [Internet]. 2016;9(3):227–9. Available from: http://www.sciencedirect.com/science/article/pii/S1936878X15008621

126. Fillinger MF, Racusin J, Baker RK, Cronenwett JL, Teutelink A, Schermerhorn ML, et al. Anatomic characteristics of ruptured abdominal aortic aneurysm on conventional CT scans: implications for rupture risk. J Vasc Surg. 2004;39(6):1243–52.

127. Mendoza DD, Kochar M, Devereux RB, Basson CT, Min JK, Holmes K, et al. Impact of Image Analysis Methodology on Diagnostic and Surgical Classification of Patients With Thoracic Aortic Aneurysms. Ann Thorac Surg [Internet]. 2011 Sep;92(3):904–12. Available from: http://www.sciencedirect.com/science/article/pii/S0003497511008447

128. Marra SP, Daghlian CP, Fillinger MF, Kennedy FE. Elemental composition, morphology and mechanical properties of calcified deposits obtained from abdominal aortic aneurysms. Acta Biomater [Internet]. 2006;2(5):515–20. Available from: http://www.sciencedirect.com/science/article/pii/S1742706106000572

129. Maier A, Gee MW, Reeps C, Eckstein H-H, Wall WA. Impact of calcifications on patient-specific wall stress analysis of abdominal aortic aneurysms. Biomech Model Mechanobiol [Internet]. 2010;9(5):511–21. Available from: https://doi.org/10.1007/s10237-010-0191-0

130. Romo A, Badel P, Duprey A, Favre J-P, Avril S. In vitro analysis of localized aneurysm rupture. J Biomech [Internet]. 2014;47(3):607–16. Available from: http://www.sciencedirect.com/science/article/pii/S0021929013006398

131. Iino M, Kuribayashi S, Imakita S, Takamiya M, Matsuo H, Ookita Y, et al. Sensitivity and Specificity of CT in the Diagnosis of Inflammatory Abdominal Aortic Aneurysms. J Comput Assist Tomogr. 2002;26(6).

132. Raghavan ML, Kratzberg J, Castro de Tolosa EM, Hanaoka MM, Walker P, da Silva ES. Regional distribution of wall thickness and failure properties of human abdominal aortic aneurysm. J Biomech [Internet]. 2006;39(16):3010–6. Available from: http://www.ncbi.nlm.nih.gov/pubmed/16337949

133. Roy CS. The Elastic Properties of the Arterial Wall. J Physiol [Internet]. 1881 Jan;3(2):125–59. Available from: http://www.ncbi.nlm.nih.gov/pmc/articles/PMC1484813/

134. Sassani SG, Kakisis J, Tsangaris S, Sokolis DP. Layer-dependent wall properties of abdominal aortic aneurysms: Experimental study and material characterization. J Mech Behav Biomed Mater [Internet]. 2015;49:141–61. Available from: http://dx.doi.org/10.1016/j.jmbbm.2015.04.027

135. Horný L, Netušil M, Vo T. Axial prestretch and circumferential distensibility in biomechanics of abdominal aorta. Biomech Model Mechanobiol. 2014;783–99.

136. Labrosse MR, Beller CJ, Mesana T, Veinot JP. Mechanical behavior of human aortas: Experiments, material constants and 3-D finite element modeling including residual stress. J Biomech. 2009;42(8):996–1004.

137. Horny L, Adamek T, Gultova E, Zitny R, Vesely J, Chlup H, et al. Correlations between age, prestrain, diameter and atherosclerosis in the male abdominal aorta. J Mech Behav Biomed Mater [Internet]. 2011;4(8):2128–32. Available from: http://dx.doi.org/10.1016/j.jmbbm.2011.07.011

138. Horny L, Adamek T, Chlup H, Zitny R. Age estimation based on a combined arteriosclerotic index. Int J Legal Med [Internet]. 2012 Mar;126(2):321–6. Available from: https://doi.org/10.1007/s00414-011-0653-7

139. Roy D, Kauffmann C, Delorme S, Lerouge S, Cloutier G, Soulez G. A Literature Review of the Numerical Analysis of Abdominal Aortic Aneurysms Treated with Endovascular Stent Grafts.

Comput Math Methods Med [Internet]. 2012;2012:1–16. Available from: http://www.hindawi.com/journals/cmmm/2012/820389/

140. Vande Geest JP, Sacks MS, Vorp DA. The effects of aneurysm on the biaxial mechanical behavior of human abdominal aorta. J Biomech [Internet]. 2006;39(7):1324–34. Available from: http://www.ncbi.nlm.nih.gov/pubmed/15885699

141. Pierce DM, Maier F, Weisbecker H, Viertler C, Verbrugghe P, Famaey N, et al. Human thoracic and abdominal aortic aneurysmal tissues: Damage experiments, statistical analysis and constitutive modeling. J Mech Behav Biomed Mater [Internet]. 2015;41:92–107. Available from: http://dx.doi.org/10.1016/j.jmbbm.2014.10.003

142. Skacel P, Bursa J. Poisson's ratio of arterial wall - Inconsistency of constitutive models with experimental data. J Mech Behav Biomed Mater [Internet]. 2016;54:316–27. Available from: http://dx.doi.org/10.1016/j.jmbbm.2015.09.029

143. Yosibash Z, Manor I, Gilad I, Willentz U. Experimental evidence of the compressibility of arteries. J Mech Behav Biomed Mater [Internet]. 2014;39:339–54. Available from: http://dx.doi.org/10.1016/j.jmbbm.2014.07.030

144. Weisbecker H, Pierce DM, Regitnig P, Holzapfel GA. Layer-specific damage experiments and modeling of human thoracic and abdominal aortas with non-atherosclerotic intimal thickening. J Mech Behav Biomed Mater [Internet]. 2012;12:93–106. Available from: http://dx.doi.org/10.1016/j.jmbbm.2012.03.012

145. Horny L, Gultova E, Chlup H, Sedlacek R, Kronek J, Vesely J, et al. Mullins effect in human aorta described with limiting extensibility evolution. IFMBE Proc. 2010;29(21):768–71.

146. Fung YC. Elasticity of soft tissues in simple elongation. Am J Physiol. 1967;213.

147. Vaishnav RN, Young JT, Janicki JS, Patel DJ. Nonlinear Anisotropic Elastic Properties of the Canine Aorta. Biophys J [Internet]. 1972;12(8):1008–27. Available from: http://www.sciencedirect.com/science/article/pii/S000634957286140X

148. Hoppmann WH, Wan L. Large deformation of elastic tubes. J Biomech [Internet]. 1970;3(6):593–600. Available from: http://www.sciencedirect.com/science/article/pii/0021929070900436

149. Raghavan ML, Vorp DA. Toward a biomechanical tool to evaluate rupture potential of abdominal aortic aneurysm: identification of a finite strain constitutivemodel and evaluation of its applicability. J Biomech. 2000;33(4):475–82.

150. He CM, Roach MR. The composition and mechanical properties of abdominal aortic aneurysms. J Vasc Surg [Internet]. 2018 Apr 10;20(1):6–13. Available from: http://dx.doi.org/10.1016/0741-5214(94)90169-4

151. Geest JP Vande, Sacks MS, Vorp DA. Age Dependency of the Biaxial Biomechanical Behavior of Human Abdominal Aorta. 2004;126(December 2004):815–22.

152. Holzapfel G a, Gasser TC, Ogden RW. A new constitutive framework for arterial wall mechanics and a comperative study of material models. J Elast. 2000;61:1–48.

153. Gasser TC, Ogden RW, Holzapfel G a. Hyperelastic modelling of arterial layers with distributed collagen fibre orientations. J R Soc Interface. 2006;3(6):15–35.

154. Haskett D, Johnson G, Zhou A, Utzinger U, Vande Geest J. Microstructural and biomechanical alterations of the human aorta as a function of age and location. Biomech Model

Mechanobiol [Internet]. 2010;9(6):725–36. Available from: http://link.springer.com/10.1007/s10237-010-0209-7

155. Annaidh AN, Gilchrist MDMD, Murphy JG. Deficiencies in numerical models of anisotropic nonlinearly elastic materials. Biomech Model Mechanobiol. 2013;781–91.

156. Labrosse MR, Gerson ER, Veinot JP, Beller CJ. Mechanical characterization of human aortas from pressurization testing and a paradigm shift for circumferential residual stress. J Mech Behav Biomed Mater [Internet]. 2012;17:44–55. Available from: http://dx.doi.org/10.1016/j.jmbbm.2012.08.004

157. Vergori L, Destrade M, McGarry P, Ogden RW. On anisotropic elasticity and questions concerning its finite element implementation. Comput Mech. 2013;52(5):1185–97.

158. Gilchrist MD, Murphy JG, Parnell W, Pierrat B. Modelling the slight compressibility of anisotropic soft tissue. Int J Solids Struct [Internet]. 2014;51(23–24):3857–65. Available from: http://dx.doi.org/10.1016/j.ijsolstr.2014.06.018

159. Merodio J, Ogden RW. Remarks on instabilities and ellipticity for a fiber-reinforced compressible nonlinearly elastic solid under plane deformation. Quart Appl Math. 2005;63:325–33.

160. Pierrat B, Murphy JG, MacManus DB, Gilchrist MD. Finite element implementation of a new model of slight compressibility for transversely isotropic materials. Comput Methods Biomech Biomed Engin [Internet]. 2015;5842(January):1–14. Available from: http://www.tandfonline.com/doi/abs/10.1080/10255842.2015.1061513?url_ver=Z39.88-2003&rfr_id=ori:rid:crossref.org&rfr_dat=cr_pub=pubmed#.Vdzjx_lVhBc%5Cnhttp://www.ncbi.nlm.nih.gov/pubmed/26252069

161. Lally C, Dolan F, Prendergast PJ. Cardiovascular stent design and vessel stresses: A finite element analysis. J Biomech. 2005;38(8):1574–81.

162. Gastaldi D, Morlacchi S, Nichetti R, Capelli C, Dubini G, Petrini L, et al. Modelling of the provisional side-branch stenting approach for the treatment of atherosclerotic coronary bifurcations: Effects of stent positioning. Biomech Model Mechanobiol. 2010;9(5):551–61.

163. Morlacchi S, Colleoni SG, Cárdenes R, Chiastra C, Diez JL, Larrabide I, et al. Patient-specific simulations of stenting procedures in coronary bifurcations: Two clinical cases. Med Eng Phys [Internet]. 2013;35(9):1272–81. Available from: http://linkinghub.elsevier.com/retrieve/pii/S1350453313000234

164. Mouktadiri G, Bou-Saïd B, Walter-Le-Berre H. Aortic endovascular repair modeling using the finite element method. J Biomed Sci Eng. 2013;6(September):917–27.

165. Perrin D, Badel P, Orgéas L, Geindreau C, Dumenil A, Albertini J-N, et al. Patient-specific numerical simulation of stent-graft deployment: Validation on three clinical cases. J Biomech [Internet]. 2015;48(10):1868–75. Available from: http://www.sciencedirect.com/science/article/pii/S0021929015002511

166. David P, Nicolas D, Pierre B, Stéphane A, Laurent O, Christian G, et al. Deployment of stent grafts in curved aneurysmal arteries: toward a predictive numerical tool. Int j numer method biomed eng [Internet]. 2015 Jan;31(1). Available from: https://doi.org/10.1002/cnm.2698

167. Langewouters GJ, Wesseling KH, Goedhard WJA. The static elastic properties of 45 human thoracic and 20 abdominal aortas in vitro and the parameters of a new model. J Biomech. 1984;17(6):425–35.

168. Labrosse MR. Internal communication. 2016.

169. Govindjee S, Mihalic PA. Computational methods for inverse finite elastostatics. Comput Methods Appl Mech Eng [Internet]. 1996;136(1):47–57. Available from: http://www.sciencedirect.com/science/article/pii/0045782596010456

170. Govindjee S, Mihalic PA. Computational methods for inverse deformations in quasi-incompressible finite elasticity. Int J Numer Methods Eng [Internet]. 1998;43(5):821–38. Available from: http:https://doi.org/10.1002/(SICI)1097-0207(19981115)43:5%3C821::AID-NME453%3E3.0.CO;2-C

171. Putter S De, Wolters BJBM, Rutten MCM, Breeuwer M. Patient-specific initial wall stress in abdominal aortic aneurysms with a backward incremental method. 2007;40:1081–90.

172. Chandra S, Riveros F, Rodriguez JF. A Methodology for the Derivation of Unloaded Abdominal Aortic Aneurysm Geometry With Experimental Validation. 2016;138(October):1–11.

173. Gee MW, Förster C, Wall WA. A computational strategy for prestressing patient-specific biomechanical problems under finite deformation. Int j numer method biomed eng [Internet]. 2010;26(1):52–72. Available from: http:https://doi.org/10.1002/cnm.1236

174. Weisbecker H, Pierce DM, Holzapfel GA. A generalized prestressing algorithm for finite element simulations of preloaded geometries with application to the aorta. Int j numer method biomed eng [Internet]. 2014;30(9):857–72. Available from: http:https://doi.org/10.1002/cnm.2632

175. Roccabianca S, Figueroa CA, Tellides G, Humphrey JD. Quantification of regional differences in aortic stiffness in the aging human. J Mech Behav Biomed Mater [Internet]. 2014;29:618–34. Available from: http://dx.doi.org/10.1016/j.jmbbm.2013.01.026

176. Polzer S, Gasser TC, Bursa J, Staffa R, Vlachovsky R, Man V, et al. Importance of material model in wall stress prediction in abdominal aortic aneurysms. Med Eng Phys [Internet]. 2013;35(9):1282–9. Available from: http://dx.doi.org/10.1016/j.medengphy.2013.01.008

177. García a., Peña E, Martínez M a. Influence of geometrical parameters on radial force during self-expanding stent deployment. Application for a variable radial stiffness stent. J Mech Behav Biomed Mater [Internet]. 2012;10:166–75. Available from: http://dx.doi.org/10.1016/j.jmbbm.2012.02.006

178. Azaouzi M, Makradi a., Belouettar S. Deployment of a self-expanding stent inside an artery: A finite element analysis. Mater Des [Internet]. 2012;41:410–20. Available from: http://dx.doi.org/10.1016/j.matdes.2012.05.019

179. De Bock S, Iannaccone F, De Santis G, De Beule M, Van Loo D, Devos D, et al. Virtual evaluation of stent graft deployment: A validated modeling and simulation study. J Mech Behav Biomed Mater [Internet]. 2012;13:129–39. Available from: http://dx.doi.org/10.1016/j.jmbbm.2012.04.021

180. De Bock S, Iannaccone F, De Beule M, Van Loo D, Vermassen F, Verhegghe B, et al. Filling the void: A coalescent numerical and experimental technique to determine aortic stent graft mechanics. J Biomech [Internet]. 2013;46(14):2477–82. Available from: http://www.ncbi.nlm.nih.gov/pubmed/23953501

181. Graham RL, Lubachevsky BD, Nurmela KJ, Östergård PRJ. Dense packings of congruent circles in a circle. Discrete Math [Internet]. 1998;181(1):139–54. Available from: http://www.sciencedirect.com/science/article/pii/S0012365X97000502

182. Circles in a circle [Internet]. 2018. Available from: http://www.packomania.com/

183. Simulia. Abaqus 6.13 Documentation [Internet]. Available from: http://dsk.ippt.pan.pl/docs/abaqus/v6.13/index.html

184. Brodie R. Internal communication. 2016.

185. Hall GJ, Kasper EP. Comparison of element technologies for modeling stent expansion. J Biomech Eng. 2006;128(5):751–6.

186. Vad S, Eskinazi A, Corbett T, McGloughlin T, Vande Geest JP. Determination of Coefficient of Friction for Self-Expanding Stent-Grafts. J Biomech Eng [Internet]. 2010;132(12):121007. Available from: http://biomechanical.asmedigitalcollection.asme.org/data/Journals/JBENDY/27182/121007_1.pdf%5Cnhttp://biomechanical.asmedigitalcollection.asme.org/article.aspx?articleid=1427723

187. Dunn AC, Zaveri TD, Keselowsky BG, Sawyer WG. Macroscopic friction coefficient measurements on living endothelial cells. Tribol Lett. 2007;27(2):233–8.

188. III WCS, Money SR, Greenberg RK, Chuter TAM. Influence of endograft oversizing on device migration, endoleak, aneurysm shrinkage, and aortic neck dilation: results from the zenith multicenter trial. J Vasc Surg [Internet]. 2004;39(1):20–6. Available from: http://www.sciencedirect.com/science/article/pii/S0741521403013855

189. Kratzberg JA, Golzarian J, Raghavan ML. Role of graft oversizing in the fixation strength of barbed endovascular grafts. J Vasc Surg [Internet]. 2009;49(6):1543–53. Available from: http://www.sciencedirect.com/science/article/pii/S0741521409002250

190. Sampaio SM, Panneton JM, Mozes G, Andrews JC, Noel AA, Kalra M, et al. Aortic neck dilation after endovascular abdominal aortic aneurysm repair: Should oversizing be blamed? Ann Vasc Surg. 2006;20(3):338–45.

191. Morlacchi S, Chiastra C, Gastaldi D, Pennati G, Dubini G, Migliavacca F. Sequential Structural and Fluid Dynamic Numerical Simulations of a Stented Bifurcated Coronary Artery. J Biomech Eng. 2011;133(12):121010.

192. Krissian K, Ellsmere J, Vosburgh K, Kikinis R, Westin C-F. Multiscale segmentation of the aorta in 3D ultrasound images. Proc 25th Annu Int Conf IEEE Eng Med Biol Soc (IEEE Cat No03CH37439). 2003;1:9–12.

193. Zhou L, Wang Y, Goh L, Kockro RA, Serra L. Stereoscopic Visualization and Editing of Automatic Abdominal Aortic Aneurysms (AAA) Measurements for Stent Graft Planning. 2006;6055:1–9.

194. Scherer S, Treichel T, Ritter N, Triebel G, Drossel WG, Burgert O. Surgical stent planning: Sparameter study for models based on DICOM standards. Int J Comput Assist Radiol Surg. 2011;6(3):319–27.

195. Perrin D, Badel P, Orgeas L, Geindreau C, Lyon U De, Lyon F-. Patient-specific simulation of endovascular repair surgery with tortuous aneurysms requiring flexible stent-grafts. 2016;63:86–99.

196. Prasad A, Xiao N, Gong X-Y, Zarins CK, Figueroa CA. A computational framework for investigating the positional stability of aortic endografts. Biomech Model Mechanobiol [Internet]. 2013;12(5):869–87. Available from: https://doi.org/10.1007/s10237-012-0450-3

197. Vascular Modeling Toolkit. p. http://www.vmtk.org/index.html.

198. Biasetti J, Hussain F, Gasser TC. Blood flow and coherent vortices in the normal and aneurysmatic aortas: a fluid dynamical approach to intra-luminal thrombus formation. J R Soc Interface [Internet]. 2011 Oct 7;8(63):1449–61. Available from: http://www.ncbi.nlm.nih.gov/pmc/articles/PMC3163425/

199. Zambrano BA, Gharahi H, Lim C, Jaberi FA, Choi J, Lee W, et al. Association of intraluminal thrombus, hemodynamic forces, and abdominal aortic aneurysm expansion using longitudinal CT images. Ann Biomed Eng [Internet]. 2016 May 1;44(5):1502–14. Available from: http://www.ncbi.nlm.nih.gov/pmc/articles/PMC4826625/

200. Stefanov F, Mcgloughlin T, Delassus P, Morris L. Hemodynamic variations due to spiral blood flow through four patient-specific bifurcated stent graft configurations for the treatment of abdominal aortic aneurysms. Vol. 29, International journal for numerical methods in biomedical engineering. 2013.

201. Raptis A, Xenos M, Kouvelos G, Giannoukas A, Matsagkas M. Haemodynamic performance of AFX and Nellix endografts: A computational fluid dynamics study. Interact Cardiovasc Thorac Surg. 2018;26.

202. Demanget N, Latil P, Orgéas L, Badel P, Avril S, Geindreau C, et al. Severe bending of two aortic stent-grafts: an experimental and numerical mechanical analysis. Ann Biomed Eng [Internet]. 2012;40(12):2674–86. Available from: http://www.ncbi.nlm.nih.gov/pubmed/22805981

203. Carroccio A, Faries PL, Morrissey NJ, Teodorescu V, Burks JA, Gravereaux EC, et al. Predicting iliac limb occlusions after bifurcated aortic stent grafting: Anatomic and device-related causes. J Vasc Surg [Internet]. 2002;36(4):679–84. Available from: http://www.sciencedirect.com/science/article/pii/S0741521402001179

204. Maldonado TS, Rockman CB, Riles E, Douglas D, Adelman MA, Jacobowitz GR, et al. Ischemic complications after endovascular abdominal aortic aneurysm repair. J Vasc Surg [Internet]. 2004;40(4):703–10. Available from: http://www.sciencedirect.com/science/article/pii/S0741521404009516

205. Winterborn RJ, Amin I, Lyratzopoulos G, Walker N, Varty K, Campbell WB. Preferences for endovascular (EVAR) or open surgical repair among patients with abdominal aortic aneurysms under surveillance. J Vasc Surg [Internet]. 2009;49(3):576–581.e3. Available from: http://www.sciencedirect.com/science/article/pii/S0741521408015966

206. Aorta. 2018. p. http://www.cardio.sk/ochorenia/aorta.

207. Terumo Aortic [Internet]. Available from: http://www.vascutek.com

208. Abaqus. UMAT for Superelasticity and Plasticity of Shape Memory Alloys. In Simulia - Dassault Systèmes; 2011.

Appendices

Appendix A – Statistical distribution of AAA variables

The statistical distribution of the variables examined in Chapter 3 are documented below. Results concern the analysis of 258 AAA patients enrolled in the 2009-2011 study: "Vascutek Anaconda stent graft system phase II IDE study".

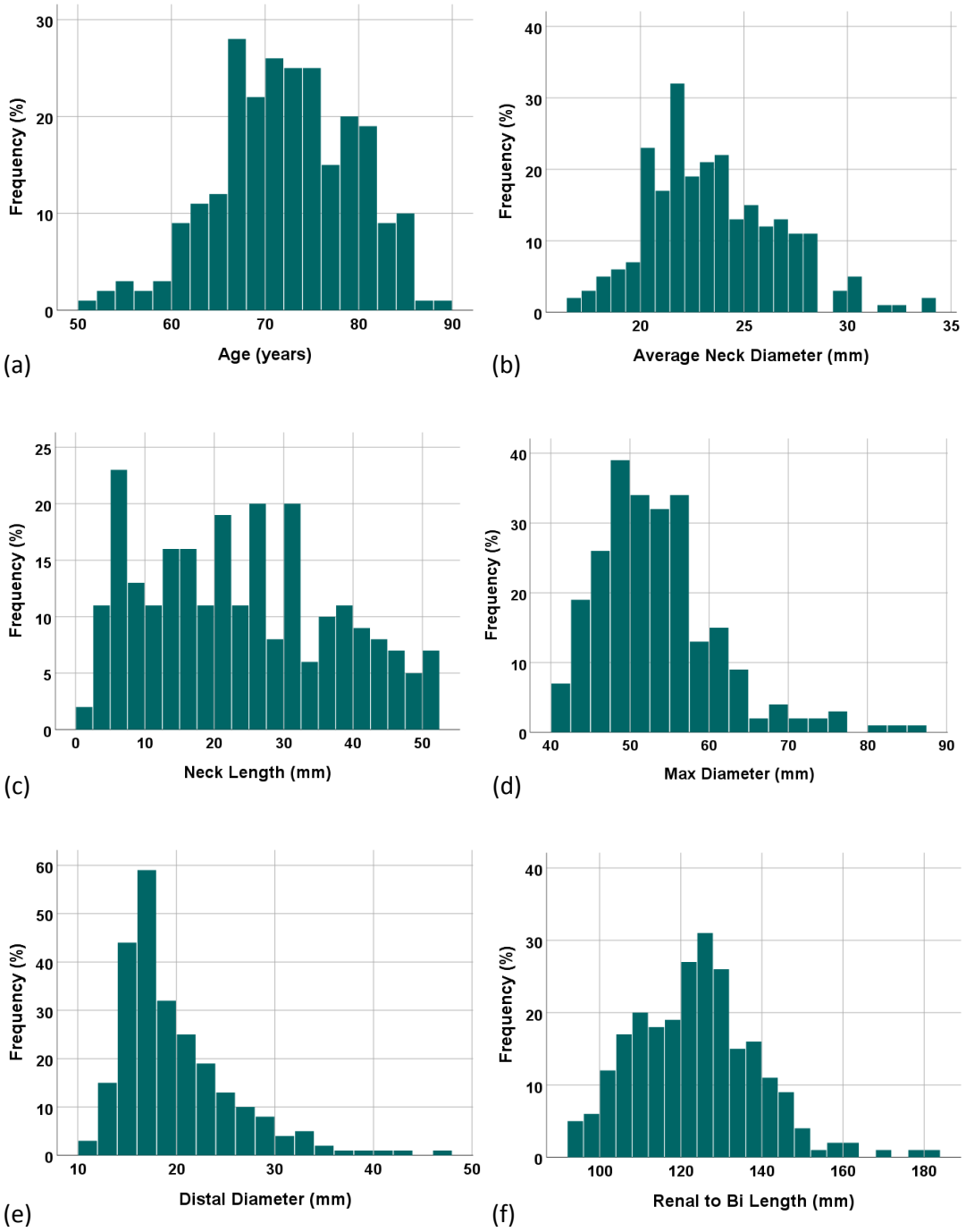

Fig. A.1 Frequency distribution of age (a), average neck diameter (b), neck length (c), maximum diameter (d), distal diameter (e) and renal to bifurcation length (f). For variable definitions refer to Section 3.1.3.

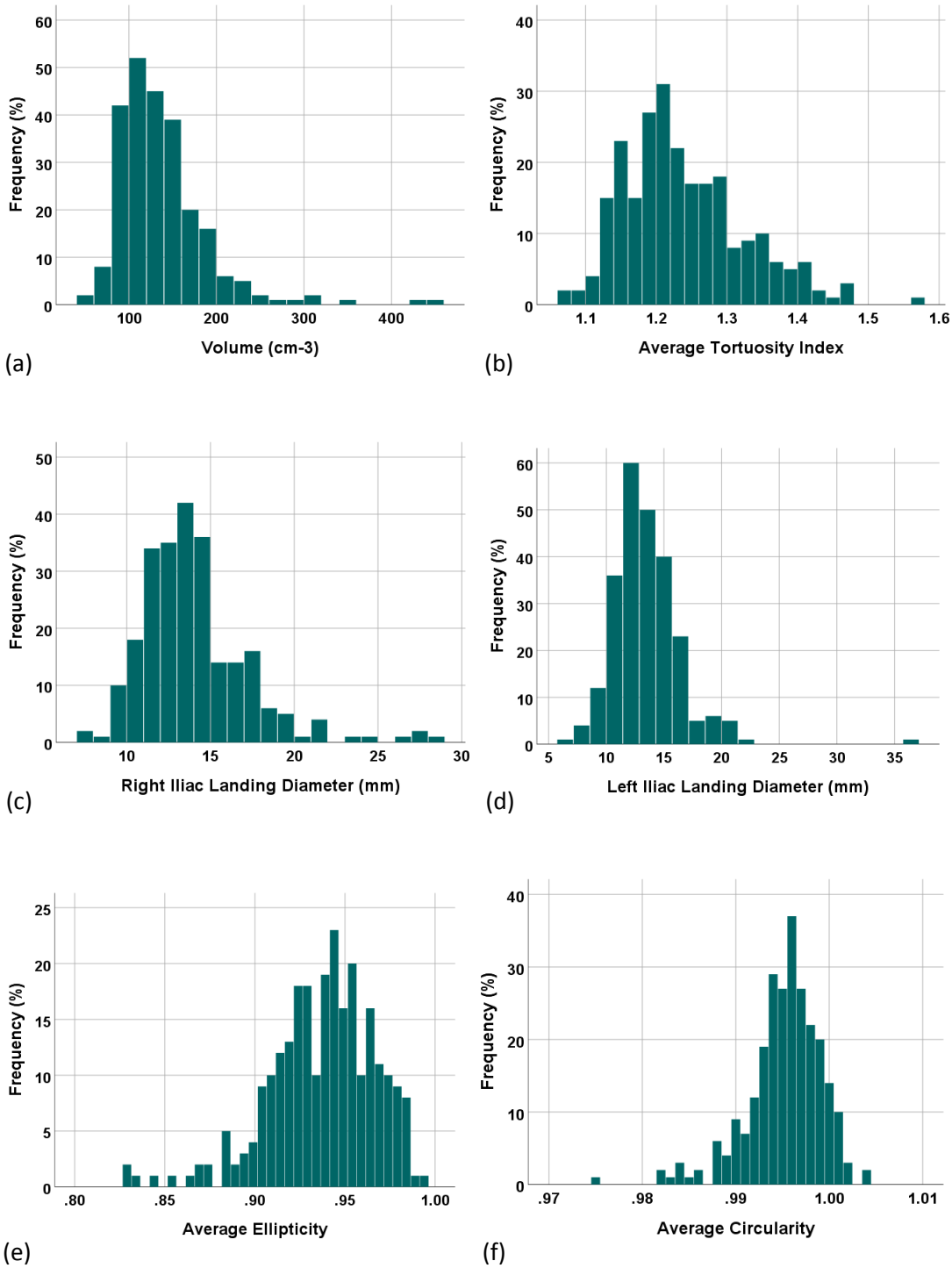

Fig. A.2 Frequency distribution of volume (a), average tortuosity index (b), right iliac landing diameter (c), left iliac landing diameter (d), average ellipticity (e) and average circularity (f). For variable definitions refer to Sections 3.1.3 and 3.1.4.

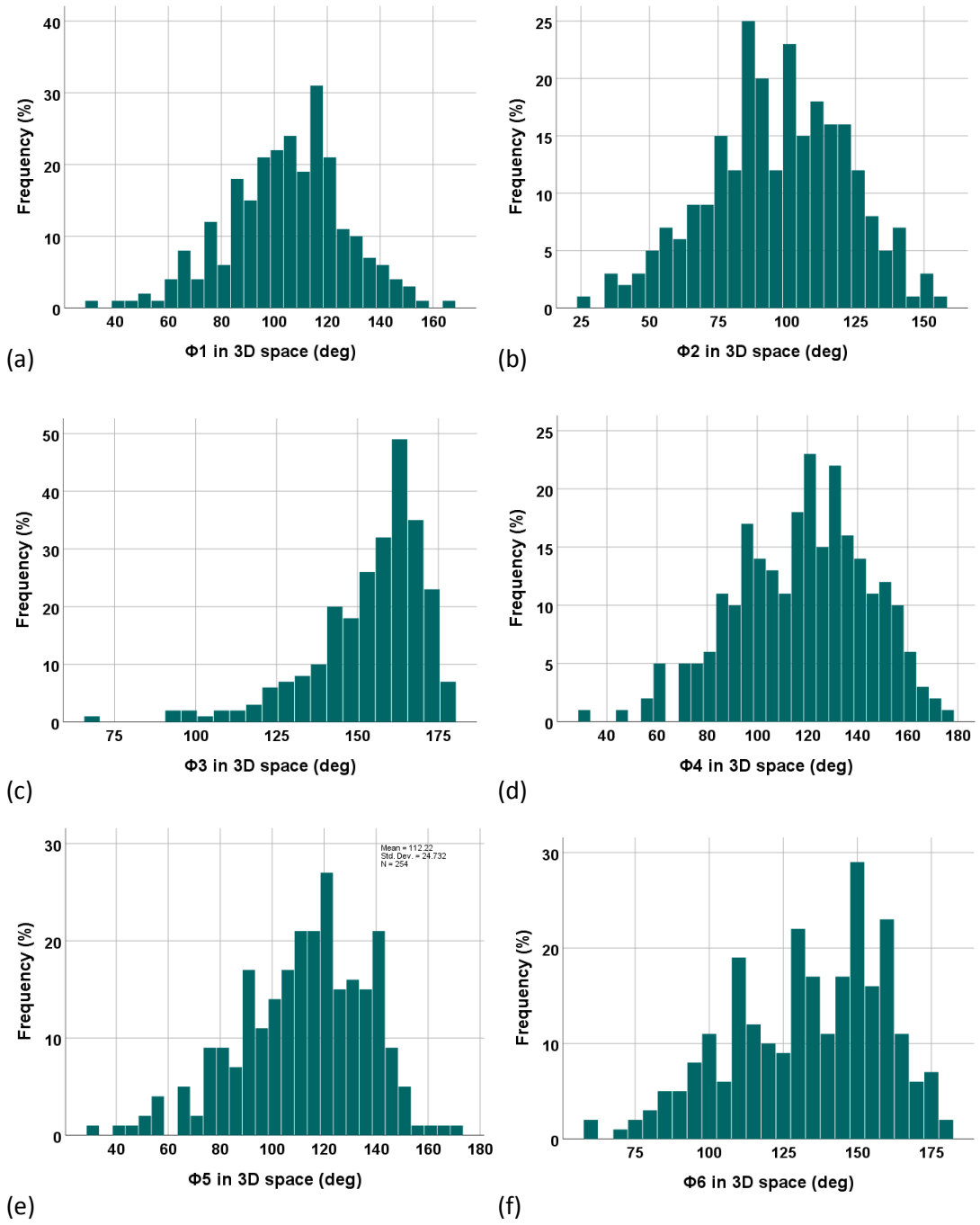

Fig. A.3 Frequency distribution of the angles $\phi_1 - \phi_6$ (images (a) – (f) respectively) in 3D space. For variable definitions refer to Section 3.1.2.

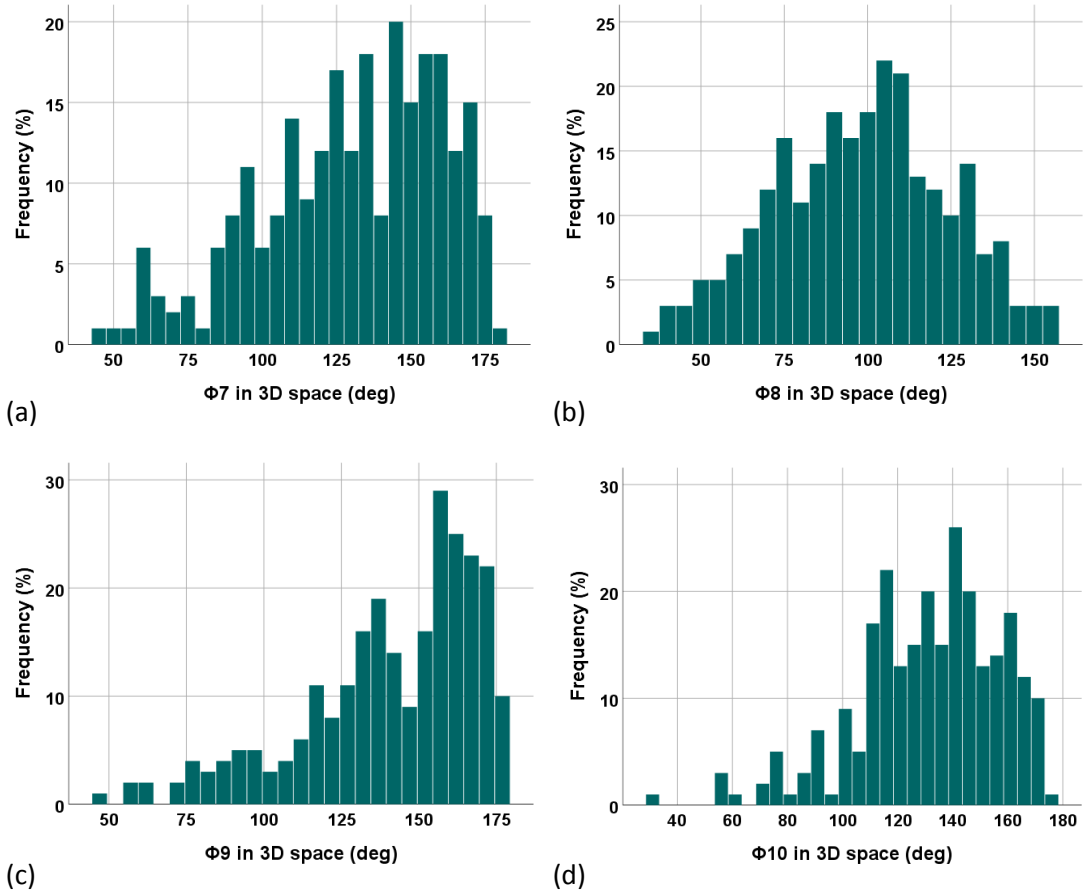

Fig. A.4 Frequency distribution of the angles ϕ_7 – ϕ_{10} (images (a) – (d) respectively) in 3D space. For variable definitions refer to Section 3.1.2.

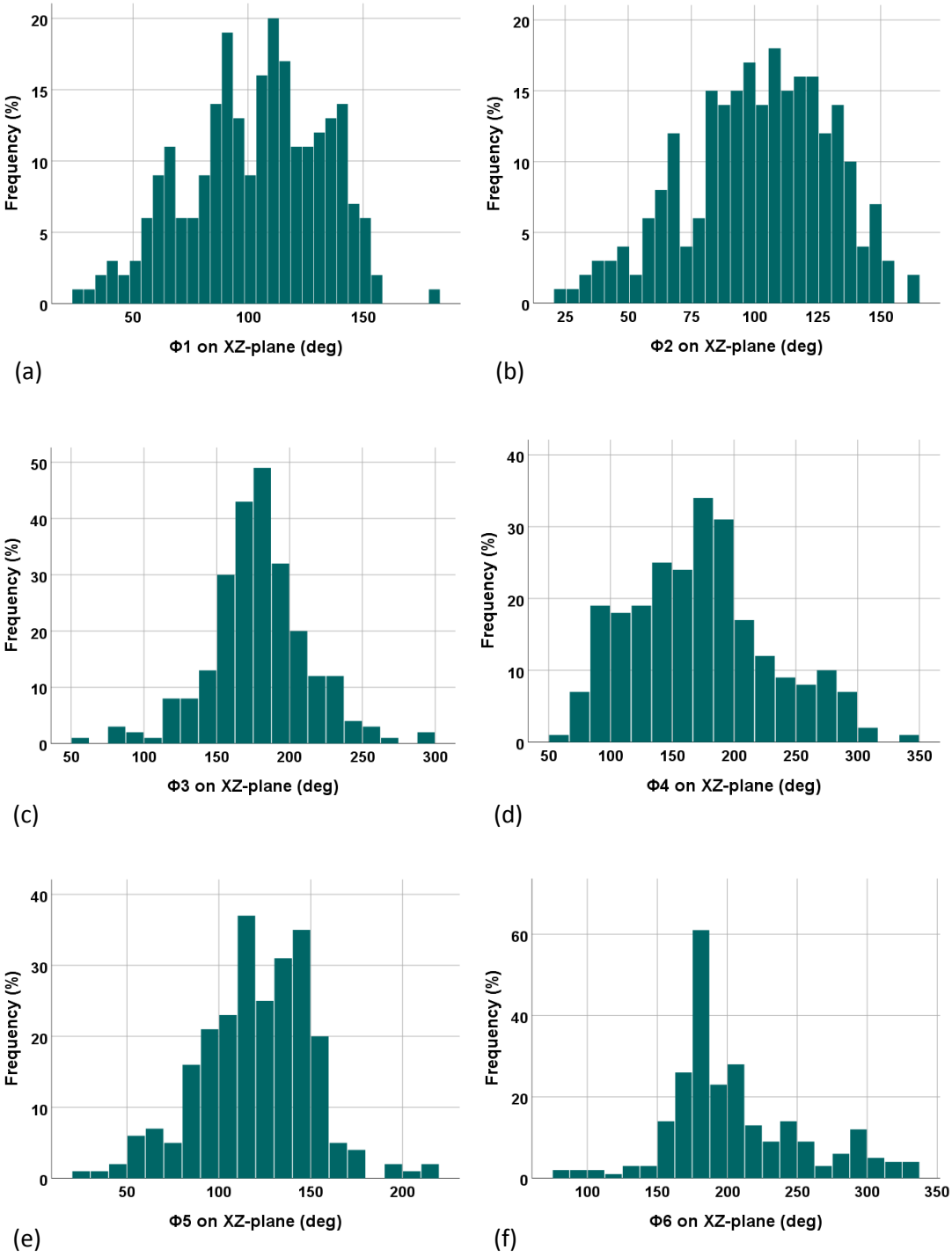

Fig. A.5 Frequency distribution of the angles $\phi_1 - \phi_6$ (images (a) – (f) respectively) on the XZ-plane. For variable definitions refer to Section 3.1.2.

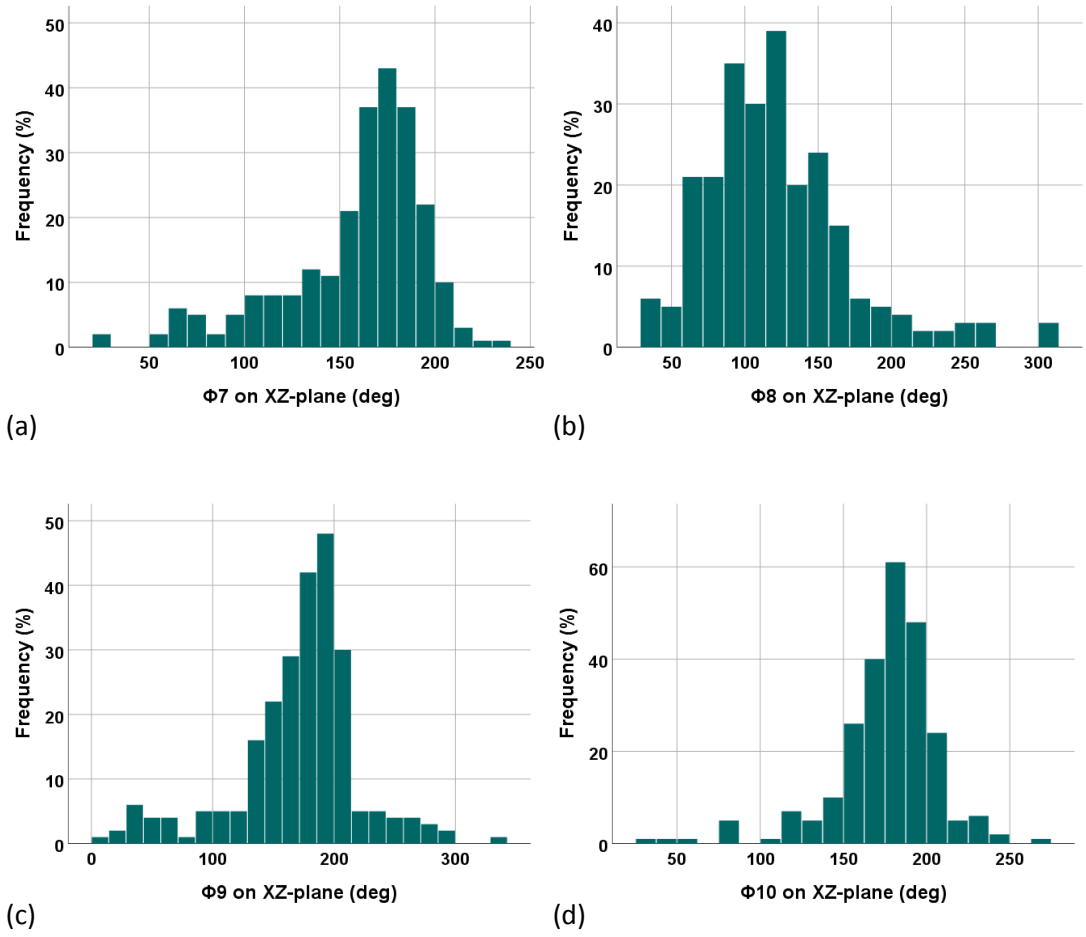

Fig. A.6 Frequency distribution of the angles $\phi_7 - \phi_{10}$ (images (a) – (d) respectively) on the XZ-plane. For variable definitions refer to Section 3.1.2.

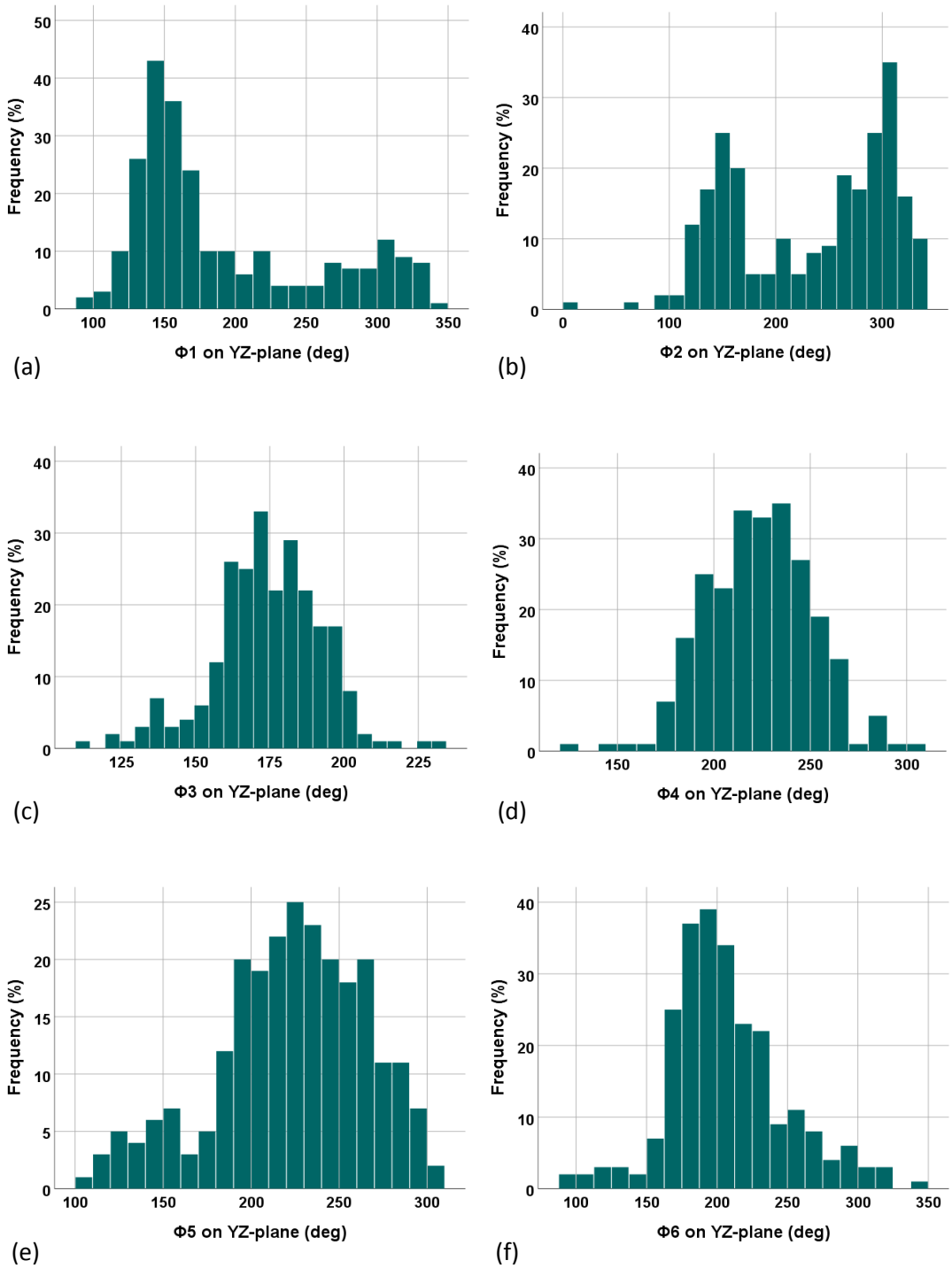

Fig. A.7 Frequency distribution of the angles $\phi_1 - \phi_6$ (images (a) – (f) respectively) on the YZ-plane. For variable definitions refer to Section 3.1.2.

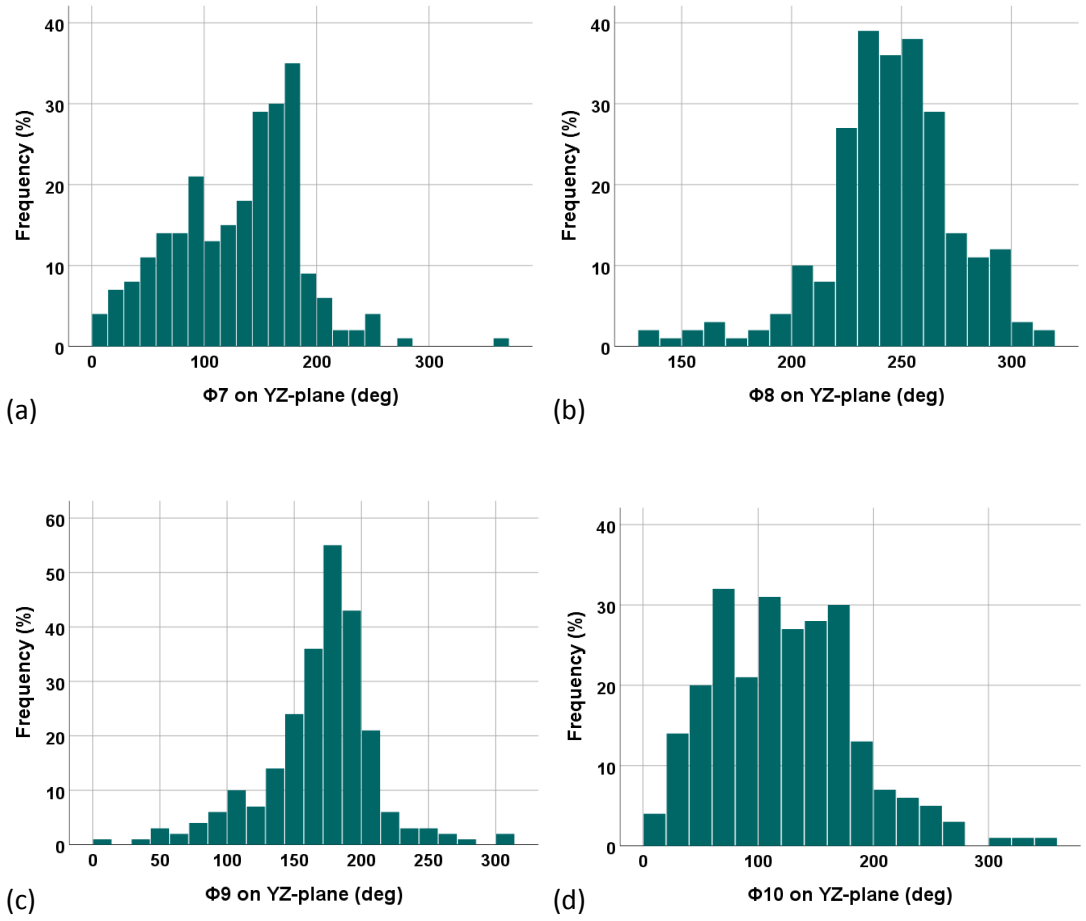

Fig. A.8 Frequency distribution of the angles $\phi_7 - \phi_{10}$ (images (a) – (d) respectively) on the YZ-plane. For variable definitions refer to Section 3.1.2.

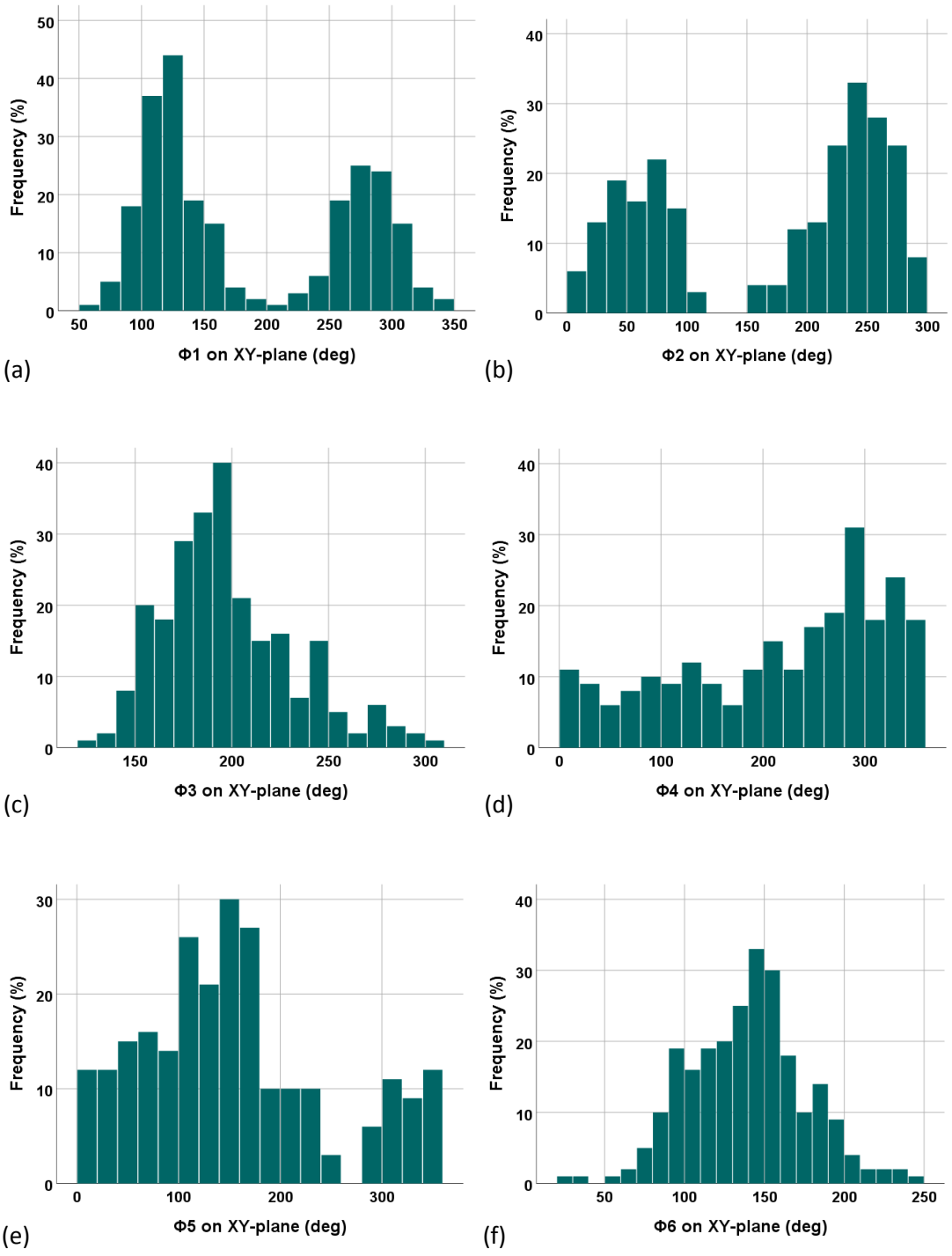

Fig. A.9 Frequency distribution of the angles ϕ_1 – ϕ_6 (images (a) – (f) respectively) on the XY-plane. For variable definitions refer to Section 3.1.2.

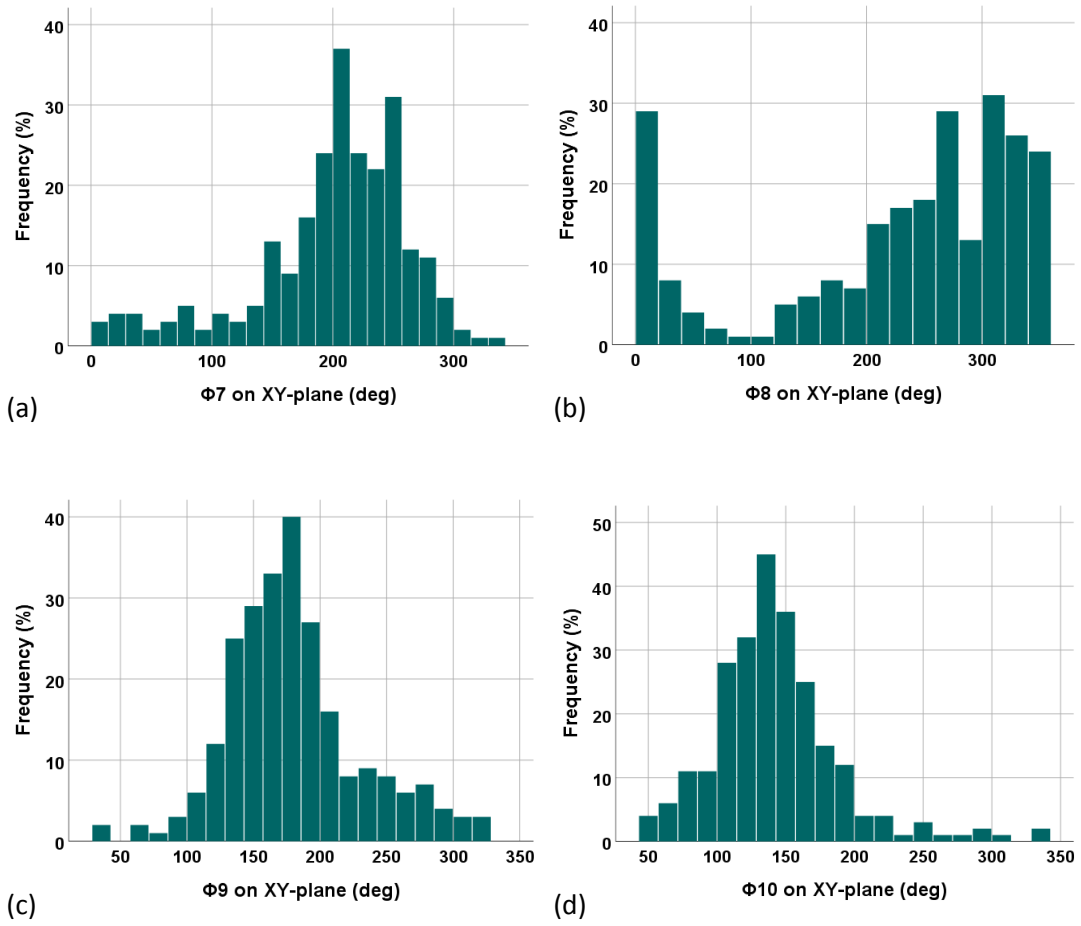

Fig. A.10 Frequency distribution of the angles ϕ_7 – ϕ_{10} (images (a) – (d) respectively) on the XY-plane. For variable definitions refer to Section 3.1.2.

Appendix B – Experimental fabric testing

The relative change of distance between the rings of all the devices tested in Section 5.2 are documented below. The baseline (0%) of the graphs corresponds to the rest state. Furthermore, the notation of the saddles follows the patient's perspective convention: Valley L refers to the left valley and is at the right side of Fig. 5.6 a. Similarly, Valley R refers to the right valley located at the left side of Fig. 5.6 a. Finally, Peak A and P correspond to the anterior and posterior sides of the image, respectively.

Each page contains the results of one device. Both the left and right columns represent the same data, but broken down differently. The left column of each page displays the data according to location whereas the right column according to the stent state.

OLB23

Along the length of the device	Along the state of the device
(A)	(B)

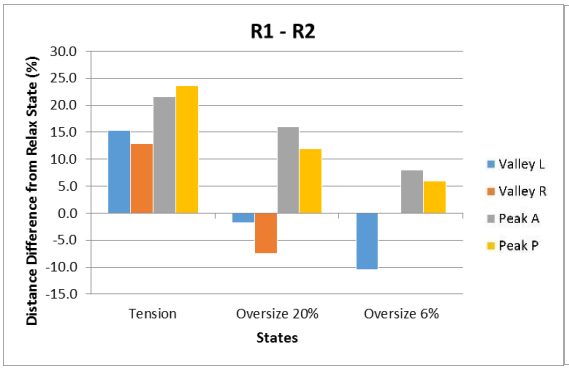

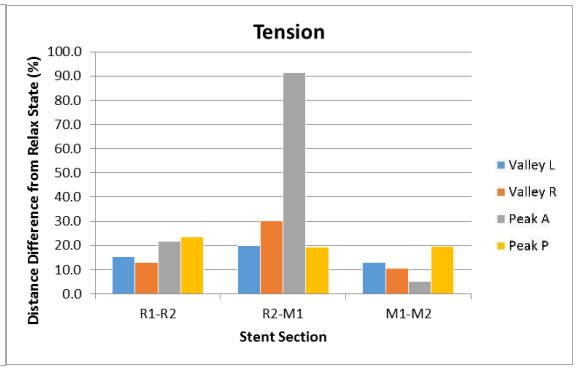

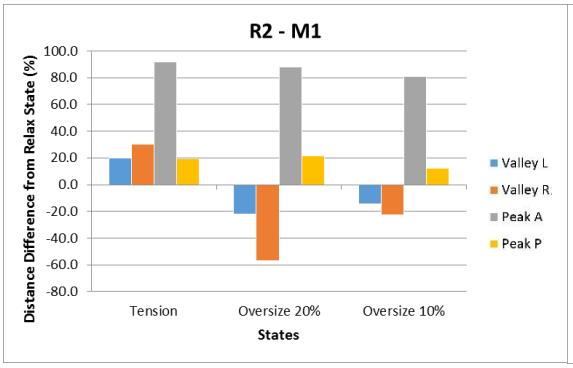

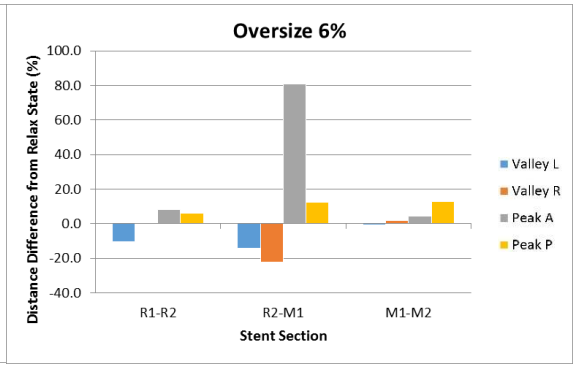

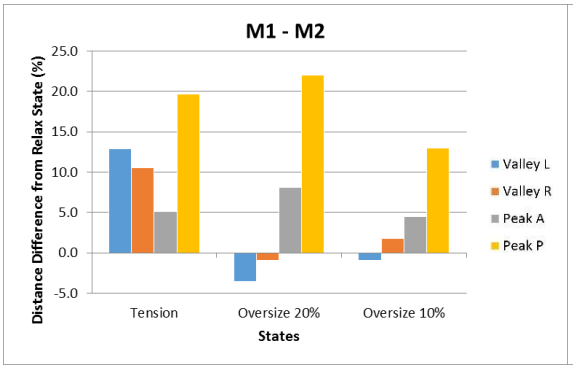

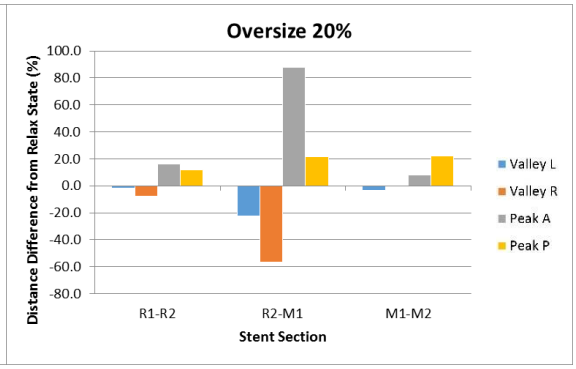

Fig. B.1 Fabric testing results of the body module of OLB23 device. Considering the rest state of the endograft as the baseline, the relative change of distance between each pair of rings is calculated per location (column A) and state (column B).

OLB25

Along the length of the device	Along the state of the device
(A)	(B)

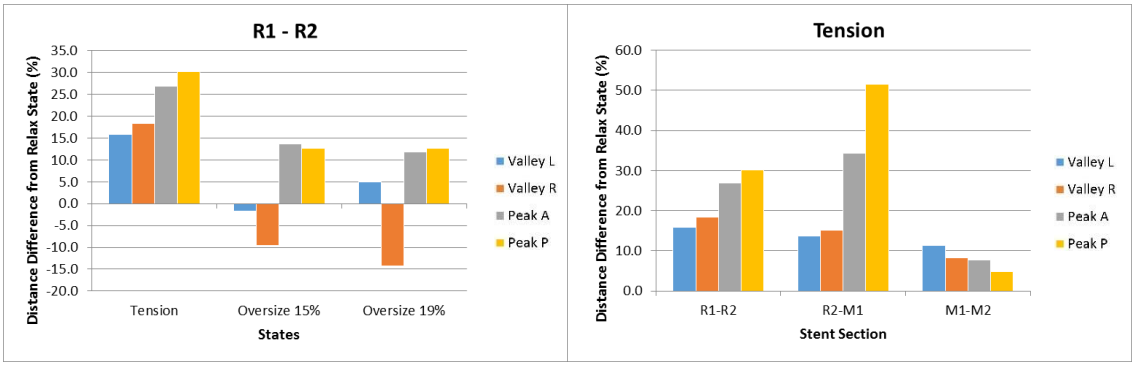

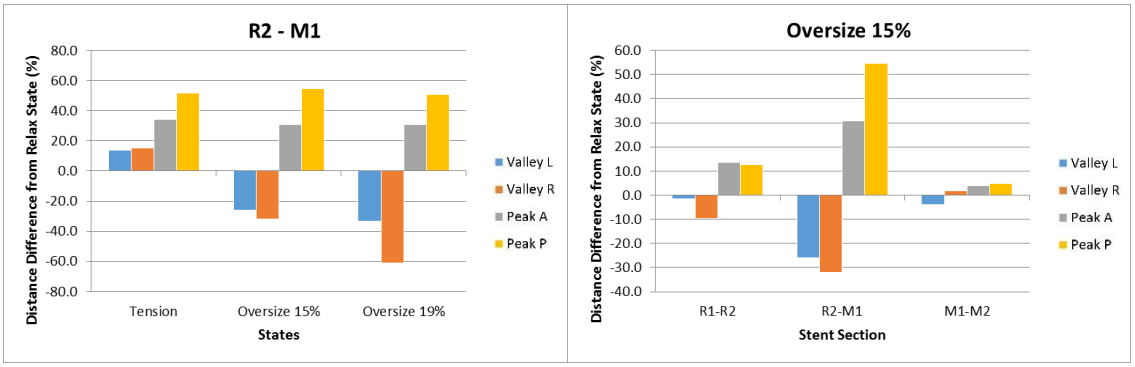

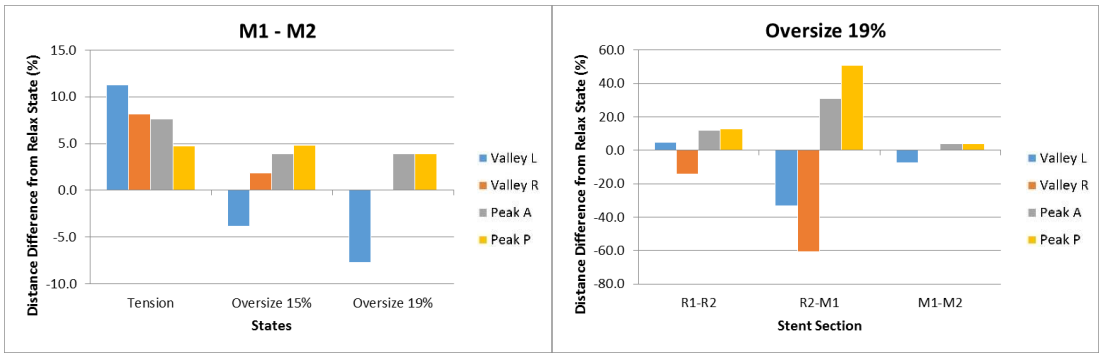

Fig. B.2 Fabric testing results of the body module of OLB25 device. Considering the rest state of the endograft as the baseline, the relative change of distance between each pair of rings is calculated per location (column A) and state (column B).

OLB28

Along the length of the device	Along the state of the device
(A)	(B)

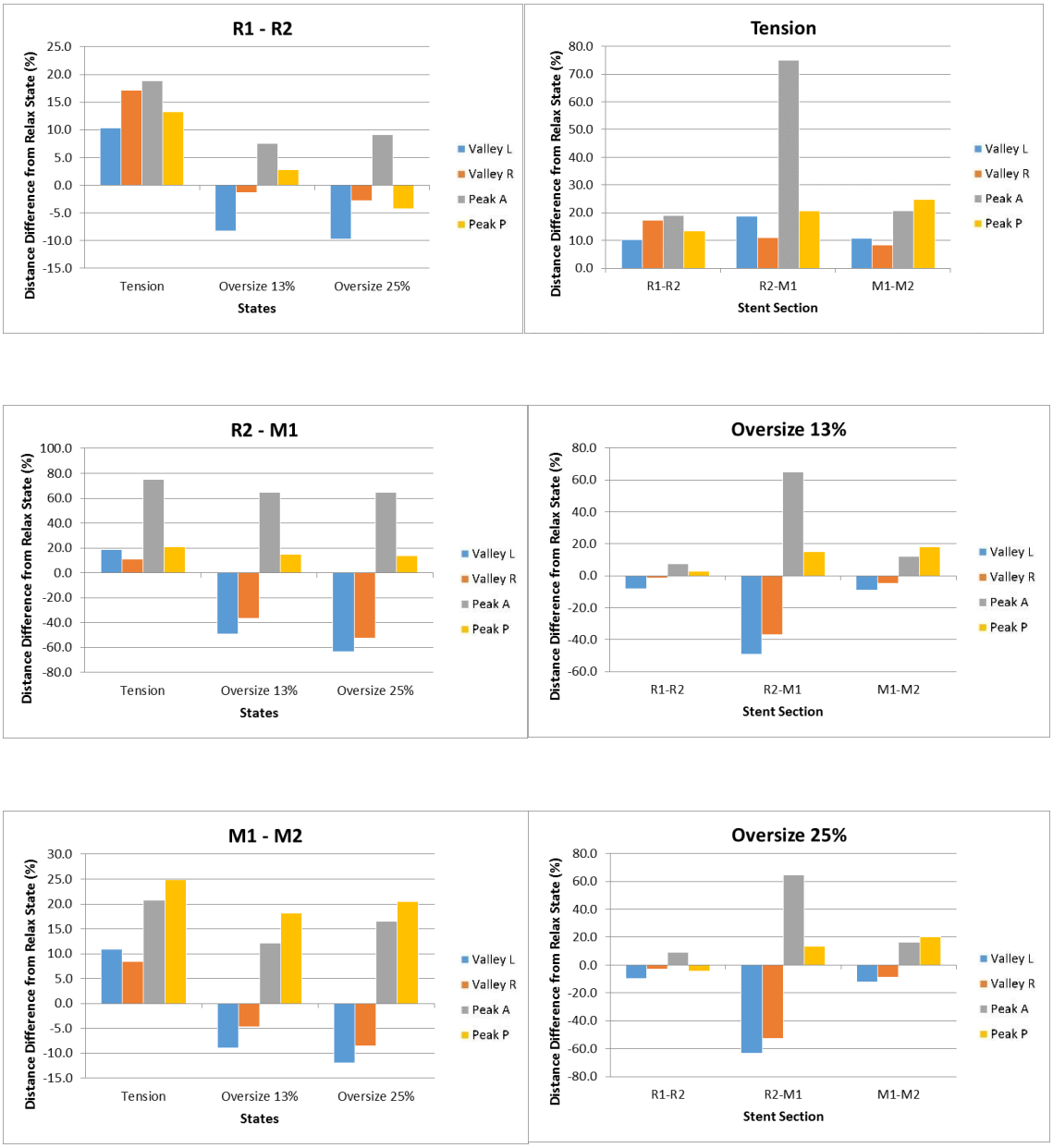

Fig. B.3 Fabric testing results of the body module of OLB28 device. Considering the rest state of the endograft as the baseline, the relative change of distance between each pair of rings is calculated per location (column A) and state (column B).

OLB30

Along the length of the device	Along the state of the device
(A)	(B)

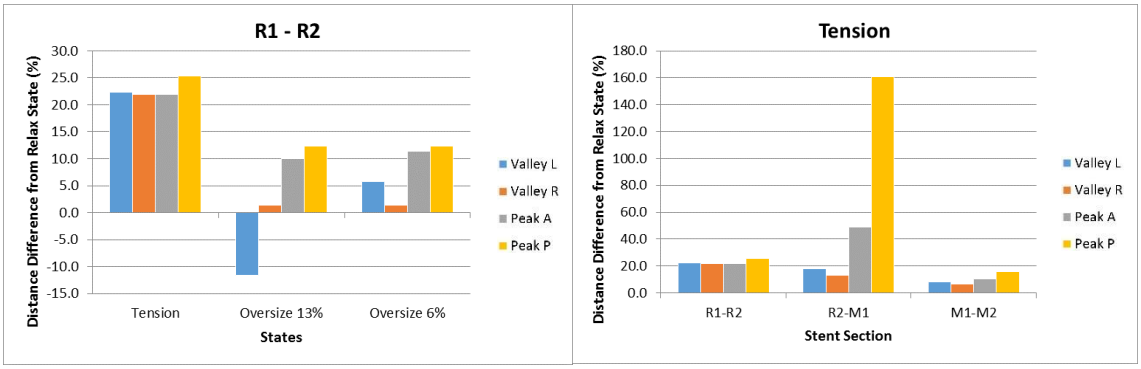

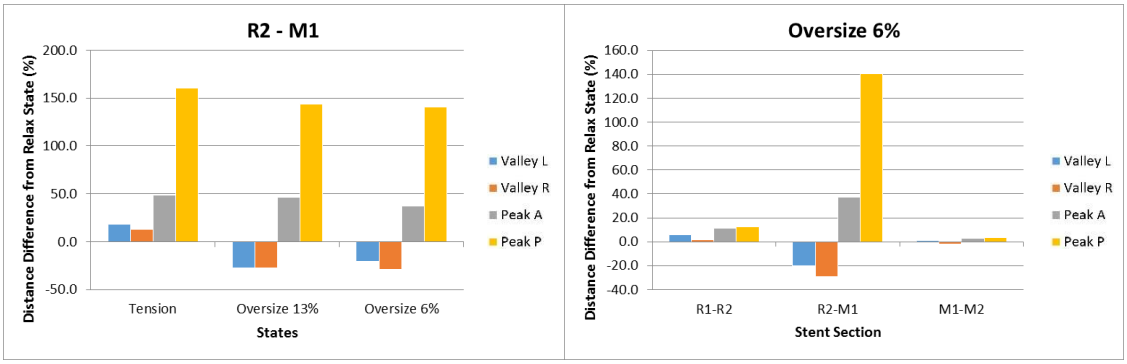

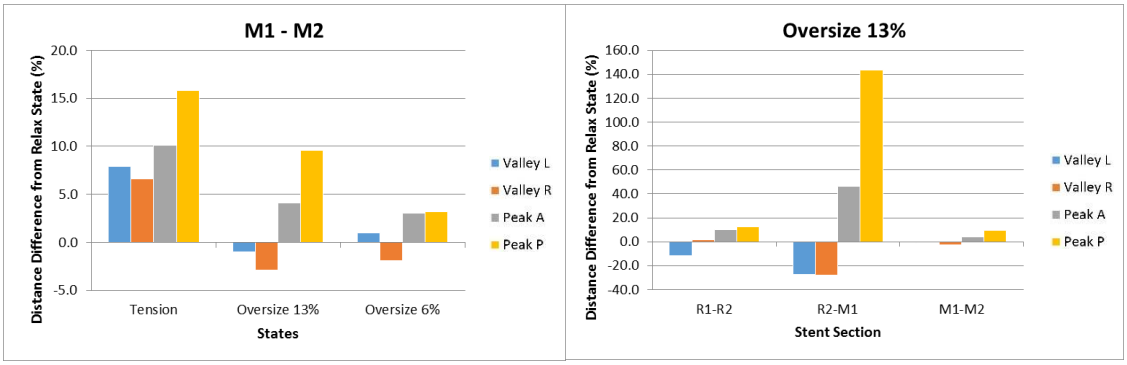

Fig. B.4 Fabric testing results of the body module of OLB30 device. Considering the rest state of the endograft as the baseline, the relative change of distance between each pair of rings is calculated per location (column A) and state (column B).

OLB32

Along the length of the device	Along the state of the device
(A)	(B)

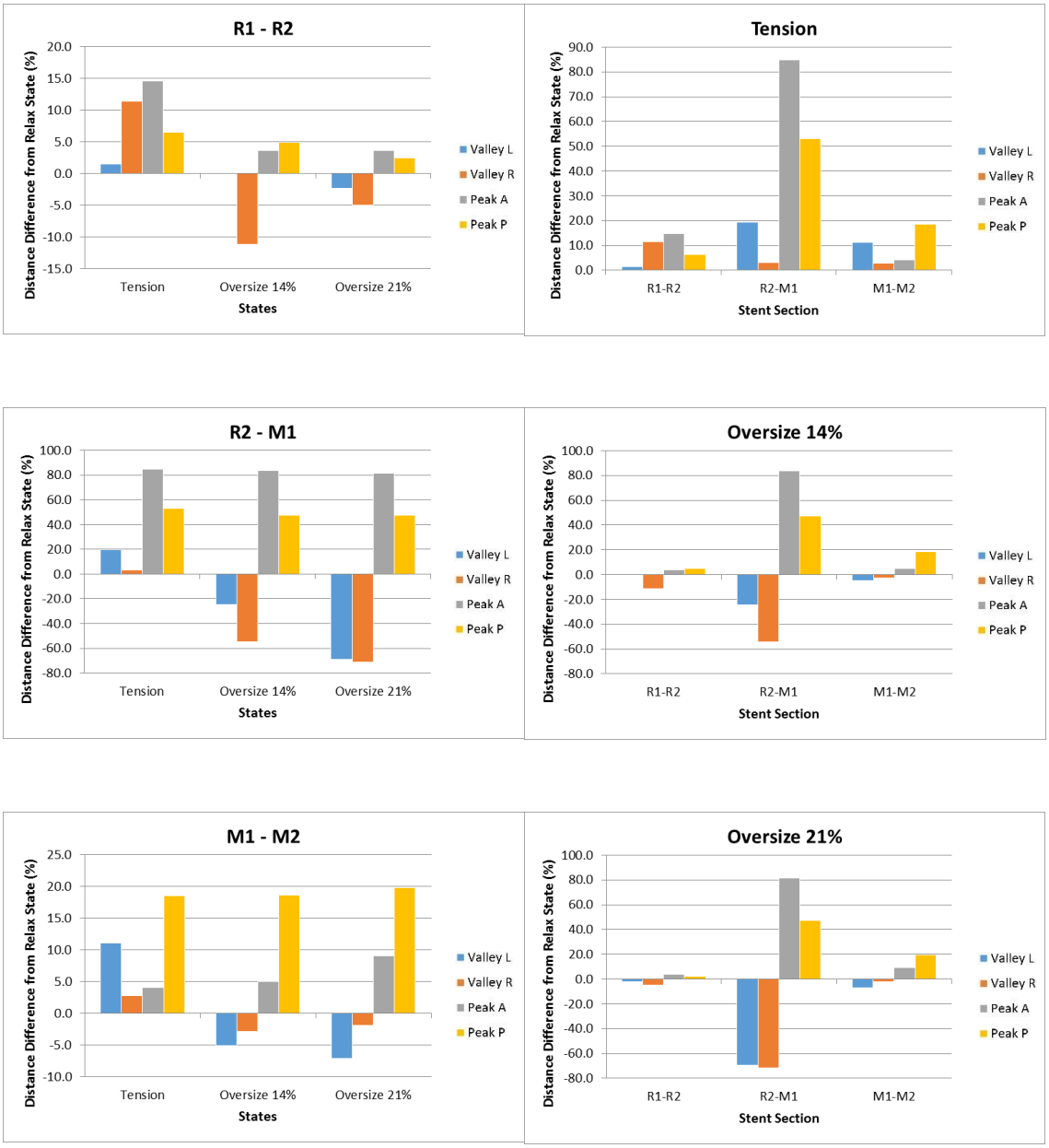

Fig. B.5 Fabric testing results of the body module of OLB32 device. Considering the rest state of the endograft as the baseline, the relative change of distance between each pair of rings is calculated per location (column A) and state (column B).

OLB34

Along the length of the device	Along the state of the device
(A)	(B)

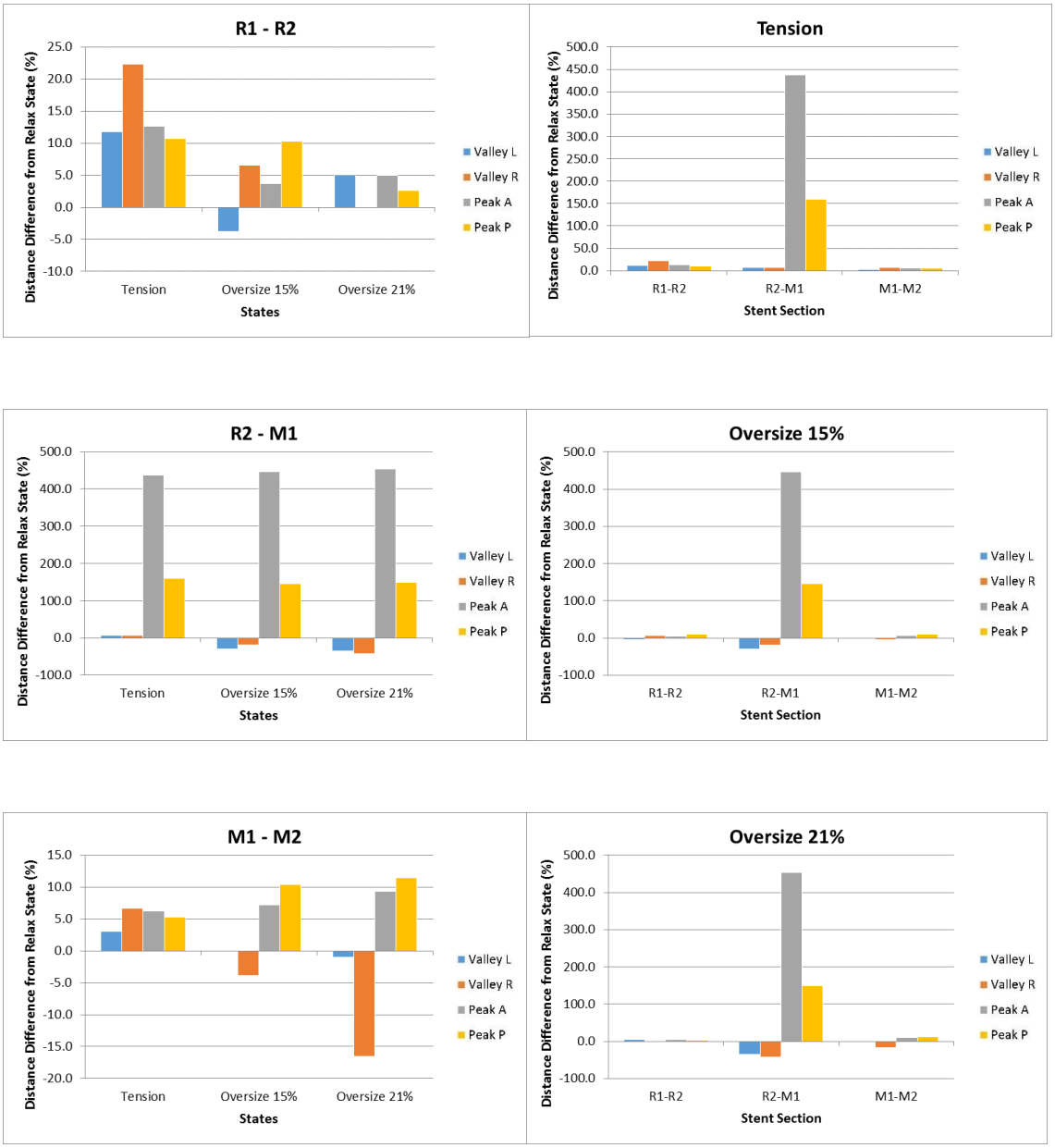

Fig. B.6 Fabric testing results of the body module of OLB34 device. Considering the rest state of the endograft as the baseline, the relative change of distance between each pair of rings is calculated per location (column A) and state (column B).